**Title**
Flame Structure and Soot Formation in Inverse Diffusion Flames (Ph.D. Dissertation)



**Author**
Mikofski, Mark A

**Publication Date**
2005-12-20

Flame Structure and Soot Formation in Inverse Diffusion Flames

by

Mark Alexander Mikofski

B.S. (Boston University) 1993
M.S. (University of California, Berkeley) 2004

A dissertation submitted in partial satisfaction of the

requirements for the degree of

Doctor of Philosophy

in

Engineering – Mechanical Engineering

in the

GRADUATE DIVISION

of the

UNIVERSITY OF CALIFORNIA, BERKELEY

Committee in charge:

Professor A. Carlos Fernandez-Pello
Professor Robert Dibble
Professor Robert Harley
Dr. Linda G. Blevins

Fall 2005

The dissertation of Mark Alexander Mikofski is approved:

| | |
|---|---|
| Chair | Date |
| | Date |
| | Date |
| | Date |

University of California, Berkeley

Fall 2005

**Abstract**

Flame Structure and Soot Formation in Inverse Diffusion Flames

by

Mark Alexander Mikofski

Doctor of Philosophy in Engineering – Mechanical Engineering

University of California, Berkeley

Professor A. Carlos Fernandez-Pello, Chair

Flame structure and soot and carbon monoxide (CO) formation were studied in laminar co-flowing co-annular inverse diffusion flames (IDFs) in normal and microgravity. An IDF is a non-premixed flame that consists of an inner air flow surrounded by a fuel flow. Soot formation is important to understand because soot particles are a health concern and have a strong influence on flame radiation, while CO formation is important because of the role it plays in fire-related deaths. Soot formation in normal diffusion flames (NDFs) is difficult to study because soot forms in the center of the flame and is oxidized so that soot cannot be sampled easily. Soot formation can be studied more easily in IDFs because soot forms on the fuel side of the reaction zone, is convected away from the reaction zone without oxidizing, and cools quickly. Therefore, in IDFs, newly formed soot is easier to sample than in NDFs. Soot formation was studied in microgravity IDFs because buoyancy-induced vortices that affect soot formation are eliminated in the absence of gravity. Flame structure of IDFs must be understood because it determines where soot and CO are formed and how they evolve.

IDFs are also useful for studying soot and CO formation in underventilated fires because both IDFs and underventilated fires have insufficient oxygen for complete combustion. Therefore, they both emit unoxidized soot, CO, and other products of incomplete combustion. Soot emission from underventilated fires also contributes to rapid fire spread due to increased radiation heat transfer.

Laser diagnostics, including planar laser-induced fluorescence of hydroxyl radicals (OH PLIF) and polycyclic aromatic hydrocarbons (PAH PLIF) and planar laser-induced incandescence of soot particles (soot PLII), thermocouple probing, and video imaging, were used to study the flame structure and distributions of temperature, soot and PAH in ethylene and methane IDFs. Comparison of OH PLIF with visible images and thermocouple temperature measurements in an ethylene IDF showed that peak OH PLIF occurred on the air side very close to the reaction zone and coincided with peak temperature. Reaction zone height determined by OH PLIF was found to be less than visible flame height because the reaction zone was masked by luminous soot in an annular region around and above the reaction zone. Reaction zone heights increased with air flow rate and were predicted well using a modified version of Roper's analysis for co-flowing co-annular NDFs.

Soot PLII was observed in ethylene IDFs on the fuel side very close to the reaction zone. Comparisons of radial profiles of soot PLII to radiation-corrected thermocouple temperature measurements in an ethylene IDF showed that, close to the reaction zone, peak soot PLII coincided with a temperature of about 1300 K. This temperature is known from the literature to be the minimum critical temperature for soot formation. Radially integrated soot PLII increased with axial position until a position

downstream of the flame height, leveling off to a maximum constant value, in agreement with the trend reported in a previously published IDF soot extinction study. The fact that the soot PLII continued to increase downstream of the flame tip suggests that soot inception ceases above the reaction zone and that soot growth can occur at temperatures below the critical inception temperature, and consequently that IDFs may be used to isolate soot growth. The maximum radially integrated soot PLII increased linearly with increasing air flow rate, indicating that bulk soot production rate is proportional to near-reaction zone residence time.

In both methane and ethylene IDFs, PAH PLIF was observed on the fuel side of the reaction zone, outside the soot zone but close to it. The proximity of PAH to the soot layer suggests it may be a constituent in soot formation, in agreement with the literature. The intensity of PAH PLIF was an order of magnitude greater in ethylene IDFs than in methane IDFs. Radially integrated PAH PLIF increased monotonically with axial position for both fuels. PAH PLIF and predicted streamlines from computer modeling indicated that buoyancy-induced vortices occurred above the reaction zone where PAH and soot were present. Comparisons of PAH PLIF to computer modeling of an ethylene IDF showed that PAH PLIF followed predicted streamlines, temperature isotherms, and contours of constant mixture fraction.

Microgravity IDFs did not flicker, were more luminous, were slightly longer, were more rounded, and radiated more energy than IDFs in normal gravity. Soot, PAH, and other condensed materials collected from post combustion gases of IDFs had a greater fraction of elemental carbon in microgravity than in normal gravity. The elemental carbon fraction increased as air flow rate increased, and was also greater in

ethylene IDFs than methane IDFs for both gravity conditions, which indicates that IDFs produce carbonized soot as well as soot precursor particles and that microgravity IDFs produce more carbonaceous soot than normal gravity NDFs. In both gravity conditions, IDFs emitted CO as a major component of the exhaust stream. Emission of CO was slightly greater in microgravity than in normal gravity and increased with air flow rate, which suggests that CO formation depends on residence time. Buoyancy-induced vortices that affected soot and PAH formation in normal gravity were eliminated in microgravity.

Chair Date

For my maternal grandmother

Isabel Salgado

(1922-2005)

an independent woman

who always lived life on her own terms.

## Table of Contents


Abstract ..... 1
Table of Contents ..... ii
List of Figures ..... v
List of Tables ..... ix
Acknowledgments ..... x
Chapter 1: Introduction ..... 1
1.1 Motivation ..... 1
1.2 Background ..... 2
1.2.1 Inverse Diffusion Flames ..... 2
1.2.2 Flame Structure and Soot Formation ..... 4
1.2.3 Laser Diagnostics ..... 5
1.2.4 Microgravity ..... 6
1.3 Organization of Chapters ..... 7
1.4 References ..... 9
Chapter 2: Literature Review ..... 12
2.1 Overview ..... 12
2.2 Inverse Diffusion Flames ..... 12
2.3 Analytical Solutions of Laminar Diffusion Flames ..... 16
2.4 Smoke Point Measurement in Laminar Diffusion Flames ..... 19
2.5 Experimental Measurements in Laminar Diffusion Flames ..... 26
2.6 References ..... 32
Chapter 3: Flame Height of Laminar Inverse Diffusion Flames ..... 36
3.1 Introduction ..... 36
3.2 Experimental Methods ..... 38
3.2.1 Apparatus ..... 38
3.2.2 Laser Diagnostics and Optics ..... 40
3.3 Analytical Methods ..... 42
3.4 Results and Discussion ..... 43
3.4.1 Experimental Results ..... 43
3.4.2 Comparison of Experiment to Analysis ..... 47
3.5 Conclusions ..... 53
3.6 References ..... 55
Chapter 4: Flame Structure of Laminar Inverse Diffusion Flames ..... 57
4.1 Introduction ..... 57
4.2 Experimental Methods ..... 59
4.2.1 Apparatus ..... 59
4.2.2 Laser Diagnostics ..... 60
4.2.2.1 Laser and Camera Configurations ..... 60
4.2.2.2 OH and PAH PLIF ..... 61
4.2.2.3 Soot PLII ..... 62
4.2.2.4 Analysis of Laser Measurements ..... 64
4.2.3 Temperature Measurements ..... 66
4.3 Computational Methods ..... 67
4.4 Results and Discussion ..... 67

4.4.1 Instantaneous Images of Flickering in PLIF and PLII of Ethylene IDFs . 67
4.4.2 Images of OH and PAH PLIF in Ethylene IDFs ... 69
4.4.3 Images of Soot PLII in Ethylene IDFs ... 72
4.4.4 Color Visible Images of Ethylene IDFs ... 74
4.4.5 Images of OH and PAH PLIF in Methane IDFs ... 75
4.4.6 Color Visible Images of Methane IDFs ... 78
4.4.7 Comparison of PAH PLIF from Ethylene IDFs Detected in Different Bands ... 79
4.4.8 Intensity of OH PLIF in Ethylene and Methane IDFs ... 80
4.4.9 Intensity of PAH PLIF in Ethylene IDFs ... 82
4.4.10 Intensity of Soot PLII in Ethylene IDFs ... 88
4.4.11 Intensity of PAH PLIF in Methane IDFs ... 91
4.4.12 Temperature, PLIF and PLII Measurements in an Ethylene IDF ... 94
4.4.13 Results of Computer Modeling of an Ethylene IDF ... 99
4.5 Summary and Conclusions ... 101
4.6 References ... 105
Chapter 5: Soot Formation in Microgravity Inverse Diffusion Flames ... 108
5.1 Introduction ... 108
5.2 Experimental Methods ... 109
5.2.1 Apparatus ... 109
5.2.2 Procedures ... 117
5.2.3 Analysis ... 119
5.3 Computational Methods ... 121
5.4 Results and Discussion ... 122
5.4.1 Images of microgravity IDFs ... 122
5.4.2 Radiometer and Temperature Measurements ... 123
5.4.3 CO Analyzer Measurements ... 125
5.4.4 OCEC Measurements ... 127
5.4.5 Computational Particle Tracking ... 129
5.5 Conclusions ... 132
5.6 References ... 134
Chapter 6: Conclusions ... 136
6.1 Flame Heights ... 136
6.2 Flame Structure ... 137
6.3 Microgravity ... 139
Chapter 7: Appendices ... 142
7.1 Matlab Functions for Analysis of Laser Diagnostics ... 142
7.1.1 OH Flame Heights ... 142
7.1.1.1 Ethylene ... 143
7.1.1.2 Methane ... 144
7.1.2 Visible Flame Heights ... 145
7.1.2.1 Visible High ... 145
7.1.2.2 Visible Low ... 146
7.1.3 Image files ... 147
7.1.3.1 Images of OH PLIF and PAH PLIF ... 147
7.1.3.2 Instantaneous Images of OH PLIF and PAH PLIF ... 148

7.1.3.3 Images of Soot PLII ..... 148
7.1.3.4 Instantaneous Images of Soot PLII ..... 149
7.1.3.5 Images of Visible IDFs ..... 150
7.1.4 Analysis ..... 151
7.1.4.1 Analysis of OH PLIF and PAH PLIF in Ethylene IDFs ..... 151
7.1.4.1.1 Ethylene IDFs from 0 to 48.2 mm above Burner ..... 151
7.1.4.1.2 Ethylene IDFs from 22.7 to 73.9 mm above Burner ..... 155
7.1.4.2 Analysis of OH PLIF and PAH PLIF in Methane IDFs ..... 157
7.1.4.3 Analysis of Soot PLII from Ethylene IDFs ..... 160
7.1.4.3.1 Ethylene IDFs from 0 to 48.2 mm above Burner ..... 160
7.1.4.3.2 Ethylene IDFs from 22.7 to 73.9 mm above Burner ..... 162
7.2 DDACS Programs ..... 164
7.3 PAH PLIF and Soot PLII Versus Non-Dimensional Height ..... 167
7.3.1 Ethylene IDFs ..... 168
7.3.2 Methane IDFs ..... 171

## List of Figures

Figure 1.1: Over and Underventilated Normal Diffusion Flames and an Inverse Diffusion Flame..... 3
Figure 3.1: Schematic diagram of burner. ..... 39
Figure 3.2: Schematic of Laser Assembly ..... 41
Figure 3.3: Images of 2.7 slpm methane IDF: (a) OH PLIF and (b) visible flame..... 44
Figure 3.4: Visible and OH PLIF flame heights of ethylene IDFs. Visible (low) shows flames with air flow rates from 1.2 slpm to 2.2 slpm with the burner in the lower position, and Visible (high) shows flames with air flow rates from 1.0 slpm to 1.8 slpm with the burner in the upper position. ..... 45
Figure 3.5: Visible and OH PLIF flame heights of methane IDFs. Visible (low) shows flames with air flow rates from 1.8 slpm to 2.7 slpm with the burner in the lower position, and Visible (high) shows flames with air flow from 1.2 slpm to 2.6 slpm with the burner in the upper position. ..... 46
Figure 3.6: Flame heights of ethylene IDFs predicted using Roper's analysis modified for IDFs compared to measured OH PLIF flame heights..... 48
Figure 3.7: Flame heights of methane IDFs predicted using Roper's analysis modified for IDFs compared to measured OH PLIF flame heights..... 49
Figure 3.8: Flame heights measured by OH PLIF from ref. [18] compared to heights predicted by Roper's analysis. ..... 51
Figure 4.1: Beam Profile and Soot PLII Correction Function ..... 64
Figure 4.2: Two instantaneous images of 1.0-slpm air flow rate ethylene IDF. (a) OH and PAH PLIF detected with 340 nm band-pass filter. (b) Soot PLII detected with 570 nm long-pass filter. ..... 69
Figure 4.3: Two instantaneous images of 2.2-slpm air flow rate ethylene IDF. (a) OH and PAH PLIF detected with 340 nm band-pass filter. (b) Soot PLII detected with 570 nm long-pass filter. ..... 69
Figure 4.4: Color-maps of time-averaged OH and PAH PLIF detected with 340 nm band pass filter from ethylene IDFs of varying air flow rates with contours of peak PLIF and PLII overlaid in white. (a) PAH PLIF from 22.7 mm to 73.9 mm above burner with scaling factor of 13440. The signal for the 1.62 slpm air flow rate IDF is low because the laser was blocked. (b) PAH and OH PLIF from 0 mm to 48.2 mm above burner with scaling factor of 10000. The intensity of the PLIF signals is color-mapped such that black, blue, green, red, and white represent increasing intensity, respectively. ..... 71
Figure 4.5: Color-maps of time-averaged soot PLII detected with 570 nm long pass filter from ethylene IDFs of varying air flow rates with contours of peak PLIF and PLII overlaid in white. (a) Soot PLII from 22.7 mm to 73.9 mm above burner with scaling factor of 33907. (b) Soot PLII from 0 mm to 48.2 mm above burner with scaling factor of 37450. The intensity of the PLII signals is color-mapped such that black, blue, green, red, and white represent increasing intensity, respectively. ..... 73
Figure 4.6: Visible color images of ethylene-air IDFs with contours of the peak time-averaged PLIF and PLII signals overlaid..... 75
Figure 4.7: Color-maps of time-averaged OH and PAH PLIF detected with 340 nm band pass filter from methane IDFs of varying air flow rates with contours of peak PLIF

overlaid in white. The intensity of the PLIF signals is scaled by a factor of 6200 and color-mapped such that black, blue, green, red, and white represent increasing intensity, respectively. ..... 77
Figure 4.8: Visible color images of methane-air IDFs with contours of the peak time-averaged PLIF signals overlaid. ..... 79
Figure 4.9: Comparison between the peak PAH PLIF position in ethylene IDFs detected with a 340 nm band-pass filter and with a combination of the 295 nm long-pass and 450 nm short-pass filters. ..... 80
Figure 4.10: Peak OH PLIF of ethylene IDFs detected with 340 nm band pass filter. .... 81
Figure 4.11: Peak OH PLIF of methane IDFs detected with 340 nm band pass filter. .... 82
Figure 4.12: PLIF detected with 340 nm band-pass filter in ethylene IDFs versus axial position. (a) Peak PAH PLIF, (b) radially integrated PLIF and (c) centerline PLIF from 0 mm to 45.1 mm, (a), (c) and (e), and 25.7 mm to 70.8 mm, (b), (d) and (f), above the burner. ..... 85
Figure 4.13: PLIF detected with 295 nm long-pass and 450 nm short-pass filters in ethylene IDFs versus axial position. (a) Peak PAH PLIF, (b) radially integrated PLIF and (c) centerline PLIF from 0 mm to 45.1 mm, (a), (c) and (e), and 25.7 mm to 70.8 mm, (b), (d) and (f), above the burner. ..... 87
Figure 4.14: Soot PLII detected with 570 nm long-pass filter in ethylene IDFs versus axial position. (a) Peak PAH PLIF, (b) radially integrated PLIF and (c) centerline PLIF from 0 mm to 45.1 mm, (a), (c) and (e), and 25.7 mm to 70.8 mm, (b), (d) and (f), above the burner. ..... 89
Figure 4.15: Maximum radially integrated soot PLII signal versus air flow rate for ethylene IDFs. ..... 90
Figure 4.16: PLIF detected with a 340 nm band-pass filter in methane IDFs versus axial position. (a) Peak PAH PLIF, (b) radially integrated PLIF and (c) centerline PLIF from 0 mm to 45.1 mm, (a), (c) and (e), and 25.7 mm to 70.8 mm, (b), (d) and (f), above the burner. ..... 92
Figure 4.17: PLIF detected with 295 nm long-pass and 450 nm short-pass fiters in methane IDFs versus axial position. (a) Peak PAH PLIF, (b) radially integrated PLIF and (c) centerline PLIF from 0 mm to 45.1 mm, (a), (c) and (e), and 25.7 mm to 70.8 mm, (b), (d) and (f), above the burner. ..... 94
Figure 4.18: Radial profiles of PLIF detected with 340 nm band-pass filter, PLIF detected with 295 nm long-pass and 450 nm short-pass filter combination, soot PLII, temperature measurements and predicted temperature from the model in a 1.6 slpm air flow rate ethylene IDF at axial positions of (a) 11 mm, (b) 15 mm, (c) 20 mm and (d) 25 mm. ..... 98
Figure 4.19: Contours of predicted mixture fraction (left) and temperature (right) overlaid on PLIF detected with 340 nm band-pass filter of 2.2-slpm air flow rate ethylene IDF. Mixture fraction contours are in increments of 0.10 and temperature contours are in increments of 500 K. The predicted stoichiometric contour (Z = 0.064) is shown as a dashed white line. ..... 99
Figure 4.20: Contours of predicted mixture fraction (left) and temperature (right) overlaid on PLIF detected with 295 nm long-pass and 450 nm short-pass filters of 2.2-slpm air flow rate ethylene IDF. Mixture fraction contours are in increments of 0.10 and

temperature contours are in increments of 500 K. The predicted stoichiometric contour (Z = 0.064) is shown as a dashed white line. ..... 100
Figure 4.21: Predicted average streamlines overlaid on average PLIF and soot PLII of a 2.2-slpm ethylene IDF. (a) PLIF detected with 340 nm band-pass filter. (b) PLIF detected with 295 nm long-pass filter and 450 nm short-pass filter. (c) Soot PLII detected with 570 nm long pass filter. ..... 101
Figure 5.1: (a) Standard NASA A-frame drop rig and (b) combustion chamber. ..... 110
Figure 5.2: Schematic of fuel and air delivery system. ..... 111
Figure 5.3: Schematic of combustion chamber fill/monitoring and vent system. ..... 112
Figure 5.4: Interconnect schematic of electrical system. ..... 115
Figure 5.5: Igniter assembly. ..... 116
Figure 5.6: Images of 2.4 slpm $CH_4$ IDF in 1-g (a) and (b) and in μ-g (c). Images (a) and (b) show two stages of 1-g fluctuations. All images were taken with an aperture setting of f/#8. ..... 122
Figure 5.7: Images of 2.4 slpm $C_2H_4$ IDF in 1-g (a) and (b) and in μ-g (c). Images (a) and (b) show two stages of 1-g fluctuations. All images were taken with an aperture setting of f/#16. ..... 123
Figure 5.8: Temporal profile of radiation from IDFs in Figure 5.6 and Figure 5.7. ..... 124
Figure 5.9: Corrected temperature from IDFs in Figure 5.6 and Figure 5.7 measured on centerline 3.5 cm above burner. ..... 124
Figure 5.10: CO concentration, calculated $CO_2$ concentration, and calculated molar concentration ratio of CO to $CO_2$ in microgravity ethylene IDFs with varying air flow rate. ..... 127
Figure 5.11: Elemental carbon fraction (EC/TC) of material collected on filters from microgravity ethylene IDFs with varying air flow rate. ..... 129
Figure 5.12: Computed temperature contours for μ-g $CH_4$ and $C_2H_4$ IDFs. Stoichiometric contours are shown in black and tracer particle trajectories are shown in white. ..... 130
Figure 5.13: Time-temperature histories of tracer particles in μ-g and 1-g $CH_4$ and $C_2H_4$ IDFs. Particles were inserted at a chosen minimum soot inception temperature of 1250 K on the fuel side of the flame and at the axial location indicated next to each curve. ..... 132
Figure 7.1: PLIF detected with 340 nm band-pass filter in ethylene IDFs versus non-dimensional height, defined as axial position divided by flame height determined by OH PLIF. (a) Peak PAH PLIF, (b) radially integrated PLIF and (c) centerline PLIF from 0 mm to 45.1 mm, (a), (c) and (e), and 25.7 mm to 70.8 mm, (b), (d) and (f), above the burner. ..... 168
Figure 7.2: PLIF detected with 295 nm long-pass and 450 nm short-pass filters in ethylene IDFs versus non-dimensional height, defined as axial position divided by flame height determined by OH PLIF. (a) Peak PAH PLIF, (b) radially integrated PLIF and (c) centerline PLIF from 0 mm to 45.1 mm, (a), (c) and (e), and 25.7 mm to 70.8 mm, (b), (d) and (f), above the burner. ..... 169
Figure 7.3: Soot PLII detected with 570 nm long-pass filter in ethylene IDFs versus non-dimensional height, defined as axial position divided by flame height determined by OH PLIF. (a) Peak PAH PLIF, (b) radially integrated PLIF and (c) centerline PLIF from 0 mm to 45.1 mm, (a), (c) and (e), and 25.7 mm to 70.8 mm, (b), (d) and (f), above the burner. ..... 170

Figure 7.4: PLIF detected with a 340 nm band-pass filter in methane IDFs versus non-dimensional height, defined as axial position divided by flame height determined by OH PLIF. (a) Peak PAH PLIF, (b) radially integrated PLIF and (c) centerline PLIF from 0 mm to 45.1 mm, (a), (c) and (e), and 25.7 mm to 70.8 mm, (b), (d) and (f), above the burner..... 171
Figure 7.5: PLIF detected with 295 nm long-pass and 450 nm short-pass fiters in methane IDFs versus non-dimensional height, defined as axial position divided by flame height determined by OH PLIF. (a) Peak PAH PLIF, (b) radially integrated PLIF and (c) centerline PLIF from 0 mm to 45.1 mm, (a), (c) and (e), and 25.7 mm to 70.8 mm, (b), (d) and (f), above the burner. ..... 172

## List of Tables

Table 3.1: Flow Conditions..... 39
Table 5.1: Parts list of components in fuel and air delivery system and combustion chamber fill/monitoring and vent system ..... 113
Table 5.2: Measurements of radiative loss and fraction, CO concentration, molar concentration ratio of CO to CO2 and elemental carbon fraction in 1-g and μ-g $CH_4$ and $C_2H_4$ IDFs..... 125

## Acknowledgments

First I would like to thank my professors who have guided and mentored me in academia and research. Carlos Fernandez-Pello introduced me to the topic of combustion and has been my research advisor for the last five years. Carlos has often gone out of his way to make sure that his students were happy. Robert Dibble served on my qualifying, master project, and dissertation committees. Although I have never taken a course from Dibble, he has supported me every step of the way through graduate school. Robert Harley served on both my qualifying and dissertation committees, and was my air quality modeling instructor. Michael Frenklach served as the chair of my qualifying committee, and was also my instructor for energy transfer. Omer Savas also served on my qualifying committee and was my instructor for fluid mechanics.

I also need to thank many other professionals who have guided my research. Linda Blevins was the principal investigator of the NASA project COSMIC, on which I've worked for the past five years. Linda has patiently guided my research and given me numerous opportunities that I could not have experienced at UC Berkeley. Chris Shaddix and Timothy Williams worked with me on laser diagnostics. Ron Davis and Elizabeth Moore helped with modeling. Peter Sunderland, Kurt Sacksteder, and Douglas Feikema were the COSMIC project contacts at NASA. Peter was especially helpful in setting up COSMIC. Lew and Mark helped with the drop tower experiments. Eric Baumann was the drop tower manager. James Withrow and many others at NASA also helped tremendously.

I must give thanks to many the people who I worked with at UC Berkeley. Nothing would get done in Hesse Hall if weren't for MaryAnne Peters, Scott McCormick, Mike Neufer, and Pete Graham. My fellow labmates, Amnon Bar-Ilan, Dave Rich, Guillermo Rein, Olivier Putzeys, Kevin Macko, Chris Lautenberger, Bennett Sprague, Sang Won Park and Albert Dato made 60 Hesse Hall a great place to work. I would also like to thank the many undergraduates who worked with me, Magu Diagne, Ryan Niblock, Mary Louie, Petar Kis, and Steve Lee. An especially big thanks to Gordon Long who helped me in the student machine shop in Etcheverry.

To my friends, Peter, Elysia, Emily, Anni, Jake, Jamie, Susan, and Suzanne, and my roommates Bonnie, Merhawi, Hannah, Maverick, and Joe, thanks for keeping me going in the hard times with laughter and fun. Finally the most important thanks go to my family, Mom, Maggie, Dave, and Grandma. Thanks for being there for me. I owe you everything.

# Chapter 1: Introduction

## 1.1 Motivation

Accidental fires in the United States have caused over 140,000 deaths since 1977, according to the National Fire Protection Safety Association. Nearly two-thirds of those deaths were caused by the inhalation of toxic emissions that may include carbon monoxide (CO), soot, and soot precursors, such as polycyclic aromatic hydrocarbons (PAH), that form in underventilated fires [1,2]. Soot is also an important factor in the rapid spread of accidental fires through radiation heat transfer [3-6]. Soot in the form of particulate matter is a health concern and also a regulated pollutant that is receiving increased attention from the government due to studies that reveal that ultra-fine particles penetrate deep into the lungs [7,8]. Some soot precursors, such as PAH, are also known carcinogens [3].

Accurate soot formation models are needed to predict and control soot formation both as a fire safety tool and to meet increasingly strict government regulations. Although soot formation models have progressed significantly, soot inception and early soot growth are still not well understood [3,9-14]. Experimental results are needed to support the development of soot inception and growth models. Although there has been significant research on soot formation in laminar normal diffusion flames (NDFs), research on soot formation in underventilated flames has been limited [15]. It has been proposed that soot formation in underventilated conditions is similar to soot formation in inverse diffusion flames (IDFs) [16]. Therefore, studying soot formation in IDFs under well controlled test conditions could give further understanding of soot formation in

general and in underventilated fires in particular. Further, examining CO formation in IDFs could give insight into the generation of toxic substances in fires. Thus examining soot and CO formation in IDFs is the object of this work.

## 1.2 Background

### 1.2.1 Inverse Diffusion Flames

Figure 1.1 shows co-flowing over ventilated and underventilated NDFs and an IDF. In a co-flowing co-annular IDF, a central air jet is surrounded by an annular fuel jet [17]. This is the inverse of a co-flowing co-annular NDF, in which a central fuel jet is surrounded by an annular air jet. Soot and CO form on the fuel side of diffusion flames [18,19]. Therefore, soot and CO form on the inside of both over ventilated and underventilated NDFs because the fuel jet is in the center. In over ventilated NDFs, the flame tip is closed, so soot and CO oxidize while passing through the flame tip and are not emitted. However, in underventilated NDFs, soot and CO pass through the open tip of the flame and escape unoxidized. In IDFs, soot and CO form on the outside of the flame because the fuel jet is in the annulus. Therefore, soot and CO also escape unoxidized from IDFs, because soot and CO in IDFs never pass through the flame but instead are convected outward to cooler regions of the fuel stream [10,20,21]. Therefore, IDFs emit considerable quantities of soot and CO similar to underventilated combustion [1,19,22,23].

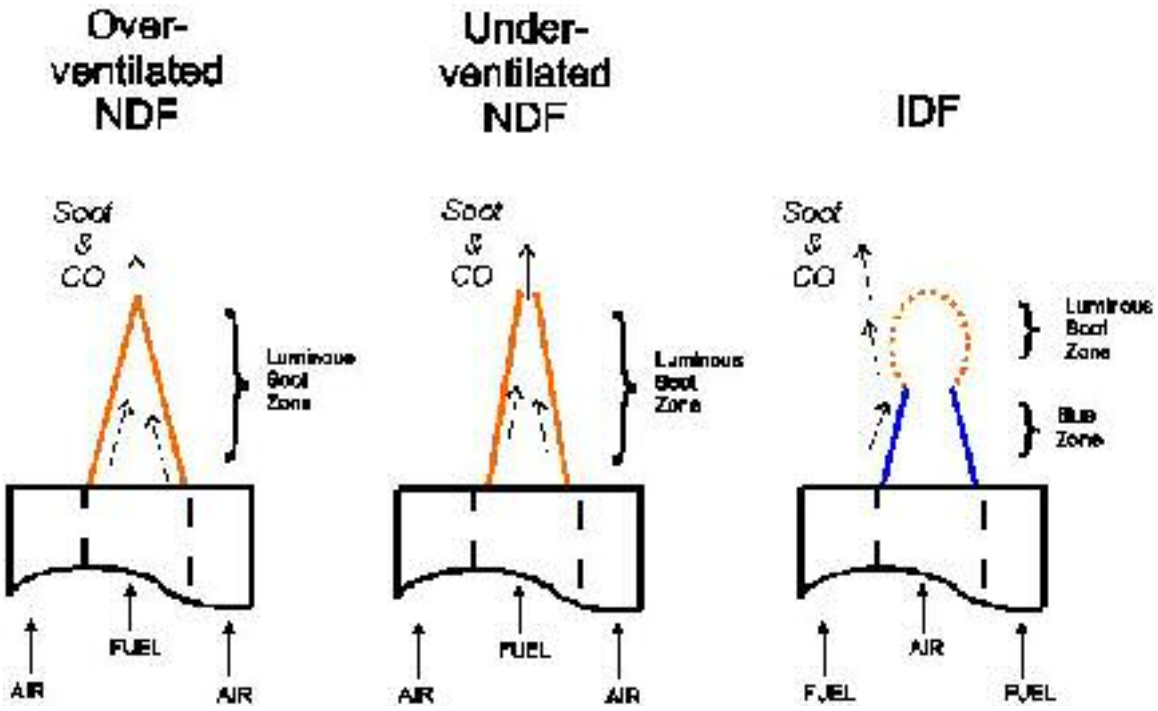


**Figure 1.1: Over and Underventilated Normal Diffusion Flames and an Inverse Diffusion Flame.**

The soot collected from IDFs is tar-like and has a high hydrogen content [24,25], similar in chemical composition and morphology to soot collected from underventilated NDFs. Since soot in IDFs forms on the outside of the flame, it may be sampled with less disturbance to the flame than in underventilated NDFs [19,23]. In addition, because IDF soot cools rapidly in the low temperature fuel stream and never passes through an oxidizing region, early soot inception and growth processes are more isolated than in NDFs, allowing a systematic study of the early stages of soot formation [10,19,23,24]. Therefore, IDFs may be used as a tool to study soot formation in underventilated fires and may provide useful insights into soot inception and growth.

### 1.2.2 Flame Structure and Soot Formation

Flame structure of diffusion flames is described in this work by the location of soot and PAH relative to the location of the reaction zone. Soot forms from pyrolyzates such as PAH on the fuel side of the flame close to the reaction zone above a critical temperature of 1300 K [3,10,26,27]. Soot is formed by inception, surface growth through coagulation and reaction with other soot particles, PAH, and intermediates of combustion, and agglomeration with other soot particles to form aggregates [10,13]. In over ventilated NDFs, soot also undergoes oxidation [28-32]. In contrast, soot escapes unoxidized in IDFs and underventilated NDFs.

PAH are located on the fuel side of diffusion flames along isotherms and contours of constant mixture fraction [19,33,34]. PAH consist of many different aromatic species, but the most abundant PAH in diffusion flames are believed to be naphthalene, acenaphthylene, and pyrene [33]. PAH are formed by thermal or oxidative pyrolysis of the fuel, and their formation is believed to be the rate limiting step in soot formation [10,34]. Pyrolysis and soot formation are strongly affected by fuel structure, temperature, fuel and radical concentrations and residence time [3,10]. At a given temperature, unsaturated fuels such as ethylene ($C_2H_4$) pyrolyze faster than saturated fuels such as methane ($CH_4$) because they dehydrogenize more easily [9,19]. Since pyrolysis and soot formation are functions of residence time at high temperature, the height of the reaction zone can be used to investigate the effect of bulk residence time on soot formation [35].

Flame structure of IDFs is the inverse of NDFs. Moving radially outward from the centerline in an IDF, the reaction zone is encountered first, then soot, and finally PAH. In an NDF, PAH is found encountered first, then soot, and finally the reaction

zone. Therefore, flame structure and near-flame soot formation in IDFs and NDFs could be similar [17]. Pyrolyzates form in the fuel stream, and soot forms from the pyrolyzates close to the reaction zone at a sufficiently high temperature [21]. The difference between soot formation in NDFs and IDFs lies in the time-temperature history of soot particles. In NDFs, soot forms inside the flame, moves by thermophoresis towards the center of the flame, and increases in temperature as it is convected upwards [29,32]. In an IDF, soot forms on the outside of the flame, is convected upwards, and moves by thermophoresis away from the flame towards cooler regions in the fuel stream where reactions are quenched [21,36]. Therefore, in IDFs, soot formation is physically isolated from soot oxidation [19,23], but there is also limited time at high temperature for soot growth, so soot inception and early soot growth can be studied [20].

### 1.2.3 Laser Diagnostics

Laser diagnostics can be used investigate flame structure and the formation of soot and PAH. Location and concentration of soot can be measured using planar laser-induced incandescence (soot PLII) [37,38]. PLII heats soot particles to vaporization temperatures, approximately 4000 K, and causes soot particles to emit thermal radiation in the visible or near infrared range of the electromagnetic spectrum [39,40]. The laser fluence dependence of soot PLII is very complex and is discussed in depth in Chapter 4.

The location and concentration of PAH can be measured by planar laser-induced fluorescence (PAH PLIF). PAH absorbs both ultraviolet (UV) and visible light and emits broadband fluorescence [34,41]. The curve of PAH PLIF emission intensity versus wavelength is roughly bell shaped with a faster drop off at shorter wavelengths. Peak

PAH PLIF emission from UV excitation occurs at a wavelength slightly greater than the excitation wavelength. As excitation wavelength is increased peak, PAH PLIF occurs closer to the excitation wavelength. Large PAH, which are thought to be more likely to participate in soot formation, form at higher temperature and are detected at longer wavelengths than smaller PAH [33,34,41-46].

The location of the reaction zone separating the fuel and oxidizer in diffusion flames can be found by PLIF of hydroxyl radicals (OH). The height of the reaction zone can also be found from OH PLIF. This is especially useful for IDFs since soot radiation masks the blue emission usually used to locate the reaction zone [16]. The reaction zone can be identified by OH PLIF since OH exists on the air side of diffusion flames very close to stoichiometric conditions and peak temperatures [47]. Excitation of OH radicals at 282 nm causes relatively temperature independent fluorescence of lines near 310 nm [48].

### 1.2.4 Microgravity

Microgravity can be used to remove buoyancy-induced vortices that cause flickering in normal gravity diffusion flames [49]. Flickering in an IDF affects soot and PAH formation in a complex manner, by mixing soot and PAH and causing recirculation of these substances into high temperature regions [37,38,42,50]. Therefore, it is desired to remove flickering to isolate soot inception and study newly formed soot particles.

In the absence of buoyancy, gas velocities are lower since there is no buoyant acceleration. Since normal and microgravity flames on circular port burners are about the same size [51], residence time for soot formation is generally longer in microgravity. In

fact, microgravity flames on circular port burners are slightly longer and wider than their normal gravity counterparts because of radial convection [52-54]. Microgravity flames are brighter and produce more soot because the residence time for soot formation is longer [3,53]. Increasing air flow rate in microgravity flames also increases residence time and soot formation tendency [10,51]. Therefore, newly formed soot particles are most easily studied in microgravity IDFs.

### 1.3 Organization of Chapters

Chapter 2 contains a literature review. The history of IDF research is discussed. Since aspects of flame structure and soot formation are similar in all diffusion flames, NDFs and counter-flow flames are also discussed. Chapter 3 presents results of IDF reaction zone height measured using OH PLIF and flame height measured visibly. In addition, in Chapter 3, a modification of Roper's analytical solution for flame height is introduced and compared with measured reaction zone height. Chapter 4 discusses the flame structure of IDFs as revealed by OH PLIF, PAH PLIF, and soot PLII. The effects of varied air flow rate on PAH and soot production is examined. Finally, the results of the laser diagnostics are overlaid on temperature measurements and computer simulations to draw conclusions about flame structure and the formation of soot and PAH. Chapter 5 present results from microgravity experiments in which images were recorded, flame radiation and temperature were measured, and post combustion gases were sampled for soot elemental carbon fraction as well as CO concentration. The effects of variation in air flow on the soot elemental carbon fraction and CO concentration in the exhaust gases

is also discussed. Chapter 6 summarizes the observations and conclusions on soot, CO, and PAH formation in IDFs found in this study.

## 1.4 References

[1]. A. Tewarson, J. Steciak, Combust. Flame 53 (1-3) (1983) 123-134.

[2]. W.M. Pitts, Prog. Energy Combust. Sci. 21 (3) (1995) 197-237.

[3]. B.S. Haynes, H.Gg. Wagner, Prog. Energy Combust. Sci. 7 (4) (1981) 229-273.

[4]. C.W. Lautenberger, J.L. de Ris, N.A. Dembsey, J.R. Barnett, H.R. Baum, Fire Safety Journal 40 ( 2) (2005) 141-176.

[5]. J.L. De Ris, P.K. Wu, G. Heskestad, in: 28th International Symposium on Combustion, Jul 30-Aug 4 2000, Combustion Institute, Edinburgh, United Kingdom, 2000, p. 2751.

[6]. J.L. De Ris, Proc. Combust. Inst. 17 (1978) 1003-1015.

[7]. J.S. Lighty, J.M. Veranth, A.F. Sarofim, Journal of the Air and Waste Management Association 50 (9) (2000) 1565-1618.

[8]. K.M. Butler, G.W. Mulholland, Fire Technology 40 (2) (2004) 149-176.

[9]. R.L. Schalla, G.E. McDonald, Proc. Combust. Inst. 5 (1955) 316-324.

[10]. I. Glassman, Proc. Combust. Inst. 22 (1988) 295-311.

[11]. I.M. Kennedy, Prog. Energy Combust. Sci. 23 (2) (1997) 95-132.

[12]. A. D'anna, A. D'alessio, J. Kent, Combust. Sci. Technol. 174 (11-2) (2002) 279-294.

[13]. M. Frenklach, Physical Chemistry Chemical Physics 4 (11) (2002) 2028-2037.

[14]. F. Liu, H.S. Guo, G.J. Smallwood, O.L. Gulder, Combustion Theory and Modelling 7 (2) (2003) 301-315.

[15]. S. Leonard , G.W. Mulholland, R. Puri, R.J. Santoro, Combust. Flame 98 (1-2) (1994) 20-34.

[16]. L.G. Blevins, R.A. Fletcher, B.A. Benner, E.B. Steel, G.W. Mulholland, Proc. Combust. Inst. 29 (2003) 2325-2333.

[17]. K.T. Wu, R.H. Essenhigh, in: Twentieth Symposium (International) on Combustion, The Combustion Institute, Pittsburgh, 1984, p. 1925.

[18]. K.T. Kang, J.Y. Hwang, S.H. Chung, W. Lee, Combust. Flame 109 (1-2) (1997) 266-281.

[19]. G.W. Sidebotham, I. Glassman , Combust. Flame 90 (3-4) (1992) 269-283.

[20]. J.H. Kent, H.G. Wagner, Zeitschrift Fur Physikalische Chemie-Wiesbaden 139 (1984) 59-68.

[21]. C.R. Shaddix, C.W. Williams, L.G. Blevins, R.W. Schefer, Proc. Combust. Inst. 30 (2005) 1501-1508.

[22]. J.R. Arthur, B.T. Commins, A.S. Gilbert, A.J. Lindsey, D.H. Napier, Combust. Flame 2 (1958) 267-272.

[23]. G.W. Sidebotham, I. Glassman , Combust. Sci. Technol. 81 (4-6) (1992) 207-219.

[24]. J.R. Arthur, D.H. Napier, Proc. Combust. Inst. 5 (1955) 303-316.

[25]. J.R. Arthur, P.K. Kapur, D.H. Napier, Nature 169 (1952) 372-373.

[26]. R.A. Dobbins, Combust. Flame 130 (3) (2002) 204-214.

[27]. J. Du, R.L. Axelbaum, Combust. Flame 100 (3) (1995) 367-375.

[28]. R.J. Santoro, H.G. Semerjian, R.A. Dobbins, Combust. Flame 51 (2) (1983) 203-218.

[29]. R.J. Santoro, H.G. Semerjian, Proc. Combust. Inst. 20 (1984) 997-1006.

[30]. R.J. Santoro, T.T. Yeh, J.J. Horvath, H.G. Semerjian, Combust. Sci. Technol. 53 (2-3) (1987) 89-115.

[31]. J.H. Kent, H.G. Wagner, Combust. Flame 47 (1) (1982) 53-65.

[32]. J.H. Kent, H.Gg. Wagner, Proc. Combust. Inst. 20 (1984) 1007-1015.

[33]. G. Prado, A. Garo, A. Ko, A.F. Sarofim, Proc. Combust. Inst. 20 (1984) 989-996.

[34]. K.C. Smyth, J.H. Miller, R.C. Dorfman, W.G. Mallard, R.J. Santoro, Combust. Flame 62 (2) (1985) 157-181.

[35]. E.J. Lee, K.C. Oh, H.D. Shin , Fuel 84 (5) (2005) 543-550.

[36]. D.B. Makel , I.M. Kennedy, Combust. Sci. Technol. 97 (4-6) (1994) 303-314.

[37]. C.R. Shaddix, K.C. Smyth, Combust. Flame 107 (4) (1996) 418-452.

[38]. C.R. Shaddix, J.E. Harrington, K.C. Smyth, Combust. Flame 99 (3-4) (1994) 723-732.

[39]. R.J. Santoro, Shaddix C.R., in: K. Kohse-Höinghaus, J.B. Jeffries (Eds.), Applied Combustion Diagnostics, Taylor & Francis, New York, 2002, p. 252.

[40]. A.C. Eckbreth, J. Appl. Phys. 48 (11) (1977) 4473-4479.

[41]. J.H. Miller, W.G. Mallard, K.C. Smyth, Combust. Flame 47 (1982) 205-214.

[42]. K.C. Smyth, C.R. Shaddix, D.A. Everest, Combust. Flame 111 (3) (1997) 185-207.

[43]. R.L. Vanderwal, K.A. Jensen, M.Y. Choi, Combust. Flame 109 (3) (1997) 399-414.

[44]. F. Ossler, T. Metz, M. Alden , Applied Physics B-Lasers and Optics 72 (4) (2001) 465-478.

[45]. F. Ossler, T. Metz, M. Alden, Applied Physics B-Lasers and Optics 72 (4) (2001) 479-489.

[46]. A. Leipertz, F. Ossler, M. Aldén, in: K. Kohse-Höinghaus, J.B. Jeffries (Eds.), Applied Combustion Diagnostics, Taylor & Francis, New York, 2002, p. 359.

[47]. K.C. Smyth, P.J.H. Tjossem, A. Hamins, J.H. Miller, Combust. Flame 79 (3-4 ) (1990) 366-380.

[48]. K.C. Smyth , D.R. Crosley, in: K. Kohse-Höinghaus, J.B. Jeffries (Eds.), Applied Combustion Diagnostics, Taylor & Francis, New York, 2002, p. 9.

[49]. V.R. Katta, L.G. Blevins, W.M. Roquemore, Combust. Flame 142 (1-2) (2005) 33-51.

[50]. J. Zhang, C.M. Megaridis, Combust. Flame 112 (4) (1998) 473-484.

[51]. F.G. Roper, Combust. Flame 29 (1977) 219-226.

[52]. C. Aalburg, F.J. Diez, G.M. Faeth, P.B. Sunderland, D.L. Urban, Z.-G. Yuan, Combust. Flame 142 (1-2) (2005) 1-16.

[53]. P.B. Sunderland, S.S. Krishnan, J.P. Gore, Combust. Flame 136 (1-2) (2004) 254-256.

[54]. P.B. Sunderland, B.J. Mendelson, Z.G. Yuan, D.L. Urban, Combust. Flame 116 (3) (1999) 376-386.

# Chapter 2: Literature Review

## 2.1 Overview

This chapter provides a review of the research conducted on IDFs. Since flame structure of IDFs is similar to other diffusion flames, and the mechanism of soot formation is believed to be similar in all diffusion flames, NDFs and counter flow flames are also discussed. Section 2.2 is devoted to the history of the study of IDFs. Section 2.3 discusses the introduction of the flame sheet concept and the development of the analytical solutions of the temperature and species fields in diffusion flames. Section 2.4 discusses the literature on soot formation in diffusion flames, beginning with the measurement of smoke point. The final section discusses published experimental measurements in diffusion flames that are used to investigate flame structure and soot formation. The final section also briefly describes the HACA method of soot and PAH growth.

## 2.2 Inverse Diffusion Flames

Burke and Schumann [1] briefly mention IDFs in their landmark paper in 1928 on the analysis of diffusion flames. Burke and Schumann compared measured heights of several IDFs of CO with calculated heights and obtained good results. Arthur and coworkers [2-4] studied IDFs of coal gas, methane, ethylene, and propane in the 1950s. Arthur and coworkers found that the soot collected from IDFs was tarry and contained higher hydrogen content than soot from NDFs. Infrared spectroscopy of the soluble fraction of soot from IDFs showed the presence of oxygen in the forms of carbonyl and

hydroxyl groups. Arthur and coworkers also found acetylene and PAH in the soot collected from IDFs.

Wu and Essenhigh, in 1984 [5], presented stability maps of methane IDFs, obtained by systematically varying air and methane flow rates. Wu and Essenhigh found that, at very low fuel co-flows, the flames were unstable. At moderate fuel flow rates, increasing air flow rate caused IDFs to transition from non-sooting to sooting conditions. They modeled an IDF using the analysis of Burke and Schumann modified by Gosman [6]. Wu and Essenhigh found good agreement between temperature and species measurements and predictions, except for higher concentrations of CO and $H_2$ measured at the tip of the IDF.

In 1984, Kent and Wagner [7] studied ethylene IDFs enclosed in a glass tube, and reported that buoyancy-induced recirculation occurred in the outer fuel stream. Kent and Wagner observed that soot formed on the fuel side 2 mm from the reaction zone and did not pass through the oxidation region. They also found that temperature in the soot formation zone was lower and had a gradient steeper in IDFs than in NDFs. Kent and Wagner postulated that the temperature in between the soot formation region and the reaction zone might influence soot formation.

Sidebotham and Glassman [8,9] published two papers on IDFs in 1992. In the first paper, Sidebotham and Glassman observed that, as oxygen was added to the fuel stream, the products of combustion shifted from pyrolyzates to oxidative products and did not cause a transition from non-sooting to sooting conditions. In the second paper, Sidebotham and Glassman stated that the formation of an aromatic ring is the controlling step in soot formation. By varying flame temperature, they observed that soot formation

occurred only when a critical temperature was exceeded in a region sufficiently far from the oxidation region on the fuel side. Fuel structure was also a parameter in determining soot formation. Methane IDFs produced considerably less acetylene than other fuels. Aromatic production also scaled with fuel sooting tendency.

In 1994, Makel and Kennedy [10] studied ethylene IDFs and compared measured and predicted temperature and soot volume fraction. They found that soot formed on the fuel side of the reaction zone at a temperature of 1300 K and was emitted unoxidized. Integrated soot volume fraction increased linearly until an axial position above the flame height, peaked, and then remained constant. This is similar to smoking underventilated NDFs [11], but it is in contrast to non-smoking over ventilated NDFs in which integrated soot volume fraction decreases to zero at an axial position close to the flame height [12]. Makel and Kennedy also reported that peak measured soot volume fractions were lower in IDFs than previously reported for NDFs.

Kang *et al.* studied IDFs and counter-flow flames in 1997 [13]. Kang *et al.* observed that in NDFs, IDFs, and counter-flow flames, soot formed on the fuel side of the reaction zone. In counter-flow flames in which the reaction zone was located on the air side of the stagnation plane and in IDFs, soot did not oxidize after formation but was convected and moved by thermophoresis away from the reaction zone.

In 2001, Kaplan and Kailasanath [14] modeled an IDF and tracked soot particles along pathlines. Kaplan and Kailasanath predicted that peak soot volume fraction was considerably less in IDFs than in NDFs. They also predicted that surface growth was slower in IDFs than in NDFs. They concluded that residence time of soot particles in the

high temperature region near the reaction zone was an influential parameter in soot formation.

Blevins *et al.* in 2002 [15] studied soot particles from an ethylene IDF using transmission electron microscopy, mass spectrometry, and analysis of organic carbon and elemental carbon fractions. Blevins *et al.* concluded that soot emitted from IDFs was chemically and morphologically similar to both precursor particles collected by Dobbins *et al.* [16,17] and soot emitted from underventilated NDFs studied by Leonard *et al.* [11]. Blevins *et al.* found that soot from IDFs was viscous and transparent and contained higher hydrogen content than soot from NDFs. PAH were also present in the IDF soot.

Sunderland *et al.* published the first images of IDFs in microgravity in 2004 [18]. Sunderland *et al.* noted that luminosity and soot formation of IDFs increased in microgravity. Microgravity IDFs were slightly longer and more rounded than normal gravity IDFs. Sunderland *et al.* also observed that IDFs reached steady state in 0.5 seconds, whereas NDFs were transient over a period of time greater than 2 seconds.

In 2004, Shaddix, *et al.* studied steady and pulsed methane and ethylene IDFs and NDFs on a Wolfhard Parker slot burner [19] using OH PLIF, PAH PLIF, and soot PLII. Shaddix *et al.* observed that the structure of IDFs is very similar to NDFs with soot forming close to the reaction zone on the fuel side and PAH forming close to soot further on the fuel side. They also observed that peak PAH PLIF signals and soot concentrations were moderately lower in IDFs than NDFs. Pulsed flames exhibited strong buoyancy-induced vortices on the fuel side that enhanced soot and PAH concentrations.

Katta *et al.* modeled an ethylene IDF in 2005 [20]. Modeling depicted strong buoyancy-induced vortices that form in the fuel stream and significantly affect PAH

concentration downstream of the reaction zone. Tracer particles, used in the model to simulate soot particles, were entrained in the vortices and did not cool monotonically.

In 2005, Oh *et al.* and Lee *et al.* studied ethylene IDFs [21,22]. Oh *et al.* observed that particles collected at low axial positions were tar-like and unagglomerated, but at increasing axial position soot particles aggregated and carbonized slightly, increasing in C/H ratio. Primary soot particles had a diameter of 20 nm measured by laser scattering. Lee *et al.* found that ethylene IDFs were more stable than the methane NDFs tested by Wu and Essenhigh [5]. Lee *et al.* observed that IDFs had flame structure similar to NDFs using OH PLIF, PAH PLIF, and laser scattering of soot particles. Flame height of IDFs in which fuel was diluted with nitrogen were predicted well by the analysis of Burke and Schumann [1]. Soot, the position of which was determined by observing visible radiation, appeared in a temperature range of 1550-1600 K. Soot growth was influenced by residence time and flame temperature.

## 2.3 Analytical Solutions of Laminar Diffusion Flames

Burke and Schumann were the first to analyze the structure of laminar co-flowing co-annular NDFs and make the assumption that chemical kinetics occurred much faster than diffusion [1]. Therefore, the reaction zone could be described by an infinitely thin flame sheet and a one-step global reaction that consumed all fuel and air in stoichiometric proportions. Species and energy conservation equations were simplified into a single scalar equation that could be solved to yield flame shape and height, as well as temperature and species profiles by making the following assumptions: constant uniform laminar axisymmetric velocity; constant uniform density, specific heat, and diffusion

coefficient; unity Lewis number; adiabatic walls; negligible radiation and buoyancy; steady state conditions; and negligible axial diffusion and conduction [23]. Despite the many seemingly improbable assumptions, solutions agreed fairly well with experiments.

Many researchers made subsequent improvements to the Burke-Schumann analysis by reducing some of the assumptions while keeping the primary assumption of infinitely fast reaction rate [6,24-30]. Mitchell *et al.* used a computer numerical code originally developed by Gosman *et al.* to solve the set of differential equations that arise when species thermodynamic properties are allowed to vary and obtained very good results with experiment [29]. Roper allowed axial velocity to vary with height and, by comparison with experiments, developed an often used correlation for NDF flame height for circular burners that depends only on fuel flow rate and stoichiometric air to fuel volume ratio of the specific fuel type. Roper also determined that, in buoyant flames on circular port burners, the competing effects of decreased advection time and decreased diffusion time cancel [27,28]. Advection time is decreased by buoyant acceleration. Diffusion time is decreased by a combination of the increased concentration gradient and decreased effective diffusion distance, which are both imposed by conservation of mass of the buoyantly accelerated flow at the flame tip. Therefore, buoyant and non-buoyant diffusion flames on circular port burners are nearly the same size. Roper analyzed square and rectangular port burners as well and developed correlations for momentum and buoyant regimes.

Schug *et al.* conducted experiments with fuels of various dilution and concluded that only flow rate of the fuel fraction determined flame height and not the total flow rate of fuel plus oxidizer [31]. Saito *et al.* varied oxygen fraction of the air and noted that

increasing oxygen content decreased flame height [32]. These effects are incorporated in Roper's analysis if the stoichiometric air to fuel volume ratio contains the pure fuel and oxygen fractions of the diluted fuel and oxidizer streams, respectively. Li *et al.* improved Roper's analysis by showing that fuel specific diffusion coefficient and flame temperature improved agreement with experiment over the use of a single correlation for all fuels [30].

With the improvements made by Schug, Saito, and Li, Roper's analysis for NDFs on circular port burners yields the following equation for flame height, $H$,

$$H = Q\frac{\left(T_0 / T_f\right)^{2/3}}{4\pi D_0}\frac{1}{\ln\left(1+1/S\right)} \tag{2.1}$$

in which $Q$ is the fuel flow rate, $T_0$ is ambient temperature, $T_f$ is the characteristic fuel specific flame temperature, and $D_0$ is the characteristic fuel specific diffusion coefficient. The stoichiometric air to fuel volume ratio, $S$, is given by the equation

$$S = \frac{\alpha x_{fuel}}{x_{O_2}} \tag{2.2}$$

in which $x_{O_2}$ is the mole fraction of oxygen in the air stream, $x_{fuel}$ is the mole fraction of pure fuel in the diluted fuel stream, and $\alpha$ for a hydrocarbon fuel, $C_nH_m$, is given by $n + m/4$. If $S$ is sufficiently large, which is the case for undiluted hydrocarbon NDFs (*e.g.* for methane $S = 9.52$), then $\ln(1 + 1/S) \approx 1/S$, and the equation for flame height becomes

$$H = \frac{QS\left(T_0 / T_f\right)^{2/3}}{4\pi D_0} = \frac{Qx_{fuel}\alpha\left(T_0 / T_f\right)^{2/3}}{4\pi x_{O_2} D_0}, \tag{2.3}$$

which explains the observations made by Schug and Saito regarding fuel dilution and oxygen enrichment. However, Eq. 2.3 is not valid for IDFs because, as will be discussed

in Chapter 3, $S$ is defined as its reciprocal and is therefore very small (*e.g.* for methane IDFs $S = 0.105$) so $\ln(1 + 1/S) \neq 1/S$.

## 2.4 Smoke Point Measurement in Laminar Diffusion Flames

Soot in laminar diffusion flames was originally studied by researchers to reduce the smoke produced by burning coal in industrial burners while increasing the radiant output, which was more effective for heat transfer [3]. Early soot research focused on the formation of smoke in NDFs [31,33]. Smoke, which contains soot, soot precursors such as PAH, and other intermediates such as CO, has often been used as an analog for soot [11,34,35]. Measurements were made of the minimum rate of fuel flow at which smoke was visibly emitted from NDFs [31,33,34,36-38]. This measurement of the propensity to form soot was called the smoke point and, since flame height is primarily determined by fuel flow rate in NDFs, the smoke point has often been reported as the minimum flame height at which smoke is emitted [37,39]. The tendency to form soot has an inverse relation with smoke point; in other words, a low smoke point means a high tendency to soot.

Observations were made of the effects on smoke point of buoyant laminar NDFs on enclosed circular port burners with air co-flows by varying different parameters such as pressure, fuel type, air co-flow, air oxygen content, flame temperature, and fuel dilution with oxygen, inert gases and other additives that either enhanced or suppressed soot formation. All fuels showed an inverse relation between smoke point and pressure, *i.e.* increasing pressure increases the tendency to form soot. This effect was observed by Schalla *et al.* over a range of pressures from 0.5 to 4 atm [33]. The effect of pressure is

caused by the inverse relation between pressure and diffusion coefficient. Therefore, as pressure increases, diffusion coefficient decreases and mixing occurs at a decreasing rate [33,34]. From Roper's analysis, Eq. 2.1, flame height is inversely proportional to diffusion coefficient [27], so decreasing diffusion coefficient increases flame length. Therefore, for a given flow rate as pressures increases so does flame length and residence time for soot formation. Increase in temperature due to increased pressure may also enhance sooting [37].

Decreasing air co-flow from twice overall stoichiometric increased flame height and decreased smoke point [36]. Conversely, increasing air co-flow from twice overall stoichiometric increased smoke point for all fuels asymptotically until a limiting smoke point was reached, and further increases in air flow did not increase the smoke point above this limit [33]. The decrease in soot tendency with increasing secondary air flow was associated with increased diffusion rate, similar to the pressure argument, and thus related to flame height [33,36]. The asymptotic effect occurs because, when secondary air is present in large excess of stoichiometric, further increase in air flow will not affect flame height [36]. Therefore, flame height and residence time are parameters that affect soot formation.

The effects of other parameters could not be explained by simple physical processes such as diffusion and were interpreted as chemical processes. Tests of blended fuels showed that initial C/H ratio does not alone determine tendency to soot [31,40]. For example, a blend of acetylene ($C_2H_2$) and ethane ($C_2H_6$) was seen to produce more soot than ethylene ($C_2H_4$) but less soot than butene ($C_4H_8$), even though in all three flames the

C/H ratio is 0.5, the fuel flow rates and hence flame heights and residence times were equal, and the measured maximum flame temperatures were very close [40].

Variation of fuel type revealed that smoke point increases with the level of saturation, and that conjugated fuels, such as butadiene, had the highest propensity to soot [31,37,41]. Aliphatic fuels such as methane and ethane were less likely to soot than aromatics such as benzene. The hierarchy of soot tendency among aliphatic fuels was alkynes > alkenes > alkanes. For example, acetylene had a lower smoke point than ethylene, which had a lower smoke point than ethane [31,33,34,37]. Iso-alkanes and other branched isomers were also more likely to soot [33,34]. A correlation was found between soot tendency and stability of carbon bonds in the fuel [33]. The alternating double and single bonds of conjugated species and the ring structure of aromatics are the most stable. Triple bonded carbons (200 kcal/mole) have a higher bond strength than double bonded carbons (150 kcal/mole), but single bonded carbons (80 kcal/mole) have an even lower bond strength than carbon-hydrogen bonds (100 kcal/mole). Since dehydrogenization is most likely to occur in unsaturated fuels, hydrogen abstraction was proposed as a crucial chemical step in pyrolysis and soot formation. The easier hydrogen is removed from a fuel, the more quickly it pyrolyzes and the greater its tendency to soot. Dehydrogenization generates hydrogen radicals (H) that accelerate pyrolysis [33,37]. Alkanes have the lowest tendency to soot because it is more likely that carbon-carbon bonds will break than that dehydrogenization will occur. However, there is recent evidence that methyl radicals may play a role in soot formation [42].

Increasing the oxygen content of the air had the very interesting result that, for fuels with a high soot tendency, smoke point first decreased and then, at a critical oxygen

fraction, began to increase. In other words, a small increase in oxygen fraction increased sooting tendency, but a large increase in oxygen fraction decreased soot tendency. For fuels with low soot tendencies, increasing oxygen content increased smoke point monotonically. Replacing nitrogen with argon in normal air increased flame temperature and caused smoke point to decrease for fuels with high soot tendencies but, as oxygen content was increased in the argon-oxygen mixture, smoke point began to increase at a lower critical oxygen fraction than it had for nitrogen-air mixtures. For fuels with low soot tendency replacing nitrogen with argon in normal air had no effect, but, as oxygen content was increased in the argon-oxygen mixture, the faster increase in smoke point than for nitrogen-air mixtures was also observed [33]. An increase in dehydrogenization of the fuel due to higher temperature as oxygen content was increased or when argon was substituted for nitrogen was postulated to be responsible for the initial increase in soot tendency for the heavily sooting fuels. Decreasing soot tendency as oxygen content was increased further was thought to be caused by direct reaction of oxygen with soot forming intermediates. For fuels with low soot tendency, increasing temperature may have caused carbon-carbon bonds to break instead of dehydrogenization, leading to quicker oxidation instead of soot formation since oxidizing reactions have a stronger dependence on temperature than pyrolysis [33,34,37].

The effect of fuel additives that either suppress soot formation, such as sulfur dioxide ($SO_2$), carbon dioxide ($CO_2$), water ($H_2O$), nitrogen ($N_2$), argon (Ar), and helium (He), or enhance soot formation, such as nitrous oxide ($N_2O$), oxygen ($O_2$), and halogenated compounds such as Freon-12 ($CCl_2F_2$), have also shed light on soot formation. Increase in smoke point by addition of inert gases and water was due to

thermal effects, as indicated by the correlation between their effectiveness in reducing soot tendency and their molar specific heats [31,34]. Decreasing temperature reduces pyrolysis and soot formation [40,43]. Since $SO_2$ has the largest molar specific heat, it reduced soot tendency the most, and likewise He, which has the smallest molar specific heat, reduced soot tendency the least of the inert diluents tested. The high diffusion coefficient of He enhanced heat transfer, making NDFs wider and reducing slightly the decrease in soot tendency.

Proposed chemical effects due to the production of hydroxyl radicals (OH) from water by reaction with H atoms produced in pyrolysis were rejected for three reasons. First, they were rejected because of the relation observed with respect to the other diluents that suppressed soot formation and their respective molar specific heats. Second, it is more likely that H atoms will react with fuel to enhance pyrolysis because of the much larger concentration of fuel. Third, because the concentration of H atoms is small compared to the concentration of other species, and H atoms react quickly, it is unlikely that H atoms will react with water. Similar arguments were used to reject hypothetical chemical effects of $SO_2$ and $CO_2$ [31,34]. Reduction in soot tendency by inert diluents could not attributed to thermal effects alone, but it was also affected by decreasing fuel concentration [40].

Since temperature is such an important parameter in pyrolysis [37], a unique set of experiments by Du and Axelbaum that combined oxygen enrichment of the air stream and nitrogen dilution of the fuel stream by reassigning nitrogen from the air stream to the fuel stream, therefore maintaining constant adiabatic flame temperature, were very important [38]. In ethylene NDFs, as nitrogen was transferred from the air side to the

fuel side, the smoke point increased monotonically. The decreased soot tendency was attributed to fuel dilution and an increase in OH radicals that consumed soot precursors.

Addition of oxidizers ($O_2$ and $N_2O$) to the fuel had an effect on smoke point similar to oxygen enrichment of the air stream. Small addition of oxidizer to the fuel stream increased soot tendency dramatically, but large addition reduced soot tendency. This effect depends on fuel structure, and even adding small amounts of oxygen to methane flames increased the smoke point [32,37]. As in the case of oxygen enriched air, alkanes are more likely to break carbon bonds, and radicals that enhance pyrolysis and soot formation are not likely to form [37]. For fuels of greater soot tendency, the initial increase in soot tendency with increasing oxidizer addition was attributed to oxidative pyrolysis and an increase in the production of OH radicals that also accelerate pyrolysis [44] as well as increase in flame temperature [37]. Since the concentration of fuel is much higher than the concentration of soot precursors, small additions of oxidizer are more likely to cause reactions between radicals, especially OH, and fuel. When large amounts of oxidizer are added, radical attack of soot precursors occurs. Therefore, enhancement of pyrolysis by small oxidizer addition increases soot formation, and consumption of soot precursors by oxidizing radicals with large oxidizer addition decreases soot formation [31,34]. The initial increase in soot tendency caused by $O_2$ addition was greater than that for addition of $N_2O$. The effect of the addition of halogenated compounds was quite surprising since halogenated compounds have been used to suppress combustion due to their high specific heat, which lowers flame temperature, and due to the removal of H atoms by halogen radicals. However, $CCL_2F_2$ (Freon-12) decreased smoke point more than both $O_2$ and $N_2O$. The proposed

explanation was that, at flame temperatures, dissociation produces halogen atoms that attack the fuel similar to oxidizing radicals that enhance pyrolysis. Similar to other chemical arguments, the concentration of fuel is much greater than H atoms and halogen radicals are more likely to react with fuel than H atoms [31,34].

Because soot forms on the fuel side outside of the reaction zone and is emitted without passing through the reaction zone and oxidizing, the concept of smoke point, when smoke is first emitted from a flame, has no meaning in an IDF [7]. However, measurements similar to smoke point in IDFs to observe the propensity to form soot have been made by dilution of the air or fuel with nitrogen or argon, by addition of oxygen to fuel, and by control of adiabatic flame temperature by using nitrogen or argon fuel dilution and oxygen air enrichment. It was found nitrogen dilution of the air or fuel stream suppressed soot formation in IDFs more than in NDFs, which was attributed to the steeper temperature gradient in the region between the reaction zone and soot region in IDFs [7]. Addition of trace oxygen to ethylene heavily diluted with nitrogen in a near sooting IDF did not cause a transition to a sooting IDF, which may have been due to the very low fuel concentration [9]. Increase in adiabatic flame temperature by replacing nitrogen with argon as fuel diluent, maintaining constant fuel concentration and oxygen enrichment of the air stream, caused a near sooting ethylene IDF to transition to sooting [8]. Increase in adiabatic flame temperature by changing oxygen enrichment of the air stream and nitrogen dilution of the fuel stream while maintaining constant flame height also caused near sooting ethylene, methane, propene ($C_3H_6$), and butene ($C_4H_8$) IDFs to transition to sooting [8]. The results show that temperature is a critical parameter in soot formation and that fuel concentration and flame height are also important.

## 2.5 Experimental Measurements in Laminar Diffusion Flames

The results of smoke point measurements yielded many important clues about the formation of soot. The most important of these was that soot formation is controlled by fuel pyrolysis [37]. Fuel pyrolysis is greatly affected by fuel structure, temperature, fuel concentration and the presence of radicals, especially OH and H. Furthermore, fuel pyrolysis occurs by dehydrogenization. By simple physical arguments, residence time was also found to be an important factor in soot formation [33,40,45]. A mechanism for soot formation began to develop, based on the connection between soot and pyrolysis, that consisted of two steps: inception and growth [33,34]. The species involved in these two steps were subjects of intense controversy, but by and large most researchers agreed that PAH built by polymerization of pyrolyzates were precursors to soot formation [2-4,41]. Researchers also speculated that other intermediates of combustion might also be involved [2-4,9]. The next stage in soot research delved into this debate by concentrating on measurements within diffusion flames of gas species, temperature, velocity, soot volume fraction, soot particle number density, mean soot particle diameter, soot morphology and soot composition to gain a better picture of the chemistry responsible for soot formation [2-5,7-13,15-17,19,21,22,29,36,37,40,42-68].

Flame configurations were not limited to co-flowing co-annular NDFs and IDFs but also included co-flowing Wolfhard-Parker (rectangular slot) NDFs and IDFs, and counter-flow diffusion flames. IDFs were used to sample soot and soot precursors without disturbing the flame greatly since soot and soot precursors form on the outside of the reaction zone. In addition, IDFs were thought to separate soot inception and growth

processes from oxidation that normally occurs in NDFs. Also, IDFs were thought to produce soot similar to underventilated combustion because the overall stoichiometry is very rich. Therefore, IDFs could yield substantially more unoxidized soot, soot precursors and CO than over-ventilated NDFs [2-5,7-10,13,15,21,22]. Wolfhard-Parker burners were used specifically with laser diagnostics because the two-dimensional flame eliminates the need for tomographic inversion that is required with circular burners [19,44,46,47,49,52]. Counter-flow flames were used because, similar to IDFs, the various stages of soot formation are separated spatially. In addition, the flat flames produced in the counter-flow configuration, like Wolfhard-Parker flames, do not require tomographic inversion when used with laser diagnostics [13,38,59,67].

A variety of diagnostic tools was used to obtain experimental measurements. Temperature was measured by thermocouple [5,7-10,29,38,40,42-46,49,59,63]. Gas species were extracted by quartz microprobe for gas chromatography (GC) [5,29] and/or mass spectrometry (MS) [8,9,15,42,48,49,63,67]. Temperature and gas species concentrations were also measured using Rayleigh and anti-Stokes Raman scattering [63]. Velocity was measured using laser Doppler velocimetry (LDV) [13,29,38,45,46,49]. Measurements were made *in situ* by laser-induced fluorescence (LIF) specifically for hydroxyl radicals (OH) [19,21,49,52] and polycyclic aromatic hydrocarbons (PAH) [12,13,19,21,43,47,48,58,61,64].

Soot volume fraction was measured using a variety of techniques including laser extinction (LE) [10,12,13,36,40,43-46,54,59,68], laser-induced incandescence (LII) [19,22,42,54,56,58,66,68], and thermocouple particle densitometry (TPD) [59]. Soot particle number density and soot mean particle size were measured using elastic laser

scattering (LS) in both the Rayleigh limit and with full Mie analysis [12,13,21,43-46,48,49,54,56,68]. Soot volume fraction, soot particle number density, and soot mean particle size were also measured using rapid insertion thermophoretic sampling on copper micro-grids coupled with transmission electron microscopy (TEM) [22,44,50,53,60,62] Soot morphology was also observed using TEM [11,15,16,21,50,51,53,57,60,62]. Soot composition was analyzed using extractive sampling onto quartz filters from which the analyzate was dissolved in solvent and analyzed by infrared absorption spectroscopy [2-4]. Another method used for the analysis of the composition of soot collected on quartz filters was a thermo-optical method which reports the organic and elemental carbon content contained on the quartz filter in units of mass per area [11,15,69]. Laser-microprobe mass spectrometry (LMMS) was also used for the analysis of soot composition [15-17]. Many other analytical methods that are too numerous to list here were also used.

Comparisons of modeling and gas and temperature experiments showed that the infinitely thin reaction sheet was a good assumption for both NDFs and IDFs [5,29]. Results of gas analysis showed that major products at various axial and radial positions scaled with local equivalence ratio [29,49]. The reaction zone, where the local equivalence ratio is near unity, was marked by the location where fuel and oxygen ($O_2$) concentrations approached zero; however, $O_2$ was found to diffuse onto the fuel side of the flame in very small concentrations [5,9,29,49]. Peak water and carbon dioxide ($CO_2$) concentrations were also located at the reaction zone [5,9,29,49]. Temperature also scaled with local equivalence ratio, and its peak also coincided with the reaction zone [5,9,29,49]. Carbon monoxide (CO) and hydrogen ($H_2$), found on the fuel side of the

reaction zone in concentrations smaller than those of other species, peaked very close to the reaction zone and also scaled with equivalence ratio [5,9,29,49]. Blue emission was located on the fuel side of the reaction zone and was associated with CH chemiluminescence [70] and the burnout of CO to energized $CO_2$ that gave off blue light as it relaxed [5,29]. Luminous yellow soot radiation was located just to the fuel side of the blue emission and obscured the blue emission at increasing height in heavily sooting flames [5,29]. The presence of $H_2$ is due to pyrolysis reactions [33]. Hydroxyl (OH) radicals were found on the air side of both NDFs and IDFs very close to the reaction zone [19,21,49,52]. One obvious difference between over ventilated NDFs and IDFs was that, above the reaction zone in over ventilated NDFs, the concentrations of fuel, intermediates of combustion, and pyrolyzates approached zero [29], but, above the reaction zone in IDFs, fuel, intermediates of combustion, and pyrolyzates were still present and $O_2$ concentration approached zero [5,9].

Acetylene ($C_2H_2$) was also found on the fuel side and peaked close to the reaction zone in both NDFs and IDFs of different fuels [8,9,49]. Butadiene ($C_4H_6$), benzene ($C_2H_6$) and various PAH were found in smaller concentrations than acetylene on the fuel side, and all peaked very close to the location of peak $C_2H_2$ [8,9,12,13,19,21,43,47-49,58,61,64]. Acetylene, butadiene, benzene and other PAH peak concentrations occurred on isotherms between 1000 and 1300 K and along contours of constant equivalence ratio [48,49]. Larger PAH were found closer to the soot layer than smaller aromatics [21,49,58]. Methane ($CH_4$) was also found on the fuel side in IDFs of different fuels [8,9]. The exhaust from ethylene IDFs contained greater concentrations of $C_2H_2$, $CH_4$, $H_2$, and CO than over ventilated NDFs [3]. Acetylene and methane form from

thermal and oxidative pyrolysis from all hydrocarbons [71]. Acetylene is a key species in the formation of larger PAH that form soot and may be the key species involved in soot particle surface growth [72]. Compared to other polycyclic aromatic hydrocarbons, naphthalene, acenaphthylene and pyrene were the most abundant [48].

Soot volume fraction was found to peak in between the peak concentration of PAH and the reaction zone at temperatures between 1200 and 1400 K [8,10,38,44,46,49]. Oxidation of soot particles was found to occur only above 1300 K [8,40]. Peak soot volume fractions in NDFs were between 1 and 10 ppm and were lower in IDFs [10,12,13,19,22,36,40,42-46,54,56,58,59,68]. Peak mean soot aggregate size in NDFs was found to be around 100 nm. In NDFs, maximum soot number density close to the reaction zone was between $10^{10}$ to $10^{12}$ $cm^{-3}$ and decreased rapidly further into the fuel stream [12,13,43-46,48,49,54,56,68]. Soot morphology showed that NDF soot particles grew by coagulation, surface reaction and agglomeration into aggregates formed of spherules 5 to 20 nm in diameter [11,15,16,21,22,50,51,53,57,60,62]. Analysis of soot particles in both NDFs and IDFs showed that they were composed of PAH and products of incomplete combustion [2-4,11,15-17]. Peak soot volume fraction varied with fuel structure in the same manner as smoke point. Addition of trace oxygen to fuel caused particle size to increase more rapidly and peak soot volume fraction to increase, but peak mean aggregate diameter was always the same [44]. Flickering in NDFs also increased soot volume fraction [54,56,61,62].

From the results of measurements within diffusion flames, a mechanism for soot formation evolved that complimented previous experiments on smoke point. Soot inception in co-flowing NDFs was found to occur low in the flame in an annular region

close to the reaction zone above a critical temperature near 1300 K by polymerization of pyrolyzates or reactive nucleation [12,43,45]. Temperature, fuel structure, fuel and radical concentration, and residence time were found to be crucial determinants of pyrolysis. Acetylene was found to be a key constituent in soot formation. After soot inception, soot growth by surface reaction with acetylene and possibly PAH and other products of combustion occurs. Soot growth can also occur by coagulation and agglomeration, whereby particles coalesce into a larger particle or join into aggregates [50,51,53]. Further research showed that soot particles become carbonized before they oxidize in over ventilated NDFs [55,57]. Newly formed soot precursor particles have a C/H ratio of about two and are tar-like and transparent to electron beams. Bulk carbonization of NDF soot particles occurs at temperatures above the soot inception temperature and abruptly raises the C/H ratio to a value between 6 and 8. The resulting carbonaceous soot particles radiate intensely at normal flame temperatures [55,73]. Many chemical and physical models have been proposed to model the growth and oxidation of particles and aggregates, but soot inception still remains a mystery [10,14,20,72,74-76].

One of the most widely accepted mechanisms for soot and PAH growth is the HACA mechanism proposed by Frenklach *et al.* [72]. HACA stands for H-abstraction/$C_2H_2$-addition. The process begins by the abstraction of a hydrogen atom from a soot particle or aromatic structure by a gaseous hydrogen atom, followed by the addition of an acetylene molecule to the radical site formed. The process repeats forming new aromatic structures causing soot and PAH growth.

## 2.6 References

[1]. S.P. Burke, T.E.W. Schumann, Proc. Combust. Inst. 1 (1928) 2.

[2]. J.R. Arthur , B.T. Commins, A.S. Gilbert, A.J. Lindsey, D.H. Napier, Combust. Flame 2 (1958) 267-272.

[3]. J.R. Arthur , D.H. Napier, Proc. Combust. Inst. 5 (1955) 303-316.

[4]. J.R. Arthur , P.K. Kapur, D.H. Napier, Nature 169 (1952) 372-373.

[5]. K.T. Wu, R.H. Essenhigh, in: Twentieth Symposium (International) on Combustion, The Combustion Institute, Pittsburgh, 1984, p. 1925.

[6]. A.D. Gosman , W.M. Pun, A.K. Runchal, D.B. Spalding, M. Wolfshtein, Heat and Mass Transfer in Recirculating Flows, Academic Press, London, 1969.

[7]. J.H. Kent, H.G. Wagner, Zeitschrift Fur Physikalische Chemie-Wiesbaden 139 (1984) 59-68.

[8]. G.W. Sidebotham, I. Glassman, Combust. Flame 90 (3-4) (1992) 269-283.

[9]. G.W. Sidebotham, I. Glassman, Combust. Sci. Technol. 81 (4-6) (1992) 207-219.

[10]. D.B. Makel , I.M. Kennedy, Combust. Sci. Technol. 97 (4-6) (1994) 303-314.

[11]. S. Leonard , G.W. Mulholland, R. Puri, R.J. Santoro, Combust. Flame 98 (1-2) (1994) 20-34.

[12]. R.J. Santoro, H.G. Semerjian, R.A. Dobbins, Combust. Flame 51 (2) (1983) 203-218.

[13]. K.T. Kang, J.Y. Hwang, S.H. Chung, W. Lee, Combust. Flame 109 (1-2) (1997) 266-281.

[14]. C.R. Kaplan, K. Kailasanath, Combust. Flame 124 (1-2) (2001) 275-294.

[15]. L.G. Blevins, R.A. Fletcher, B.A. Benner, E.B. Steel, G.W. Mulholland, Proc. Combust. Inst. 29 (2003) 2325-2333.

[16]. R.A. Dobbins, R.A. Fletcher, H.C. Chang, Combust. Flame 115 (3) (1998) 285-298.

[17]. R.A. Dobbins, R.A. Fletcher, W. Lu, Combust. Flame 100 (1-2) (1995) 301-309.

[18]. P.B. Sunderland, S.S. Krishnan, J.P. Gore, Combust. Flame 136 (1-2) (2004) 254-256.

[19]. C.R. Shaddix, C.W. Williams, L.G. Blevins, R.W. Schefer, Proc. Combust. Inst. 30 (2005) 1501-1508.

[20]. V.R. Katta, L.G. Blevins, W.M. Roquemore, Combust. Flame 142 (1-2) (2005) 33-51.

[21]. E.J. Lee, K.C. Oh, H.D. Shin , Fuel 84 (5) (2005) 543-550.

[22]. K.C. Oh, U.D. Lee, H.D. Shin, E.J. Lee, Combust. Flame 140 (3) (2005) 249-254.

[23]. I. Glassman, Combustion, Academic Press, San Diego, CA, 1996.

[24]. J. Barr, B.P. Mullins, Fuel 28 (9) (1949) 207-200.

[25]. J.A. Fay, Journal of the Aeronautical Sciences 21 (10) ( 1954) 681-689.

[26]. J.F. Clarke, Proc. R. Soc. London, A 296 (1447) (1967) 519-545.

[27]. F.G. Roper, Combust. Flame 29 (1977) 219-226.

[28]. F.G. Roper, C. Smith, A.C. Cunningham, Combust. Flame 29 (1977) 227-234.

[29]. R.E. Mitchell, A.F. Sarofim, L.A. Clomburg, Combust. Flame 37 (3) (1980) 227-244.

[30]. S.C. Li, A.S. Gordon, F.A. Williams, Combust. Sci. Technol. 104 (1-3) (1995) 75-91.

[31]. K.P. Schug, Y. Manheimertimnat, P. Yaccarino, I. Glassman, Combust. Sci. Technol. 22 (5-6) (1980) 235-250.

[32]. K. Saito, F.A. Williams, A.S. Gordon, Combust. Sci. Technol. 47 (3-4 ) (1986) 117-&.

[33]. R.L. Schalla, G.E. McDonald, Proc. Combust. Inst. 5 (1955) 316-324.

[34]. B.S. Haynes, H.Gg. Wagner, Prog. Energy Combust. Sci. 7 (4) (1981) 229-273.

[35]. K.M. Butler, G.W. Mulholland , Fire Technology 40 (2) (2004) 149-176.

[36]. F.G. Roper, C. Smith, Combust. Flame 36 (1979) 125-138.

[37]. I. Glassman, Proc. Combust. Inst. 22 (1988) 295-311.

[38]. J. Du, R.L. Axelbaum, Combust. Flame 100 (3) (1995) 367-375.

[39]. G.H. Markstein, Proc. Combust. Inst. 20 (1984) 1055-1061.

[40]. J.H. Kent, H.Gg. Wagner, Proc. Combust. Inst. 20 (1984) 1007-1015.

[41]. A. Thomas, Combust. Flame 6 (1962) 46-62.

[42]. J.F. Roesler, S. Martinot, C.S. McEnally, L.D. Pfefferle, J.L. Delfau, C. Vovelle, Combust. Flame 134 (3) (2003) 249-260.

[43]. R.J. Santoro, H.G. Semerjian, Proc. Combust. Inst. 20 (1984) 997-1006.

[44]. C. Wey, E.A. Powell, J.I. Jagoda, 20 (1984) 1017-1024.

[45]. R.J. Santoro, T.T. Yeh, J.J. Horvath, H.G. Semerjian, Combust. Sci. Technol. 53 (2-3) (1987) 89-115.

[46]. J.H. Kent, H.G. Wagner, Combust. Flame 47 (1) (1982) 53-65.

[47]. J.H. Miller, W.G. Mallard, K.C. Smyth, Combust. Flame 47 (1982) 205-214.

[48]. G. Prado, A. Garo, A. Ko, A.F. Sarofim, Proc. Combust. Inst. 20 (1984) 989-996.

[49]. K.C. Smyth, J.H. Miller, R.C. Dorfman, W.G. Mallard, R.J. Santoro, Combust. Flame 62 (2) (1985) 157-181.

[50]. R.A. Dobbins, C.M. Megaridis , Langmuir 3 (2) (1987) 254-259.

[51]. C.M. Megaridis, R.A. Dobbins , Proc. Combust. Inst. 22 (1988) 353-362.

[52]. K.C. Smyth, P.J.H. Tjossem, A. Hamins, J.H. Miller, Combust. Flame 79 (3-4 ) (1990) 366-380.

[53]. C.M. Megaridis, R.A. Dobbins , Combust. Sci. Technol. 71 (1-3) (1990) 95-109.

[54]. C.R. Shaddix, J.E. Harrington, K.C. Smyth, Combust. Flame 99 (3-4) (1994) 723-732.

[55]. R.A. Dobbins, G.J. Govatzidakis, W. Lu, A.F. Schwartzman, R.A. Fletcher, Combust. Sci. Technol. 121 (1-6) (1996) 103-121.

[56]. C.R. Shaddix, K.C. Smyth, Combust. Flame 107 (4) (1996) 418-452.

[57]. R.L. Vanderwal, Combust. Sci. Technol. 126 (1-6) (1997) 333-&.

[58]. R.L. Vanderwal, K.A. Jensen, M.Y. Choi, Combust. Flame 109 (3) (1997) 399-414.

[59]. C.S. Mcenally, U.O. Koylu, L.D. Pfefferle, D.E. Rosner, Combust. Flame 109 (4) (1997) 701-720.

[60]. U.O. Koylu, C.S. McEnally, D.E. Rosner, L.D. Pfefferle, Combust. Flame 110 (4) (1997) 494-507.

[61]. K.C. Smyth, C.R. Shaddix, D.A. Everest, Combust. Flame 111 (3) (1997) 185-207.

[62]. J. Zhang, C.M. Megaridis, Combust. Flame 112 (4) (1998) 473-484.

[63]. C.S. Mcenally, L.D. Pfefferle, A.M. Schaffer, M.B. Long, R.K. Mohammed, M.D. Smooke, M.B. Colket, Proc. Combust. Inst. 28 (2000) 2063-2070.

[64]. F. Ossler, T. Metz, M. Alden, Applied Physics B-Lasers and Optics 72 (4) (2001) 479-489.

[65]. D.R. Snelling, K.A. Thomson, G.J. Smallwood, O.L. Gulder, E.J. Weckman, R.A. Fraser, Aiaa Journal 40 (9) (2002) 1789-1795.

[66]. D.R. Snelling, F. Liu, G.J. Smallwood, O.L. Gulder, Combust. Flame 136 (1-2) (2004) 180-190.

[67]. A. Kitajima, T. Hatanaka, M. Takeuchi, H. Torikai, T. Miyadera, Combust. Flame 142 (1-2) (2005) 72-88.

[68]. K. Lee, Y. Han, W. Lee, J. Chung, C. Lee, Measurement Science and Technology 16 (2) (2005) 519-528.

[69]. M.E. Birch, R.A. Cary, Aerosol Science and Technology 25 (3) (1996) 221-241.

[70]. P.B. Sunderland, B.J. Mendelson, Z.G. Yuan, D.L. Urban, Combust. Flame 116 (3) (1999) 376-386.

[71]. C.K. Westbrook, F.L. Dryer, Prog. Energy Combust. Sci. 10 (1) (1984) 1-57.

[72]. M. Frenklach, Physical Chemistry Chemical Physics 4 (11) (2002) 2028-2037.

[73]. R.A. Dobbins, Combust. Flame 130 (3) (2002) 204-214.

[74]. F. Liu, H.S. Guo, G.J. Smallwood, O.L. Gulder, Combustion Theory and Modelling 7 (2) (2003) 301-315.

[75]. A. D'anna, A. D'alessio, J. Kent, Combust. Sci. Technol. 174 (11-2) (2002) 279-294.

[76]. I.M. Kennedy, Prog. Energy Combust. Sci. 23 (2) (1997) 95-132.

# Chapter 3: Flame Height of Laminar Inverse Diffusion Flames

## 3.1 Introduction

Flame height is an important characteristic of laminar diffusion flames. Flame height measurements have been used to test models of flame structure [1-3] and to calculate residence times of soot particles [4,5]. The most commonly accepted definition of flame height is the distance from the burner to the position on the centerline where the fuel and oxidizer are in stoichiometric proportions [6]. The most frequently used method of measuring flame height is by visually inspecting the flame to determine the height of the blue reaction zone [5,7] since stoichiometric conditions occur on the oxygen side of a blue reaction zone caused by $CO_2$ and CH chemiluminescence [8]. A more consistent measurement of flame height can be made by measuring the peak blue intensity on the flame axis recorded with a color charge-coupled device (CCD) camera and a line filter centered near 431 nm to enhance CH chemiluminescence and attenuate soot radiation [9,10]. Because the blue region in sooting NDFs is often difficult to detect, the height of the visible luminous yellow region has often been reported with the assumption that it is very close to the stoichiometric flame height in lightly sooting, non-smoking NDFs [10-13]. However, for heavily sooting and smoking NDFs the luminous yellow extends above the reaction zone, and hence the visible height is longer than the stoichiometric flame height [11,12,14,15]. Therefore, some researchers have used gas sampling on the centerline to measure flame height [6]. Since the flame temperature peaks at or near stoichiometric conditions, other researchers have reported the flame height by measuring the maximum temperature on the centerline using a thermocouple or Rayleigh scattering

[2,3,16]. The position of the reaction zone can also be found by examining the position of planar laser-induced fluorescence of hydroxyl radicals (OH PLIF), since measurements of OH PLIF have shown that the maximum concentration of OH lies just to the lean side of the stoichiometric mixture in laminar diffusion flames [17]. Therefore OH PLIF can also be used to measure flame height in co-flowing laminar diffusion flames [18].

Measurement of flame height in IDFs is complicated because soot forms in an annular region outside and above the flame and radiates, obscuring the blue reaction zone [19,20]. Therefore, measurement of stoichiometric flame height by OH PLIF is particularly suited to IDFs since visible images may not reveal information about the flame structure, and since gas sampling and temperature measurements along the centerline are intrusive and may alter the flame structure.

Theoretical consideration of flame height of laminar co-flow diffusion flames was first developed by Burke and Schumann. Although they made many assumptions in their analysis, they obtained good agreement between predicted and measured flame heights of NDFs and IDFs [21]. Several researchers expanded upon the work of Burke and Schumann by reducing the number of assumptions, but they did not apply their solutions to IDFs [8,13-15,22-25]. Roper developed the theoretical correlations most commonly used for predicting NDF flame height [6,14,26]. However, the applicability of these correlations has not been demonstrated for IDFs. Wu and Essenhigh [16] compared theoretical flame shapes of IDFs based on the relations developed by Gosman *et al.* [25] to experiment and found reasonably good agreement. In their words, "…mathematically the normal and inverse flames are, indeed, essentially indistinguishable from each other,

…with prediction of the alternate type simply obtained by treating the oxygen as fuel and the fuel as oxygen." Therefore, one would expect Roper's correlations to apply to IDFs with flame height increasing with rate of air flow.

The objectives of this chapter are to (1) examine the relationship between flame heights of IDFs obtained from visible images and OH PLIF, and (2) compare these with flame heights calculated using Roper's analysis [14] modified for IDFs.

## 3.2 Experimental Methods

### 3.2.1 Apparatus

The co-annular burner used to support laminar IDFs in this study is similar to the one used by Blevins *et al.* [19]. The burner consisted of three concentric tubes as shown in Figure 3.1. The tube edges were sharpened to reduce shear at the boundaries between flows. Air flowed through a 1-cm diameter central tube, which contained a screen to flatten the velocity profile. Fuel flowed in the annulus between a 3-cm diameter tube and the central air tube. The fuel annulus contained a honeycomb to flatten the velocity profile. To prevent secondary flames from forming between the fuel and ambient air, nitrogen flowed at a rate of 30 standard liters per minute (slpm, where standard conditions are 293 K and 101 kPa) through a second annulus formed between a 6.4-cm diameter outer tube and the 3-cm diameter tube. The nitrogen annulus contained screens and glass beads to straighten the flow. Table 3.1 lists the air and fuel flow rates for the methane and ethylene IDFs tested. Flows rates were metered by calibrated mass flow controllers. To reduce flame instabilities caused by room air currents, the burner was

surrounded by a metal shield with openings to admit laser light and to provide optical access for a camera.

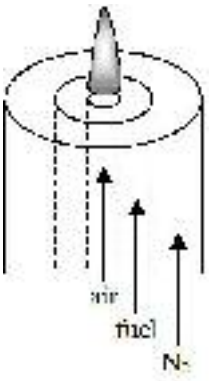

**Figure 3.1: Schematic diagram of burner.**

**Table 3.1: Flow Conditions**

| Fuel | $Q_{fuel}$ [a] | $Q_{air}$ [b] | $V_{fuel}$ [c] | $V_{air}$ [d] | $V_{air}/V_{fuel}$ | $Re_{fuel,Dc}$ [e] | $Re_{air,Dair}$ [f] | $\Phi_{overall}$ [g] | $HRR_{air}$ [h] |
|---|---|---|---|---|---|---|---|---|---|
| | slpm | slpm | cm/s | cm/s | | | | | W |
| $CH_4$ | 3.8 | 1.2 | 10 | 26 | 2.5 | 120 | 170 | 30 | 70 |
| | | 1.3 | | 28 | 2.7 | | 180 | 28 | 76 |
| | | 1.6 | | 34 | 3.3 | | 230 | 23 | 93 |
| | | 1.7 | | 36 | 3.5 | | 240 | 22 | 99 |
| | | 1.8 | | 38 | 3.8 | | 250 | 20 | 110 |
| | | 2.0 | | 42 | 4.2 | | 280 | 18 | 120 |
| | | 2.2 | | 47 | 4.6 | | 310 | 17 | 130 |
| | | 2.4 | | 51 | 5.0 | | 340 | 15 | 140 |
| | | 2.6 | | 55 | 5.4 | | 370 | 14 | 150 |
| | | 2.7 | | 57 | 5.6 | | 380 | 14 | 160 |
| $C_2H_4$ | 2.7 | 1.0 | 7.2 | 21 | 2.9 | 170 | 140 | 39 | 64 |
| | | 1.2 | | 26 | 3.5 | | 170 | 32 | 77 |
| | | 1.4 | | 30 | 4.1 | | 200 | 28 | 90 |
| | | 1.6 | | 34 | 4.8 | | 230 | 24 | 100 |
| | | 1.8 | | 38 | 5.3 | | 250 | 22 | 120 |
| | | 2.0 | | 42 | 5.9 | | 280 | 19 | 130 |
| | | 2.2 | | 47 | 6.5 | | 310 | 18 | 140 |

[a] $Q_{fuel}$, volume flow rate of fuel (at 293 K and 101 kPa).
[b] $Q_{air}$, volume flow rate of air (at 293 K and 101 kPa).
[c] $V_{fuel}$, average cold-flow fuel velocity at the burner exit.
[d] $V_{air}$, average cold-flow air velocity at the burner exit.
[e] $Re_{fuel,Dc}$, Reynolds number based on the cold-flow conditions of the fuel at the burner exit and the hydraulic diameter, $D_c$ = 2-cm.
[f] $Re_{air,Dair}$, Reynolds number based on the cold-flow conditions of the air at the burner exit and the air tube diameter, $D_{air}$ = 1-cm.
[g] $\Phi_{overall}$, overall equivalence ratio, defined as the fuel-to-air ratio divided by the stoichiometric fuel-to-air ratio.
[h] $HRR_{air}$, the estimated heat release rate based on the heating value of the fuel assuming all of the air reacts completely.

### 3.2.2 Laser Diagnostics and Optics

The experimental method used to obtain OH PLIF measurements is the same as used by Shaddix *et al.* [20]. A schematic of the laser assembly is shown in Figure 3.2. A frequency doubled Nd:YAG laser at 532 nm was used to pump a dye laser tuned to 283.57 nm. Hydroxyl radicals were excited by the ultraviolet (UV) laser in the relatively temperature insensitive $Q_{21}(8)$ line of the (1,0) band of the $A^2\Sigma^+ - X^2\Pi_i$ electronic system and detected at 308.9nm in the (0,0) band. Cylindrical lenses were used to form a laser sheet, 51.2 mm high with a thickness of 250 μm, aligned vertically with the central axis of the burner and positioned from 3 mm below to 48.2 mm above the burner exit. A gated, intensified charge-coupled device (ICCD) camera with 45 mm focal length f/1.8 UV lens collected OH PLIF perpendicular to the laser sheet at a rate of 2.5 frames per second for 40 seconds totaling 100 frames. A 340 nm (80 nm FWHM) band-pass filter was used to reject scattered laser light and $C_2$ swan band emission (at 516 nm) and to reduce natural flame radiation and broadband fluorescence from polycyclic aromatic hydrocarbons (PAH). The ICCD camera stores the output for each pixel as a 16-bit absolute intensity value. Flame heights were determined from the position of the OH layer by measuring the vertical distance from the burner exit to the maximum OH PLIF intensity on the centerline.

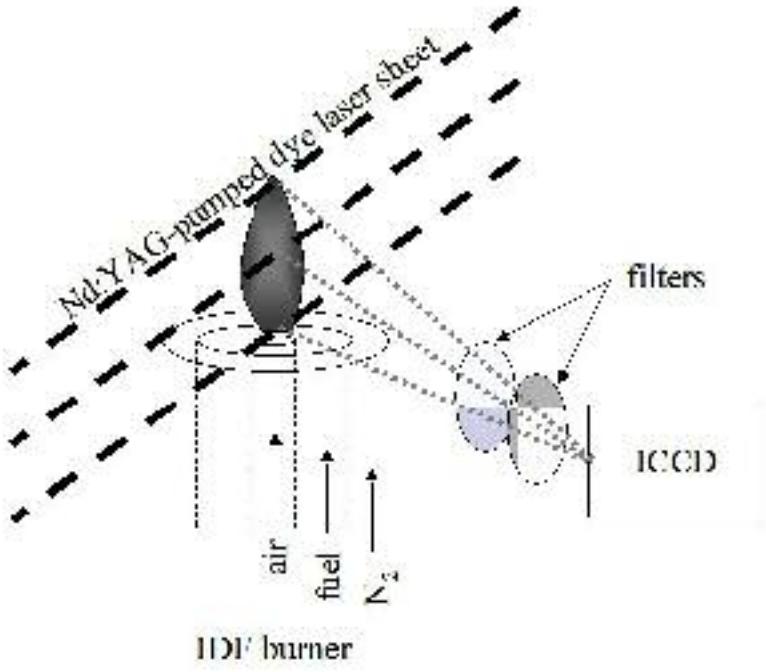


**Figure 3.2: Schematic of Laser Assembly**

Measurements of visible flame height were made from images of natural flame radiation recorded using the ICCD camera with the laser off and no filters. The ICCD camera without filters detects wavelengths of light between 200 nm and 900 nm. The images were collected at a rate of 2.5 frames per second for 8 seconds totaling 20 frames. Because several flames extended above the vertical domain of the ICCD camera, two sets of images were recorded, one with the burner in the original position, and another with the burner repositioned lower to record images of the flame from 22.7 mm to 73.9 mm above the burner exit.

Visible flame height measurements were defined as the distance on the centerline from the burner exit to the first pixel from the top of the image with an intensity greater than a threshold value of 800 (out of 65535 maximum), which is three times the average background intensity far from the flames for all of the recorded images. The precision in

visible and OH PLIF flame height measurements was ±0.5 mm, and the precision in air flow rate measurements was ±0.1 slpm.

### 3.3 Analytical Methods

Calculations of flame height were based on the analytical solution derived by Roper for the height of the reaction zone of an NDF on a circular port burner,

$$H/Q = \{4\pi D_0 \ln(1+1/S)\}^{-1}(T_0/T_f)^{0.67}, \quad (3.1)$$

where $H$ is the diffusion flame height (cm), $Q$ is the volumetric flow rate of fuel gas ($cm^3/s$) corrected to ambient temperature and pressure, $D_0$ is the diffusion coefficient at ambient temperature ($cm^2/s$), $S$ is the ratio of the volume of air to volume of fuel gas for complete combustion, $T_0$ is the ambient temperature (K), and $T_f$ is the characteristic temperature (K) for calculation of diffusivity [14]. The following modifications to Eq. 3.1 were made for IDFs: (1) air flow rate was used instead of fuel flow rate for $Q$, and (2) stoichiometric fuel to air volume ratio was used instead of stoichiometric air to fuel volume ratio for $S$. Since Roper's analysis requires the assumption that the diffusion coefficient of all species be equal, $D_0$ represents an effective diffusion coefficient. Roper *et al*. approximated $D_0$ as the binary diffusion coefficient of oxygen into nitrogen at $T_0 = 293$ K ($D_0 = 0.20$ $cm^2/s$) [6]. However, other researchers have suggested that in NDFs fuel dominates diffusion and have found better agreement between measured and predicted flame heights when $D_0$ was approximated as the binary diffusion coefficient of the fuel into nitrogen [13,15].

Roper *et al.* measured the heights of many NDFs of different fuels and consequently determined that a linear relationship existed between the ratio $H/Q$ and the

term $[\ln(1 + 1/S)]^{-1}$ except for flames shorter than six times the diameter of the central fuel tube, which Roper hypothesized were shortened by axial diffusion, which was neglected in the analysis [6]. The measured linear relationship is consistent with Eq. 3.1 if $D_0$ and $T_f$ are constant. Roper and colleagues determined the linear constant for this relationship and expressed it in the following correlation for NDFs of all fuels:

$$H/Q = (0.133 \text{ s/cm}^2)[\ln(1 + 1/S)]^{-1}. \quad (3.2)$$

Comparing Eqs. 3.1 and 3.2, Roper calculated the characteristic diffusion temperature, $T_f$, as 1500 K for NDFs and argued that this was a reasonable mean temperature for the flame region controlling diffusion.

## 3.4 Results and Discussion

### 3.4.1 Experimental Results

An image of average OH PLIF from a 2.7 slpm methane-air IDF is shown in Figure 3.3 (a). Very faint PAH PLIF is present on the outside of the reaction zone in the image. A visible image of a 2.7 slpm methane-air IDF is shown in Figure 3.3 (b). The flame appears qualitatively longer in the visible image of Figure 3.3 (b) than in the OH PLIF image of Figure 3.3 (a).

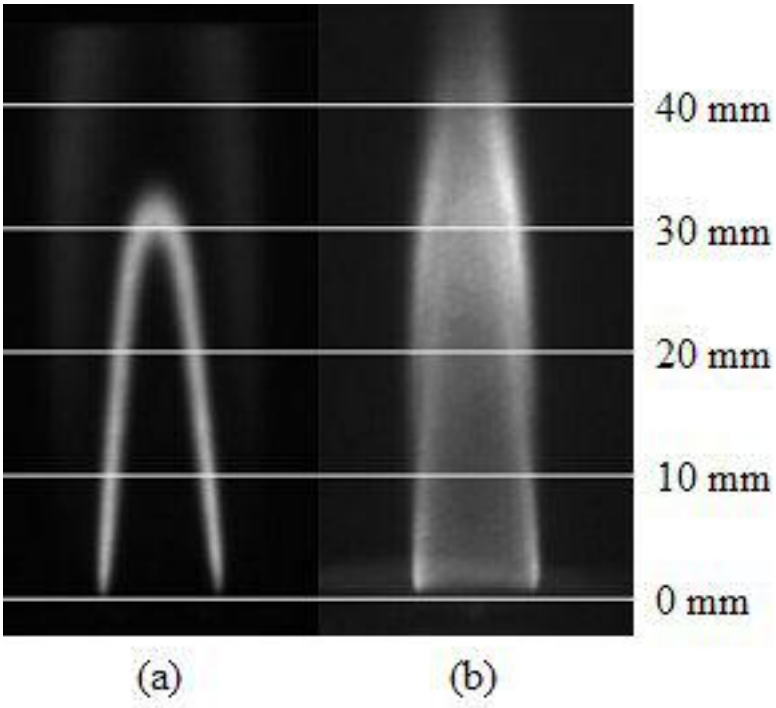


**Figure 3.3: Images of 2.7 slpm methane IDF: (a) OH PLIF and (b) visible flame.**

The measured flame heights from both ethylene and methane IDFs are depicted in Figure 3.4 and Figure 3.5, respectively. The vertical bars on the visible flame heights and OH PLIF heights represent one standard deviation in height. The standard deviation of the visible ethylene flame heights increases with increasing air flow rates, reflecting an increase in the effects of buoyancy induced flame instabilities with increasing flame height [27]. The flame heights increase with increasing rate of air flow for both fuels. The visible flame heights are longer than the flame heights from OH PLIF, since there is visibly radiating soot surrounding and extending above the reaction zone. Therefore, visible flame heights of IDFs overestimate the height of the reaction zone.

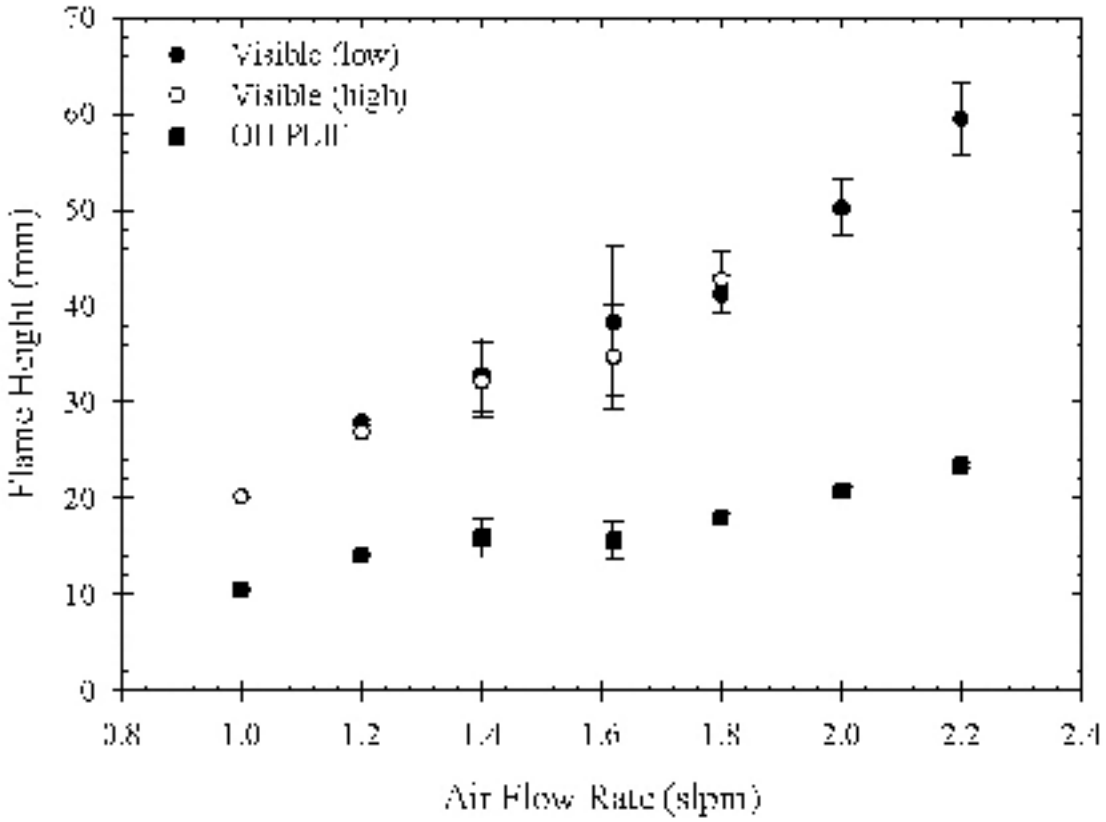


**Figure 3.4: Visible and OH PLIF flame heights of ethylene IDFs. Visible (low) shows flames with air flow rates from 1.2 slpm to 2.2 slpm with the burner in the lower position, and Visible (high) shows flames with air flow rates from 1.0 slpm to 1.8 slpm with the burner in the upper position.**

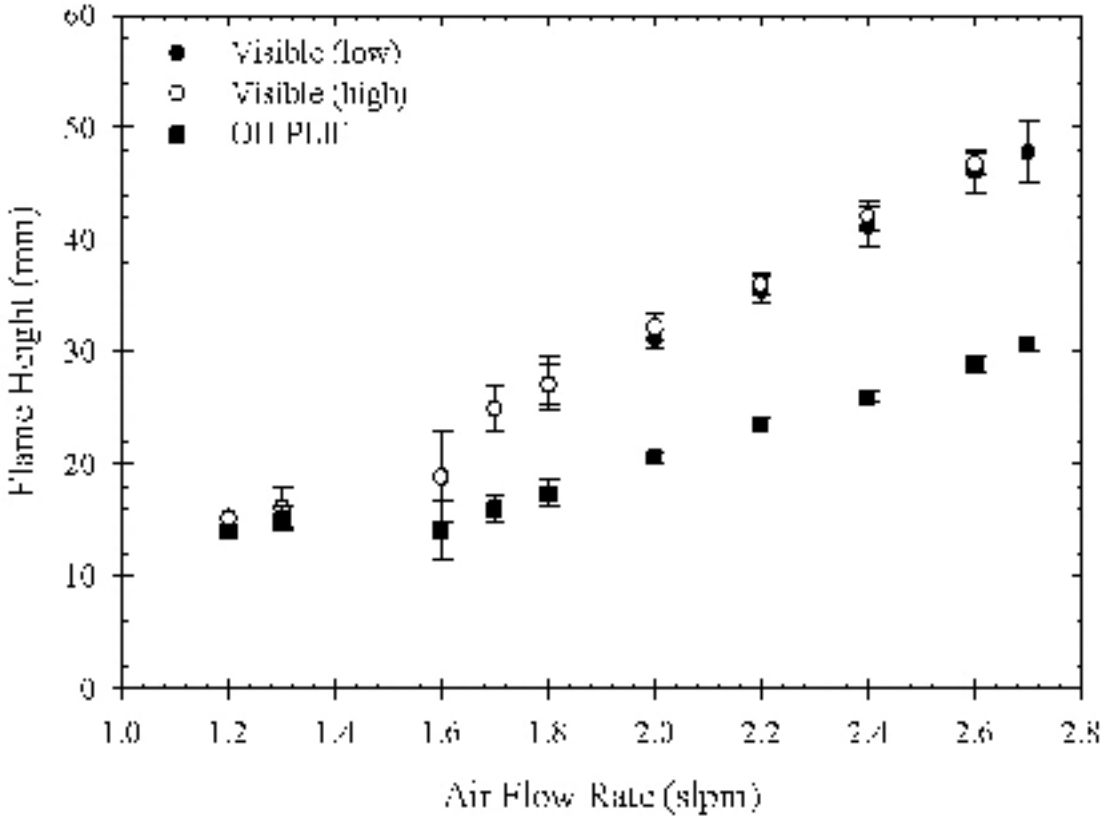


**Figure 3.5: Visible and OH PLIF flame heights of methane IDFs. Visible (low) shows flames with air flow rates from 1.8 slpm to 2.7 slpm with the burner in the lower position, and Visible (high) shows flames with air flow from 1.2 slpm to 2.6 slpm with the burner in the upper position.**

There is a discontinuity centered at an air flow rate of 1.6 slpm in the flame heights from OH PLIF and in the visible flame heights due to an instability observed in the flame. This instability is also responsible for the larger standard deviation at this flow rate. The flames in this study have Froude numbers between 0.2 and 0.4 which makes them slightly buoyant and near transition to momentum control. The smallest flames, which have the lowest Froude numbers and are therefore most buoyant, were observed to be the most stable. Therefore, it is unlikely that the instability was caused by the low fuel co-flow since it does not affect the most buoyant flames. The instability may have been

caused by the exhaust fan ducting, which may have enhanced the natural flickering of the flame.

### 3.4.2 Comparison of Experiment to Analysis

Flame heights predicted using Roper's analysis modified for IDFs are compared to OH PLIF measurements in Figure 3.6 and Figure 3.7. The dotted lines in Figure 3.6 and Figure 3.7 indicate predicted flame heights calculated from Roper's correlation (Eq. 3.2) [6]. When Roper's correlation is applied, flame heights are under predicted for all ethylene flames and almost all methane flames. This may be due oxygen diffusing upward in the flames because the flames in this study are all shorter than six times the diameter of the central air tube, and, therefore, axial diffusion may be important [6]. The height of the methane flame with an air flow rate of 1.6 slpm is over predicted, but this flame was probably shortened by instability-induced mixing.

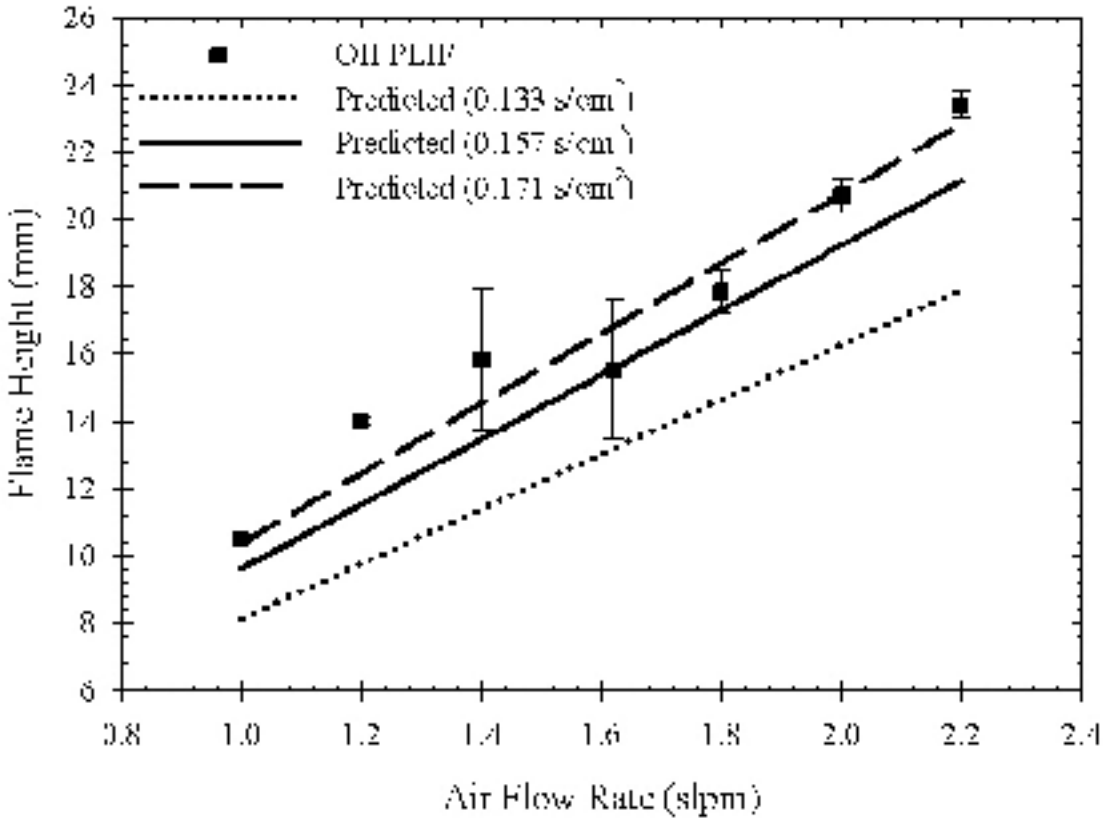


**Figure 3.6: Flame heights of ethylene IDFs predicted using Roper's analysis modified for IDFs compared to measured OH PLIF flame heights.**

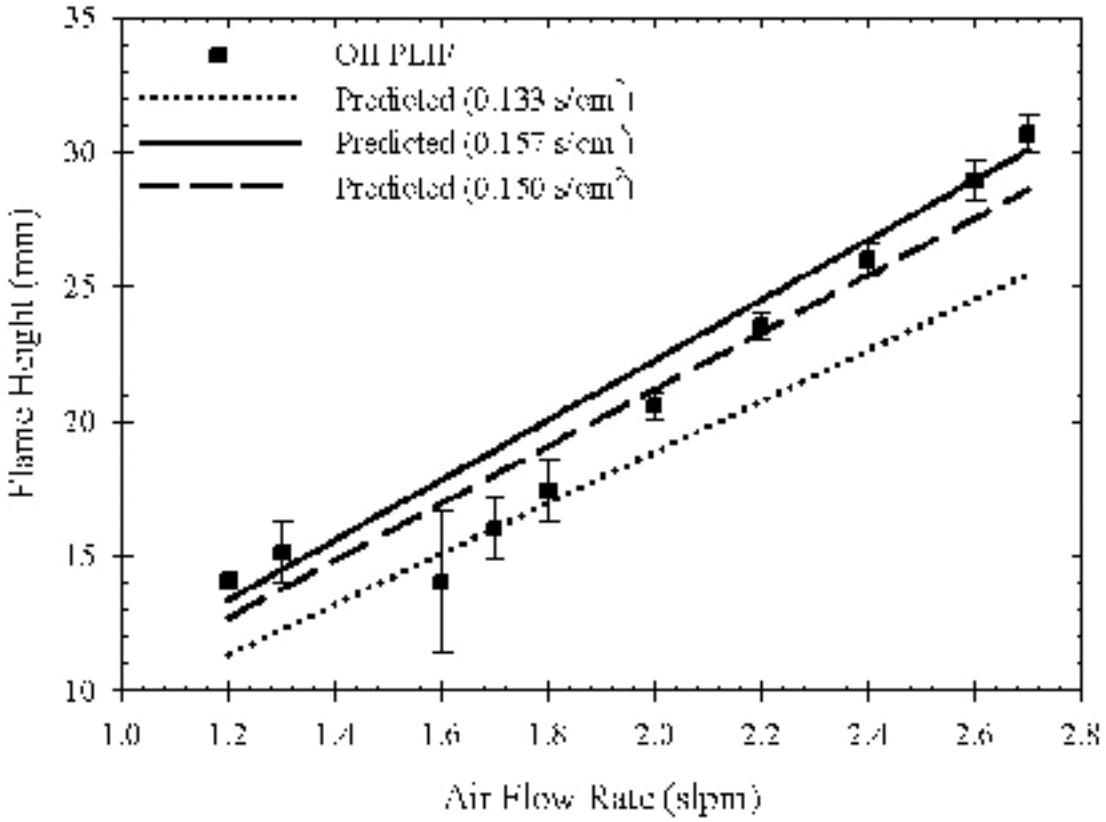


**Figure 3.7: Flame heights of methane IDFs predicted using Roper's analysis modified for IDFs compared to measured OH PLIF flame heights.**

A modified Roper's correlation optimized for all OH PLIF flame heights from both ethylene and methane IDFs (disregarding the unstable methane flame with an air flow rate of 1.6 slpm) was generated by adjusting the coefficient of the correlation in Eq. 3.2. The resulting correlation,

$$H/Q = (0.157 \text{ s/cm}^2)[\ln(1 + 1/S)]^{-1}, \tag{3.3}$$

has the same parameter definitions as Eq. 3.1. The predicted flame heights calculated using Eq. 3.3, represented by solid lines in Figure 3.6 and Figure 3.7, agree with the OH PLIF measurements better than flame heights predicted with Eq. 3.2. However, the

errors for ethylene flame heights are greater than the errors for methane flame heights. This suggests that a fuel-independent correlation may not exist for IDFs.

A least squares fit of the OH PLIF flame heights for only ethylene IDFs was used to generate a modified Roper's correlation for ethylene IDFs:

$$H/Q = (0.171 \text{ s/cm}^2)[\ln(1 + 1/S)]^{-1}. \quad (3.4)$$

The dashed line in Figure 3.6 represents predicted flame heights calculated using Eq. 3.4. The difference between Eqs. 3.3 and 3.4 may be due to the effect of uncertainty in the value of the diffusion coefficient, $D_0$. Comparing Eqs. 3.1 and 3.4, using Roper's suggested diffusion coefficient, $D_0 = 0.20$ cm$^2$/s, results in an average temperature of $T_f = 1033$ K, which is significantly lower than Roper's average temperature of $T_f = 1500$ K. This suggests that a different diffusion coefficient should be used. Using the binary diffusion coefficient of ethylene into nitrogen calculated from Leonard-Jones parameters at 293 K ($D_0 = 0.153$ cm$^2$/s [26]) yields a temperature of $T_f = 1541$ K, which is a much more reasonable average flame temperature.

It is useful to test the application of Roper's analysis using IDF OH PLIF flame heights reported in the literature. Flame heights measured by OH PLIF for ethylene/air IDFs from ref. [18] are compared to flame heights predicted by Eqs. 3.2, 3.3, and 3.4 in Figure 3.8. Roper's correlation (Eq. 3.2) under predicts the flame heights as it did for the ethylene IDFs in Figure 3.6, perhaps due to oxygen diffusing upward because the heights of these IDFs are also less than six times the diameter of the central air tube, so again axial diffusion may be important. Flame heights are also under predicted using Eq. 3.3, but agree slightly better with the OH PLIF measurements than flame heights predicted with Eq. 3.2. This is further evidence that a single correlation may not be sufficient to

predict flame heights of IDFs of different fuels. Nearly perfect agreement is obtained using Eq. 3.4, the modified correlation for ethylene IDFs. However, note that the calculated heights are less than the measured heights when the fuel is most diluted, and as the fuel mole fraction approaches one, the calculated heights better predict the measured heights. This is because increasing fuel dilution lowers the adiabatic flame temperature, effectively increasing the flame height since diffusion occurs more slowly at lower temperatures and the reactants will have more time to advect downstream. This implies that temperature differences between flames should be considered when applying Eq. 3.1.

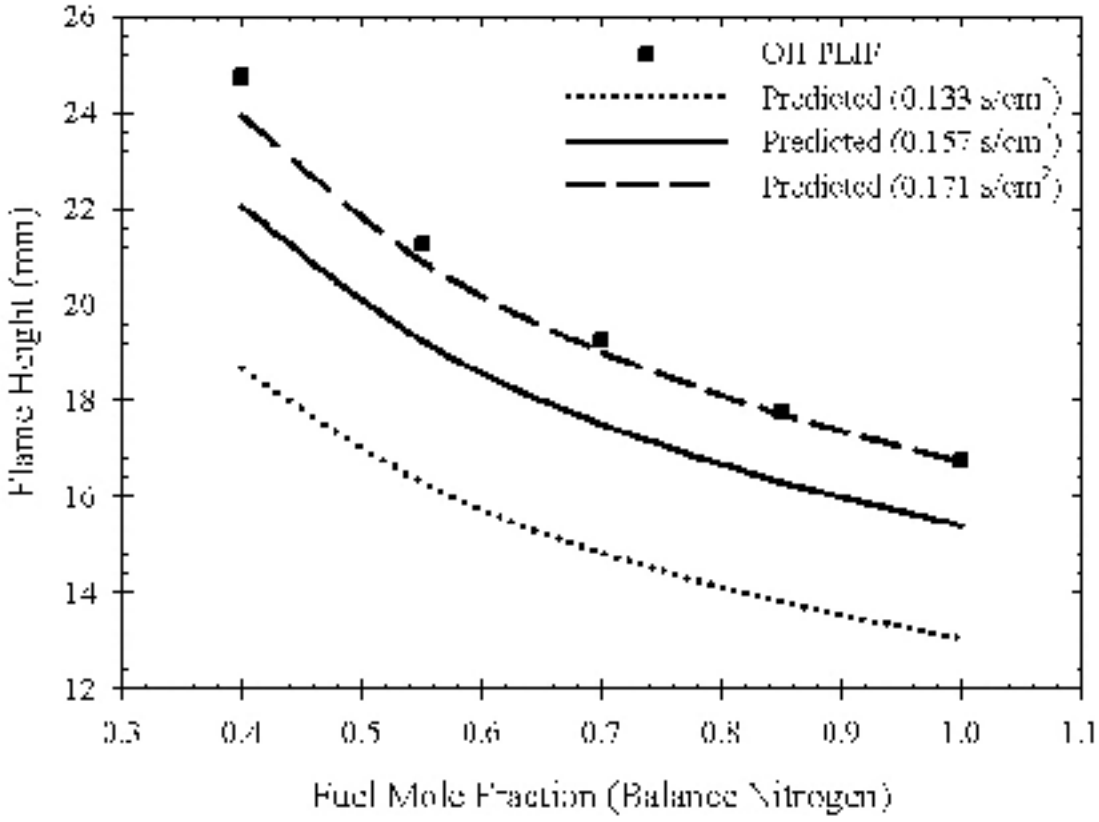


**Figure 3.8: Flame heights measured by OH PLIF from ref. [18] compared to heights predicted by Roper's analysis.**

It would be of interest to develop a strategy for applying Eq. 3.1 to IDFs. Since the average temperature, $T_f$, in Eq. 3.1, should vary from flame to flame, a good approximation of $T_f$ is the average of the adiabatic flame temperature and the ambient temperature, $T_0$. This temperature will be used with Eqs. 3.1 and 3.4 to determine the diffusion coefficient, $D_0$, that best fits the data. For ethylene selecting an average temperature of $T_f = 1331$ K, which is the average of the adiabatic flame temperature of ethylene (2369 K [26]) and $T_0 = 293$ K, results in a diffusion coefficient of $D_0 = 0.169$ cm$^2$/s. This diffusion coefficient is between the suggested extremes, but closer to the binary diffusion coefficient of ethylene into nitrogen, which is less than the binary diffusion coefficient of oxygen into nitrogen. This suggests that $D_0$ should be between the binary diffusion coefficient of oxygen into nitrogen and the binary diffusion coefficient of the fuel into nitrogen, but will be closer to the lesser of the two diffusion coefficients.

The preceding strategy was used to predict methane IDF flame heights. First a least squares fit of the OH PLIF flame heights for only methane (disregarding the unstable methane flame with an air flow rate of 1.6 slpm) was used to generate a modified Roper's correlation for methane IDFs:

$$H/Q = (0.150 \text{ s/cm}^2)[\ln(1 + 1/S)]^{-1}. \tag{3.5}$$

The predicted flame heights calculated using Eq. 3.5 are represented by a dashed line in Figure 3.7. Comparing Eqs. 3.1 and 3.5, using an average temperature of $T_f = 1260$ K, which is the average of the adiabatic flame temperature of methane (2226 K [26]) and $T_0 = 293$ K, yields a diffusion coefficient of $D_0 = 0.200$ cm$^2$/s. This diffusion coefficient is between the binary diffusion coefficient of oxygen into nitrogen ($D_0 = 0.198$ cm$^2$/s

[26]) and the binary diffusion coefficient of methane into nitrogen ($D_0 = 0.212$ cm$^2$/s [26]) calculated from Leonard-Jones parameters at 293 K, but closer to the binary diffusion coefficient of oxygen into nitrogen which is the lesser of the two diffusion coefficients. Therefore, the strategy is effective. However, longer IDFs should be measured and more fuels should be tested to verify this strategy. Nevertheless, the fact that Roper's treatment applies to IDFs is an indication that IDFs are similar in structure to NDFs [4,7,16,18,20,28].

## 3.5 Conclusions

Flame heights of ethylene-air and methane-air laminar IDFs were measured for several air flow rates. The visible flame height was found to be greater than the height of the reaction zone determined by OH PLIF because of luminous soot above the reaction zone, and hence not an effective measure of flame height. Roper's analysis was found to provide good agreement with measured OH PLIF flame heights over the range of air flow rates examined in the present study and for literature data, when the following modifications were made to Eq. 3.1:

(1) rate of air flow was used instead of fuel flow for $Q$,

(2) fuel-to-air ratio was used instead of air-to-fuel ratio for $S$,

(3) the average of the adiabatic flame temperature of the fuel and ambient temperature was used for $T_f$, and

(4) a diffusion coefficient in between the binary diffusion coefficient of oxygen into nitrogen and the binary diffusion coefficient of the fuel into nitrogen, but closer to the lesser of the two diffusion coefficients, was used for $D_0$.

The fact that Roper's analysis applies to IDFs is evidence that IDFs are similar in structure to NDFs.

## 3.6 References

[1]. A. D'anna, A. D'alessio, J. Kent, Combust. Sci. Technol. 174 (11-2) (2002) 279-294.

[2]. D.B. Makel, I.M. Kennedy, Combust. Sci. Technol. 97 (4-6) (1994) 303-314.

[3]. C.S. Mcenally, L.D. Pfefferle, A.M. Schaffer, M.B. Long, R.K. Mohammed, M.D. Smooke, M.B. Colket, Proc. Combust. Inst. 28 (2000) 2063-2070.

[4]. K.C. Oh, U.D. Lee, H.D. Shin, E.J. Lee, Combust. Flame 140 (3) (2005) 249-254.

[5]. J. Du, R.L. Axelbaum, Combust. Flame 100 (3) (1995) 367-375.

[6]. F.G. Roper, C. Smith, A.C. Cunningham, Combust. Flame 29 (1977) 227-234.

[7]. G.W. Sidebotham, I. Glassman, Combust. Flame 90 (3-4) (1992) 269-283.

[8]. R.E. Mitchell, A.F. Sarofim, L.A. Clomburg, Combust. Flame 37 (3) (1980) 227-244.

[9]. P.B. Sunderland, B.J. Mendelson, Z.G. Yuan, D.L. Urban, Combust. Flame 116 (3) (1999) 376-386.

[10]. P.B. Sunderland, S.S. Krishnan, J.P. Gore, Combust. Flame 136 (1-2) (2004) 254-256.

[11]. K.P. Schug, Y. Manheimertimnat, P. Yaccarino, I. Glassman, Combust. Sci. Technol. 22 (5-6) (1980) 235-250.

[12]. K. Saito, F.A. Williams, A.S. Gordon, Combust. Sci. Technol. 47 (3-4 ) (1986) 117-&.

[13]. S.C. Li, A.S. Gordon, F.A. Williams, Combust. Sci. Technol. 104 (1-3) (1995) 75-91.

[14]. F.G. Roper, Combust. Flame 29 (1977) 219-226.

[15]. A.S. Gordon, S.C. Li, F.A. Williams, Combust. Sci. Technol. 141 (1-6) (1999) 1-18.

[16]. K.T. Wu, R.H. Essenhigh, in: Twentieth Symposium (International) on Combustion, The Combustion Institute, Pittsburgh, 1984, p. 1925.

[17]. K.C. Smyth, P.J.H. Tjossem, A. Hamins, J.H. Miller, Combust. Flame 79 (3-4 ) (1990) 366-380.

[18]. E.J. Lee, K.C. Oh, H.D. Shin , Fuel 84 (5) (2005) 543-550.

[19]. L.G. Blevins, R.A. Fletcher, B.A. Benner, E.B. Steel, G.W. Mulholland, Proc. Combust. Inst. 29 (2003) 2325-2333.

[20]. C.R. Shaddix, C.W. Williams, L.G. Blevins, R.W. Schefer, Proc. Combust. Inst. 30 (2005)

[21]. S.P. Burke , T.E.W. Schumann, Proc. Combust. Inst. 1 (1928) 2.

[22]. J. Barr, B.P. Mullins, Fuel 28 (9) (1949) 207-200.

[23]. J.A. Fay, Journal of the Aeronautical Sciences 21 (10) ( 1954) 681-689.

[24]. J.F. Clarke, Proc. R. Soc. London, A 296 (1447) (1967) 519-545.

[25]. A.D. Gosman, W.M. Pun, A.K. Runchal, D.B. Spalding, M. Wolfshtein, Heat and Mass Transfer in Recirculating Flows, Academic Press, London, 1969.

[26]. S.R. Turns, An Introduction to Combustion: Concepts and Applications, McGraw-Hill, U.S.A, 2000, p. 656.

[27]. V.R. Katta, L.G. Blevins, W.M. Roquemore, Combust. Flame 142 (1-2) (2005) 33-51.

[28]. J.H. Kent, H.G. Wagner, Zeitschrift Fur Physikalische Chemie-Wiesbaden 139 (1984) 59-68.

# Chapter 4: Flame Structure of Laminar Inverse Diffusion Flames

## 4.1 Introduction

It is of interest to study the structure of IDFs to examine the formation of soot and PAH. It has been shown that the flame structure of IDFs is similar to NDFs [1]. Therefore, soot and PAH formation in IDFs may also similar to that in NDFs. The inverted nature of the IDF flame structure with respect to NDF flame structure allows soot and PAH to be emitted from IDFs so that their formation can be studied more easily than in NDFs. However, most of the research on diffusion flames has focused on NDFs and counter-flow flames [2-14]. Although there have been some studies on IDFs [1,12,15-19], measurements of soot and PAH concentrations, temperatures, and flow fields have not been combined to give a complete picture of IDF flame structure. Measurements of OH PLIF, PAH PLIF, and planar laser-induced incandescence (PLII) of soot particles can be used to study flame structure by describing the locations of soot and PAH formation regions with respect to the reaction zone. Combined with temperature measurements and flow field visualization, these measurements of IDF flame structure can be used to investigate soot and PAH formation.

The structure of diffusion flames can be described by the locations of the formation regions of soot and PAH with respect to the reaction zones and the gas temperatures in those regions. The reaction zone can be located by OH PLIF (as was seen in Chapter 3) because large concentrations of OH radicals occur very close to the reaction zone on the air side of the flame [4,12,20,21]. Soot forms on the fuel side of the flame close to the reaction zone at a minimum critical temperature of 1300 K

[2,4,7,14,16,22-24]. PAH forms on the fuel side of the soot, along isotherms and contours of constant mixture fraction [4,8]. Knowledge of this structure has lead to an increased understanding of soot and PAH formation. The presence of PAH close to the soot formation region and the presence of PAH in soot suggest that PAH are soot precursors [4,6,8,16,23,25-30].

This structure has only recently begun to be examined in a few IDFs. Kang *et al.* measured soot scattering and PAH fluorescence in a nitrogen-diluted propane co-flowing co-annular IDF with oxygen enrichment [18]. Lee *et al.* measured soot scattering, PAH fluorescence in two bands, and OH fluorescence in ethylene co-flowing co-annular IDFs of varying dilution and flame temperature [21]. Shaddix *et al.* measured soot PLII, OH PLIF, and PAH PLIF in a methane-air IDF and an ethylene-air IDF on a co-flowing Wolfhard-Parker burner [12].

In this study, flame structure of a co-flowing co-annular IDF was examined using OH PLIF, soot PLII, PAH PLIF, temperature measurements, and computer modeling. Air flow rate was varied to change flame height, so that the effect of residence time on soot and PAH formation could be investigated. As was seen in Chapter 3, flame height is proportional to air flow rate in IDFs. Increased flame height has been shown to increase soot and PAH amounts in NDFs by increasing residence time [23,31]. In the high temperature region in buoyant flames, the initial velocity is negligible compared to the buoyant component of velocity. Therefore, the velocity field is similar in the high temperature region for flames of different air flow rate. Different flame heights thus imply different residence times when comparing buoyant flames with any rate of air flow. Undiluted fuel and normal air were used in the present study to maintain constant flame

temperature for a given fuel because soot formation is strongly dependent on flame temperature [23]. Two different fuels, methane and ethylene, were used in the present study to examine the effect of fuel structure on soot formation. It has been shown that unsaturated fuels, such as ethylene, have a greater propensity to soot than saturated fuels, such as methane, due to faster pyrolysis rates [32].

The objectives of this chapter are (1) to study the effect of residence time and fuel structure on soot inception and early soot growth in IDFs and (2) to examine the detailed structure of IDFs to gain insight into soot inception and early soot growth. The detailed measurements reported in this chapter provide a more complete understanding of IDF flame structure than was previously possible.

## 4.2 Experimental Methods

### 4.2.1 Apparatus

The co-annular burner used was described in Chapter 3 and was shown in Figure 3.1. The burner was attached to a translation stage that could be adjusted vertically with a precision of 0.5 mm. Table 3.1 lists the air and fuel flow rates for the methane and ethylene IDFs tested. Fuel, air and nitrogen were provided by calibrated mass flow controllers. Nitrogen flow was fixed at 30 slpm. Fuel flow rates were held constant for each fuel type, while air flow was varied to change the flame height. To reduce flame instabilities caused by room air currents, the burner was surrounded by a metal shield with openings to admit laser light and to provide optical access for a camera. An exhaust fan operating at 1500 cfm was positioned 2 meters above the burner to prevent build up of dangerous fuel rich gases in the laboratory.

### 4.2.2 Laser Diagnostics

#### 4.2.2.1 Laser and Camera Configurations

The laser and camera configuration were the same as in Chapter 3 and are shown in Figure 3.2. Laser light at 283.6 nm was used to simultaneously excite OH fluorescence on lines near 310 nm, broadband PAH fluorescence and emission by PLII. The ultraviolet (UV) laser light was provided by a dye laser pumped by a pulsed, frequency-doubled Nd:YAG laser. The laser was pulsed at 10 Hz, the pulse width was approximately 8 ns per pulse and the energy per pulse was approximately 12 mJ. Cylindrical lenses were used to form a laser sheet that was 51.2 mm high and 0.3 mm wide. Therefore, the laser fluence per pulse was about 0.09 J/cm$^2$, and the laser flux was about $10^7$ W/cm$^2$. The laser sheet was aligned vertically with the central axis of the burner. By repositioning the burner relative to the laser sheet, measurements were made at two vertical locations, from 3 mm below to 48.2 mm above the burner exit, and from 22.6 mm to 73.8 mm above the burner exit.

The same gated, intensified charge-coupled device (ICCD) camera with 45mm focal length f/1.8 UV lens described in Chapter 3 was used to collect OH and PAH PLIF and soot PLII at a rate of 2.5 frames per second for 40 seconds totaling 100 frames. The camera was positioned perpendicular to the laser sheet as shown in Figure 3.2. The ICCD camera stored the output for each pixel as a 16-bit absolute intensity value. Due to the irising effect of the slow gating ICCD camera, pixels in the center of the ICCD array were given more weight than those on the perimeter. Without filters the ICCD camera

detected wavelengths of light between 200 nm and 900 nm. A 295 nm long-pass filter eliminated reflections from the laser and scattering from soot particles.

Visible color images of the flames were recorded with a CCD camera (Panasonic WV-CP454) with a 16-mm focal length, f/8 Cosmicar lens at a rate of 30 frames per second for 8 seconds totaling 240 frames. Visible color images were time-average using all 240 frames.

#### 4.2.2.2 OH and PAH PLIF

Measurements of OH and PAH PLIF were taken with an additional 450 nm short-pass filter to attenuate soot PLII, $C_2$ Swan band emission at 516 nm [11] and visible and infrared (IR) natural flame radiation. An additional 340 nm (80 nm FWHM) band-pass filter was also used with ethylene flames to further attenuate soot PLII and better balance PAH and OH PLIF since ethylene produced more PAH than methane. The 450 nm short-pass and 340 nm band-pass filters were also used to attempt to identify and locate different size aromatics since larger aromatics have been detected at longer wavelengths than smaller aromatics [9,33,34]. Instead of prompt gating, a longer 200-ns gate was used for PLIF measurements to reduce irising effects of the slow gating ICCD camera. The camera gate was opened 100 ns before the laser pulse. Both OH and PAH PLIF measurements were corrected for spatial variations in the beam profile by measuring Rayleigh scattering through room temperature air to obtain the spatial variation of the beam profile and then assuming a linear relation between measured PLIF and incident laser fluence. Considering beam correction, long gate delay, and irising effects of the camera, the OH PLIF and PAH PLIF should be considered as qualitative measurements.

#### 4.2.2.3 Soot PLII

Measurements of soot PLII were made with a 570 nm long-pass filter to eliminate $C_2$ Swan band emission, which occurs at 516.5 nm. A 200-ns gate was used beginning 100 ns after the laser pulse to eliminate short lived OH PLIF and to attenuate PAH PLIF which has a lifetime of about 10 to 100 ns [9,35]. Examination of PAH PLIF and soot PLII signals with the 570 nm long pass filter showed that PAH PLIF accounted for less than 10% of the measured soot PLII signal. Measurements of natural flame radiation, also made with the 570 nm long-pass filter but with the laser off, were subtracted from the soot PLII measurements to remove interference from natural flame radiation.

The Rayleigh scattering measurements were not used to correct the soot PLII. The relation between soot PLII and laser fluence is complicated by many other factors including laser wavelength, laser temporal profile, soot absorption function, soot particle diameter, detection gating and detection wavelength [36-38]. Experiments on fluence dependence of soot PLII show a rapid rise in soot PLII until a critical fluence is reached, followed by a "plateau" region where the slope is significantly less although still rising. Vaporized soot particles reach temperatures of 4000 K but may be super heated with increased laser fluence [11,36,37]. The complicated dependence of soot PLII on laser fluence may be explained by the vaporization of soot particles and subsequent superheating. The steep rise in soot PLII for low laser fluence is due to heating of soot particles below their vaporization temperature. The critical laser fluence corresponds to vaporization of soot particles. The significantly slower increase in soot PLII above the critical laser fluence is due to super heating of vaporized particles [36-38].

A critical laser fluence of 0.2 mJ/cm$^2$ has been reported using a 532 nm wavelength Nd:YAG laser with a 10-ns Gaussian temporal profile [37,38]. Since soot absorption is inversely proportional to wavelength, laser light at shorter wavelengths is absorbed more, and less fluence is needed to heat soot particles [37]. Therefore, at a wavelength of 283 nm, a fluence of 0.1 mJ/cm$^2$ may have been very close to the critical fluence level. Eckbreth calculated the critical laser flux to vaporize soot particles, less than 100 nm in diameter, as $10^7$ W/cm$^2$ [36]. Therefore, due to variations in beam profile some particles may have been vaporized and others may not. Soot PLII signal decay time is on the order of 100 to 200 ns [9,37,38]. The soot vaporization time constant for laser flux of $10^7$ W/cm$^2$ is on the order of 50 ns [36]. Therefore, the 100 ns gate delay and irising effects of the camera will significantly affect the measured soot PLII. Small soot particles or particles with significantly different absorption function may not be detected.

The measured soot PLII was corrected for spatial variations in the beam profile and the irising effects of the slow gating ICCD camera by applying a 5th-order polynomial correction function optimized by fitting soot PLII measurements in the region from 22.6 mm to 48.2 mm above the burner exit, which was overlapped by the two vertical locations where measurements were taken. At each axial position, $z$, relative to the top of the burner, soot PLII signal was corrected by dividing by the correction function, $f(z)$, given below:

$$f(z) = a_5\left(\tfrac{z}{512}\right)^5 + a_4\left(\tfrac{z}{512}\right)^4 + a_3\left(\tfrac{z}{512}\right)^3 + a_2\left(\tfrac{z}{512}\right)^2 + a_1\left(\tfrac{z}{512}\right) + a_0 \qquad (4.1)$$

with $a_5 = 0.448844168$, $a_4 = 0.162445221$, $a_3 = 0.109049614$, $a_2 = 0.049878732$, $a_1 = -0.047844824$, and $a_0 = 0.277627088$. A comparison of the beam profile and the soot PLII soot correction function, shown in Figure 4.1, suggests that a hot spot near the

bottom of the beam profile caused a large increase in soot PLII. Considering the UV wavelength excitation, long gate delay and gate width, and variations in soot primary particle size, the soot PLII signal should be considered qualitative.

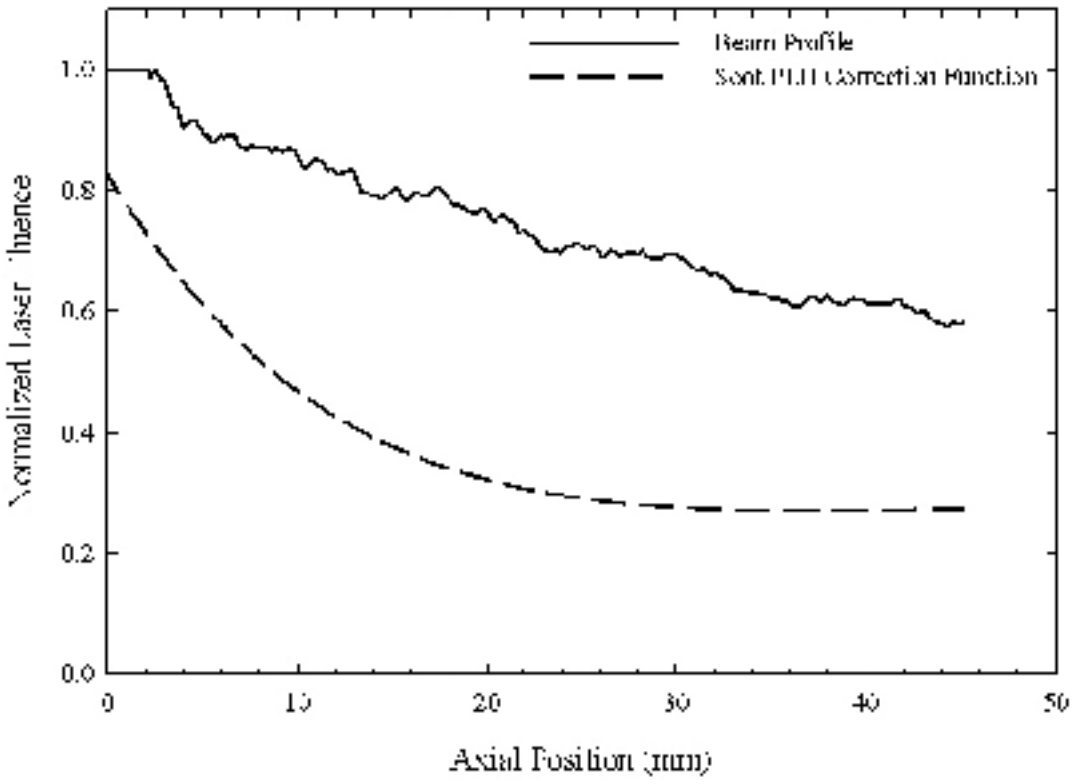


**Figure 4.1: Beam Profile and Soot PLII Correction Function**

#### 4.2.2.4 Analysis of Laser Measurements

Measurements of PLIF and soot PLII signals were time averaged using all 100 frames recorded by the ICCD camera. Radially integrated PLIF and soot PLII signals, $S(z)$, were obtained for each axial position by applying the following formula

$$S(z) = \frac{2\pi}{\pi R^2}\int_0^R rs(r,z)\mathrm{d}r = \frac{2\pi}{\pi R^2}\sum_{i=1}^{256} r_i s(r_i,z)\Delta r \qquad (4.2)$$

where $r$ and $z$ are the radial and axial positions with respect to the centerline and the top of the burner, $R$ is the radius of the integrated path length (256 pixels = 25.6 mm), $s(r,z)$ is the signal at $(r,z)$ and $\Delta r$ is one pixel width (1 pixel = 0.1 mm). Radially integrated signals provide a measure of the total PAH or soot content at each axial position [5,24,39]. Equation 4.2 was derived by multiplying the signal strength of the pixel at each radial position by the area of the annular ring that passes through the radial position, summing all of the products, and then normalizing the sum by dividing by the area of the circle that contains all radial positions.

The following criteria determined the lowest axial positions where PLIF and soot PLII signals could be measured. The lowest axial position for the soot PLII signal in ethylene IDFs was where either (a) there was no minimum between the peaks of the PAH PLIF and soot PLII signals or (b) the signal on the centerline was greater than or equal to the peak soot PLII signal. These conditions were chosen because in case (a), the PAH PLIF and soot PLII signals cannot be distinguished, and in case (b), the soot PLII and background signals cannot be distinguished. The lowest axial position for the PAH PLIF signal in methane IDFs was where the PLIF PAH signal fell below the threshold value of 270 arbitrary units (a.u.), which represents the average background signal (165 a.u.) plus three times the standard deviation of the background (35 a.u.). The background and standard deviation were taken from 100 x 100 pixel squares in the corners of the images. The size of the squares was chosen so that the background and standard deviation measurements were independent of the size of the squares. This threshold was chosen because the background signal has a 99.7% probability of being less than this value, assuming a normal distribution. No criterion was required to distinguish the PAH PLIF

signal in the ethylene IDFs because at all axial positions it was more than three times the background signal. The OH PLIF signals in both flames and the PAH PLIF signal in ethylene flames were all clearly distinguished from the background; however, the PAH PLIF signal in methane IDFs was low, and the soot PLII signal in methane IDFs was too weak to measure. Three centimeters of data were discarded from the top and bottom of the measured signals to remove effects from laser deflection around the top and bottom of the openings in the metal shield surrounding the burner and from the irising effects of the slow gating ICCD camera.

### 4.2.3 Temperature Measurements

Radial profiles of temperature were measured in the ethylene IDF with an air flow rate of 1.6 slpm at axial positions of 1.1 cm, 1.5 cm, 2.0 cm, and 2.5 cm. An axial profile of temperature was measured along the centerline in the same flame. An S-type platinum – 10%-platinum/rhodium thermocouple with a wire diameter of 127 μm was used. The thermocouple was welded to S-type 254 μm diameter thermocouple wire, passed through a ceramic insulator and connected to extension grade thermocouple wire. Thermocouple voltages were amplified with a gain of 207 and recorded on a data acquisition computer at 50 ms intervals. Only twenty data points could be recorded before excessive soot deposition on the thermocouple altered the measurements. A micrometer translation stage with 0.01 mm resolution was used for radial positioning of the thermocouple bead, and vertical position was obtained with a large translation stage and a millimeter ruler with a precision of 0.5 mm. The thermocouple measurements were corrected for radiation heat loss assuming a cylindrical bead geometry [4,40,41].

## 4.3 Computational Methods

Computations of the effects of changing air flow on the ethylene flame temperatures, shapes, flow fields and mixture fractions were performed. Calculations were carried out for the 1.6 and 2.2 slpm air flow rate flames using direct numerical simulation (DNS) of the time-dependent Navier Stokes and conserved variable equations for an axisymmetric laminar flame [42]. The model employs assumptions of low Mach number, infinite-rate chemical kinetics (Burke-Schumann flame sheet), unity Lewis number, variable thermophysical properties, a semi-infinite surrounding fuel-stream, and negligible radiation heat transfer. Mixture fraction, $Z$, was calculated based on the mass fractions of fuel ($Y_{fuel}$), oxygen ($Y_{O2}$), and nitrogen ($Y_{N2}$) according to the formula

$$Z = Y_{fuel} + \left(1 - Y_{fuel} - Y_{O_2} - Y_{N_2}\right)\frac{W_{fuel}}{W_{fuel} + \alpha W_{O_2}} \tag{4.3}$$

where $W_{fuel}$ and $W_{O2}$ are the molecular weights of ethylene (28.054 g/mol) and oxygen (31.999 g/mol), respectively, and $\alpha$ is the stoichiometric molar ratio of oxygen to fuel, which is 3 for the ethylene [43].

## 4.4 Results and Discussion

### 4.4.1 Instantaneous Images of Flickering in PLIF and PLII of Ethylene IDFs

Figure 4.2 and Figure 4.3 demonstrate the degree of buoyancy-induced flickering by showing instantaneous images of OH and PAH PLIF and soot PLII from 1.0-slpm and 2.2-slpm air flow rate ethylene IDFs, respectively. The four images in Figure 4.2 (a) and Figure 4.3 (a) show OH and PAH PLIF observed with the 340 nm band-pass filter at two instants in time (left and right sides). The four images in Figure 4.2 (b) and Figure 4.3 (b)

show soot PLII detected with the 570 nm long-pass filter also at two instants in time (left and right sides). The top figures show images of the flames from 22.8 mm to 73.9 mm above the burner, and the bottom figures show images of the flames from the 0 mm to 48.2 mm above the burner. It should be noted that the regions in the top and bottom panes of the figures overlap from 22.5 to 48.2 mm above the burner.

Figure 4.2 (a) demonstrates that, in the 1.0-slpm air flow rate flame, flickering is not very strong near the base of the flame, but downstream it has an observable effect on the PAH layer with regular vortices forming on both sides of the flame. Figure 4.2 (b) shows that the soot layer is only affected by flickering in the flow field far downstream above the OH layer. Figure 4.2 (b) also shows PAH PLIF detected with the 570 nm long-pass filter that is observed near the base of the flame adjacent to and outside the soot layer.

The vortices observed in the PAH layer in the 2.2-slpm air flow rate IDF depicted in Figure 4.3 (a) are considerably larger than the vortices in the PAH layer in the 1.0-slpm air flow rate IDF shown in Figure 4.2 (a). The vortices also occur noticeably lower in the flame in Figure 4.3 (a) than in Figure 4.2 (a). Figure 4.3 (b) shows that the soot layer is also affected by the vortices in the flow field lower in the flame than in Figure 4.2 (b).

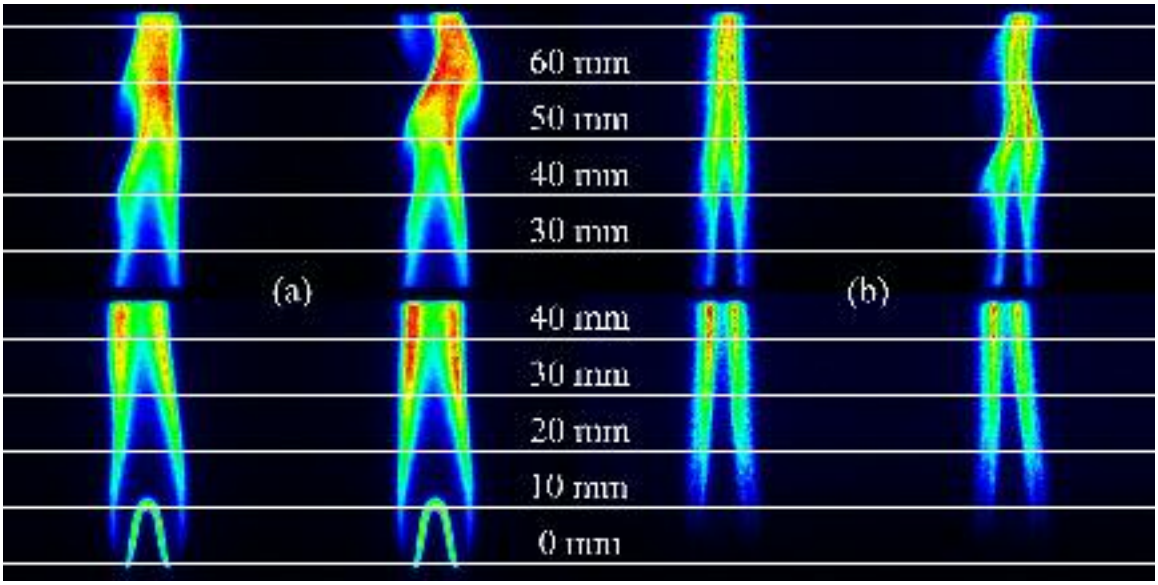


**Figure 4.2: Two instantaneous images of 1.0-slpm air flow rate ethylene IDF. (a) OH and PAH PLIF detected with 340 nm band-pass filter. (b) Soot PLII detected with 570 nm long-pass filter.**

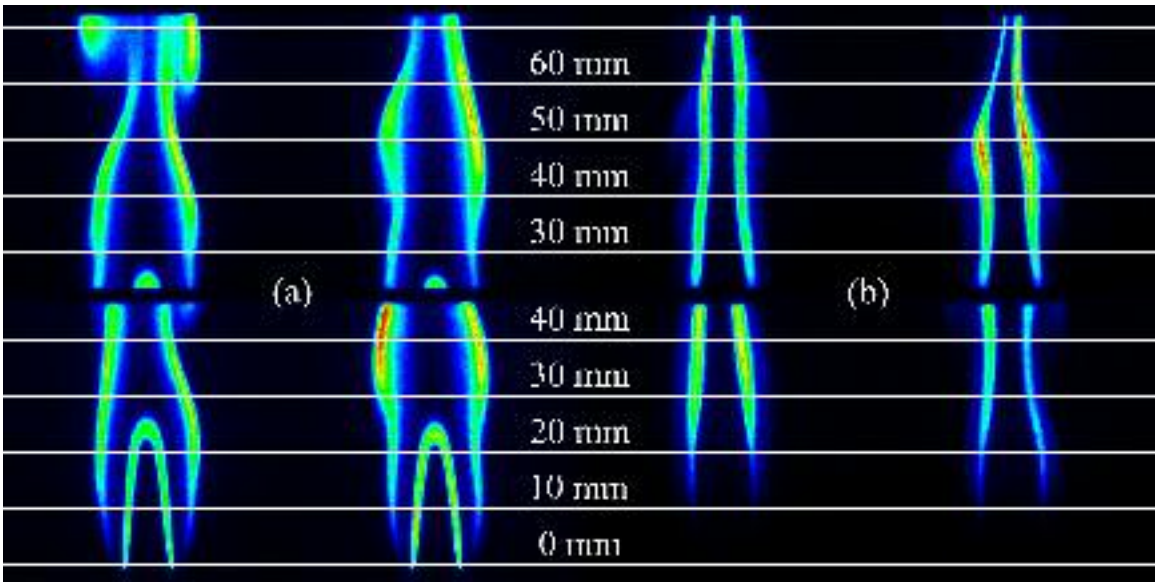


**Figure 4.3: Two instantaneous images of 2.2-slpm air flow rate ethylene IDF. (a) OH and PAH PLIF detected with 340 nm band-pass filter. (b) Soot PLII detected with 570 nm long-pass filter.**

### 4.4.2 Images of OH and PAH PLIF in Ethylene IDFs

Figure 4.4 depicts images of averaged OH and PAH PLIF from ethylene IDFs detected using the 340 nm band-pass filter. White contours are overlaid to show the

locations of peak OH and PAH PLIF and peak soot PLII signals. The peak PAH and soot contours and the OH layer position are pointed out by labeled arrows. Figure 4.4 (a) shows the upper region of the flame, and Figure 4.4 (b) shows the lower region. The high temperature reaction zone is represented by OH radicals [4,20]. The OH layer originates at the top of the burner on the air side and is approximately 2 mm thick. Flickering causes the OH layer to appear spread out at the tip in the longest flames. Instability in the 1.6 slpm air flow rate IDF causes OH layer to appear thicker than those in the other flames. This instability may also cause mixing, unusually shortening the flame.

Originating at the top of the burner, PAH PLIF is present on the outside of the flame in the fuel region. Near the base of the flame, peak PAH PLIF is observed at increasing radial distance from the central axis as axial distance increases. However, above the top of the reaction zone at increasing height above the burner, PAH PLIF signal is found closer to the central axis. As air flow rate increases, peak PAH PLIF is observed further from the central axis, but never more than 10 mm away. Flickering increases as air flow rate increases and causes PAH PLIF to appear spread out at increasing height. The PLIF images qualitatively show that peak PAH PLIF apparently decreases as air flow increases. This may be due to consumption of PAH in soot formation and growth reactions in longer flames that produce more soot; it may also be because the PAH are spatially distributed.

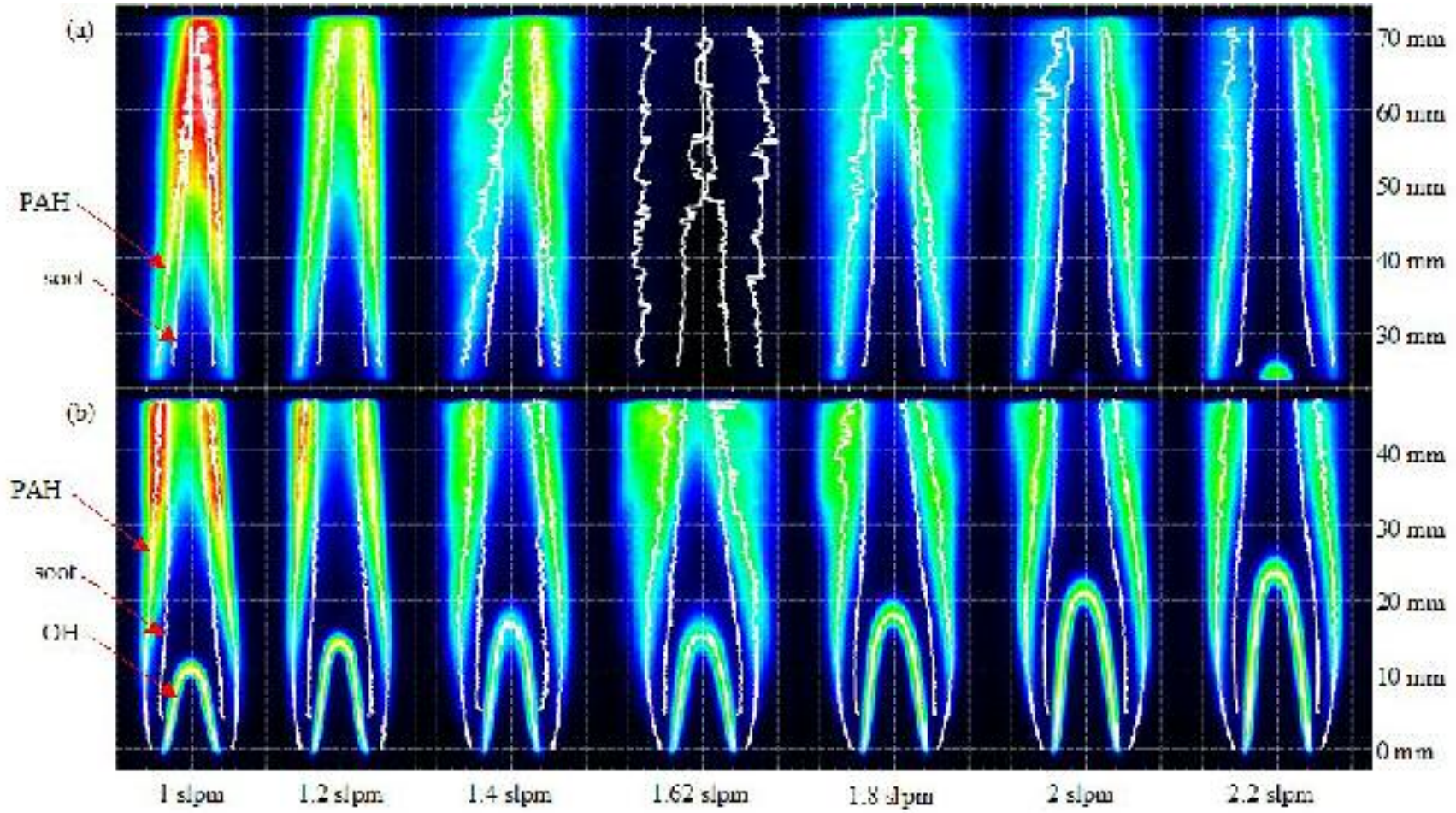


**Figure 4.4: Color-maps of time-averaged OH and PAH PLIF detected with 340 nm band pass filter from ethylene IDFs of varying air flow rates with contours of peak PLIF and PLII overlaid in white. (a) PAH PLIF from 22.7 mm to 73.9 mm above burner with scaling factor of 13440. The signal for the 1.62 slpm air flow rate IDF is low because the laser was blocked. (b) PAH and OH PLIF from 0 mm to 48.2 mm above burner with scaling factor of 10000. The intensity of the PLIF signals is color-mapped such that black, blue, green, red, and white represent increasing intensity, respectively.**

### 4.4.3 Images of Soot PLII in Ethylene IDFs

Figure 4.5 depicts averaged images of soot PLII from ethylene IDFs detected using the 570 nm long-pass filter. White contours are overlaid to show the locations of peak OH and PAH PLIF and peak soot PLII signals. Figure 4.5 (a) shows the upper region of the flame, and Figure 4.5 (b) shows the lower region. Soot PLII is present within 2-4 mm of the reaction zone on the fuel side of the flame in between the PAH and OH PLIF, which compares well with the position of soot relative to the reaction zone in many previous studies of both NDFs and IDFs [2,4,7,8,10,12,15,21,22,24]. Soot PLII does not originate at the burner exit but is first observed low in the flames and near the same location for all flames, about 5 mm from the top of the burner. This corresponds to a chemical time for soot inception in ethylene IDFs of between 10 and 20 ms, assuming a buoyant acceleration of 27 $m/s^2$ and using the initial air and fuel velocities as the upper and lower bounds. Soot inception time has been previously reported in the range of 10 ms for diffusion flames [44]. The soot PLII signal is consistently 2-4 mm away from the PAH layer. The position of soot relative to PAH also compares well with previous measurements in both NDFs and IDFs [4,5,8-10,12,18,21]. The soot PLII images qualitatively show that the peak soot PLII signal and the apparent width of the soot layer increase with increasing air flow rate. Flickering does not appear to affect the soot layer as significantly as it affects the PAH layer, since the soot layer is not as spread out as the PAH PLIF and does not appear to have the bulges associated with vortices. An instability at an air flow rate of 1.6 slpm is observed in both the PAH PLIF and the soot PLII, causing the signals to appear spread out.

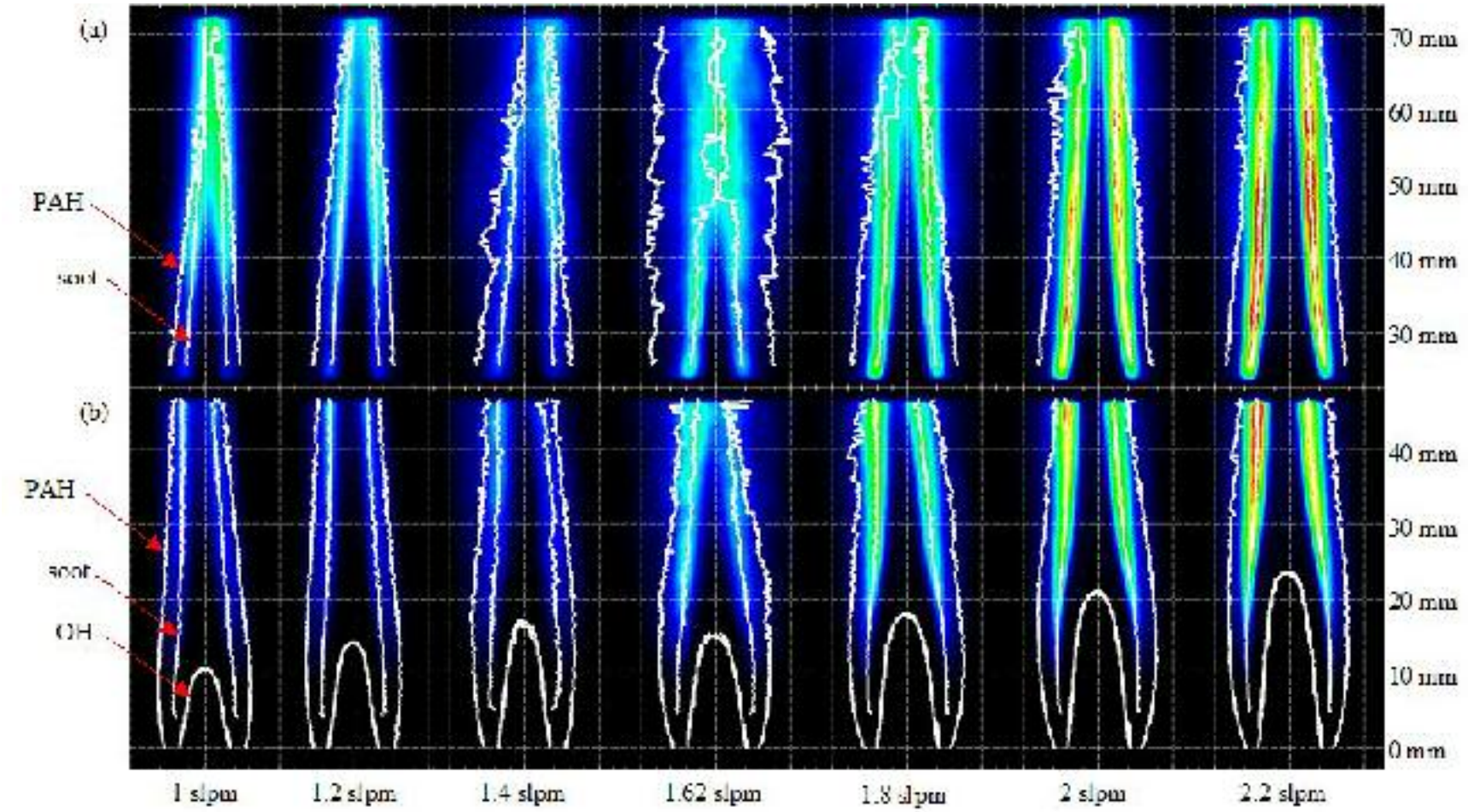


**Figure 4.5: Color-maps of time-averaged soot PLII detected with 570 nm long pass filter from ethylene IDFs of varying air flow rates with contours of peak PLIF and PLII overlaid in white. (a) Soot PLII from 22.7 mm to 73.9 mm above burner with scaling factor of 33907. (b) Soot PLII from 0 mm to 48.2 mm above burner with scaling factor of 37450. The intensity of the PLII signals is color-mapped such that black, blue, green, red, and white represent increasing intensity, respectively.**

### 4.4.4 Color Visible Images of Ethylene IDFs

Depicted in Figure 4.6 are visible color images of ethylene IDFs with contours of the peak OH and PAH PLIF and soot PLII signals overlaid in white. The blue reaction zone is only visible near the base of the ethylene IDFs. The contour of the peak OH PLIF signal lies on the air side of the blue reaction zone. This agrees with the observation made by other researchers that OH radicals are found on the lean side of the stoichiometric contour, and that the stoichiometric contour lies on the lean side of the blue reaction zone [4,20,45]. For all air flow rates, luminous soot begins roughly 3 mm from the burner exit, obscures the top of the blue reaction zone, and extends above the peak OH PLIF contour. Luminous soot in the visible color images begins slightly lower than the peak soot PLII signal, which occurs about 5 mm above the burner for all flames, possibly because incipient soot particles are more difficult to detect by PLII than larger soot particles [11]. The peak soot PLII contour closely follows the outer edge of the luminous soot cone. The peak PAH PLIF contour lies outside the luminous soot, and PAH are not visible in the color images. Therefore, flickering observed in the PAH PLIF is not visible in the color images. This is consistent with the fact that soot LII was not affected very much by flickering; the visible images capture soot radiation.

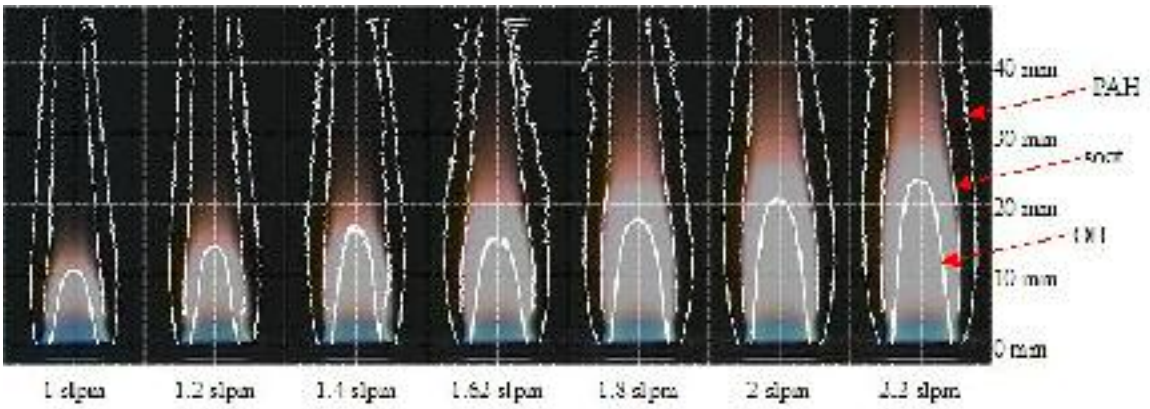


**Figure 4.6: Visible color images of ethylene-air IDFs with contours of the peak time-averaged PLIF and PLII signals overlaid.**

### 4.4.5 Images of OH and PAH PLIF in Methane IDFs

Figure 4.7 depicts images of averaged OH and PAH PLIF in the lower region of methane IDFs detected with the 340 nm band-pass filter. Contours of the peak OH and PAH PLIF signals are overlaid in white. Many features of the methane IDFs are similar to those of ethylene IDFs. The OH layer begins at the burner exit and is about 2 mm thick, except at the tip where flickering makes the averaged OH layer appear to spread out for longer flames.

As in ethylene IDFs, PAH PLIF is on the fuel side of the flame. The radial location of the peak PAH PLIF decreases with increasing height above the burner. As air flow rate increases, peak PAH PLIF is observed further from the central axis, but never more than 10 mm away. In the methane IDFs, unlike in the ethylene IDFs, the PAH PLIF does not originate at the burner exit. Instead, it begins about 10 mm above the top of the burner. The slow formation of PAH in methane IDFs is possibly due to the slow formation of methyl radicals in methane flames [16]. The formation of PAH from methane initially requires two methyl radicals to form acetylene, but the formation of methyl radicals from the pyrolysis of methane is slow because of the high bond strength

between carbon and hydrogen in methane [46]. The slower formation rate of PAH in methane IDFs may lead to a lower ratio of pyrolysis products to oxidation products involved in soot growth [16,17].

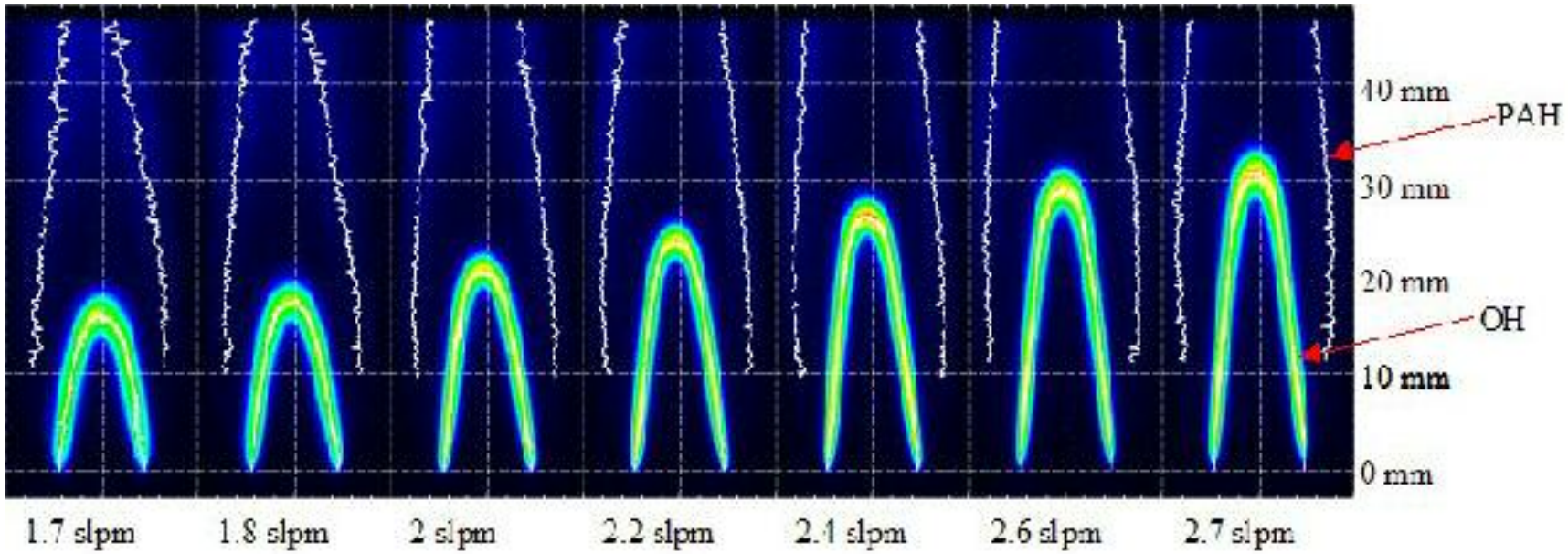


**Figure 4.7: Color-maps of time-averaged OH and PAH PLIF detected with 340 nm band pass filter from methane IDFs of varying air flow rates with contours of peak PLIF overlaid in white. The intensity of the PLIF signals is scaled by a factor of 6200 and color-mapped such that black, blue, green, red, and white represent increasing intensity, respectively.**

Soot PLII could not be measured in methane IDFs using the laser and camera configuration in this study. Methane, an alkane, has a lower propensity to soot than ethylene, an alkene [31,32]. This is due to the barrier to aromatic formation from pyrolysis of methane [46]. Therefore, the concentration of soot in methane IDFs was too low to generate a sufficient PLII signal to measure. Also, since the methane soot may be more organic than elemental, absorption and emission may be lower. Furthermore, since the concentration of PAH is low, soot growth may also be low, and soot particles may be too small to detect.

### 4.4.6 Color Visible Images of Methane IDFs

Figure 4.8 depicts visible color images of methane IDFs with contours of peak OH and PAH PLIF overlaid in white. The blue reaction zone is visible for the first centimeter of methane IDFs, although it is dimmer than the blue region in ethylene IDFs. As in ethylene IDFs, the peak OH PLIF contour is on the air side of the blue reaction zone. Even though the OH layer begins at the burner exit, the blue reaction zone in methane IDFs with air flows greater than 1.2 slpm is lifted about 1-2 mm above the burner exit. Luminous soot is visible even though soot PLII was not detected. The soot cone is dimmer than the bright yellow soot region in the ethylene IDFs. It may also be due to lower soot emissivity. The soot annulus begins roughly 10 mm from the top of the burner, which corresponds to the location where PAH PLIF originates. Data not shown in Figure 4.8 indicate that methane IDFs with heights less than 10 mm do not have visible luminous soot cones. In methane IDFs longer than 10 mm, luminous soot blurs or obscures the tip of the blue reaction zone and extends above the OH PLIF contour.

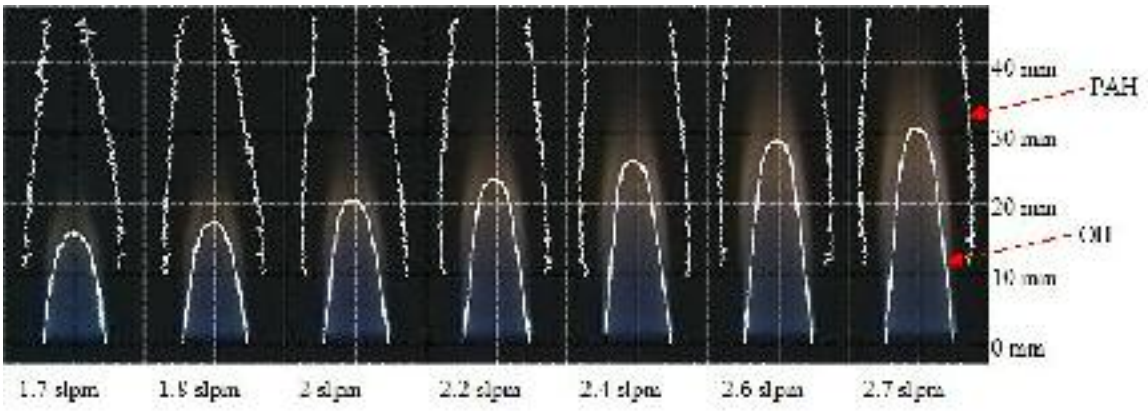


**Figure 4.8: Visible color images of methane-air IDFs with contours of the peak time-averaged PLIF signals overlaid.**

### 4.4.7 Comparison of PAH PLIF from Ethylene IDFs Detected in Different Bands

Figure 4.9 shows a comparison between the peak PAH PLIF position in ethylene IDFs detected with a 340 nm band-pass filter and with a combination of the 295 nm long-pass and 450 nm short-pass filters. For all air flow rates, PAH PLIF in both detection bands is located on the fuel side of the reaction zone. However, PAH PLIF detected with the combination of the 295 nm long-pass and 450 nm short-pass filters is closer to the reaction zone and hence occurs in a higher temperature region than PAH PLIF detected with the 340 nm band-pass filter. Other researchers have reported that the shift is due to the presence of large aromatics which are detected at longer wavelengths and which form at higher temperatures than small aromatics [4,8,9,33].

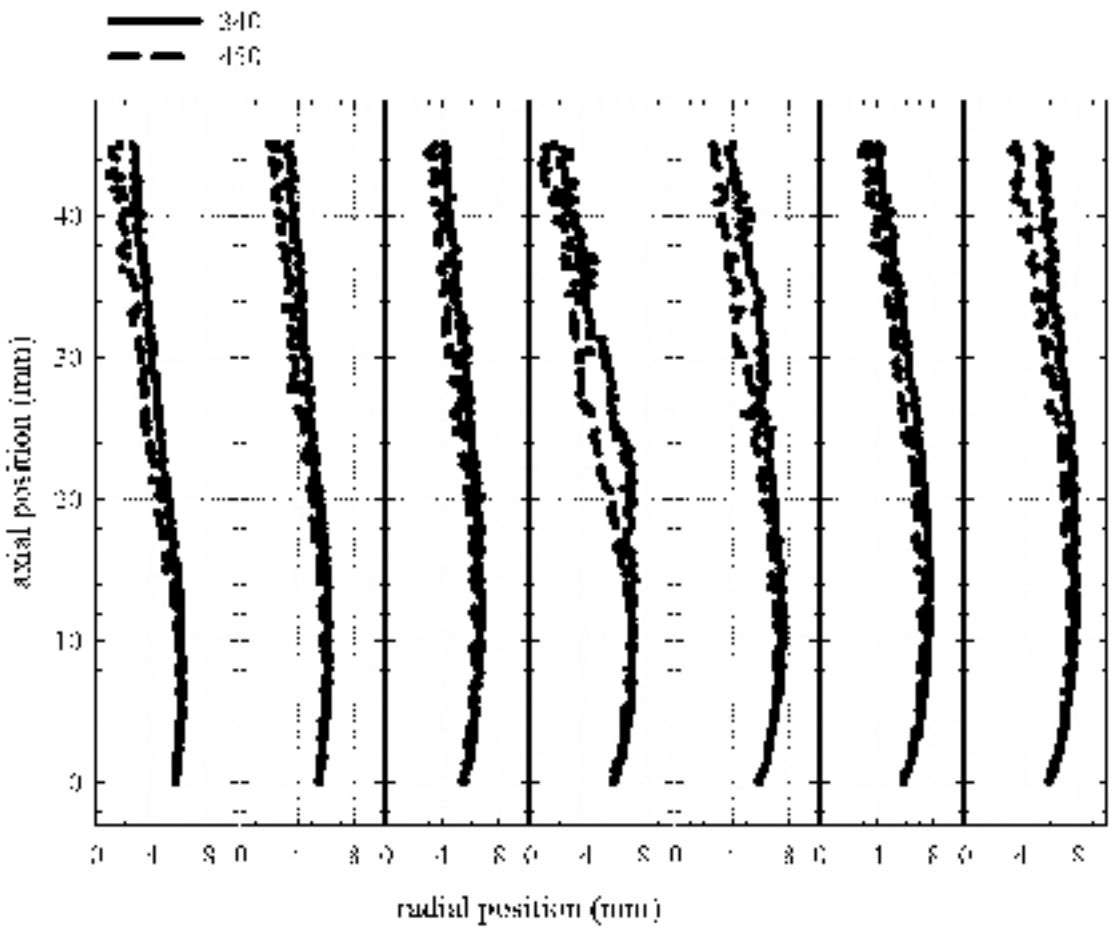


**Figure 4.9: Comparison between the peak PAH PLIF position in ethylene IDFs detected with a 340 nm band-pass filter and with a combination of the 295 nm long-pass and 450 nm short-pass filters.**

### 4.4.8 Intensity of OH PLIF in Ethylene and Methane IDFs

Figure 4.10 and Figure 4.11 show the intensity of peak OH PLIF detected with the 340 nm band pass filter as a function of axial position of ethylene and methane IDFs, respectively. The ordinate ranges of the two figures are the same (5000 arbitrary units). For each fuel type, peak OH PLIF increases steadily for the first 4 mm of the flame. Next, OH PLIF reaches a constant maximum value until the top of the reaction zone. For each fuel type, the maximum constant value is also constant for all air flow rates, with the exception of 1.4 and 1.6 slpm in the ethylene IDFs. Instability in these flames, discussed

in Chapter 3, may have caused mixing of the radicals with fuel, pyrolyzates, and intermediates of combustion, which consumed the radicals. The maximum constant OH PLIF in ethylene IDFs is more than 50% greater than that of methane IDFs.

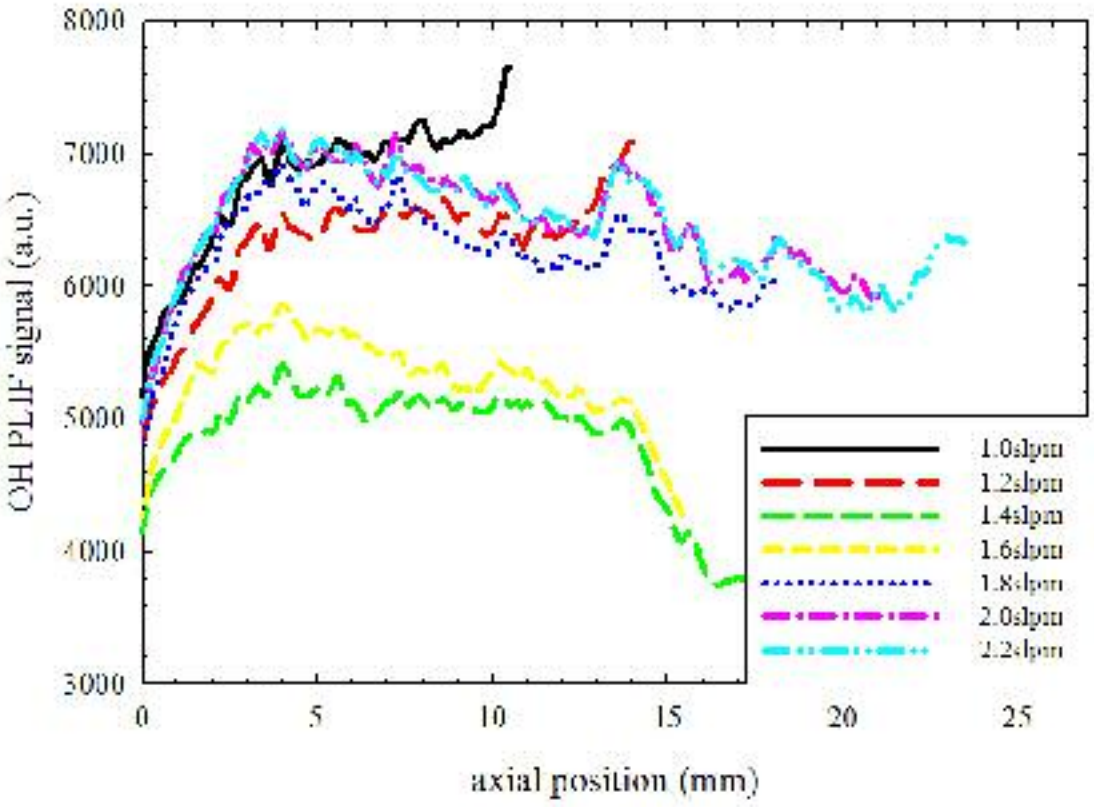


**Figure 4.10: Peak OH PLIF of ethylene IDFs detected with 340 nm band pass filter.**

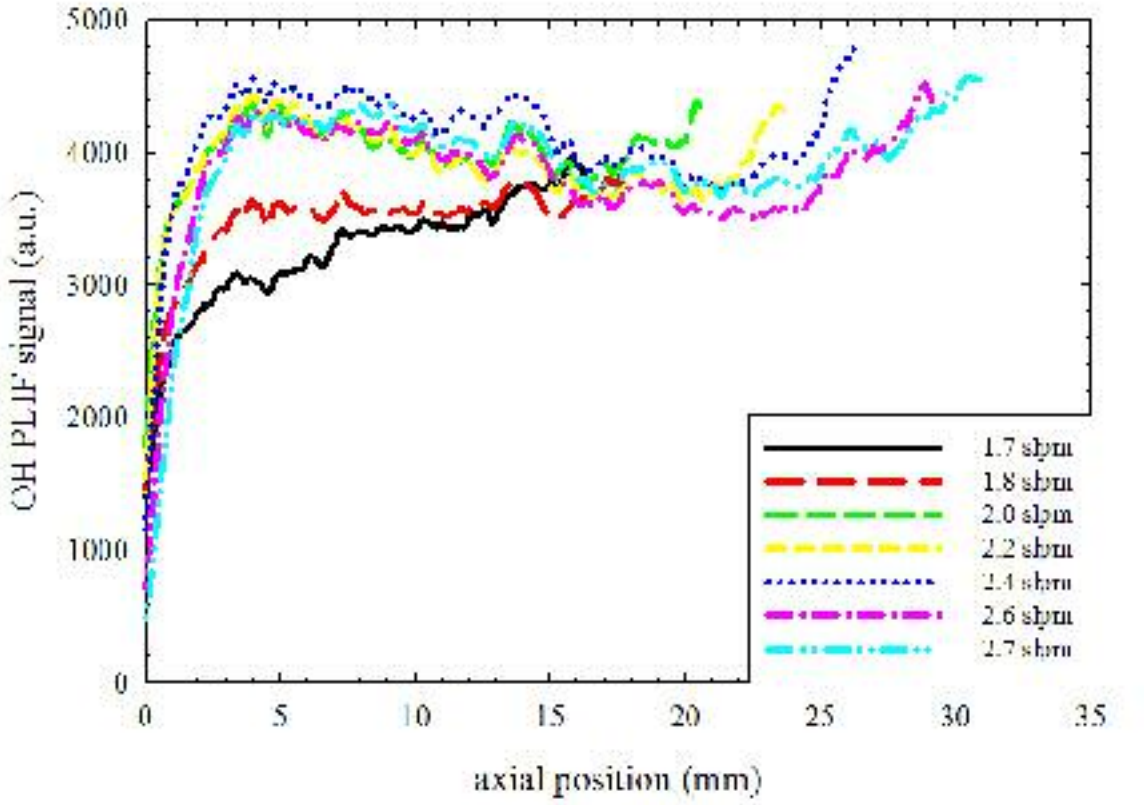


**Figure 4.11: Peak OH PLIF of methane IDFs detected with 340 nm band pass filter.**

### 4.4.9 Intensity of PAH PLIF in Ethylene IDFs

Intensity of PAH PLIF was affected by the irising effects of the slow gating camera. This effect artificially caused the top, bottom and sides of each measurement to be under reported as those areas of the ICCD array are open for less time than the center. Three millimeters of data have been discarded from the areas most affected by the irising effect, but it is important to consider this effect when interpreting the data. Comparisons of the overlap region between the measurements taken with the laser sheet from 0 to 45.1 mm and from 25.7 to 70.8 mm can be used to check when irising effects should be considered.

Figure 4.12 shows the PLIF intensity in ethylene IDFs detected with the 340 nm band pass filter. The 1.6 slpm air flow rate flame PAH PLIF was not measured above 45.1 mm, because the laser was accidentally blocked. Figure 4.12 (a) and Figure 4.12 (b) depict peak PAH PLIF in the lower and upper regions of the flames, respectively. Peak PAH PLIF increases from the base of the flame at the same rate for all air flow rates up to 15 mm. Above 15 mm, peak PAH PLIF appears to plateau in the 1.4, 1.6, and 1.8 slpm air flow rate IDFs because of an anomalous instability that increased flickering, and in the 2.0 and 2.2 slpm air flow rate IDFs because they are longer and flicker strongly. Flickering spreads PAH over a larger, area decreasing the peak. For the 1.0 and 1.2 slpm air flow rate IDFs, peak PAH PLIF continues to increase until further downstream, because they are shorter and are affected less by flickering.

Radially integrated PLIF signals in the lower and upper regions of the flames are shown in Figure 4.12 (c) and Figure 4.12 (d), respectively. Both OH and PAH PLIF are present in the integrated signal from the base of the flame until the top of the OH layer, above which only the PAH PLIF is present. Above the OH layer, integrated PAH PLIF increases monotonically for all air flow rates, clearly showing that the plateaus observed in Figure 4.12 (a) and Figure 4.12 (b) are caused by flickering. The 1.4, 1.6 and 1.8 slpm air flow rate IDFs have the greatest integrated signals and the largest slopes, possibly because instability observed in those flames brought fuel into hotter regions of the flame enhancing pyrolysis and increasing the yield of PAH [10]. The 2.0 and 2.2 slpm air flow rate IDFs have greater integrated signals than the 1.0 and 1.2 slpm air flow rate IDFs because they are longer and hence fuel has more time at high temperature to pyrolyze and form PAH, and also because strong flickering brought fuel into hotter regions, enhancing

pyrolysis and PAH formation. Above 60 mm, the integrated signals for some of the air flow rates appear to decrease, which is probably due to the irising effect of the camera but may also be due to scavenging of PAH by soot.

Centerline PLIF signals in the lower and upper regions of the flames are shown in Figure 4.12 (e) and Figure 4.12 (f), respectively. The large spikes represent the OH layer. Immediately following the OH layer there is virtually no PAH signal, but higher on the flame centerline PAH signal increases for all air flow rates as PAH is brought to the center by diffusion and recirculation. Centerline PAH PLIF increases with decreasing rate of air flow. The centerline PAH increases most rapidly with respect to changes in axial distance for the lowest air flow rate IDFs because, in shorter flames, the PAH layer is closer to the centerline.

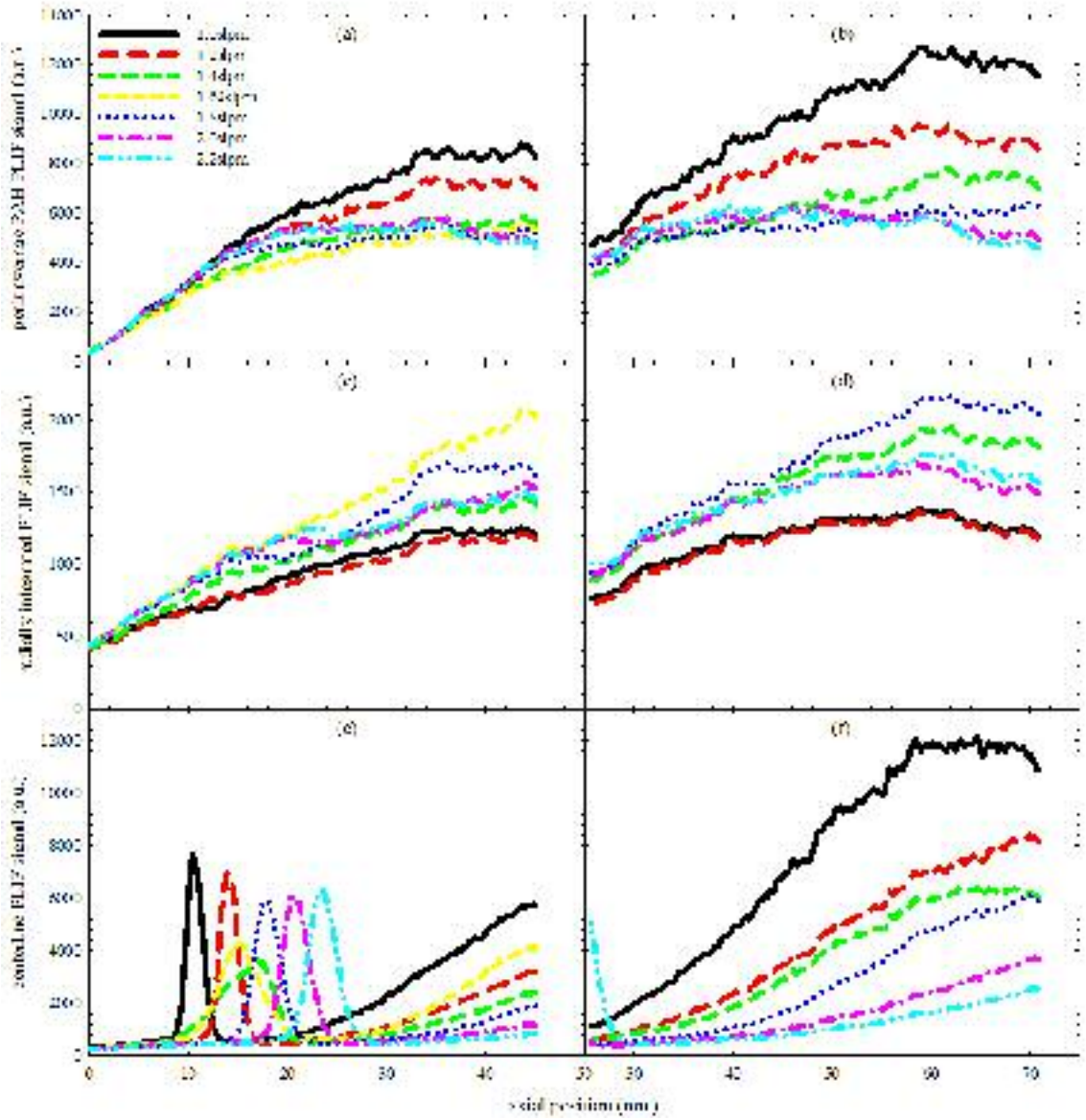

**Figure 4.12: PLIF detected with 340 nm band-pass filter in ethylene IDFs versus axial position. (a) Peak PAH PLIF, (b) radially integrated PLIF and (c) centerline PLIF from 0 mm to 45.1 mm, (a), (c) and (e), and 25.7 mm to 70.8 mm, (b), (d) and (f), above the burner.**

Figure 4.13 shows PLIF for ethylene IDFs detected using the 295 nm long-pass and 450 nm short-pass filters. Figure 4.13 (a) and Figure 4.13 (b) depict peak PAH PLIF in the lower and upper regions of the flames, respectively. Peak PAH PLIF in Figure 4.13 (a) and Figure 4.13 (b) is four times greater than it was in Figure 4.12 (a) and Figure

4.12 (b). Peak PAH PLIF in Figure 4.13 (a) and Figure 4.13 (b) increases more rapidly with respect to axial distance than in Figure 4.12 (a) and Figure 4.12 (b) because peak PAH PLIF is closer to the reaction zone where temperature is greater and pyrolysis and PAH formation rates are faster. Flickering affects peak PAH PLIF in Figure 4.13 (a) and Figure 4.13 (b) further downstream than in Figure 4.12 (a) and Figure 4.12 (b) because peak PAH PLIF is closer to the centerline and thus less affected by flickering in the co-flow. Peak PAH PLIF increases at the same rate with respect to increasing axial distance for all air flow rates until 40 mm above the burner where flickering spreads PAH over a larger area decreasing the peak for 1.4 to 2.2 slpm air flow rate IDFs. Peak PAH PLIF in 1.0 and 1.2 slpm air flow rate IDFs continues to increase and is not affected by flickering until 50 mm.

Radially integrated combined OH and PAH PLIF signals in the lower and upper regions of the flames are depicted in Figure 4.13 (c) and Figure 4.13 (d), respectively. Both OH and PAH PLIF are present in the radially integrated signal from the base of the flame until the top of the OH layer, above which only the PAH PLIF is present. The 1.4, 1.6, and 1.8 slpm air flow rate flame have the largest integrated signals, perhaps because instability-induced mixing promoted PAH production. The 2.0 and 2.2 slpm air flow rate flames have longer residence times and are more affected by flickering, so they have larger integrated signals than the 1.0 and 1.2 slpm air flow rate flames.

Centerline PLIF signals in the lower and upper regions of the flames are shown in Figure 4.13 (e) and Figure 4.13 (f), respectively. The large spikes indicate the OH layer. After the OH peak, PAH PLIF is observed and increases with height as PAH diffuses to

the center. PAH diffuses to the centerline more rapidly for the shortest flames because the PAH layer is closer to the centerline.

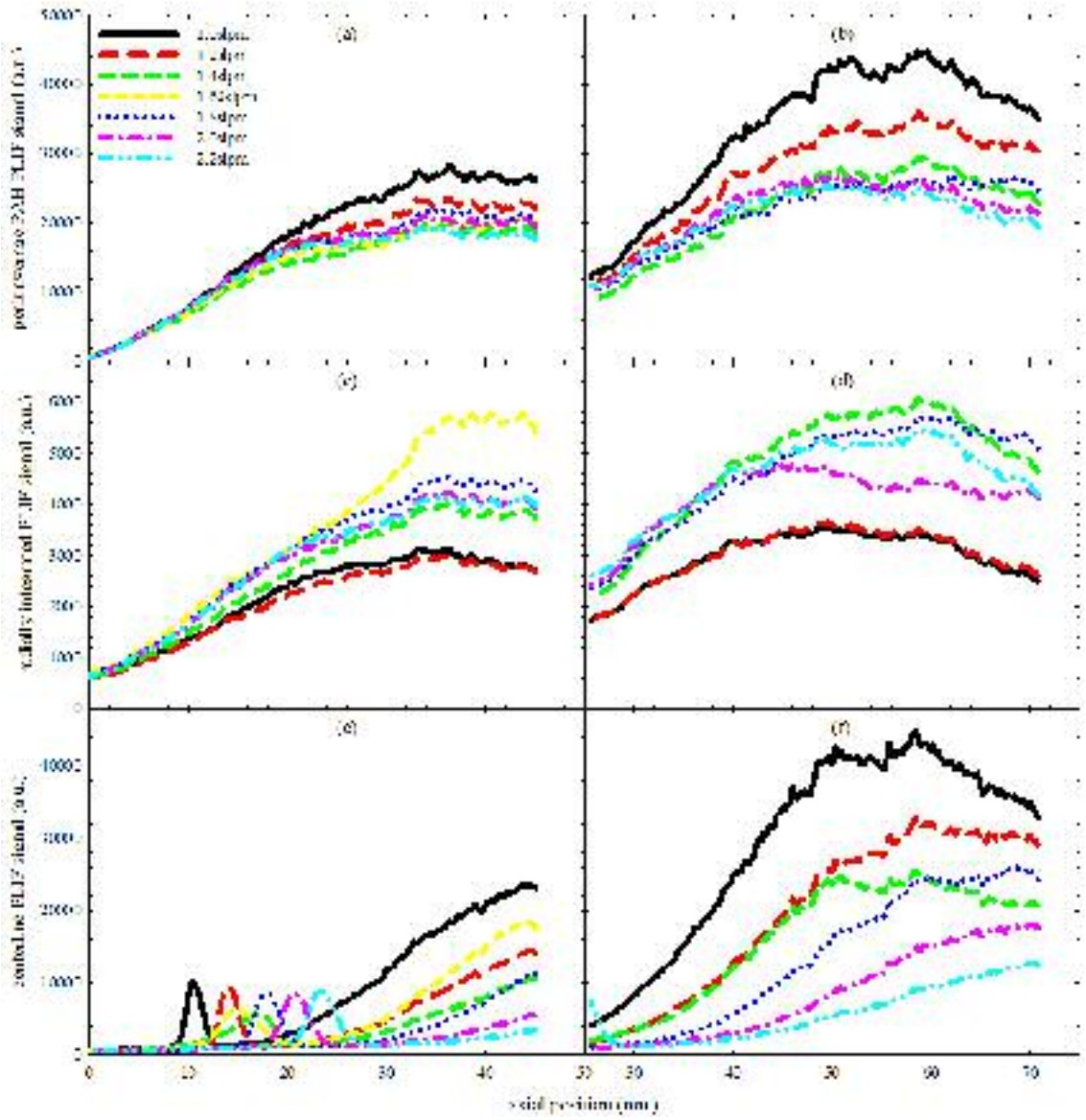

**Figure 4.13: PLIF detected with 295 nm long-pass and 450 nm short-pass filters in ethylene IDFs versus axial position. (a) Peak PAH PLIF, (b) radially integrated PLIF and (c) centerline PLIF from 0 mm to 45.1 mm, (a), (c) and (e), and 25.7 mm to 70.8 mm, (b), (d) and (f), above the burner.**

### 4.4.10 Intensity of Soot PLII in Ethylene IDFs

Soot PLII detected with a 570 nm long-pass filter from ethylene IDFs is depicted in Figure 4.14. Peak soot PLII signals are shown in Figure 4.14 (a) and Figure 4.14 (b) in the lower and upper regions of the flame, respectively. Peak soot PLII could not be distinguished from a ring of PAH PLIF around the base of the burner until 5 mm above the burner for all air flow rate IDFs. Peak soot PLII increases as a function of axial distance and has the largest slope for the highest air flow rate IDF. Peak soot PLII signal increases until above the top of the OH layer, and then the slope decreases. This may indicate that soot inception has ceased, and peak soot PLII signal is increasing due to soot growth. High in the flame, peak soot PLII reaches a maximum and remains nearly constant. Peak soot PLII signal decreases slightly for the highest air flow rate flames, presumably because flickering spreads the soot over a larger area, decreasing the peak

Radially integrated soot PLII signal is shown in Figure 4.14 (c) and Figure 4.14 (d) in the lower and upper regions of the flame, respectively. The rate of increase in integrated signal increases with air flow rate, but is nearly constant for 1.6, 1.8, 2.0, and 2.2 slpm air flow rate flames. Signals for the flames with air flow rates of 1.0, 1.2, and 1.4 slpm also appear to have very similar slopes. Integrated signals increase until after the top of the high temperature reaction zone. High in the flames, at 35 mm above the burner, the integrated signals approach constant values, as soot formation and growth mechanisms become frozen. This agrees well with the radially integrated data reported by Makel and Kennedy [24].

Centerline soot PLII signals are reported in Figure 4.14 (e) and Figure 4.14 (f) in the lower and upper regions of the flame, respectively. The figures show that inside the

flame, there is no soot present. Downstream of the reaction zone, soot diffuses or is advected to the centerline. The soot PLII signals increase most rapidly with respect to axial distance for the shortest flames and for the flames with strong instabilities such as the 1.6 slpm air flow rate IDF.

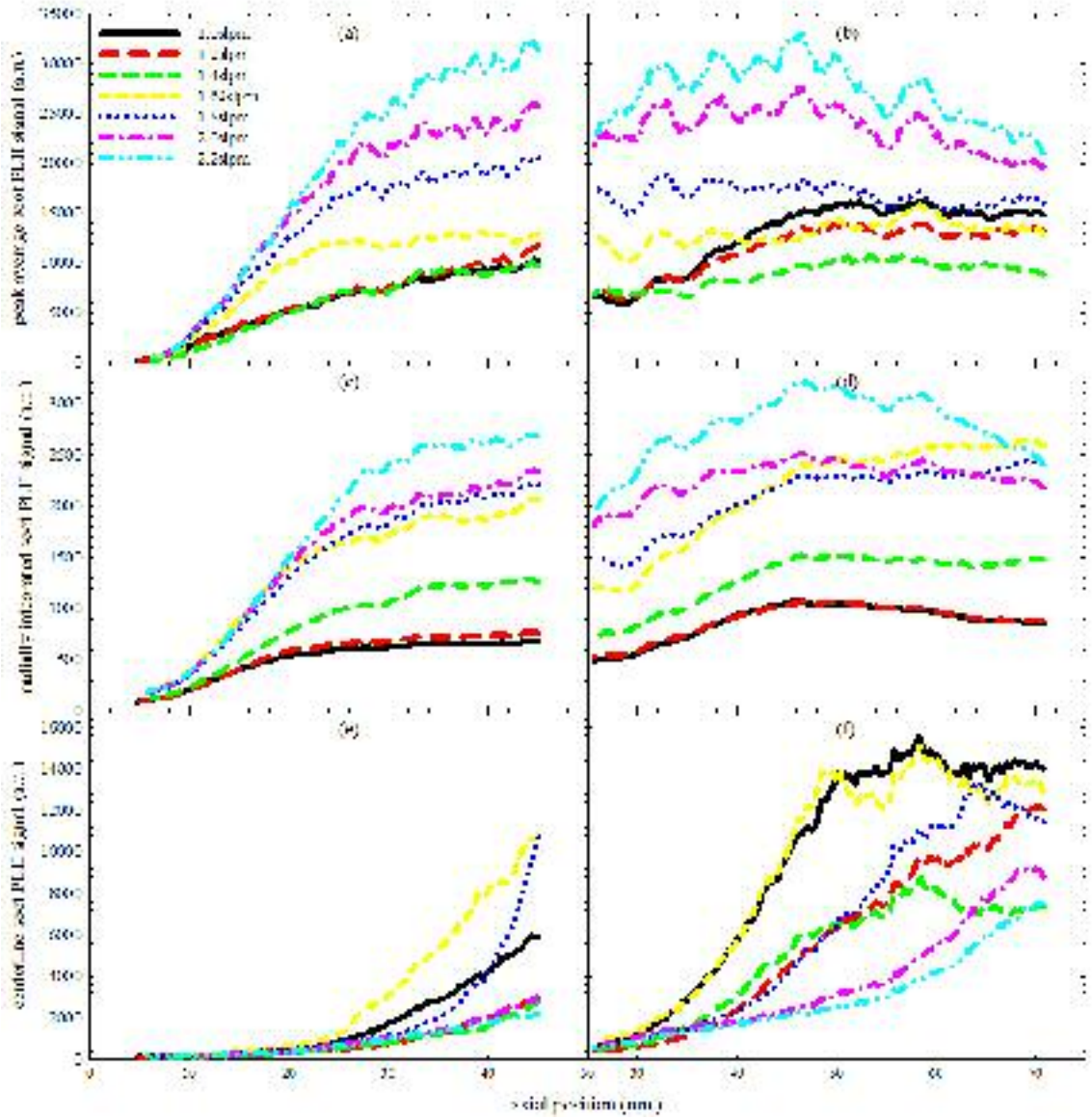


**Figure 4.14: Soot PLII detected with 570 nm long-pass filter in ethylene IDFs versus axial position. (a) Peak PAH PLIF, (b) radially integrated PLIF and (c) centerline PLIF from 0 mm to 45.1 mm, (a), (c) and (e), and 25.7 mm to 70.8 mm, (b), (d) and (f), above the burner.**

Figure 4.15 shows that the maximum radially integrated soot PLII signal increases linearly with air flow rate for ethylene IDFs. Since, in IDFs, flame height and residence time are determined by air flow rate, Figure 4.15 indicates that the global flame soot production rate is directly proportional to flame height and residence time. Extrapolation of Figure 4.15 also predicts that an ethylene IDF with an air flow rate less than 0.6 slpm will produce no soot. This measurement is very similar to traditional smoke point measurements in NDFs, where fuel flow rate is varied until a flame emits smoke or observed to form soot.

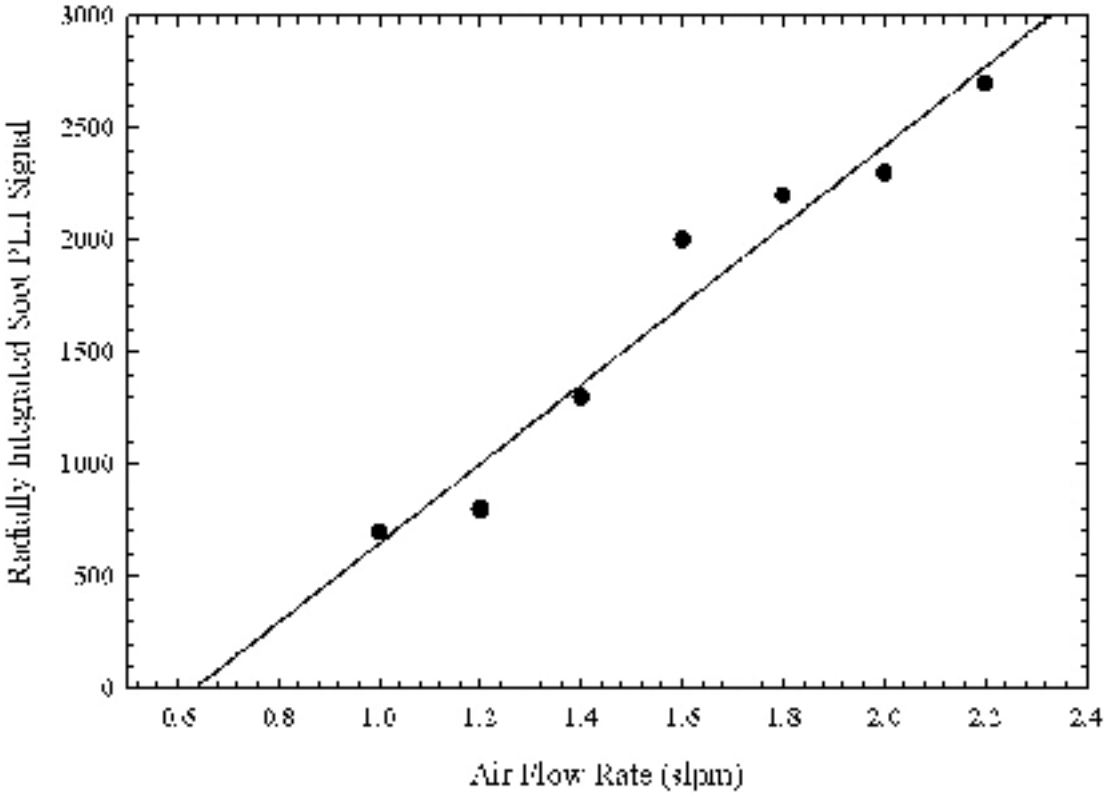


**Figure 4.15: Maximum radially integrated soot PLII signal versus air flow rate for ethylene IDFs.**

### 4.4.11 Intensity of PAH PLIF in Methane IDFs

Figure 4.16 shows PLIF in methane IDFs detected with the 340 nm band-pass filter. Figure 4.16 (a) and Figure 4.16 (b) depict peak PAH PLIF in the lower and upper regions of the flames, respectively. There is no PAH PLIF detected below 10 mm for all air flow rates. Peak PAH PLIF has the same slope for all air flow rates until 35 mm, where flickering influences the signal. Above 35 mm, the peak PAH PLIF signal decreases as the rate of air flow increases. Also above 35 mm the rate of increase in peak PAH PLIF decreases with increasing air flow rate, because longer flames were more affected by flickering, causing the peak signal to drop as PAH PLIF is spread over a larger area.

Figure 4.16 (c) and Figure 4.16 (d) show radially integrated OH and PAH PLIF in the lower and upper regions of the flames, respectively. The radially integrated signal combines OH and PAH PLIF until the end of the OH layer, after which there is only PAH PLIF. The radially integrated PAH PLIF increases monotonically at nearly the same rate with respect to axial position for all air flow rates.

Figure 4.16 (e) and Figure 4.16 (f) show centerline PLIF in the lower and upper regions of the flames, respectively. The large spikes are due to OH PLIF. Downstream of the OH spike, PAH diffuses to the centerline. The centerline PAH increases most rapidly with respect to axial distance for the lowest air flow rate because it is closest to the centerline.

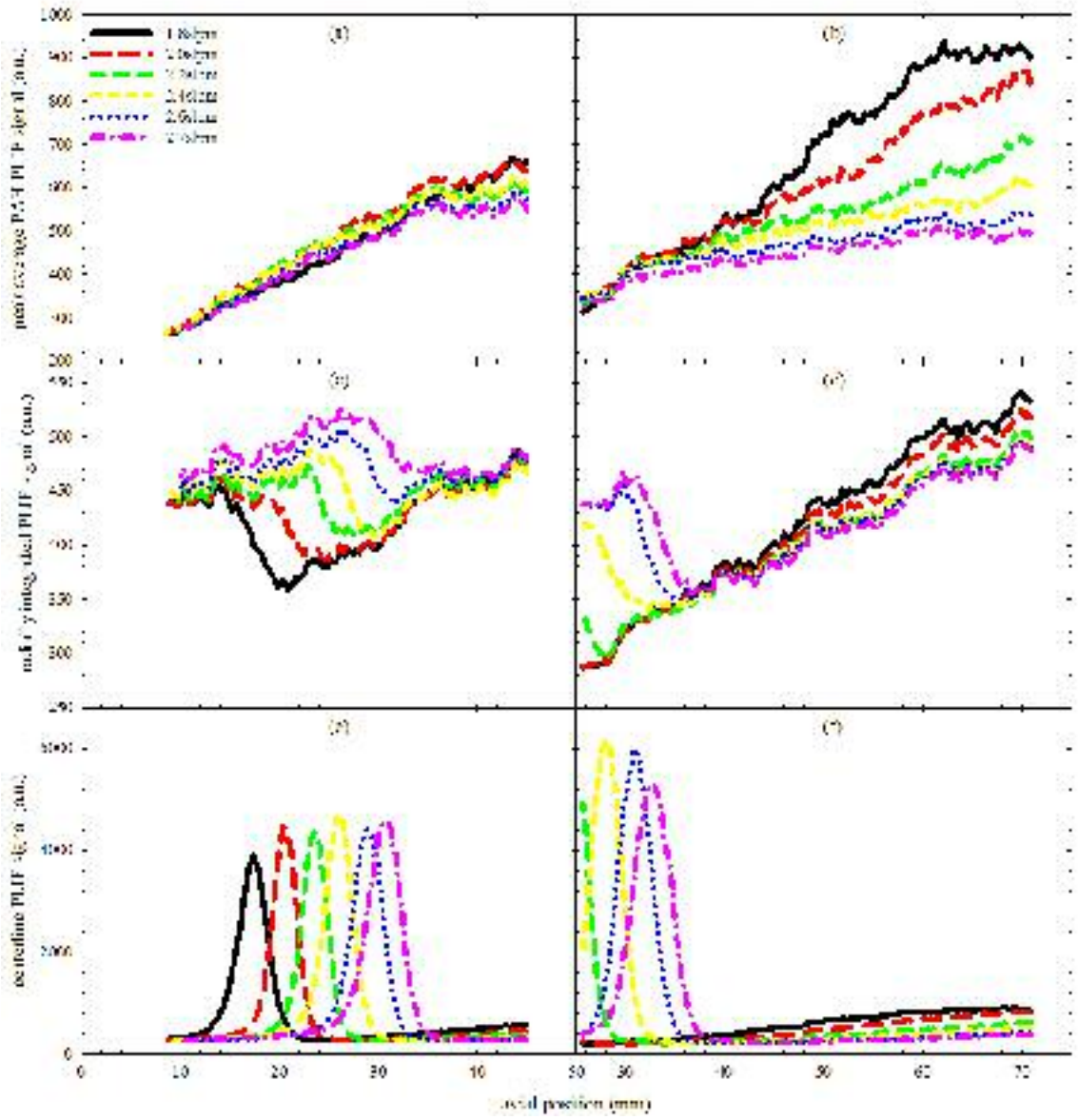

**Figure 4.16: PLIF detected with a 340 nm band-pass filter in methane IDFs versus axial position. (a) Peak PAH PLIF, (b) radially integrated PLIF and (c) centerline PLIF from 0 mm to 45.1 mm, (a), (c) and (e), and 25.7 mm to 70.8 mm, (b), (d) and (f), above the burner.**

Figure 4.17 shows PLIF in methane IDFs detected with the 295 nm long-pass and 450 nm short-pass filters. Figure 4.17 (a) and Figure 4.17 (b) depict peak PAH PLIF in methane IDFs in the lower and upper regions of the flames, respectively. PAH PLIF originates at 5 mm for all air flow rates, which is lower than the location of minimum

detectable PAH with the 340 nm band-pass filter. Peak PAH PLIF detected in this band is twice the intensity of PAH PLIF detected with the 340 nm band pass filter. Therefore, the PAH PLIF detected with the 340 nm band-pass filter appeared to originate higher because of very low signal to noise ratio at positions lower than 10 mm. Peak PAH PLIF increases with decreasing rate of air flow. Peak PAH PLIF has the same slope for all air flow rates until 20 mm, above which the slope increases with decreasing air flow rate.

Figure 4.17 (c) and Figure 4.17 (d) show radially integrated PLIF in the lower and upper regions of the flames, respectively. The radially integrated signal combines OH and PAH PLIF until the end of the OH layer, after which there is only PAH PLIF. Radially integrated PAH PLIF above the OH layer increases monotonically for all air flow rates, and the curves for the lower air flow rate IDFs have larger slopes.

Figure 4.17 (e) and Figure 4.17 (f) show centerline PLIF in the lower and upper regions of the flames, respectively. The large spikes in the centerline signal are due to OH radicals. Above the OH spike PAH diffuses or advects to the centerline. The centerline PAH PLIF increases most rapidly with respect to axial distance for the lower air flow rate IDFs.

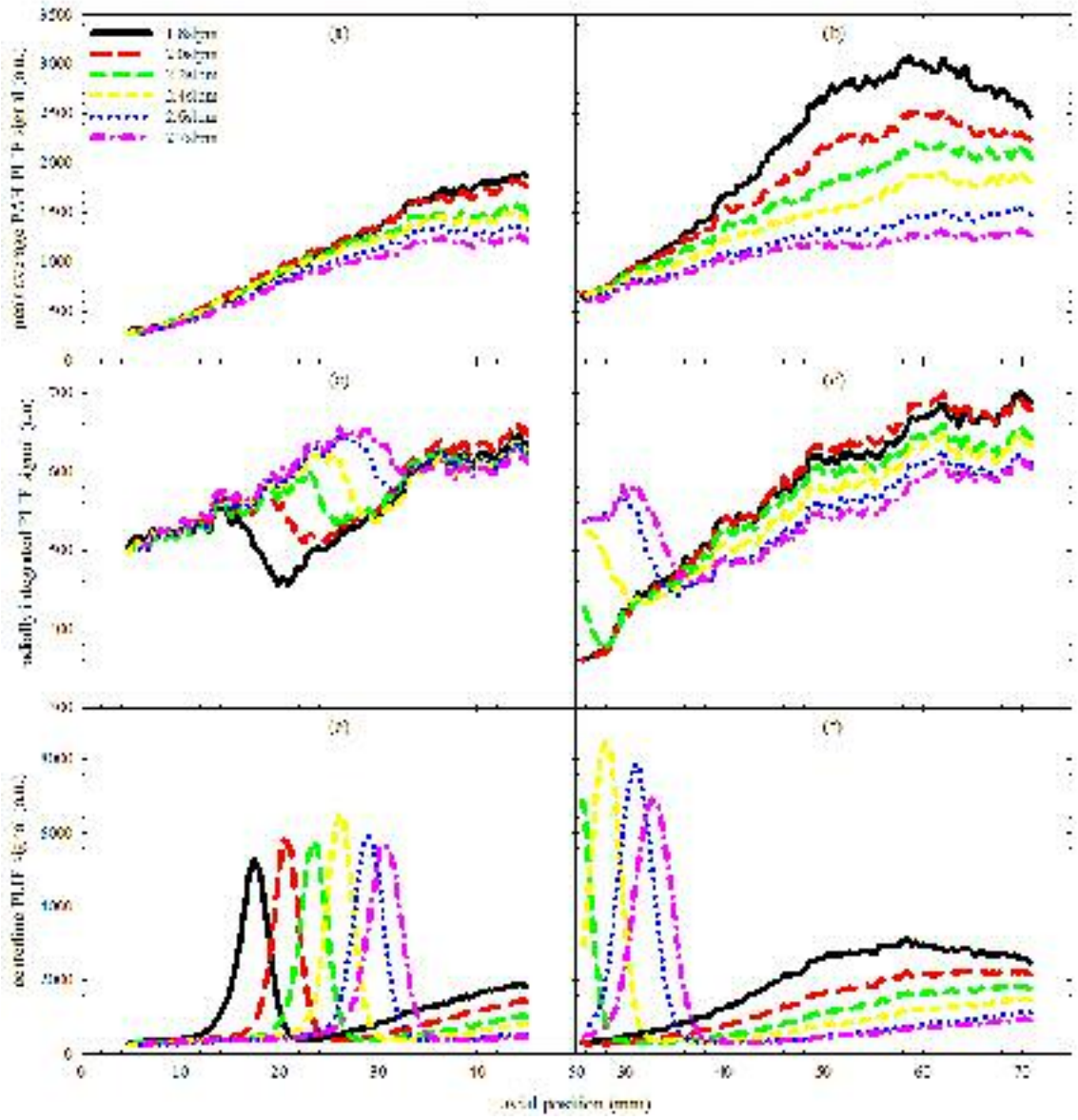

**Figure 4.17: PLIF detected with 295 nm long-pass and 450 nm short-pass fiters in methane IDFs versus axial position. (a) Peak PAH PLIF, (b) radially integrated PLIF and (c) centerline PLIF from 0 mm to 45.1 mm, (a), (c) and (e), and 25.7 mm to 70.8 mm, (b), (d) and (f), above the burner.**

### 4.4.12 Temperature, PLIF and PLII Measurements in an Ethylene IDF

Figure 4.18 contains radial profiles of PLIF detected with the 340 nm band-pass filter, PLIF detected with the 295 nm long-pass and 450 nm short-pass filter, soot PLII, temperature measurements, and temperature predictions from the model at four axial

positions taken from an ethylene IDF with an air flow rate of 1.6 slpm. Figure 4.18 (a) contains data from an axial position of 11 mm above the burner. The OH PLIF peaks, which are observed in both PLIF detection bands, coincide with the temperature peak, consistent with previous research indicating that the OH layer lies close to the air side of the stoichiometric contour which is very close to the peak temperature [4,20]. The soot PLII and both PAH PLIF peaks all occur on the fuel side of the flame consistent with the fact that PAH form by pyrolysis of fuel, and that soot forms from PAH [23]. The soot PLII peak occurs closer to the flame than the PAH peaks because soot requires higher temperature to form than PAH. The soot PLII peak is located where the temperature measurements indicate the gas temperature is about 1300 K at 5 mm from the centerline. This coincides with the lower limit for soot inception cited in numerous other works [14,47]. The slope of the radial temperature profile changes slightly where the soot peak occurs, perhaps due to heat losses from the hot product gases to the soot. At the edge of the soot peak furthest from the centerline the temperature profile changes slightly again, perhaps due to soot radiation and convective heat transfer to the surrounding cooler gases. The PAH PLIF peak detected with the 295 nm long-pass and 450 nm short-pass filter combination is located where the temperature measurements indicate that the gases are at a temperature of ~900 K, about 7.1 mm from the centerline. The PAH PLIF peak detected with the 340 nm band-pass filter is located where the temperature measurements indicate that the gases are at a temperature of ~700 K, about 7.5 mm from the centerline. This is in agreement with many previous studies that have shown that PAH at higher temperatures are detected at longer wavelengths [4,9]. These studies have also suggested

that PAH detected at higher temperatures are made up of large aromatics that are more likely to contribute to soot growth and play a role in soot inception.

Figure 4.18 (b) shows data from an axial position of 15 mm above the burner. This axial position is very close to the flame height based on both peak OH PLIF and peak temperature measurements. The OH PLIF peak and temperature peaks are very close to the centerline. There is a change in slope of the measured temperature profile at a temperature of about 1300 K and at a radial distance of 4.4 mm from the centerline that coincides with soot PLII peak. The PAH PLIF peak detected with the 295 nm long-pass and 450 nm short-pass filter combination is again located where the temperature measurements indicate that the gases have a temperature of ~900 K, about 6.5 mm from the centerline. The PAH PLIF peak detected with the 340 nm band-pass filter is located where the temperature measurements indicate that the gases have a temperature of ~700 K, about 7.5 mm from the centerline. Figure 4.18 (c) shows radial profiles at an axial position of 20 mm. This axial position is above the flame height, so there is no OH PLIF. The soot PLII peak is located at a temperature of 1200 K at a radial position of 4.2 mm. The PAH PLIF peak detected in the 295-450 nm band is located at about 1000 K at a radial distance of 5.8 mm, and the PAH PLIF peak detected with the 340 nm band-pass filter is located at about 700 K at about 7.2 mm from the centerline. Figure 4.18 (d) depicts radial profiles at a height of 25 mm. The soot peak is now at 1000 K at a radial distance of 3.8 mm. The PAH PLIF peaks detected in the 295-450 nm band are located at about 1000 K at 4.8 mm. The PAH PLIF peak detected with the 340 mm band pass filters is located at 700 K at a radial distance of 6.6 mm. At all four axial positions, the PAH PLIF peak detected with the 295 nm long pass and 450 nm short pass filter

combination is always found where the measured temperature is between 900 K and 1000 K, whereas the PAH PLIF peak detected with the 340 nm band-pass filter is always found at a gas temperature of 700 K. At axial distances less than and equal to the flame height, the soot peak was found near 1300 K. However, downstream of the flame height, the soot peak was found at lower temperature, even though the soot peak value continued to rise, which may be due to soot growth.

Figure 4.18 can be used to test the model. The locations of peak temperature were predicted within 0.1 mm by the model. Temperatures were predicted with an average error of less than 50 K where PAH PLIF was detected with the 340 nm band-pass filter. Temperatures were under predicted near the burner because the model assumes fuel and air exit the burner at ambient temperature, but heat transfer at the base of the flame causes the fuel and air to exit the burner at a slightly higher temperature. The model over predicted the peak temperature and temperature in the soot layer by 300 K, because it neglects heat losses due to radiation and also assumes that the only products of combustion are $CO_2$, $H_2O$, and $N_2$. Considering only these products and performing chemical equilibrium calculations (using STANJAN) yields an adiabatic flame temperature for a stoichiometric ethylene-air mixture of 2566 K, which agreed well with the maximum temperature obtained in the model. This temperature is higher than the most often cited adiabatic flame temperature for ethylene of 2369 K, [43] because the adiabatic flame temperature is usually calculated considering many major and minor products implying a degree of incomplete combustion that lowers the heat of reaction and hence the flame temperature.

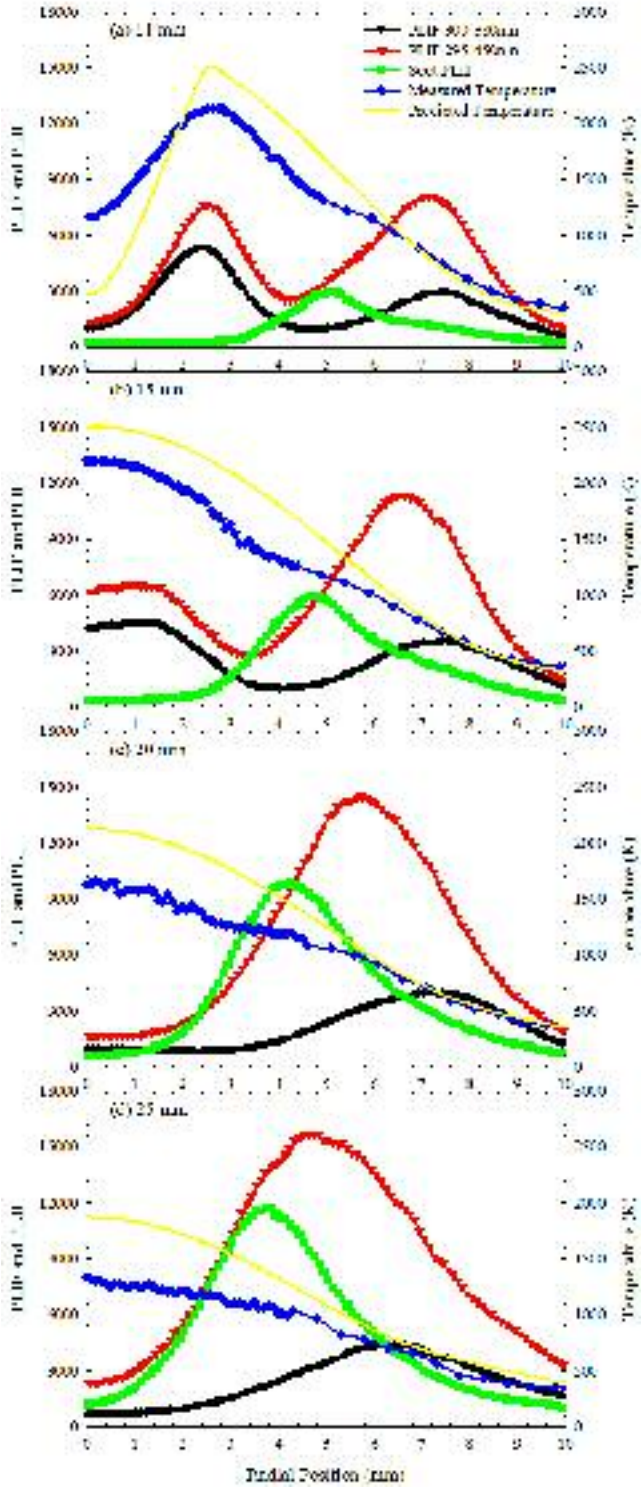

**Figure 4.18: Radial profiles of PLIF detected with 340 nm band-pass filter, PLIF detected with 295 nm long-pass and 450 nm short-pass filter combination, soot PLII, temperature measurements and predicted temperature from the model in a 1.6 slpm air flow rate ethylene IDF at axial positions of (a) 11 mm, (b) 15 mm, (c) 20 mm and (d) 25 mm.**

### 4.4.13 Results of Computer Modeling of an Ethylene IDF

Depicted in Figure 4.19 is average OH and PAH PLIF detected with the 340 nm band-pass filter with contours of predicted average temperature (right) and mixture fraction (left). The predicted stoichiometric and peak temperature contour is shown as a white dashed line. The model under predicts the location of the OH layer because it over estimates the peak temperature (and diffusion coefficient scales with temperature). The PAH PLIF lies within the 500 K and 1000 K predicted temperature contours and within the 0.61 and 0.91 predicted mixture fraction contours everywhere in the flame. The formation of vortices in the predicted contours at 3 cm is close to where the PAH PLIF begins to spread out due to flickering.

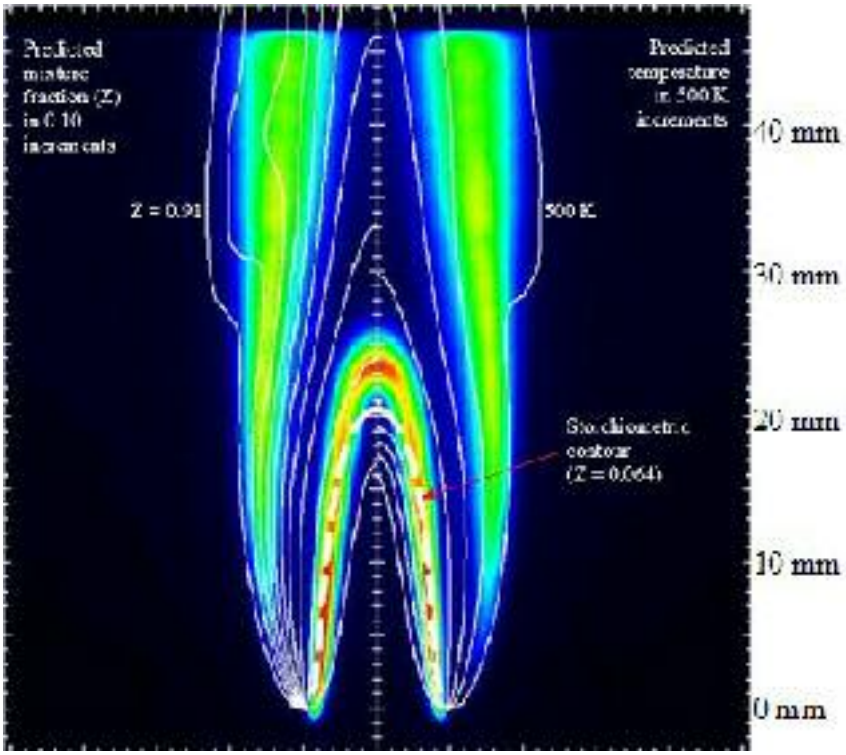


**Figure 4.19: Contours of predicted mixture fraction (left) and temperature (right) overlaid on PLIF detected with 340 nm band-pass filter of 2.2-slpm air flow rate ethylene IDF. Mixture fraction contours are in increments of 0.10 and temperature contours are in increments of 500 K. The predicted stoichiometric contour (Z = 0.064) is shown as a dashed white line.**

Figure 4.20 shows average PLIF detected with a 295 nm long-pass and a 450 nm short-pass filter combination with predicated average temperature (right) and mixture fraction contours overlaid. The peak PAH PLIF is located where the predicted temperature is 1000 K and where the predicted mixture fraction is 0.61 everywhere in the flame.

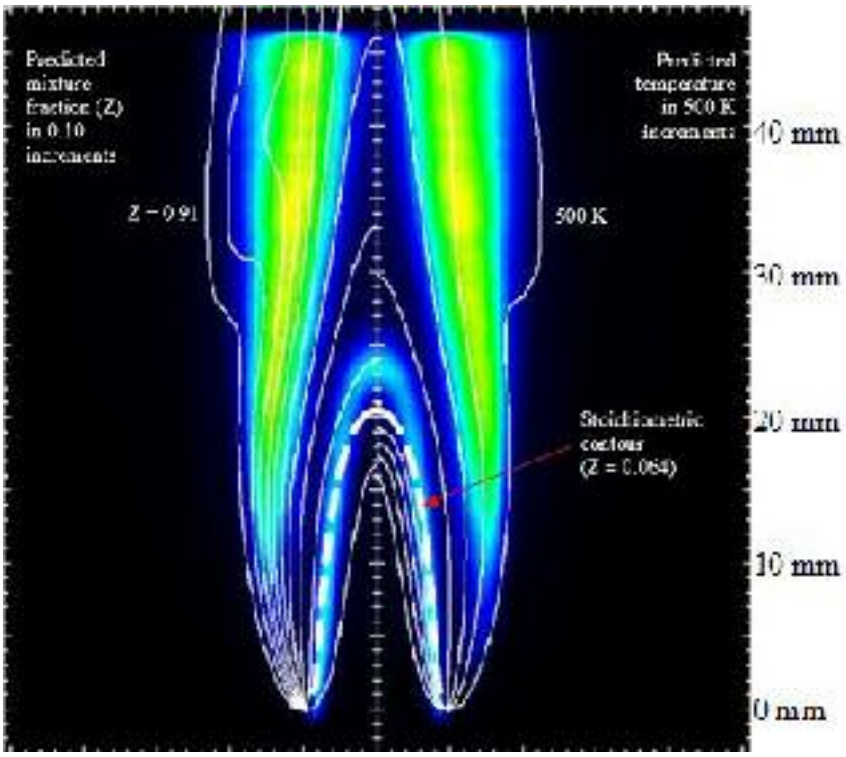


**Figure 4.20: Contours of predicted mixture fraction (left) and temperature (right) overlaid on PLIF detected with 295 nm long-pass and 450 nm short-pass filters of 2.2-slpm air flow rate ethylene IDF. Mixture fraction contours are in increments of 0.10 and temperature contours are in increments of 500 K. The predicted stoichiometric contour (Z = 0.064) is shown as a dashed white line.**

Figure 4.21 (a) shows predicted average streamlines overlaid on PLIF detected with a 340 nm band-pass filter. The PAH PLIF loosely follows along the curve of the streamlines from where it is first observed near the base of the burner to the top of the figure. At a height of 3 cm the bends in the streamlines indicate that vortices are forming in the flow field. Figure 4.21 (b) shows predicted streamlines with the PAH PLIF

detected in the 295-450 nm band. The PAH in Figure 4.21 (b) also appears to follow the streamlines except high in the flame where PAH maybe diffusing to the centerline. Predicted streamlines with soot PLII depicted in Figure 4.21 (c) show that soot PLII also appears to follow the predicted streamlines, except near the top of the flame where soot may be forced outwards by thermophoresis.

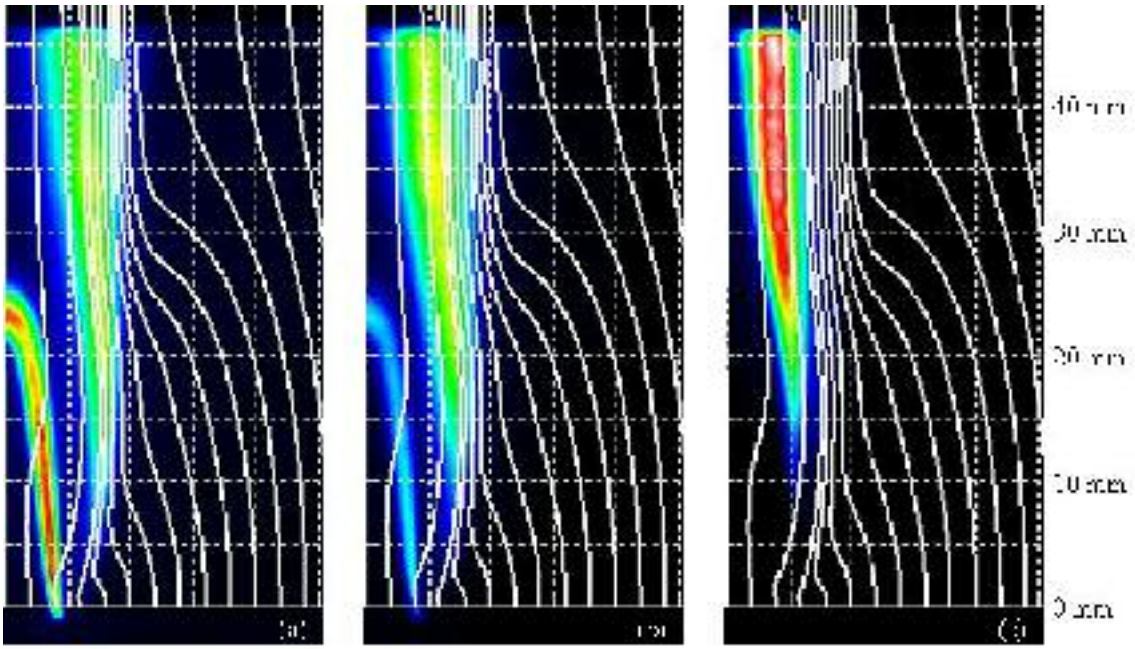

**Figure 4.21: Predicted average streamlines overlaid on average PLIF and soot PLII of a 2.2-slpm ethylene IDF. (a) PLIF detected with 340 nm band-pass filter. (b) PLIF detected with 295 nm long-pass filter and 450 nm short-pass filter. (c) Soot PLII detected with 570 nm long pass filter.**

## 4.5 Summary and Conclusions

The amplitude of flickering in visible images and in the PAH layer was greater in ethylene IDFs than methane IDFs, which may be due to the difference in temperatures and co-flow fuel velocities between the two flames. The flickering amplitude was also greater in longer flames of both fuels, perhaps because buoyant acceleration greatly increased downstream velocities, inducing vortices. It was also observed that buoyancy-induced vortices were either larger or occurred at a lower axial position in longer flames.

Vortices occurred in the PAH layer and enhanced radial convection of PAH. The soot layer was also affected by these vortices in the flow field, but radial convection of soot was not increased as greatly as that of PAH. Flickering complicated interpretation of PAH PLIF and soot PLII. In a few very unstable ethylene IDFs, flickering appeared to increase radially integrated PAH PLIF, perhaps because buoyancy-induced vortices caused recirculation of fuel into hotter regions, enhancing pyrolysis. Flickering also seemed to shorten one particularly unstable ethylene IDF, perhaps by enhancing mixing in the reaction zone. Therefore, the effect of flickering is troublesome. If it can be removed, for example, by using microgravity, it may simplify investigations into IDF flame structure and soot formation.

Flame structure in methane and ethylene co-flowing co-annular IDFs was investigated using OH PLIF, PAH PLIF, soot PLII, temperature measurements, and computer modeling. Peak OH PLIF was observed just inside the blue emission from the reaction zone in visible images. Therefore, OH radicals are indicative of the reaction zone. PAH PLIF occurred on the fuel side of the reaction zone. PAH PLIF detected with the 295 nm long-pass and 450 nm short-pass filters was found closer to the reaction zone than PAH PLIF detected with the 340 nm band-pass filter. Soot PLII in ethylene IDFs was detected very close to the reaction zone on the fuel side in between the reaction zone and PAH PLIF. Therefore, IDF structure is the inverse of NDF structure [4].

Temperature measurements were taken in an ethylene IDF with a 1.6 slpm air flow rate. The location of peak OH PLIF was found to coincide with the location of peak temperature. This also indicates that OH radicals occur near the reaction zone. Peak soot PLII was found at a measured temperature of 1300 K, which corresponds to the critical

soot inception temperature [47]. Peak PAH PLIF detected with the 295 nm long-pass and 450 nm short-pass filters was found at 1000 K, and PAH PLIF detected with the 340 nm band-pass filter was found at 700 K, at all measured axial locations. This supports the observation that larger aromatics, which form at higher temperatures closer to the reaction zone, may be detected by PAH PLIF at longer wavelengths [9]. Computer modeling was reported for an ethylene IDF with a 2.2 slpm air flow rate. Peak PAH PLIF followed predicated streamlines, isotherms and contours of constant mixture fraction, which has been observed in NDFs [8]. Peak soot moved towards cooler regions at increasing height, probably due to thermophoresis.

PAH amounts in ethylene IDFs were greater than those in methane IDFs. PAH also formed lower in ethylene IDFs than in methane IDFs. Soot PLII was not detected in methane IDFs with the laser configuration in the current study, even though it was observed in visible images of methane IDFs. These observations support the fact that ethylene, because it is an unsaturated fuel, has a greater tendency to pyrolyze and form soot than methane, which is a saturated fuel. The lowest axial position at which soot PLII was detected in all ethylene IDFs was 5 mm above the burner, which corresponds to an estimated soot inception time of 10-20 ms. This is similar to the timescale for soot inception reported in NDFs [44]. The proximity of PAH to the soot layer in IDFs suggests that PAH may be involved in soot formation. The presence of PAH in IDF soot corroborates this theory [25,28-30]. PAH is thought to play a key role in soot formation in NDFs. Soot PLII in ethylene IDFs increased with flame height and residence time. This is similar to NDFs, in which residence time also increases soot amounts [7]. Therefore, soot formation in IDFs and NDFs may share some similarities.

In contrast to over ventilated NDFs, soot and PAH did not cross the high temperature reaction zone and were not oxidized in ethylene IDFs. Soot PLII and PAH PLIF increased or leveled off after passing the stoichiometric flame height and did not decrease. Therefore, soot inception is isolated from oxidation in IDFs. A decrease in slope just above the flame height of the soot PLII with respect to axial position suggested that soot inception may have ceased and that only soot growth was occurring. Measured temperatures along the peak soot PLII contour, in a 1.6 slpm air flow rate ethylene IDF, decreased above the flame height. This suggests that soot growth can occur at temperatures below the soot inception temperature. The peak radially integrated soot PLII in ethylene IDFs was found to increase linearly with air flow. This suggests that the global flame soot production rate is directly proportional to residence time. By extrapolation the minimum air flow rate for soot production in an ethylene IDF was found to be about 0.6 slpm. This information might be used to tailor a flame that produces only incipient soot particles.

## 4.6 References

[1]. K.T. Wu, R.H. Essenhigh, in: Twentieth Symposium (International) on Combustion, The Combustion Institute, Pittsburgh, 1984, p. 1925.

[2]. J.H. Kent, H.G. Wagner, Combust. Flame 47 (1) (1982) 53-65.

[3]. J.H. Kent, H.Gg. Wagner, Proc. Combust. Inst. 20 (1984) 1007-1015.

[4]. K.C. Smyth, J.H. Miller, R.C. Dorfman, W.G. Mallard, R.J. Santoro, Combust. Flame 62 (2) (1985) 157-181.

[5]. R.J. Santoro, H.G. Semerjian, R.A. Dobbins, Combust. Flame 51 (2) (1983) 203-218.

[6]. R.J. Santoro, H.G. Semerjian, Proc. Combust. Inst. 20 (1984) 997-1006.

[7]. R.J. Santoro, T.T. Yeh, J.J. Horvath, H.G. Semerjian, Combust. Sci. Technol. 53 (2-3) (1987) 89-115.

[8]. G. Prado, A. Garo, A. Ko, A.F. Sarofim, Proc. Combust. Inst. 20 (1984) 989-996.

[9]. R.L. Vanderwal, K.A. Jensen, M.Y. Choi, Combust. Flame 109 (3) (1997) 399-414.

[10]. K.C. Smyth, C.R. Shaddix, D.A. Everest, Combust. Flame 111 (3) (1997) 185-207.

[11]. C.R. Shaddix, K.C. Smyth, Combust. Flame 107 (4) (1996) 418-452.

[12]. C.R. Shaddix, C.W. Williams, L.G. Blevins, R.W. Schefer, Proc. Combust. Inst. 30 (2005) 1501-1508.

[13]. C.R. Shaddix, J.E. Harrington, K.C. Smyth, Combust. Flame 99 (3-4) (1994) 723-732.

[14]. J. Du, R.L. Axelbaum, Combust. Flame 100 (3) (1995) 367-375.

[15]. J.H. Kent, H.G. Wagner, Zeitschrift Fur Physikalische Chemie-Wiesbaden 139 (1984) 59-68.

[16]. G.W. Sidebotham, I. Glassman , Combust. Flame 90 (3-4) (1992) 269-283.

[17]. G.W. Sidebotham, I. Glassman , Combust. Sci. Technol. 81 (4-6) (1992) 207-219.

[18]. K.T. Kang, J.Y. Hwang, S.H. Chung, W. Lee, Combust. Flame 109 (1-2) (1997) 266-281.

[19]. K. Lee, Y. Han, W. Lee, J. Chung, C. Lee, Measurement Science and Technology 16 (2) (2005) 519-528.

[20]. K.C. Smyth, P.J.H. Tjossem, A. Hamins, J.H. Miller, Combust. Flame 79 (3-4 ) (1990) 366-380.

[21]. E.J. Lee, K.C. Oh, H.D. Shin , Fuel 84 (5) (2005) 543-550.

[22]. C. Wey, E.A. Powell, J.I. Jagoda, 20 (1984) 1017-1024.

[23]. I. Glassman, Proc. Combust. Inst. 22 (1988) 295-311.

[24]. D.B. Makel , I.M. Kennedy, Combust. Sci. Technol. 97 (4-6) (1994) 303-314.

[25]. L.G. Blevins, R.A. Fletcher, B.A. Benner, E.B. Steel, G.W. Mulholland, Proc. Combust. Inst. 29 (2003) 2325-2333.

[26]. R.A. Dobbins, R.A. Fletcher, W. Lu, Combust. Flame 100 (1-2) (1995) 301-309.

[27]. R.A. Fletcher, R.A. Dobbins, H.C. Chang, Anal. Chem. 70 (13) (1998) 2745-2749.

[28]. J.R. Arthur, B.T. Commins, A.S. Gilbert, A.J. Lindsey, D.H. Napier, Combust. Flame 2 (1958) 267-272.

[29]. J.R. Arthur, D.H. Napier, Proc. Combust. Inst. 5 (1955) 303-316.

[30]. J.R. Arthur, P.K. Kapur, D.H. Napier, Nature 169 (1952) 372-373.

[31]. B.S. Haynes, H.Gg. Wagner, Prog. Energy Combust. Sci. 7 (4) (1981) 229-273.

[32]. R.L. Schalla, G.E. McDonald, Proc. Combust. Inst. 5 (1955) 316-324.

[33]. J.H. Miller, W.G. Mallard, K.C. Smyth, Combust. Flame 47 (1982) 205-214.

[34]. A. Leipertz, F. Ossler, M. Aldén, in: K. Kohse-Höinghaus, J.B. Jeffries (Eds.), Applied Combustion Diagnostics, Taylor & Francis, New York, 2002, p. 359.

[35]. F. Ossler, T. Metz, M. Alden , Applied Physics B-Lasers and Optics 72 (4) (2001) 465-478.

[36]. A.C. Eckbreth, J. Appl. Phys. 48 (11) (1977) 4473-4479.

[37]. R.J. Santoro, Shaddix C.R., in: K. Kohse-Höinghaus, J.B. Jeffries (Eds.), Applied Combustion Diagnostics, Taylor & Francis, New York, 2002, p. 252.

[38]. D.R. Snelling, F. Liu, G.J. Smallwood, O.L. Gulder, Combust. Flame 136 (1-2) (2004) 180-190.

[39]. F.G. Roper, C. Smith, Combust. Flame 36 (1979) 125-138.

[40]. C.S. Mcenally, U.O. Koylu, L.D. Pfefferle, D.E. Rosner, Combust. Flame 109 (4) (1997) 701-720.

[41]. C.R. Shaddix, in: Proceedings of the 33rd National Heat Transfer Conference, ASME, New York, 1999,

[42]. R.W. Davis , E.F. Moore, R.J. Santoro, J.R. Ness, Combust. Sci. Technol. 73 (4-6) (1990) 625-635.

[43]. S.R. Turns, An Introduction to Combustion: Concepts and Applications, McGraw-Hill, U.S.A, 2000, p. 656.

[44]. A. Thomas, Combust. Flame 6 (1962) 46-62.

[45]. R.E. Mitchell, A.F. Sarofim, L.A. Clomburg, Combust. Flame 37 (3) (1980) 227-244.

[46]. C.K. Westbrook, F.L. Dryer, Prog. Energy Combust. Sci. 10 (1) (1984) 1-57.

[47]. R.A. Dobbins, Combust. Flame 130 (3) (2002) 204-214.

# Chapter 5: Soot Formation in Microgravity Inverse Diffusion Flames

## 5.1 Introduction

It was shown in Chapters 3 that IDFs and NDFs could be treated with the same flame height analysis. In Chapter 4, it was demonstrated that IDFs and NDFs have very similar flame structure. The main difference between IDFs and NDFs with respect to soot formation is the time-temperature history of the soot particles. In NDFs, soot forms inside the flame and heats up as it approaches the reaction zone [1,2]. In NDFs, soot oxidizes as it passes through the reaction zone [3]. In IDFs, soot forms outside of the flame and cools down as it moves away from the reaction zone [4]. In IDFs, soot never oxidizes because it never crosses the reaction zone [5]. Temperature and residence time are very important parameters in the inception and growth of soot particles [6]. Therefore, the difference in time-temperature histories of soot particles in IDFs will affect soot inception and growth. In IDFs, soot inception and growth are isolated from oxidation [7,8]. Therefore, IDFs can be used as a tool to study soot inception and early soot growth.

In normal gravity, buoyancy causes NDFs and IDFs to flicker [9]. Flickering enhances soot and PAH formation in NDFs and IDFs [4,10-12]. Flickering is caused by buoyantly induced vortices. As shown in Chapter 4, buoyantly induced vortices in IDFs cause recirculation and mixing of soot and PAH into the higher temperature regions downstream of the flame tips. Therefore, flickering alters the time-temperature history of soot particles in IDFs. Flickering can be removed by using microgravity [13,14]. In microgravity, soot particles in IDFs will not experience the recirculation into high

temperatures but will cool monotonically. Therefore, microgravity IDFs may offer an ideal environment for the isolation of soot inception and growth mechanism.

In microgravity, IDFs are slightly longer, rounder, and brighter [15]. In the absence of buoyant acceleration, gas velocities in microgravity IDFs should be slower. Hence, there will be more residence time for soot, PAH and CO formation. From the analysis of IDF flame height in Chapter 3, increasing air flow rate will also increase the residence time for soot, PAH and CO formation. The objectives of this chapter are to investigate the effects of microgravity, air flow rate, and fuel type on soot and CO formation in IDFs.

## 5.2 Experimental Methods

### 5.2.1 Apparatus

Microgravity experiments were conducted in the NASA 2.2-Second Drop Tower Facility in Cleveland, Ohio. In this facility, the experiment is placed in a drag shield and dropped 80 feet, obtaining microgravity by freefall. The experimental apparatus was mounted on a standard NASA A-frame drop rig, which is shown in Figure 5.1 (a). The burner used for microgravity experiments was the one used for normal gravity experiments described in Chapters 3 and 4 and shown in Figure 3.1. The flow straightening beads, in the annulus used for nitrogen co-flow in normal gravity, were removed from the burner for microgravity experiments. The burner was mounted inside a 27-L cylindrical combustion chamber, shown attached to the rig in Figure 5.1 (b), which has one window for optical access. The nitrogen co-flow used for the normal

gravity experiments described in Chapters 3 and 4 was not used. Instead, the chamber was evacuated and filled with one atmosphere of nitrogen.

(a)  (b) 

**Figure 5.1: (a) Standard NASA A-frame drop rig and (b) combustion chamber.**

Figure 5.2 shows a schematic of the fuel and air delivery systems on the drop rig. Fuel and air were metered by calibrated mass flow meters and fine metering valves. Solenoids were used to control flow through the fuel and air delivery systems. Two redundant solenoids were used for each side of the delivery system. The fuel and air flow pressures were set using a pressure regulator and monitored using 0 to 100 psig pressure transducers. Two 500-$cm^3$ stainless steel cylinders were used for storing fuel and air. Pressures in the fuel and air cylinders were monitored using 0 to 250 psig pressure transducers. Ball valves closed the system at both ends. Figure 5.3 shows a schematic of the fill/monitoring and vent systems for the combustion chamber. This system was used to evacuate the combustion chamber through the vent and to fill the combustion chamber with nitrogen through the fill. This system was also used with the sampling system, which will be described later. Pressure in the combustion chamber was monitored using a 0 to 50 psia pressure transducer. A needle valve controlled the flow rate of nitrogen into the combustion chamber. Ball valves closed both ends of the fill/monitoring and

vent system for the combustion chamber. A list of the parts used in the fuel and air delivery system and in the combustion chamber fill/monitoring and vent system is provided in Table 5.1.

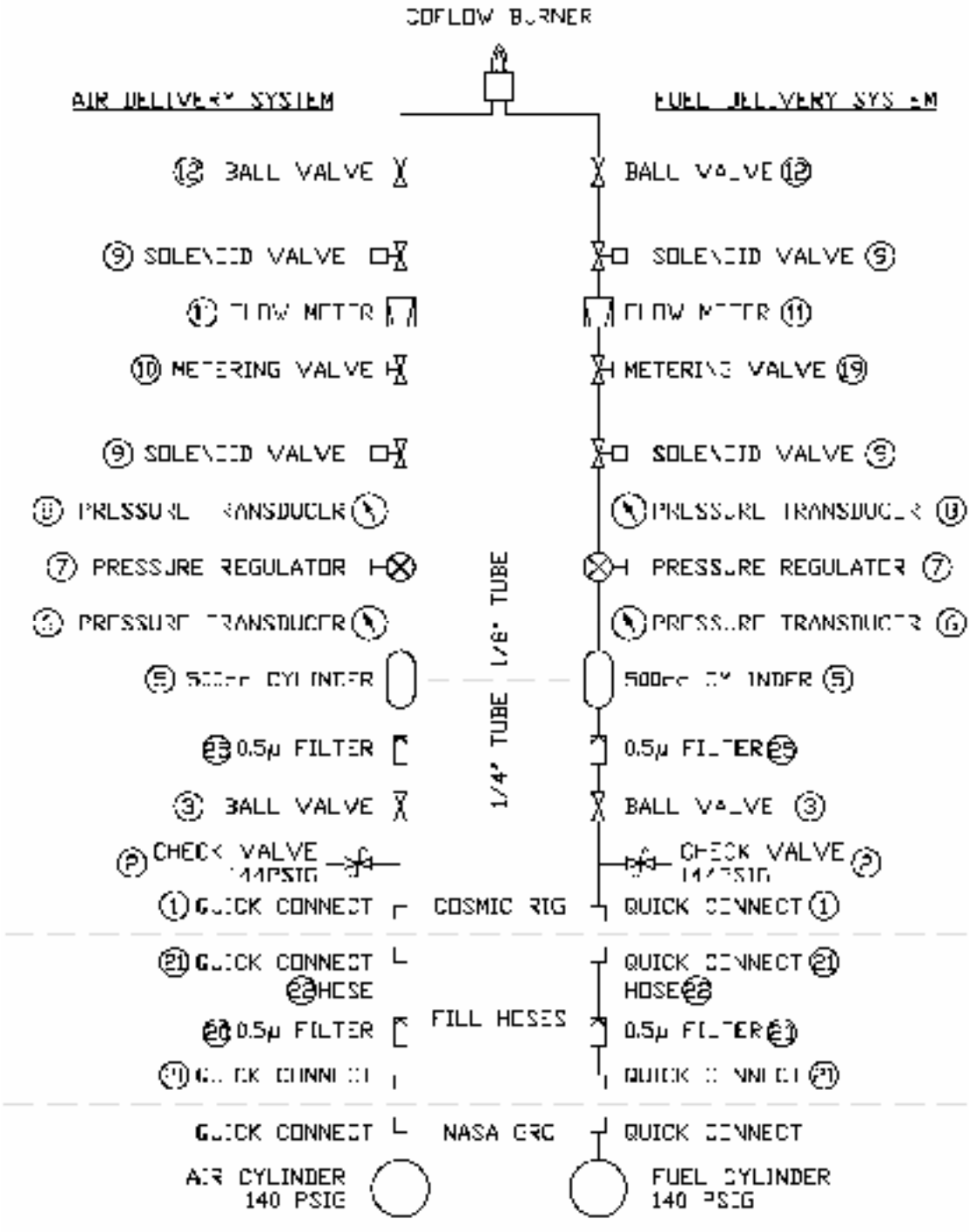


**Figure 5.2: Schematic of fuel and air delivery system.**

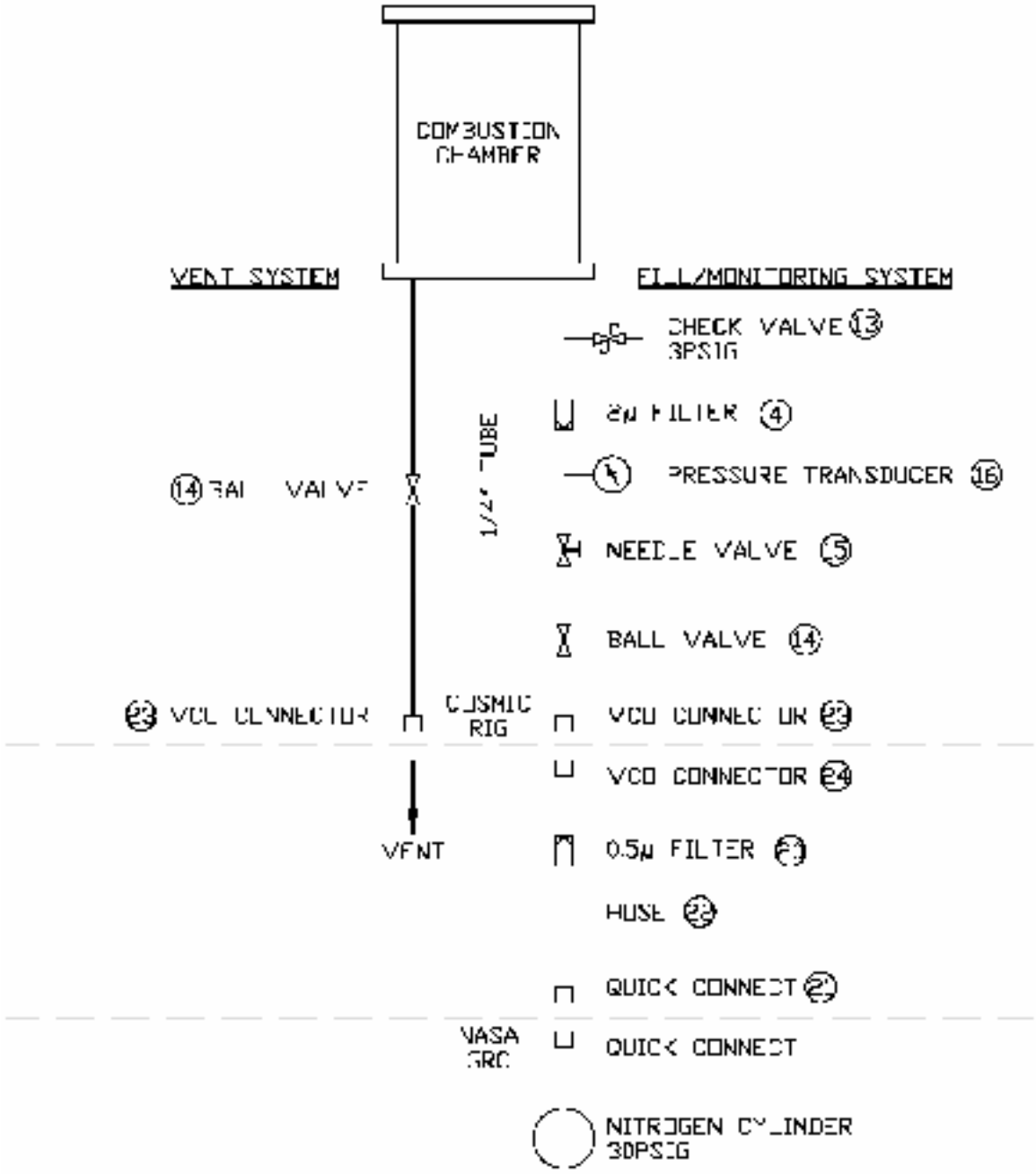


**Figure 5.3: Schematic of combustion chamber fill/monitoring and vent system.**

**Table 5.1: Parts list of components in fuel and air delivery system and combustion chamber fill/monitoring and vent system**

| Item | Description | Manufacturer | Part Number | $P_{max}$ (psig) |
|---|---|---|---|---|
| - | ¼" tube and Swagelok fittings | Swagelok | - | 4000 |
| - | ⅛" tube and Swagelok fittings | Swagelok | - | 8500 |
| - | ¼" male NPT fittings | Swagelok | - | 8000 |
| - | ⅛" male NPT fittings | Swagelok | - | 10000 |
| 1 | Quick-connect body, bulkhead | Swagelok | SS-QC4-B1-400 | 250 *uncoupled* 3000 *coupled* |
| 2 | Check valve, cracking pressure 144psig | Swagelok | SS-4CA-150 | 144 *cracking* 3000 |
| 3 | Ball valve | Swagelok | SS-42S4 | 2500 |
| 4 | 0.5µ filter | Swagelok | SS-4FWS-05 | 600 *differential* 6000 |
| 5 | 500cc cylinder | Swagelok | 304L-HDF4-500 | 1800 |
| 6 | Pressure transducer, 0-250psig | Texas Instruments | 61CP-02-2-0250-G-V-YD2-C | 375 |
| 7 | Pressure regulator, hand-loaded | Tescom | 44-2262-241 | 3500 *input* 100 *output* |
| 8 | Pressure transducer, 0-100psig | Texas Instruments | 61CP-02-2-0100-G-V-YD2-C | 375 |
| 9 | Solenoid valve | ASCO | U8225B6V | 125 *differential* 500 |
| 10 | Metering valve | Parker | 2F-H3L-V-SS-TC | 250 |
| 11 | Flow meter | Sierra | 822S-L-2-OV1-PV1-V1-MP-A1 | 1000 |
| 12 | Ball valve | Swagelok | SS-41S2 | 2500 |
| 13 | Check valve, cracking pressure 3psig | Swagelok | SS-4CA-50 | 3 *cracking* 3000 |
| 14 | Ball valve | Swagelok | SS-43S4 | 3000 |
| 15 | Needle valve | Swagelok | SS-1RS4 | 5000 |
| 16 | Pressure transducer, 0-50psia | Setra | 270 | 75 |
| 19 | Metering valve | Parker | 2F-H4L-V-SS-TC | 250 |
| 20 | 0.5µ filter | Swagelok | SS-4F-05 | 600 *differential* 3000 |
| 21 | Quick-connect stem | Swagelok | SS-QC4-D-400 | 250 *uncoupled* 3000 *coupled* |
| 22 | Hose | Swagelok | SS-4BHT-48 | 3000 |
| 23 | VCO connector, bulkhead | Swagelok | SS-4-VCO-A1-400 | 13400 |
| 24 | VCO connector | Swagelok | SS-4-WVCO-6-400 | 9500 |
| 25 | 0.5µ filter | Swagelok | SS-4FWS-05 | 600 *differential* 6000 |

Figure 5.4 shows a interconnect schematic of the electrical system on the rig. Two 24-V batteries and a NASA power distribution module (PDM) regulated voltage and provided power to the instruments on the rig. A NASA droppable data acquisition and control system (DDACS) controlled the instrumentation and stored data. An optical

transmitter for video signals was connected to video equipment in the control panel on the top floor of the drop tower via a tethered fiber optic cable to allow video recording during the drop. The control panel at the top of the drop tower also contains switches that allow the experimenter to initiate steps in the DDACS computer program. The switches were connected to banana plugs on top of the rig, which were connected to the digital input switches on the DDACS. The banana plugs also serve to initiate the drop. When the rig begins to fall, the plugs are pulled loose, opening the digital input switches on the DDACS. The computer program for the DDACS is in the appendix.

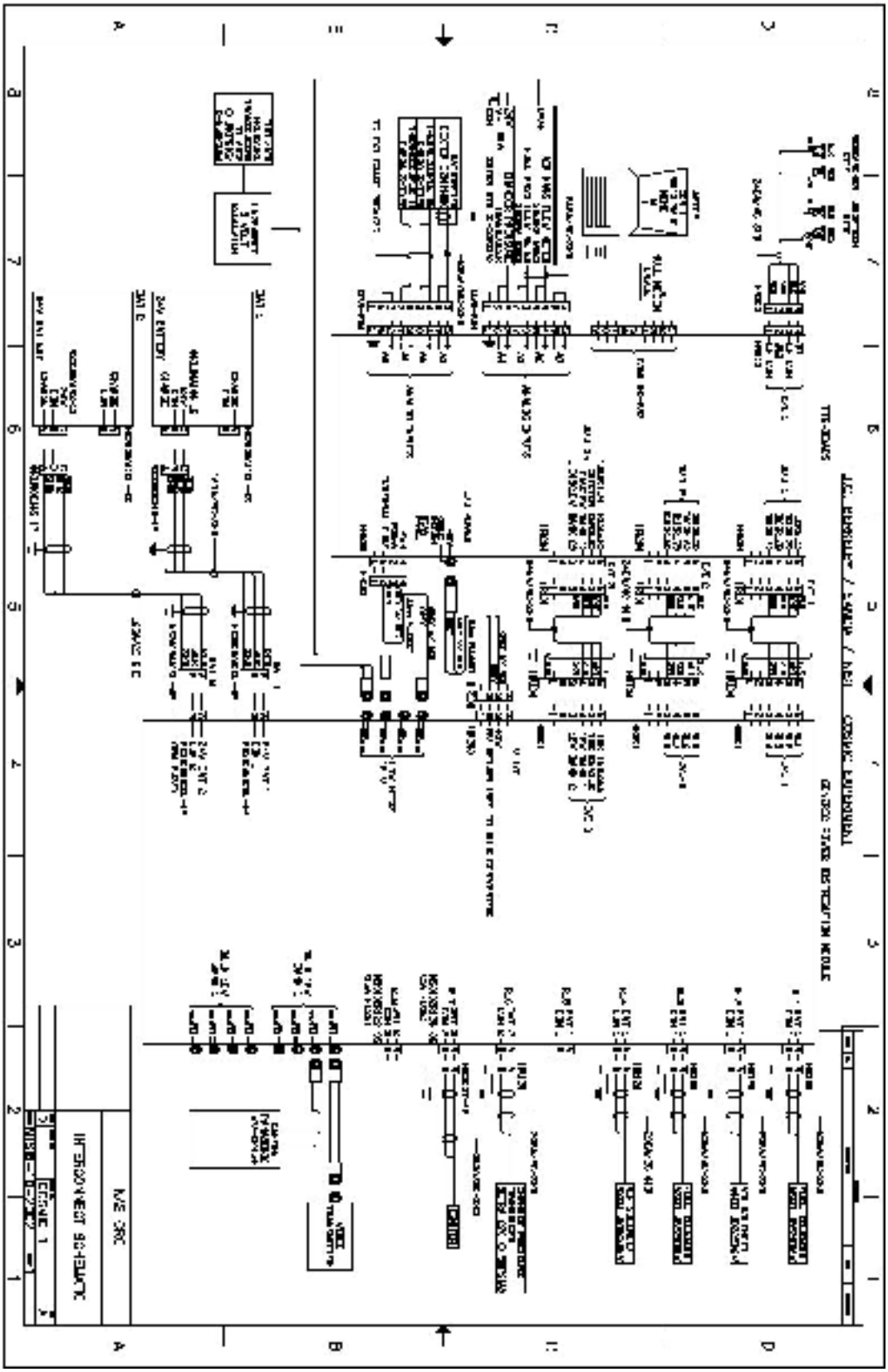

**Figure 5.4: Interconnect schematic of electrical system.**

Flames were ignited using a spring-loaded, 32 mm long, 320 μm diameter nichrome wire (13.7 Ω/m) placed across the top of the burner at a height of 8 to 9 mm from the burner surface and 3 to 4 mm from the centerline. The nichrome wire had one loop or kink in the center, increasing its surface area and assisting ignition. A picture of the igniter assembly is in Figure 5.5.

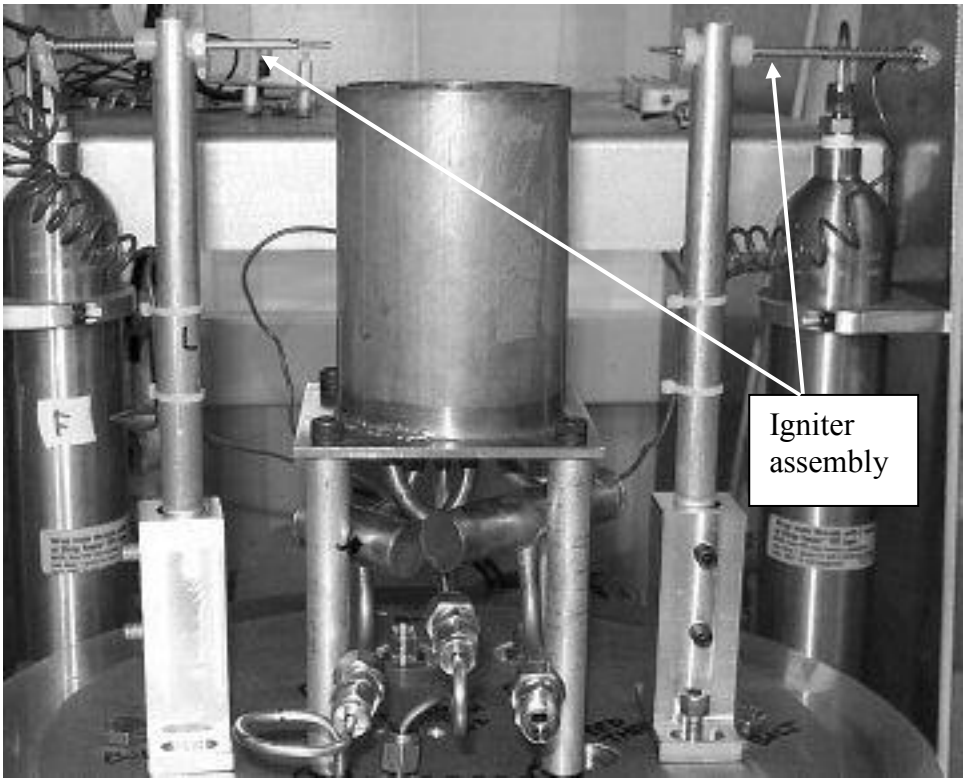


**Figure 5.5: Igniter assembly.**

Temperature during the drop was measured with the same thermocouple assembly described in Chapter 4, which was rigidly mounted inside the combustion chamber. The bead of the thermocouple was positioned on the burner centerline at a height of 3.5 cm from the burner surface. The cold junction was measured via an integrated circuit temperature sensor mounted on the DDACS input board. The thermocouple

measurements were corrected for radiation heat loss as described in Chapter 4. The estimated thermocouple time constant is 150 ms.

Flame radiation was measured with a thin film thermopile radiometer with a $CaF_2$ window. The $CaF_2$ window transmits radiation between 0.13 and 11 μm. The radiometer was mounted inside the chamber at a height of 12 mm above top of the burner and a radial location of 75 mm away from the axis of symmetry. The radiometer position was selected so that it would capture radiation from the entire length of flames with heights of 4 cm or less. Radiometer output voltages were amplified by a gain of 99 and recorded on the DDACS. Radiometer output voltage was calibrated for flame radiation by using a blackbody generator with a 2 cm diameter opening in place of the flame. The calibration constant was 543 W/V. Flame radiation calculated using this calibration should be considered approximate, because flames do not radiate as perfect black bodies, flame heights were not exactly 2 cm, and flames were not round in shape. The first-order radiometer time constant is 85 ms. Temperature compensation of the radiometer was not performed.

The CCD camera used to record color images of IDFs in Chapter 4 was rigidly mounted outside the combustion chamber window and aligned with the burner centerline.

### 5.2.2 Procedures

Before each drop, a fresh igniter wire was installed. Next, the fuel and air cylinders on the rig were filled to 125 psig and flushed three times each to minimize contamination. Then, the fuel and air flow rates were set using the mass flow meters and fine metering valves. Fuel and air flow rates are listed in Table 3.1. The fuel and air

flow pressures were set at 50 psig for all tests. The chamber was sealed and evacuated to approximately 0.1 psia before being filled to atmospheric pressure with nitrogen. The rig was then loaded into the NASA drop tower drag shield, and the fiber-optic cable was attached. Next, the drag shield and rig were hoisted to the top of the drop tower. A SVHS videocassette tape was queued in the video equipment. The DDACS program was executed. Five seconds of baseline data were collected. Next, the solenoids were opened and, after three seconds of pre-flow, the rig was dropped. As the banana plugs on the top of the rig were pulled loose, the opening of the DDACS digital input switches triggered the igniter. During the drop, data were collected every 15 ms for 2.1 seconds, after which the solenoids were closed and the igniter de-energized. The rig landed in an air bag at the bottom of the tower. Three seconds of post-drop data were then collected. After the rig was retrieved, radiometer and thermocouple data from the drop were downloaded from the DDACS and the combustion chamber pressure was recorded.

After each drop, the contents of the combustion chamber were analyzed to determine the amount of CO and soot generated during the drop. A closed-loop sampling system, consisting of a 47-mm quartz filter holder, a pump, pressure gauges, a rotameter, and a non-dispersive infrared (NDIR) CO analyzer, was used to analyze the chamber contents. The sampling system was connected to the combustion chamber fill/monitoring and vent system. The contents of the chamber passed sequentially through the filter, the pump, the CO analyzer and back to the chamber. The closed-loop sampling system was operated at 1 atm and at a flow rate of 1 slpm for 15 minutes, which was sufficient for the CO analyzer to reach a steady state value. The CO analyzer was used in the 0 – 200 ppm range and was calibrated with a span gas of 211 ppm CO in $N_2$.

### 5.2.3 Analysis

The soot samples collected on the quartz filters were analyzed for organic and elemental carbon contents and total soot mass using thermal-optical organic carbon and elemental carbon (OCEC) analyzer [16]. The general OCEC steps are (1) initial heating in an $O_2$-free environment to remove all OC and (2) subsequent heating in an $O_2$-containing environment to remove all EC. After each step, the removed carbon is converted to $CH_4$ and detected using a flame ionization detector. A laser transmission measurement through the filter is used to correct for pyrolytic conversion of OC to EC during the $O_2$-free heating step. The measured carbon masses are used to calculate the organic and elemental fractions.

The molar concentration ratio of CO to $CO_2$ of the post combustion gases in the combustion chamber was calculated by assuming that all of the oxygen in the air had reacted, and that the only products of combustion were CO, $CO_2$, $H_2O$, $N_2$ and excess fuel. An algebraic equation for the amount of $CO_2$, depending only on the amounts of air and CO, can be derived by balancing species. The amount of air can be calculated using the given flow rates and the duration of the experiment. The amount of CO is estimated by assuming that the post combustion gases are ideal and using the measured pressure and temperature of the post combustion gases and the volume of the combustion chamber.

A balanced chemical equation of the global reaction, assuming all oxygen in the air reacts and that the only products are $H_2O$, CO, $CO_2$, $N_2$, and excess fuel, is given in

Eq. 5.1. Since the excess fuel and nitrogen do not react, they appear on both sides of the chemical equation and are thus not shown in Eq. 5.1.

$$a(\text{fuel}) + b(O_2) \rightarrow w(H_2O) + x(CO) + y(CO_2) \tag{5.1}$$

In Eq. 5.1, the stoichiometric coefficients $a$, $b$, $w$, $x$, and $y$ represent the number of moles of reactants and products. The stoichiometric coefficient $a$ only represents the fraction of the fuel that reacts and does not include the excess fuel. The number of moles of $O_2$, $b$, can be calculated using Eq. 5.2,

$$b = (x_{O2})(Q_{air})(t_{drop})P_0/RT_0, \tag{5.2}$$

in which $x_{O2}$ is the molar fraction of $O_2$ in the air (21%), $Q_{air}$ is the volume flow rate of air in the experiment, $t_{drop}$ is the time duration of the drop (2.2 s), $R$ is the universal gas constant (8.3145 J/mol-K), and $P_0$ and $T_0$ are the ambient pressure (1 atm) and temperature (294 K), respectively. Assuming the products in combustion chamber are ideal gases, the number of moles of CO, $x$, can be calculated as follows:

$$x = ([CO]_{\text{measured}})(P_f V_{chamber}/RT_f) \tag{5.3}$$

in which $[CO]_{\text{measured}}$ is the measured concentration of CO, $V_{chamber}$ is the volume of the combustion chamber (25 L), and $P_f$ and $T_f$ are the final pressure and temperature, respectively, in the combustion chamber after the drop.

Balancing species in Eq. 5.1 with methane as the fuel yields the number of moles of $CO_2$, $y$, produced.

$$y = (2b - 3x)/4. \tag{5.4}$$

For ethylene, the number of moles of $CO_2$, $y$, produced is given by Eq. 5.5.

$$y = 2(b - x)/3 \tag{5.5}$$

Therefore, the CO to $CO_2$ molar concentration ratio of the products in the combustion chamber is given by the expression $x/y$, which can be evaluated by substituting the values of $b$, $x$, and $y$ from Eqs. 5.2, 5.3 and 5.4 for methane and Eqs. 5.2, 5.3 and 5.5 for ethylene.

## 5.3 Computational Methods

The computational model used to characterize the temperature, mixture fraction, and flow fields is the one described in Chapter 4. The model also includes dilute-condition particle tracking incorporating the effects of inertial, thermophoretic, and gravitational forces [17]. Tracer particles, 40 nm in diameter with a density of 1.8 $g/m^3$ and a temperature-varying specific heat of amorphous carbon from Ref. [18], were introduced at axial positions of 0.025 mm, 0.5 cm, 1.0 cm, 1.5 cm, and 2.0 cm above the burner and at radial positions corresponding to a gas temperature of 1250 K. This temperature were chosen based on the lower temperature limit for soot formation [3,19,20]. Although the simulation does not model soot formation, the trajectories and time-temperature histories of the tracer particles may mimic soot particles passing through the flame. Although the predicted trajectories and time-temperature histories of the tracer particles are qualitative, they serve as a theoretical tool for discussing the differences in soot residence time at high temperature and their effect on soot formation in normal and microgravity IDFs.

## 5.4 Results and Discussion

### 5.4.1 Images of microgravity IDFs

All of the IDFs in Figure 5.6 and Figure 5.7 were stabilized inside the combustion chamber filled with $N_2$, and no $N_2$ co-flow was used. Figure 5.6 depicts photographs of 2.4 slpm air flow rate $CH_4$ IDFs in normal (1-g) and microgravity (μ-g) conditions. The bright horizontal line above the flames is the thermocouple. The $CH_4$ flames are imperfectly attached to the burner rim. The 1-g flame flickers. The longest (3.2 cm) and shortest (2.7 cm) flames in the 1-g flickering cycle are shown in Figure 5.6 (a) and Figure 5.6 (b), respectively. The μ-g flame in Figure 5.6 (c) has a visible height of about 3.5 cm and does not flicker. The μ-g flame is slightly longer and more rounded than the 1-g flame, which agrees with previous observations of non-buoyant diffusion flames [13-15,21]. In contrast to the faint soot cap of the 1-g flame, the μ-g $CH_4$ flame has a bright soot annulus that extends along most of its length.

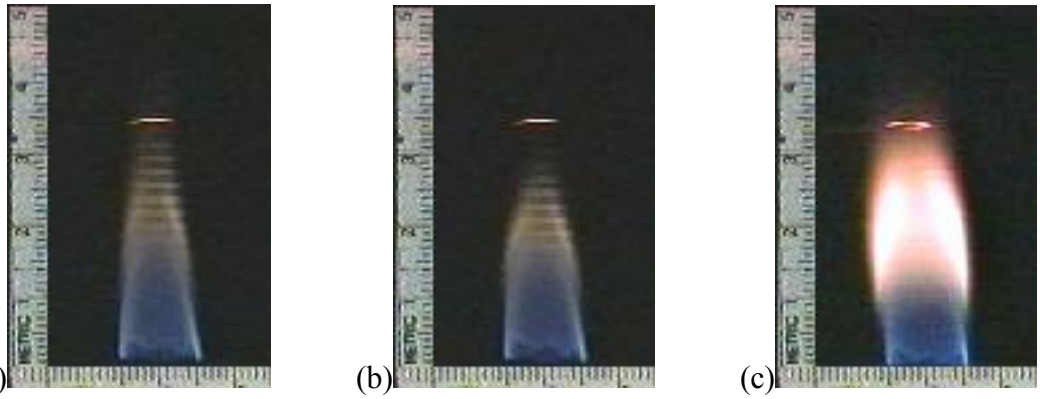


**Figure 5.6: Images of 2.4 slpm $CH_4$ IDF in 1-g (a) and (b) and in μ-g (c). Images (a) and (b) show two stages of 1-g fluctuations. All images were taken with an aperture setting of f/#8.**

Figure 5.7 shows photographs of 1.6 slpm air flow rate $C_2H_4$ IDFs in 1-g and μ-g conditions. The $C_2H_4$ flames are fully attached to the burner rim. Figure 5.7 (a) and Figure 5.7 (b) correspond to longest (3 cm) and shortest (2.4 cm) flames of the flicker

cycle, respectively. During the flicker, the flame shape and height change. The μ-g flame shown in Figure 5.7 (c) is about 3.2 cm long. Like the $CH_4$ flame, the μ-g $C_2H_4$ flame is longer and more rounded than the 1-g flame. Both the 1-g and μ-g $C_2H_4$ flames have soot annuli that begin near the burner and exist over most of their heights.

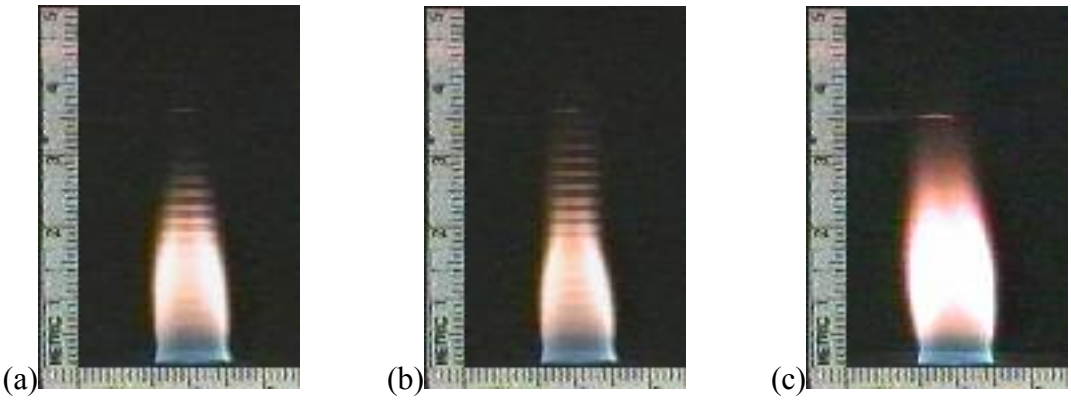


**Figure 5.7: Images of 2.4 slpm $C_2H_4$ IDF in 1-g (a) and (b) and in μ-g (c). Images (a) and (b) show two stages of 1-g fluctuations. All images were taken with an aperture setting of f/#16.**

### 5.4.2 Radiometer and Temperature Measurements

Temporal profiles of calibrated radiative heat loss and corrected thermocouple temperature measurements during the 2.2-second drop for the IDFs in Figure 5.6 and Figure 5.7 are provided in Figure 5.8 and Figure 5.9, respectively. The data shown in Figure 5.8 and Figure 5.9 demonstrate that the flames achieve steady state thermally during the first 0.5 s of the drop. This is significant because previous drop tower tests with normal flames have shown that they do not reach or just barely reach steady state during the 2.2 second duration of the test [15]. Inverse flames are thus more suitable for drop tower examination than normal flames. The radiometer signal for $C_2H_4$ exhibits a spike upon flame ignition that is not present for $CH_4$; this is attributed to a brief flare-up of combustion that occurs as soon as the igniter is energized for $C_2H_4$ under both gravity conditions. The ignition upset was not observed for $CH_4$.

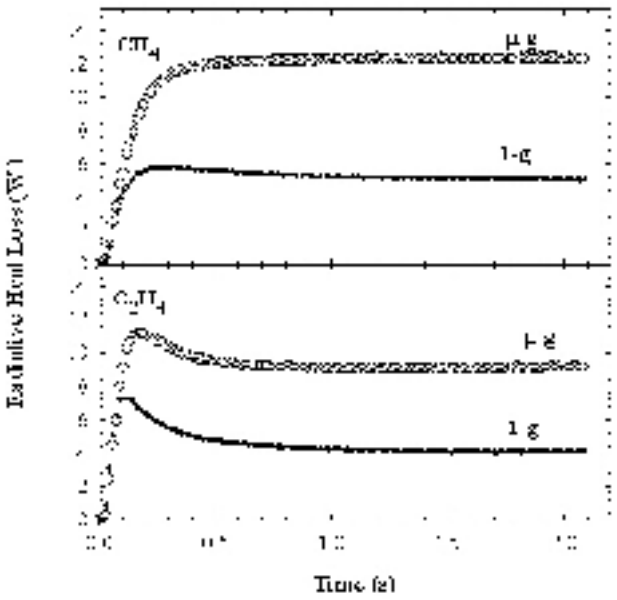

**Figure 5.8: Temporal profile of radiation from IDFs in Figure 5.6 and Figure 5.7.**

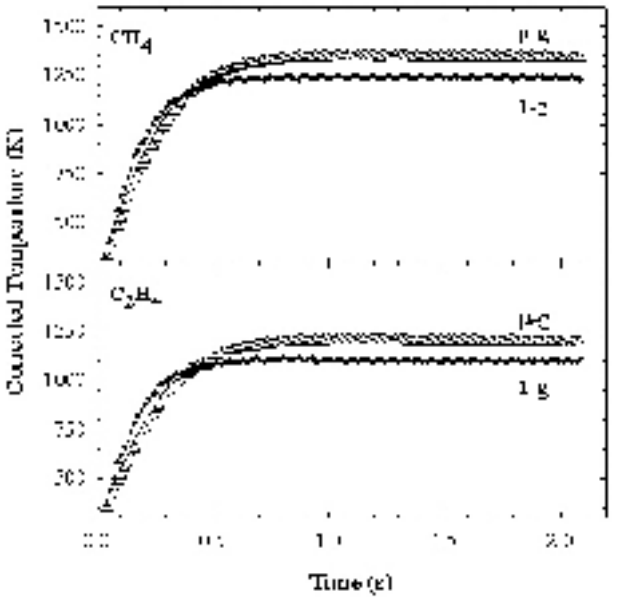

**Figure 5.9: Corrected temperature from IDFs in Figure 5.6 and Figure 5.7 measured on centerline 3.5 cm above burner.**

Table 5.2 contains the average steady state values for the radiometer readings in Figure 5.8. The variations shown with the averages are equal to plus or minus one standard deviation. All of the flames radiate less energy in normal gravity than in microgravity. The 1-g flames may radiate less because they have less soot. The visible images in Figure 5.6 and Figure 5.7 indicate this may be true, but care must be taken in inferring infrared radiation amounts from visible images. The radiative fractions of heat release rate of the $CH_4$ and $C_2H_4$ flames, assuming all $O_2$ reacts are shown in Table 5.2. The heat release rates, assuming all $O_2$ reacts, are given in Table 3.1. The radiative fractions demonstrate that the flames lose twice as much radiation in microgravity as in normal gravity. There is no significant difference in the radiative fractions for $CH_4$ and $C_2H_4$ fuels.

**Table 5.2: Measurements of radiative loss and fraction, CO concentration, molar concentration ratio of CO to CO2 and elemental carbon fraction in 1-g and μ-g $CH_4$ and $C_2H_4$ IDFs.**

| Fuel | g | Air flow rate (slpm) | Radiative loss (W) | Radiative fraction (%) | [CO] (ppm, wet) | [CO]/ [$CO_2$] | EC/TC (%) |
|---|---|---|---|---|---|---|---|
| $CH_4$ | 1-g | 2.4 | 5.35 ± 0.12 | 4 | 167 ± 3 | 0.65 | 0 |
| $CH_4$ | μ-g | 2.4 | 12.12 ± 0.12 | 9 | 180 ± 4 | 0.73 | 7 |
| $C_2H_4$ | 1-g | 1.6 | 4.41 ± 0.15 | 4 | 261 ± 1 | 1.54 | 13 |
| $C_2H_4$ | μ-g | 1.6 | 8.83 ± 0.24 | 8 | 308 ± 10 | 2.24 | 24 |

### 5.4.3 CO Analyzer Measurements

Table 5.2 shows the measured CO concentrations in the combustion chamber for the IDFs in Figure 5.6 and Figure 5.7. Assuming that all of the carbon in the fuel consumed by stoichiometric combustion forms either CO or $CO_2$, the computed molar concentration ratio of CO to $CO_2$ is also shown in Table 5.2. Both fuel types produce

slightly more CO in microgravity than in normal gravity. In addition, the molar concentration ratio of CO to $CO_2$ increases in microgravity relative to that for normal gravity. The CO to $CO_2$ molar concentration ratio of laminar, underventilated normal flames was measured to be 0.5 in a previous study [22]. Hence, inverse flames produce CO to $CO_2$ molar concentration ratios that are slightly larger than those of underventilated flames. This demonstrates that inverse flames can be used to gain insight into CO formation in underventilated fires where CO is a major component rather than a trace component.

Figure 5.10 shows CO concentration measurements versus air flow rate for ethylene IDFs in microgravity. The calculated $CO_2$ concentrations and molar concentration ratios of CO to $CO_2$ are also shown. As air flow rate increases, CO concentration and calculated $CO_2$ concentration both increase, but the molar ratio of CO to $CO_2$ concentration decreases. The increase in CO and $CO_2$ concentrations is due to the increase in air flow, which causes more fuel to react, increasing the amount of carbon in the products. The decrease in molar concentration of CO to $CO_2$ may be due to the increase in $O_2$ concentration as air flow rate is increased, leading to an increase in the oxidation of CO to $CO_2$. As more CO is oxidized to $CO_2$, the flame temperature in the reaction zone will increase, which may affect soot formation. Also, the conversion of CO to $CO_2$ may be due to an increase in OH radicals on the fuel side of the flame.

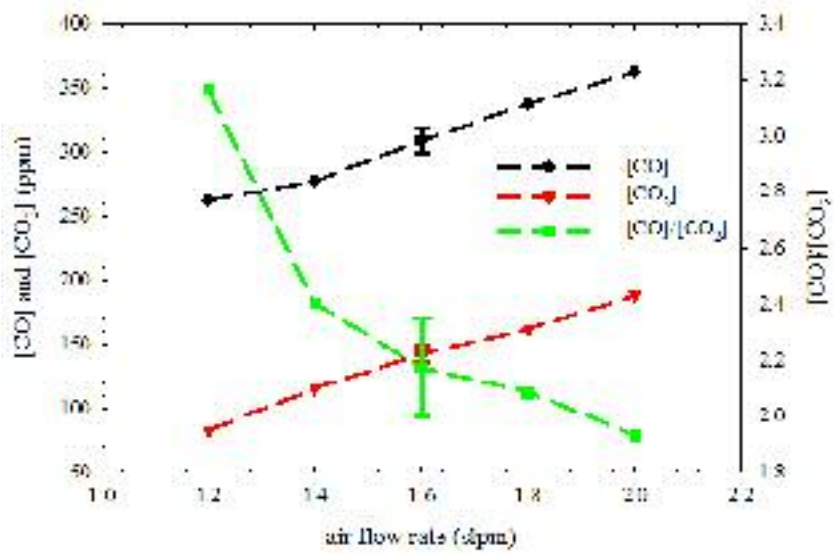


**Figure 5.10: CO concentration, calculated $CO_2$ concentration, and calculated molar concentration ratio of CO to $CO_2$ in microgravity ethylene IDFs with varying air flow rate.**

### 5.4.4 OCEC Measurements

Table 5.2 also shows the fraction of elemental carbon collected (EC/TC) from the IDFs in Figure 5.6 and Figure 5.7. The fraction of elemental carbon is a measure of soot carbonization or dehydrogenization. The remaining organic carbon fraction is a measure of soot precursors and PAH that have condensed either on particles or in the sampling system. Since IDFs and underventilated NDFs emit soot precursors and PAH that are not oxidized, the organic carbon fraction is higher than in over ventilated NDFs. Léonard *et al.* [22] collected soot samples from methane and ethylene NDFs with overall equivalence ratios of 1, 2, and 4. They found that as NDFs became more underventilated, elemental carbon fraction decreased from 96% to 16% for methane and from 96% to 47% for ethylene. The IDFs in Table 5.2 have lower elemental carbon fractions than the NDFs in the study by Léonard *et al.* [22]. This shows that an IDF is an extreme case of an underventilated NDF, since the overall equivalence ratios of the IDFs in this study

(listed in Table 3.1) are between 15 and 40. In both gravity conditions, ethylene IDFs have greater elemental carbon fractions than methane IDFs. This also agrees with the results by Léonard *et al.* [22] showing that ethylene NDFs emit soot with greater elemental carbon fraction than methane NDFs.

The elemental carbon fraction is greater for both fuels in microgravity than in normal gravity. This agrees well with the images in Figure 5.6 and Figure 5.7, which show greater soot loading in visible flames in microgravity. This also agrees with the increased radiometer measurements in Figure 5.8 and in Table 5.2 that show increased radiation in microgravity, since carbonized soot particles are strong emitters, whereas organic soot is thought to be transparent. The increased elemental carbon may be due to longer residence time for soot carbonization and dehydrogenization in non-buoyant flames. Figure 5.11 shows elemental carbon fraction versus air flow rate in ethylene IDFs in microgravity. The dashed line represents a linear regression of the data points. As air flow rate increases, the elemental carbon fraction also increases. In Chapter 3, it was shown that increasing air flow rate increases IDF flame length. Therefore, the increase in elemental carbon fraction may be due to increased residence time for soot carbonization and dehydrogenization, as flame length is increased by increasing air flow rate. Soot carbonization occurs at temperatures above the critical soot inception temperature [19,23]. In Chapter 4, soot PLII was observed at temperatures above 1300 K, and computer modeling showed that streamlines originating close to the reaction zone moved to lower temperature. Therefore, soot may be forming at very high temperature close to the reaction zone and carbonizing as it follows streamlines until its temperature decreases below 1300 K. Carbonization times are very short at high

temperature, on the order of 1-10 ms [19], so there may be sufficient time for carbonization of soot that forms close to the reaction zone. Also, the fact that visible radiation was observed is evidence that soot carbonization is occurring, since precursors are transparent, and carbonaceous soot radiates strongly. Therefore, IDFs appear to emit partially carbonized soot as well as soot precursor particles and PAH.

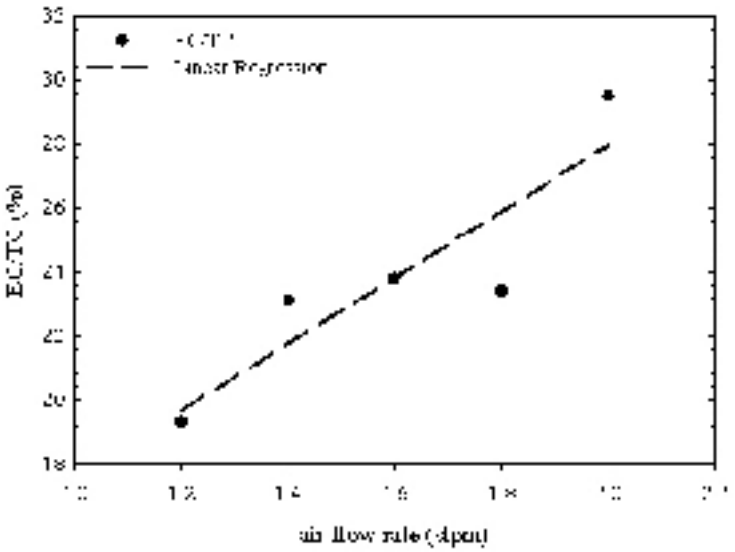


**Figure 5.11: Elemental carbon fraction (EC/TC) of material collected on filters from microgravity ethylene IDFs with varying air flow rate.**

### 5.4.5 Computational Particle Tracking

The model is used to generate time-temperature pathways for tracer particles placed in the flame where inception is believed to occur. Figure 5.12 shows computed temperature contours for the μ-g $CH_4$ and $C_2H_4$ flames shown in Figure 5.6 and Figure 5.7. The white lines in Figure 5.12 show tracer particle tracks. For both μ-g flames in Figure 5.12, the tracer particles appear to closely follow the fluid streamlines. The paths demonstrate that soot particles formed low in the flame move away from the flame for IDFs and can escape with minimal oxidation for both gravity conditions.

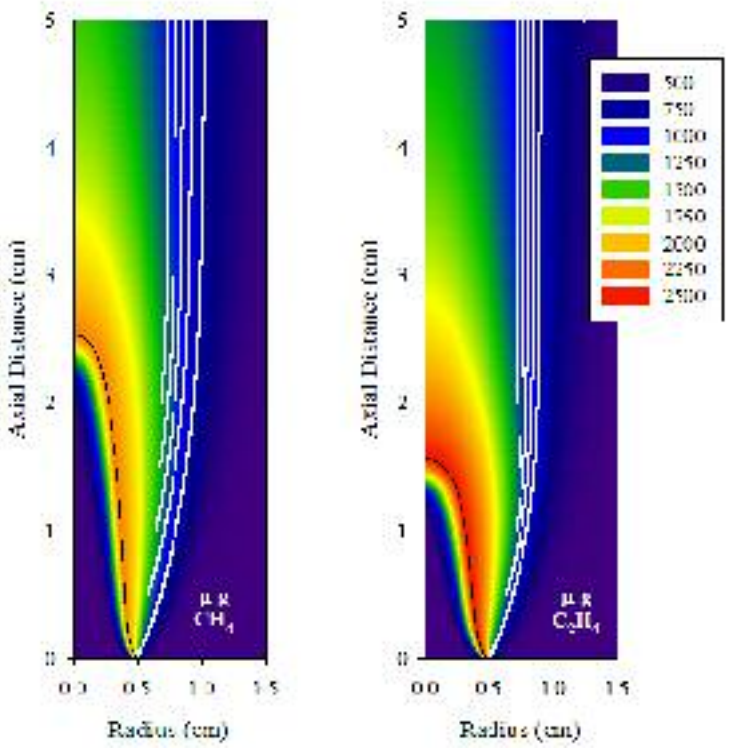


**Figure 5.12: Computed temperature contours for μ-g $CH_4$ and $C_2H_4$ IDFs. Stoichiometric contours are shown in black and tracer particle trajectories are shown in white.**

Figure 5.13 shows predicted time-temperature histories for the tracer particles in the $CH_4$ and $C_2H_4$ μ-g and 1-g flames depicted in Figure 5.6 and Figure 5.7. The axial location of tracer particle injection is noted for each time-temperature line in Figure 5.13. The time-temperature lines correspond to the trajectories shown in Figure 5.12 for the μ-g flames. In all of the flames, tracer particles move away from the high temperature region after formation. Particles in the 1-g $CH_4$ and $C_2H_4$ flames spend less time at high temperature than those in the μ-g flames because of buoyant acceleration. Therefore, residence time is longer for soot carbonization and dehydrogenization in microgravity than in normal gravity IDFs. This may explain why the elemental carbon fraction of the soot collected on filters was greater for microgravity than normal gravity IDFs.

Temperatures of the particles in the μ-g $C_2H_4$ flame reduce monotonically after they form. Temperatures of some of the tracer particles in the 1-g $C_2H_4$ flame do not decrease monotonically because of buoyancy-induced vortices in the flow field. It was seen in Chapter 4 that buoyancy-induced vortices cause recirculation of soot into the high temperature zone bringing the particles into contact with soot precursors and PAH that may increase the organic carbon fraction of the soot. Figure 5.13 dramatically demonstrates the differences in time-temperature histories between μ-g and 1-g flames. This is significant because it allows one to select flames with different soot particle pathways, collect and analyze the soot particles formed by the different pathways, and draw conclusions about the effect of local conditions on the soot formation.

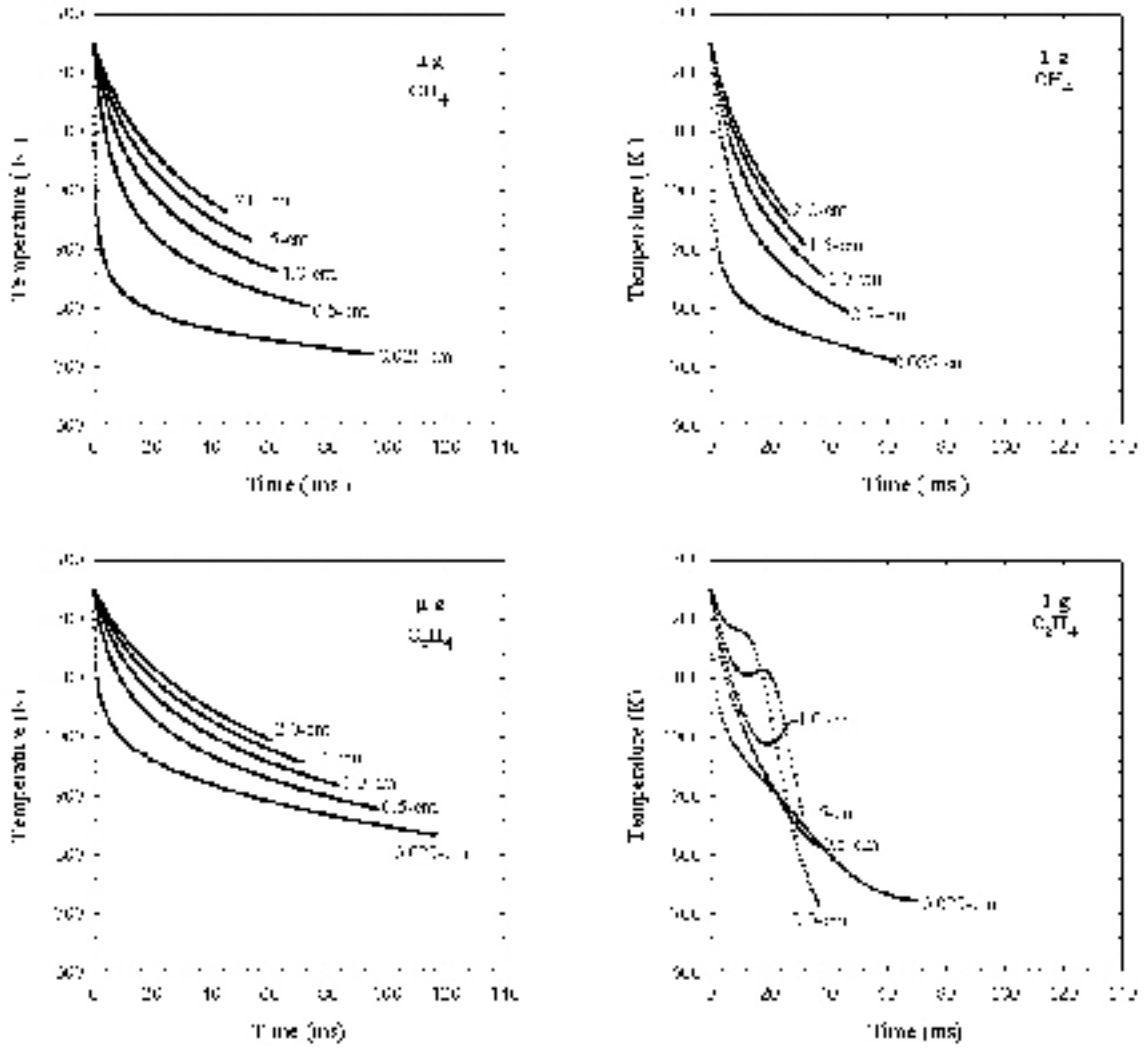

**Figure 5.13: Time-temperature histories of tracer particles in μ-g and 1-g $CH_4$ and $C_2H_4$ IDFs. Particles were inserted at a chosen minimum soot inception temperature of 1250 K on the fuel side of the flame and at the axial location indicated next to each curve.**

## 5.5 Conclusions

IDFs were tested in microgravity to remove buoyancy-induced vortices that influence soot formation and to isolate soot formation from oxidation. IDFs reached steady state more quickly than NDFs in microgravity, which makes IDFs ideal to study in short duration drop-tower tests. All of the microgravity IDFs were more luminous, were slightly longer, were more rounded, and radiated more energy than their normal gravity

counterparts. Microgravity IDFs emitted slightly more unoxidized CO than their normal gravity counterparts. The molar concentration ratio of CO to $CO_2$ was also greater in microgravity than in normal gravity. In microgravity ethylene IDFs, CO concentration increased with air flow rate. However, the calculated molar concentration ratio of CO to $CO_2$ of ethylene IDFs in microgravity decreased as air flow increased, indicating that increased air flow increase oxidation of CO.

The material collected on filters from ethylene IDFs also contained a higher elemental carbon fraction than from methane IDFs for both gravity conditions. This may be due to the lower soot tendency of methane. Materials collected on filters from the microgravity IDFs had a greater elemental carbon fraction than normal gravity IDFs. Increasing air flow rate in microgravity ethylene IDFs also increased the elemental carbon fraction of the material collected on the filters. This indicates that residence time plays a role in soot carbonization, since the elemental carbon fraction in the soot collected from IDFs is evidence of partial soot carbonization.

It is possible that the soot and CO differences exist because of different post-flame particle pathways induced by buoyancy. Computational modeling of time-temperature histories of tracer particles demonstrated that soot particles in microgravity IDFs cool monotonically. Tracer particles in microgravity IDFs also spent longer time at high temperature demonstrating that the increase in elemental carbon fraction observed in microgravity IDFs is due to increased residence time. The results of these experiments show that microgravity IDFs can be used to isolate soot formation from soot oxidation so that a better understanding of the earliest steps in soot formation can be gained.

## 5.6 References

[1]. R.J. Santoro, H.G. Semerjian, Proc. Combust. Inst. 20 (1984) 997-1006.

[2]. J.H. Kent, H.Gg. Wagner, Proc. Combust. Inst. 20 (1984) 1007-1015.

[3]. R.J. Santoro, T.T. Yeh, J.J. Horvath, H.G. Semerjian, Combust. Sci. Technol. 53 (2-3) (1987) 89-115.

[4]. C.R. Shaddix, C.W. Williams, L.G. Blevins, R.W. Schefer, Proc. Combust. Inst. 30 (2005) 1501-1508.

[5]. D.B. Makel, I.M. Kennedy, Combust. Sci. Technol. 97 (4-6) (1994) 303-314.

[6]. I. Glassman, Proc. Combust. Inst. 22 (1988) 295-311.

[7]. J.H. Kent, H.G. Wagner, Zeitschrift Fur Physikalische Chemie-Wiesbaden 139 (1984) 59-68.

[8]. G.W. Sidebotham, I. Glassman, Combust. Sci. Technol. 81 (4-6) (1992) 207-219.

[9]. V.R. Katta, L.G. Blevins, W.M. Roquemore, Combust. Flame 142 (1-2) (2005) 33-51.

[10]. K.C. Smyth, C.R. Shaddix, D.A. Everest, Combust. Flame 111 (3) (1997) 185-207.

[11]. C.R. Shaddix, J.E. Harrington, K.C. Smyth, Combust. Flame 99 (3-4) (1994) 723-732.

[12]. J. Zhang, C.M. Megaridis, Combust. Flame 112 (4) (1998) 473-484.

[13]. P.B. Sunderland, B.J. Mendelson, Z.G. Yuan, D.L. Urban, Combust. Flame 116 (3) (1999) 376-386.

[14]. K.C. Lin, G.M. Faeth, P.B. Sunderland, D.L. Urban, Z.G. Yuan, Combust. Flame 116 (3) (1999) 415-431.

[15]. P.B. Sunderland, S.S. Krishnan, J.P. Gore, Combust. Flame 136 (1-2) (2004) 254-256.

[16]. M.E. Birch, R.A. Cary, Aerosol Science and Technology 25 (3) (1996) 221-241.

[17]. R.W. Davis , E.F. Moore, M.R. Zachariah, J. Cryst. Growth 132 (3-4) (1993) 513-522.

[18]. F.P. Incropera, D.P. Dewitt, Fundamentals of Heat and Mass Transfer, John Wiley & Sons, New York, NY, 1990.

[19]. R.A. Dobbins, Combust. Flame 130 (3) (2002) 204-214.

[20]. J. Du, R.L. Axelbaum, Combust. Flame 100 (3) (1995) 367-375.

[21]. C. Aalburg, F.J. Diez, G.M. Faeth, P.B. Sunderland, D.L. Urban, Z.-G. Yuan, Combust. Flame 142 (1-2) (2005) 1-16.

[22]. S. Leonard , G.W. Mulholland, R. Puri, R.J. Santoro, Combust. Flame 98 (1-2) (1994) 20-34.

[23]. R.A. Dobbins, G.J. Govatzidakis, W. Lu, A.F. Schwartzman, R.A. Fletcher, Combust. Sci. Technol. 121 (1-6) (1996) 103-121.

# Chapter 6: Conclusions

## 6.1 Flame Heights

Flame heights of ethylene and methane IDFs of various air flow rates were measured using visible images and OH PLIF. Measured visible flame heights were longer than flame heights measured using OH PLIF because of the visibly radiating soot above and around the reaction zone. Therefore, visible images of IDFs do not reveal information about the reaction zone. Both visible and OH PLIF flame heights increased linearly with air flow rate.

Roper's analysis predicted IDF reaction zone heights when the following modifications were made to Eq. 3.1:

(1) air flow rate was used instead of fuel flow rate as the primary flow rate, $Q$, that determines flame height,

(2) stoichiometric fuel-to-air ratio was used instead of air-to-fuel ratio for the stoichiometric parameter, $S$,

(3) an average of the ambient and adiabatic flame temperatures was used as the characteristic temperature in the diffusion zone, $T_f$,

(4) a diffusion coefficient between the binary diffusion coefficient of the fuel into nitrogen and the binary diffusion coefficient of oxygen into nitrogen, but closer to the lesser of the two binary diffusion coefficients was used as the characteristic diffusion coefficient, $D_0$.

The fact that Roper's analysis applies to IDFs is evidence that IDFs are similar in structure to NDFs.

**6.2 Flame Structure**

Flame structure and soot and PAH formation of the methane and ethylene IDFs were studied using OH PLIF, PAH PLIF, soot PLII, thermocouple temperature measurements, and computer modeling of temperature, flow field, and mixture fraction. Peak OH PLIF occurred just inside the outer boundary of the blue emission in visible images and coincided with peak measured temperature. This indicates that OH PLIF can be used to locate the reaction zone in IDFs.

The lowest axial position where soot PLII could be detected was approximately 5 mm above the burner for ethylene IDFs at any air flow rate. Soot PLII showed that soot was formed on the outside of ethylene IDFs about 2-4 mm from the fuel side of the reaction zone, as indicated by OH PLIF. The location of peak soot PLII near the reaction zone coincided with a measured temperature of 1300 K in one flame. These findings suggest that soot requires a minimum chemical time for inception, and that inception only occurs above a minimum critical temperature. This structure is similar, but inverse to the structure of NDFs in which soot forms on the inside.

Radially integrated soot PLII increased with axial position below the flame height. Above the flame height, it increased with a lower slope, reaching a maximum constant value at a point downstream of the reaction zone. This suggests that soot inception ceases above the reaction zone and that soot growth can occur at temperatures below the critical inception temperature. Therefore, IDFs may be used to isolate early soot growth downstream of the flame tip. The maximum constant value varied linearly with air flow rate, indicating that soot production rate is proportional to residence time. By extrapolation, the minimum air flow rate for a soot producing ethylene IDF was

0.6 slpm. Therefore, it may be possible to tailor IDFs to produce only soot precursor particles by choosing a low air flow rate.

Soot PLII could not be observed for methane IDFs using the laser configuration in this study. This suggests that methane may produce less soot, soot with smaller diameter, or soot with lower emissivity than ethylene soot.

Flickering, caused by buoyancy-induced vortices or instability, was observed above and outside the flames and complicated interpretation of the PAH PLIF results. Vortices were larger and occurred lower in longer flames than in shorter flames. Vortices were also smaller in methane IDFs than in ethylene IDFs. Flickering caused mixing and recirculation of fuel and PAH into hotter regions, enhancing PAH production.

PAH PLIF was found at all axial locations, about 2-4 mm to the fuel side of the soot layer on the outside of ethylene IDFs. The proximity of PAH to the soot layer suggests it may be a constituent in soot formation. This structure is also similar but inverse to NDFs, in which PAH is found on the inside. PAH PLIF detected at longer wavelengths were found closer to the soot formation region than PAH PLIF detected with shorter wavelength. In one ethylene IDF, the location of peak PAH PLIF, at axial positions above and below the flame height, coincided with measured temperatures of 1000 K for the long wavelength detection band and 700 K for the shorter wavelength detection band. This may indicate that fluorescence of larger aromatics, which form at higher temperature and are believed to play a greater role in soot formation, can be detected at longer wavelength. Modeling showed that PAH PLIF followed isotherms, contours of constant mixture fraction, and streamlines. This suggests that aromatics of certain size form at certain temperatures and mixture fractions.

Radially integrated PAH PLIF in ethylene IDFs increased monotonically with axial position for all air flow rates at approximately the same rate until high in the flames where scavenging by soot particles may have occurred.

PAH PLIF in methane IDFs was found 6-8 mm away from the reaction zone, as indicated by OH PLIF. The lowest axial position of PAH PLIF detection was about 10 mm for all methane IDFs. This corresponded to the axial location of luminous soot in visible images. This demonstrates that PAH must form before soot can form. It also demonstrates that PAH and soot formation rates are both slower in methane IDFs than in ethylene IDFs.

Radially integrated PAH PLIF in methane IDFs also increased monotonically with axial position, at approximately the same rate for all air flow rates. This may indicate that PAH forms at a constant rate, possibly due to thermal pyrolysis.

### 6.3 Microgravity

Methane and ethylene IDFs of varying air flow rates were tested in the 2.2-second drop tower at NASA Glen Research Center. Visible images were recorded with a color CCD camera, temperature was measured via thermocouple, and a calibrated thin film radiometer measured flame radiation. Post combustion gases were sampled for CO concentration and were passed through a quartz filter for organic carbon and elemental carbon (OCEC) analysis of the soot and other condensed species. The measured CO concentration was used to calculate the molar concentration ratio of CO to $CO_2$ by balancing species. Computer modeling was also used to predict time-temperature histories of tracer particles injected into the model to mimic soot particles.

All microgravity IDFs were more luminous, slightly longer, and more rounded than their normal gravity counterparts. Temperature and radiometer measurements showed that IDFs achieve a steady state in about 0.5 s, which makes them ideal for short duration microgravity tests such as those possible in a drop tower. Temperature measurement and videos indicated that microgravity flames did not flicker. Therefore, microgravity eliminated buoyant flickering. Radiometer measurements showed that flame radiation was twice as much in microgravity than in normal gravity. The elemental carbon fraction of the material sampled on the filters from the post combustion gases was also greater in microgravity than in normal gravity. These measurements indicate that microgravity IDFs produce more carbonaceous soot than normal gravity NDFs. They also indicate the IDFs produce carbonized soot as well as soot precursor particles. Increasing air flow rate in microgravity ethylene IDFs also increased the elemental carbon fraction. This corroborates the findings in Chapter 4 that increasing residence time increases soot production.

Computer modeling showed that soot particles in microgravity IDFs cool monotonically but spend longer at high temperature than normal gravity soot particles. This supports the conclusion that increased residence time at high temperature increases soot production, since microgravity IDFs produced more soot than normal gravity IDFs. Tracer particles in normal gravity IDFs were accelerated by buoyancy, which caused the particles to cool quickly but not monotonically because of buoyancy-induced vortices. This supports the conclusion that buoyancy-induced flickering complicates the investigation of soot in normal gravity but that microgravity can be used to eliminate flickering.

Measurements of CO concentration from ethylene IDFs were slightly greater in microgravity than in normal gravity. CO concentration of ethylene IDFs in microgravity also increased with increasing air flow. This suggests that CO formation depends on residence time at high temperature. The calculated CO to $CO_2$ molar ratio decreased with increasing air flow rate, indicating that more CO was oxidizing. This may indicate that more oxygen was diffusing to the fuel side, which may have implications for soot formation.

# Chapter 7: Appendices

## 7.1 Matlab Functions for Analysis of Laser Diagnostics

Matlab functions were used to convert the output from the ICCD camera of OH PLIF, PAH PLIF and soot PLII (called SPE files) from 16-bit IEEE floating point with little-endian byte ordering to 16-bit integer format, and to organize them for analysis. The analysis consisted of finding the centerline and peak signals and radially integrating signals at each axial position. Matlab functions were also used to make images from the SPE files that were color-mapped to show the relative intensity at each point. As described in Chapter 4, OH PLIF and PAH PLIF were corrected for beam profile variations using a profile obtained from Rayleigh scattering through room temperature air. The normalized values of the Rayleigh scattering at each axial position were stored as an array in a file called "Beamprofile_GOLAY.mat" which was used in the functions. The values in the array are in Figure 4.1. Soot PLII was corrected using a $5^{th}$ order polynomial function, the coefficients of which were stored as an array in a file called "soot_correction.mat" which is used in the functions. The coefficients are in Chapter 4 in Eq. 4.1.

### 7.1.1 OH Flame Heights

The following Matlab functions were used to read in SPE files and find the height of the OH layer on the centerline which were reported in Chapter 3.

#### 7.1.1.1 Ethylene

Since PAH PLIF was very intense on the centerline above the OH layer in ethylene IDFs a separate script was used that searched for the "saddle" in between the PAH and OH on the centerline.

```
function [avg, stdev, height, saddles] = OHflameht(SPE_file)

% 2/14/2005 Mark Mikofski, U.C. Berkeley
% OHflameht loads an '.SPE' 16-bit image sequence of OH* LIF of a C2H4 IDF,
% corrects the beam profile and finds the average and standard deviation of
% the height of the maximum intensity on the centerline only.

load('Beamprofile_GOLAY.mat');  % load beamprofile correction file
b = Beamprofile' * ones(1, 512); % create matrix with the beamprofile correction as
columns
scale = 10; %  scale is the number of pixels per millimeter.
base = 482; %  base is the number of pixels from the top of the image to the burner exit.
Nframes = 100; %  Nframes is the number of frames in the files.
Ncol = 512; % number of columns (width) in SPE image
Nrow = 512; % number of rows (height) in SPE image
Nheader = 4100; % number of BYTES in Header
FrameNumberStart = 1; % first frame to readin
top = 32; % starting point of search, must be the same or greater as polyfit width

% matrix to contain the image data from the SPE sequence
ImageDATA = zeros(Ncol, Nrow);
IMAGE_ARRAY = zeros(Ncol, Nrow, Nframes);

% open SPE_file for reading, IEEE floating point with little-endian byte ordering
fid = fopen(SPE_file, 'r', 'ieee-le');
origin = 'bof'; % origin = begining of file

% readin SPE_file
for i = 1:Nframes
    position = Nheader + Ncol*Nrow*2*(FrameNumberStart - 1) + Ncol*Nrow*2*(i - 1);
    fseek(fid, position, origin); % set file position indicator
    [ImageDATA, count] = fread(fid, [Ncol, Nrow], 'uint16'); % copy data to ImageDATA in
16 bit integer format
    ImageDATA = fliplr(rot90(ImageDATA,3)); % transpose imageDATA
    ImageDATA = ImageDATA./b; % correct imageDATA for beamprofile
    IMAGE_ARRAY(:,:,i) = ImageDATA; % copy ImageDATA to IMAGE_ARRAY
    if mod(i,10) == 0, disp(i); end % show progress
end
fclose(fid); % close SPE_file

for j = 1:Nframes

    % subroutine to find offset
    CL = IMAGE_ARRAY(:,round(Ncol/2),j); % copy intensities of centerline
    CL = CL';
    i = top+1; % start at top
    pCL = polyfit(i-32:i+32,CL(i-32:i+32),2); % make a parabolic curve-fit around i
    dp = polyder(pCL);
    dCL = polyval(dp,i); % calculate derivative of curve-fit at i
    while dCL>0; % move to peak PAH
        i = i+8;
        pCL = polyfit(i-32:i+32,CL(i-32:i+32),2); % make a parabolic curve-fit around i
        dp = polyder(pCL);
        dCL = polyval(dp,i); % calculate derivative of curve-fit at i
    end
    while dCL<1 % look for saddle
        i = i+8;
        pCL = polyfit(i-32:i+32,CL(i-32:i+32),2); % make a parabolic curve-fit around i
        dp = polyder(pCL);
        dCL = polyval(dp,i); % calculate derivative of curve-fit at i
    end
    saddle = i;
    saddles(j) = (base-saddle)/scale;
```

```
    [intensity,row] = max(IMAGE_ARRAY(saddle+1:Nrow, round(Ncol/2), j)); % find the index
of the max intensity above the burner
    height(j) = (base - (saddle + row))/scale; % the height of the flame in mm

end
avg = mean(height)
stdev = std(height)
```

### 7.1.1.2 Methane

Methane IDFs had very low PAH PLIF on the centerline compared to OH PLIF. Therefore there was no need to find the "saddle" between the PAH and OH, and a simpler script was used for methane IDFs than for ethylene IDFs.

```
function [avg, stdev, height] = OHflameht_CH4(SPE_file)

% 2/23/2004 Mark Mikofski, U.C. Berkeley
% OHflameht_CH4 loads an '.SPE' 16-bit image sequence of OH* LIF, corrects the
% beam profile and finds the average and standard deviation of the height
% of the maximum intensity on the centerline only.

load('Beamprofile_GOLAY.mat');  % load beamprofile correction file
b = Beamprofile' * ones(1, 512); % create matrix with the beamprofile correction as
columns
scale = 10; %  scale is the number of pixels per millimeter.
base = 482; %  base is the number of pixels from the top of the image to the burner exit.
Nframes = 100; %  Nframes is the number of frames in the files.
Ncol = 512; % number of columns (width) in SPE image
Nrow = 512; % number of rows (height) in SPE image
Nheader = 4100; % number of BYTES in Header
FrameNumberStart = 1; % first frame to readin

% matrix to contain the image data from the SPE sequence
ImageDATA = zeros(Ncol, Nrow);
IMAGE_ARRAY = zeros(Ncol, Nrow, Nframes);

% open SPE_file for reading, IEEE floating point with little-endian byte ordering
fid = fopen(SPE_file, 'r', 'ieee-le');
origin = 'bof'; % origin = begining of file

% readin SPE_file
for i = 1:Nframes
    position = Nheader + Ncol*Nrow*2*(FrameNumberStart - 1) + Ncol*Nrow*2*(i - 1);
    fseek(fid, position, origin); % set file position indicator
    [ImageDATA, count] = fread(fid, [Ncol, Nrow], 'uint16'); % copy data to ImageDATA in
16 bit integer format
    ImageDATA = fliplr(rot90(ImageDATA,3)); % transpose imageDATA
    ImageDATA = ImageDATA./b; % correct imageDATA for beamprofile
    IMAGE_ARRAY(:,:,i) = ImageDATA; % copy ImageDATA to IMAGE_ARRAY
    if mod(i,10) == 0, disp(i); end % show progress
end
fclose(fid); % close SPE_file

% find OH flame heights
[intensity,row] = max(IMAGE_ARRAY(:, round(Ncol/2), :)); % find the index of the max
intensity above the burner
height = (base - row)/scale; % the height of the flame in mm
height = reshape(height,100,1);
avg = mean(height)
stdev = std(height)
```

### 7.1.2 Visible Flame Heights

The following Matlab functions were used to read in SPE files and find the visible flame heights that were reported in Chapter 3.

#### 7.1.2.1 Visible High

This script was used for SPE files obtained when the burner was in the high position, allowing the camera to focus on the flame from the 0 to 48 mm above the burner.

```
function [avght, shot_ht, sd, bad] = laserimageht(SPE_file, I_crit)

% 12/15/04 laserimageht finds the height of the visible flame image

if nargin < 2, I_crit = 1000; end % minimum signal to noise ratio for averaged image
heights
scale = 10; % scale is the number of pixels per millimeter
base = 482; % base is the number of pixels from the top of the image to the burner exit
top = 30; % top is the number of pixels from the top of the image where the laser was
clipped
Nframes = 20; % Nframes is the number of frames in the files
Ncol = 512; % number of columns (width) in SPE image
Nrow = 512; % number of rows (height) in SPE image
Nheader = 4100; % number of BYTES in Header
FrameNumberStart = 1; % first frame to read in

% matrix to contain the image data from the SPE sequence
ImageDATA = zeros(Ncol,Nrow);
IMAGE_ARRAY = zeros(Ncol,Nrow,Nframes);

% open SPE_file for reading, IEEE floating point with little-endian byte ordering
fid = fopen(SPE_file,'r','ieee-le');
origin = 'bof'; % origin = begining of file
for i = 1:Nframes
    position = Nheader+Ncol*Nrow*2*(FrameNumberStart-1)+Ncol*Nrow*2*(i-1);
    fseek(fid,position,origin); % set file position indicator
    [ImageDATA,count] = fread(fid,[Ncol,Nrow],'uint16'); % copy data to ImageDATA in 16
bit integer format
    ImageDATA = fliplr(rot90(ImageDATA,3)); % transpose imageDATA
    IMAGE_ARRAY(:,:,i) = ImageDATA; % copy ImageDATA to IMAGE_ARRAY
    if mod(i,10) == 0, disp(i); end % show progress
end
fclose(fid); % close SPE_file
ImageDATA = mean(IMAGE_ARRAY,3); % average all frames

% find height of averaged image
row = 1; % start from top
while ImageDATA(row,round(Ncol/2))<I_crit, row = row+1; end
avght = (base-row+1)/scale

% find shot to shot height and standard deviation
for frameN = 1:Nframes
    row = 1; % start from top
    while IMAGE_ARRAY(row,round(Ncol/2),frameN)<I_crit; row = row+1; end
    if row~=1
        h_frame(frameN) = (base-row)/scale;
    else
        h_frame(frameN) = 0;
    end
```

```
end
bad = 20-nnz(h_frame)
shot_ht = mean(nonzeros(h_frame))
sd = std(nonzeros(h_frame))
```

### 7.1.2.2 Visible Low

This Matlab script was used for SPE files obtained when the burner was in the low position, allowing the camera to focus on the flame from 22.7 to 73.9 mm above the burner.

```
function [avght, shot_ht, sd, bad] = laserimageht75(SPE_file, thresh)

% 12/15/04 laserimageht75 finds the height of the visible flame image

if nargin < 2, thresh = 1000; end % minimum signal to noise ratio for averaged image
heights
scale = 10; % scale is the number of pixels per millimeter
base = 739; % base is the number of pixels from the top of the image to the burner exit
top = 30; % top is the number of pixels from the top of the image where the laser was
clipped
Nframes = 20; % Nframes is the number of frames in the files
Ncol = 512; % number of columns (width) in SPE image
Nrow = 512; % number of rows (height) in SPE image
Nheader = 4100; % number of BYTES in Header
FrameNumberStart = 1; % first frame to read in

% matrix to contain the image data from the SPE sequence
ImageDATA = zeros(Ncol,Nrow);
IMAGE_ARRAY = zeros(Ncol,Nrow,Nframes);

% open SPE_file for reading, IEEE floating point with little-endian byte ordering
fid = fopen(SPE_file,'r','ieee-le');
origin = 'bof'; % origin = begining of file
for i = 1:Nframes
    position = Nheader+Ncol*Nrow*2*(FrameNumberStart-1)+Ncol*Nrow*2*(i-1);
    fseek(fid,position,origin); % set file position indicator
    [ImageDATA,count] = fread(fid,[Ncol,Nrow],'uint16'); % copy data to ImageDATA in 16
bit integer format
    ImageDATA = fliplr(rot90(ImageDATA,3)); % transpose imageDATA
    IMAGE_ARRAY(:,:,i) = ImageDATA; % copy ImageDATA to IMAGE_ARRAY
    if mod(i,10) == 0, disp(i); end % show progress
end
fclose(fid); % close SPE_file
ImageDATA = mean(IMAGE_ARRAY,3); % average all frames

% find height of averaged image
row = top; % start from top
while ImageDATA(row,round(Ncol/2))>thresh & row<Nrow, row = row+1; end
while ImageDATA(row,round(Ncol/2))<thresh & row<Nrow, row = row+1; end
avght = (base-row+1)/scale

% find shot to shot height and standard deviation
for frameN = 1:Nframes
    row = top; % start from top
    while IMAGE_ARRAY(row,round(Ncol/2),frameN)>thresh & row<Nrow; row = row+1; end
    while IMAGE_ARRAY(row,round(Ncol/2),frameN)<thresh & row<Nrow; row = row+1; end
    if row~=1 & row~=Nrow
        h_frame(frameN) = (base-row)/scale;
    else
        h_frame(frameN) = 0;
   end
end
bad = 20-nnz(h_frame)
shot_ht = mean(nonzeros(h_frame))
sd = std(nonzeros(h_frame))
```

### 7.1.3 Image files

The following Matlab functions were used to read in SPE files and create the images of IDFs that are in Chapters 3 and 4.

#### 7.1.3.1 Images of OH PLIF and PAH PLIF

```
function [pixelmax] = bmpfilemaker(SPE_file, normalize)

% 2/22/2004 Mark Mikofski, U.C. Berkeley
% bmpfilemaker reads a 16bit SPE file, averages the frames, and saves a
% color and grayscale image named after the SPE file. Images are
% normalized using the input argument specified. If no argument is
% specified the normalization factor is the max pixel.

% load colormap for converting greyscale images to color, black->blue->aqua->green-
>yellow->red->white
load Colourmap.mat;

load('Beamprofile_GOLAY.mat');  % load beamprofile correction file
b = Beamprofile' * ones(1, 512); % create matrix with the beamprofile correction as
columns

Nframes = 100; % number of frames
Ncol = 512; % number of columns (width) in SPE image
Nrow = 512; % number of rows (height) in SPE image
Nheader = 4100; % number of BYTES in Header
FrameNumberStart = 1; % first frame to readin

% matrix to contain the image data from the SPE sequence
ImageDATA = zeros(Ncol, Nrow);
FrameDATA = zeros(Ncol, Nrow);

% open SPE_file for reading, IEEE floating point with little-endian byte ordering
fid = fopen(SPE_file, 'r', 'ieee-le');
origin = 'bof'; % origin = begining of file

% readin SPE_file
for i = 1:Nframes
    position = Nheader + Ncol*Nrow*2*(FrameNumberStart - 1) + Ncol*Nrow*2*(i - 1);
    fseek(fid, position, origin); % set file position indicator
    [FrameDATA, count] = fread(fid, [Ncol, Nrow], 'uint16'); % copy data to FrameDATA in
16 bit integer format
    FrameDATA = fliplr(rot90(FrameDATA,3)); % transpose FrameDATA
    FrameDATA = FrameDATA./b; % apply beamfile correction
    ImageDATA = ImageDATA + FrameDATA; % add FrameDATA to ImageDATA
    if mod(i,10) == 0, disp(i);end % show progress
end

fclose(fid); % close SPE_file

ImageDATA = ImageDATA/Nframes; % average data
maxpixel = max(max(ImageDATA)) % display max pixel intensity for reference
if nargin < 2, normalize = maxpixel; end
ImageDATA = ImageDATA/normalize; % normalize
pixelmax = max(max(ImageDATA)) % display max pixel intensity for reference

% make filenames
Nletters = length(SPE_file);
output_bw = [SPE_file(7:Nletters-4),'_BW.bmp']
output_rgb = [SPE_file(7:Nletters-4),'_RGB.bmp']

% save bmp files
imwrite(ImageDATA,output_bw,'bmp');
ImageDATA = ImageDATA *255;
imwrite(ImageDATA, colourmap,output_rgb,'bmp');
```

### 7.1.3.2 Instantaneous Images of OH PLIF and PAH PLIF

```
function instantframes(SPE_file, normalize)

% load colormap for converting greyscale images to color, black->blue->aqua->green-
>yellow->red->white
load Colourmap.mat;

load('Beamprofile_GOLAY.mat');  % load beamprofile correction file
b = Beamprofile' * ones(1, 512); % create matrix with the beamprofile correction as
columns

Nframes = 100; % number of frames
Ncol = 512; % number of columns (width) in SPE image
Nrow = 512; % number of rows (height) in SPE image
Nheader = 4100; % number of BYTES in Header
FrameNumberStart = 1; % first frame to readin

% matrix to contain the image data from the SPE sequence
ImageDATA = zeros(Ncol, Nrow);
IMAGE_ARRAY = zeros(Ncol,Nrow,Nframes);
FrameDATA = zeros(Ncol, Nrow);

% open SPE_file for reading, IEEE floating point with little-endian byte ordering
fid = fopen(SPE_file, 'r', 'ieee-le');
origin = 'bof'; % origin = begining of file

% readin SPE_file
for i = 1:Nframes
    position = Nheader + Ncol*Nrow*2*(FrameNumberStart - 1) + Ncol*Nrow*2*(i - 1);
    fseek(fid, position, origin); % set file position indicator
    [FrameDATA, count] = fread(fid, [Ncol, Nrow], 'uint16'); % copy data to FrameDATA in
16 bit integer format
    FrameDATA = fliplr(rot90(FrameDATA,3)); % transpose FrameDATA
    FrameDATA = FrameDATA./b; % apply beamfile correction
    IMAGE_ARRAY(:,:,i) = FrameDATA; % copy ImageDATA to IMAGE_ARRAY
    if mod(i,10) == 0, disp(i);end % show progress
end
fclose(fid); % close SPE_file
pixelmax = max(max(max(IMAGE_ARRAY))) % display max pixel intensity for reference
if nargin < 2, normalize = pixelmax; end

Nletters = length(SPE_file);
for i = 10:10:Nframes
    ImageDATA = IMAGE_ARRAY(:,:,i)/normalize; % normalize
    % make filenames
    output_bw = [SPE_file(7:Nletters-4),'_',num2str(i),'_BW.bmp'];
    output_rgb = [SPE_file(7:Nletters-4),'_',num2str(i),'_RGB.bmp'];
    % save bmp files
    imwrite(ImageDATA,output_bw,'bmp');
    ImageDATA = ImageDATA *255+1;
    imwrite(ImageDATA,colourmap,output_rgb,'bmp');
end

% make avi
output = [SPE_file(7:Nletters-4),'.avi'];
for i = 1:Nframes
    ImageDATA = IMAGE_ARRAY(:,:,i)/normalize*255+1; % normalize
    mov(i) = im2frame(ImageDATA,colourmap);
end
movie2avi(mov,output,'compression','None','fps',2.5);
```

### 7.1.3.3 Images of Soot PLII

```
function [pixelmax] = sootbmpfilemaker(SPE_file, SPE_fileNL, normalize)

% 3/18/2004 Mark Mikofski, U.C. Berkeley

if nargin < 3, normalize = 65535; end

% load colormap for converting greyscale images to color, black->blue->aqua->green-
>yellow->red->white
load Colourmap.mat;
load('soot_correction.mat');  % load soot correction polynomial
```

```
b = polyval(soot_correction,(1:512)/512)'* ones(1, 512); % create matrix with the soot
correction as a column

Nframes = 100; % number of frames
Ncol = 512; % number of columns (width) in SPE image
Nrow = 512; % number of rows (height) in SPE image
Nheader = 4100; % number of BYTES in Header
FrameNumberStart = 1; % first frame to readin

% matrix to contain the image data from the SPE sequence
ImageDATA = zeros(Ncol, Nrow);
IMAGE_ARRAY = zeros(Ncol, Nrow, Nframes);

% open SPE_file for reading, IEEE floating point with little-endian byte ordering
fid = fopen(SPE_file, 'r', 'ieee-le');
origin = 'bof'; % origin = begining of file
for i = 1:Nframes
    position = Nheader + Ncol*Nrow*2*(FrameNumberStart - 1) + Ncol*Nrow*2*(i - 1);
    fseek(fid, position, origin); % set file position indicator
    [ImageDATA, count] = fread(fid, [Ncol, Nrow], 'uint16'); % copy data to ImageDATA in
16 bit integer format
    ImageDATA = fliplr(rot90(ImageDATA,3)); % transpose imageDATA
    ImageDATA = ImageDATA./b; % apply soot correction
    IMAGE_ARRAY(:,:,i) = ImageDATA; % copy ImageDATA to IMAGE_ARRAY
    if mod(i,10) == 0, disp(i); end % show progress
end
fclose(fid); % close SPE_file

ImageDATA = mean(IMAGE_ARRAY,3); % average all frames

% matrix to contain the image data from the NL.SPE sequence
ImageDATANL = zeros(Ncol, Nrow);
IMAGE_ARRAYNL = zeros(Ncol, Nrow, Nframes);

% open SPE_file for reading, IEEE floating point with little-endian byte ordering
fid = fopen(SPE_fileNL, 'r', 'ieee-le');
origin = 'bof'; % origin = begining of file
for i = 1:Nframes
    position = Nheader + Ncol*Nrow*2*(FrameNumberStart - 1) + Ncol*Nrow*2*(i - 1);
    fseek(fid, position, origin); % set file position indicator
    [ImageDATANL, count] = fread(fid, [Ncol, Nrow], 'uint16'); % copy data to ImageDATANL
in 16 bit integer format
    ImageDATANL = fliplr(rot90(ImageDATANL,3)); % transpose ImageDATANL
    ImageDATANL = ImageDATANL./b; % apply soot correction
    IMAGE_ARRAYNL(:,:,i) = ImageDATANL; % copy ImageDATANL to IMAGE_ARRAYNL
    if mod(i,10) == 0, disp(i); end % show progress
end
fclose(fid); % close SPE_file

ImageDATANL = mean(IMAGE_ARRAYNL,3); % average all frames

ImageDATA = ImageDATA - ImageDATANL;

maxpixel = max(max(ImageDATA)) % display max pixel intensity for reference
if nargin < 3, normalize = maxpixel; end
ImageDATA = ImageDATA/normalize; % normalize
pixelmax = max(max(ImageDATA)) % display max pixel intensity for reference

% make filenames
Nletters = length(SPE_file);
output_bw = [SPE_file(7:Nletters-4),'_BW.bmp']
output_rgb = [SPE_file(7:Nletters-4),'_RGB.bmp']

% save bmp files
imwrite(ImageDATA,output_bw,'bmp');
ImageDATA = ImageDATA *255;
imwrite(ImageDATA, colourmap,output_rgb,'bmp');
```

### 7.1.3.4 Instantaneous Images of Soot PLII

```
function sootframes(SPE_file, normalize)

% load colormap for converting greyscale images to color, black->blue->aqua->green-
>yellow->red->white
load Colourmap.mat;

load('soot_correction.mat');  % load soot correction polynomial
```

```
b = polyval(soot_correction,(1:512)/512)'* ones(1, 512); % create matrix with the soot
correction as a column

Nframes = 100; % number of frames
Ncol = 512; % number of columns (width) in SPE image
Nrow = 512; % number of rows (height) in SPE image
Nheader = 4100; % number of BYTES in Header
FrameNumberStart = 1; % first frame to readin

% matrix to contain the image data from the SPE sequence
ImageDATA = zeros(Ncol, Nrow);
IMAGE_ARRAY = zeros(Ncol,Nrow,Nframes);
FrameDATA = zeros(Ncol, Nrow);

% open SPE_file for reading, IEEE floating point with little-endian byte ordering
fid = fopen(SPE_file, 'r', 'ieee-le');
origin = 'bof'; % origin = begining of file

% readin SPE_file
for i = 1:Nframes
    position = Nheader + Ncol*Nrow*2*(FrameNumberStart - 1) + Ncol*Nrow*2*(i - 1);
    fseek(fid, position, origin); % set file position indicator
    [FrameDATA, count] = fread(fid, [Ncol, Nrow], 'uint16'); % copy data to FrameDATA in
16 bit integer format
    FrameDATA = fliplr(rot90(FrameDATA,3)); % transpose FrameDATA
    FrameDATA = FrameDATA./b; % apply beamfile correction
    IMAGE_ARRAY(:,:,i) = FrameDATA; % copy ImageDATA to IMAGE_ARRAY
    if mod(i,10) == 0, disp(i);end % show progress
end
fclose(fid); % close SPE_file
pixelmax = max(max(max(IMAGE_ARRAY))) % display max pixel intensity for reference
if nargin < 2, normalize = pixelmax; end

Nletters = length(SPE_file);
for i = 10:10:Nframes
    ImageDATA = IMAGE_ARRAY(:,:,i)/normalize; % normalize
    % make filenames
    output_bw = [SPE_file(7:Nletters-4),'_',num2str(i),'_BW.bmp'];
    output_rgb = [SPE_file(7:Nletters-4),'_',num2str(i),'_RGB.bmp'];
    % save bmp files
    imwrite(ImageDATA,output_bw,'bmp');
    ImageDATA = ImageDATA *255+1;
    imwrite(ImageDATA,colourmap,output_rgb,'bmp');
end

% make avi
output = [SPE_file(7:Nletters-4),'.avi'];
for i = 1:Nframes
    ImageDATA = IMAGE_ARRAY(:,:,i)/normalize*255+1; % normalize
    mov(i) = im2frame(ImageDATA,colourmap);
end
movie2avi(mov,output,'compression','None','fps',2.5);
```

### 7.1.3.5 Images of Visible IDFs

```
function [pixelmax] = imagefilemaker(SPE_file, normalize)

% load colormap for converting greyscale images to color, black->blue->aqua->green-
>yellow->red->white
load Colourmap.mat;

Nframes = 20; % number of frames
Ncol = 512; % number of columns (width) in SPE image
Nrow = 512; % number of rows (height) in SPE image
Nheader = 4100; % number of BYTES in Header
FrameNumberStart = 1; % first frame to readin

% matrix to contain the image data from the SPE sequence
ImageDATA = zeros(Ncol, Nrow);
FrameDATA = zeros(Ncol, Nrow);

% open SPE_file for reading, IEEE floating point with little-endian byte ordering
fid = fopen(SPE_file, 'r', 'ieee-le');
origin = 'bof'; % origin = begining of file

% readin SPE_file
for i = 1:Nframes
```

```
    position = Nheader + Ncol*Nrow*2*(FrameNumberStart - 1) + Ncol*Nrow*2*(i - 1);
    fseek(fid, position, origin); % set file position indicator
    [FrameDATA, count] = fread(fid, [Ncol, Nrow], 'uint16'); % copy data to FrameDATA in
16 bit integer format
    FrameDATA = fliplr(rot90(FrameDATA,3)); % transpose FrameDATA
    ImageDATA = ImageDATA + FrameDATA; % add FrameDATA to ImageDATA
    if mod(i,10) == 0, disp(i);end % show progress
end

fclose(fid); % close SPE_file

ImageDATA = ImageDATA/Nframes; % average data
maxpixel = max(max(ImageDATA)) % display max pixel intensity for reference
if nargin < 2, normalize = maxpixel; end
ImageDATA = ImageDATA/normalize; % normalize
pixelmax = max(max(ImageDATA)) % display max pixel intensity for reference

% make filenames
Nletters = length(SPE_file);
output_bw = [SPE_file(7:Nletters-4),'_BW.bmp']
output_rgb = [SPE_file(7:Nletters-4),'_RGB.bmp']

% save bmp files
imwrite(ImageDATA,output_bw,'bmp');
ImageDATA = ImageDATA *255;
imwrite(ImageDATA, colourmap,output_rgb,'bmp');
```

### 7.1.4 Analysis

The following Matlab functions were used to find the centerline and peak intensities and to radially integrate the intensity at each axial position for OH PLIF, PAH PLIF, and soot PLII. There are separate functions for each fuel type and for each burner position due to differences in the search routines used.

#### 7.1.4.1 Analysis of OH PLIF and PAH PLIF in Ethylene IDFs

##### 7.1.4.1.1 Ethylene IDFs from 0 to 48.2 mm above Burner

```
function [noise, background, Height, Center] = peakLIF_C2H4all(SPE_file, SNR)

% 9/10/2004 Mark Mikofski, U.C. Berkeley
% peakLIF_C2H4all loads a 16-bit SPE image sequence of a C2H4 flame,
% corrects the data for beamprofile and stores the position and
% intensity of the pixels that represent the peak PAH and OH LIF.

if nargin<2, SNR = 3; end % set default SNR if none entered
load('Beamprofile_GOLAY.mat'); % load beamprofile correction file
beam = Beamprofile' * ones(1,512); % create matrix with the beamprofile correction as
columns
scale = 10; % scale is the number of pixels per millimeter
base = 482; % base is the number of pixels from the top of the image to the burner exit
top = 30; % top is the number of pixels from the top of the image where the laser was
clipped
noiseP = 70; % number of pixels to use for noise
Nframes = 100; % Nframes is the number of frames in the files
Ncol = 512; % number of columns (width) in SPE image
Nrow = 512; % number of rows (height) in SPE image
Nheader = 4100; % number of BYTES in Header
FrameNumberStart = 1; % first frame to read in

% matrix to contain the image data from the SPE sequence
```

```
ImageDATA = zeros(Ncol,Nrow);
IMAGE_ARRAY = zeros(Ncol,Nrow,Nframes);

% open SPE_file for reading, IEEE floating point with little-endian byte ordering
fid = fopen(SPE_file,'r','ieee-le');
origin = 'bof'; % origin = begining of file
for i = 1:Nframes
    position = Nheader+Ncol*Nrow*2*(FrameNumberStart-1)+Ncol*Nrow*2*(i-1);
    fseek(fid,position,origin); % set file position indicator
    [ImageDATA,count] = fread(fid,[Ncol,Nrow],'uint16'); % copy data to ImageDATA in 16
bit integer format
    ImageDATA = fliplr(rot90(ImageDATA,3)); % transpose imageDATA
    ImageDATA = ImageDATA./beam; % correct imageDATA for beamprofile
    IMAGE_ARRAY(:,:,i) = ImageDATA; % copy ImageDATA to IMAGE_ARRAY
    if mod(i,10) == 0, disp(i); end % show progress
end
fclose(fid); % close SPE_file
ImageDATA = mean(IMAGE_ARRAY,3); % average all frames

% noise
background = ImageDATA(top+1:top+noiseP,1:noiseP); % upper left corner
background = [background,ImageDATA(top+1:top+noiseP,Ncol-noiseP+1:Ncol)]; % upper right
corner
background = [background,ImageDATA(Nrow-top-noiseP+1:Nrow-top,1:noiseP)]; % bottom left
corner
background = [background,ImageDATA(Nrow-top-noiseP+1:Nrow-top,Ncol-noiseP+1:Ncol)]; %
bottom right corner
background = reshape(background,4*noiseP^2,1);
noise = std(background); % calculate standard deviation of background noise
background = mean(background); % calculate average of background noise

% find peak boundaries of OHc search
[peakiL,IcolL] = max(ImageDATA(base,1:round(Ncol/2))); % find the peak OH and column
index at the base on left side
[peakiR,IcolR] = max(ImageDATA(base,round(Ncol/2)+1:Ncol)); % find the peak OH and column
index at the base on right side
IcolR = round(Ncol/2)+IcolR;
Lside = IcolL; Rside = IcolR; % left and right boundaries of search
CL = ImageDATA(:,round(Ncol/2)); % copy intensities of centerline
CL = CL';
i = top+1; % start at top
pCL = polyfit(i-16:i+16,CL(i-16:i+16),2); % make a parabolic curve-fit around i
dp = polyder(pCL);
dCL = polyval(dp,i); % calculate derivative of curve-fit at i
while dCL>0; % move to peak PAH
    i = i+4;
    pCL = polyfit(i-16:i+16,CL(i-16:i+16),2); % make a parabolic curve-fit around i
    dp = polyder(pCL);
    dCL = polyval(dp,i); % calculate derivative of curve-fit at i
end
while dCL<0 % look for saddle
    i = i+4;
    pCL = polyfit(i-16:i+16,CL(i-16:i+16),2); % make a parabolic curve-fit around i
    dp = polyder(pCL);
    dCL = polyval(dp,i); % calculate derivative of curve-fit at i
end
saddle = i;

% check saddle
[peakiL,Crow] = max(ImageDATA(saddle+1:base,round(Ncol/2))); % find the row of peak OH on
centerline
Crow = Crow+saddle; % adjust position
[peakiL,IrowL] = max(ImageDATA(saddle+1:base,Lside)); % check left side of burner
[peakiR,IrowR] = max(ImageDATA(saddle+1:base,Rside)); % check right side of burner
IrowL = IrowL+saddle; IrowR = IrowR+saddle; % adjust positions
while IrowL<=Crow
    Lside = Lside+1; % adjust Lside if too wide
    [peakiL,IrowL] = max(ImageDATA(saddle+1:base,Lside)); % check left side of burner
    IrowL = IrowL+saddle; % adjust position
end
while IrowR<=Crow
    Rside = Rside-1; % adjust Lside if too wide
    [peakiR,IrowR] = max(ImageDATA(saddle+1:base,Rside)); % check right side of burner
    IrowR = IrowR+saddle; % adjust position
end

% find peak OH intensity in each column above burner
[intensity,row] = max(ImageDATA(saddle+1:base,Lside:Rside)); % find the index of the max
intensity above the burner
[Hrow,Hcol] = min(row); % find height and center of OH layer
Hrow = Hrow+saddle; Hcol = Lside-1+Hcol; % adjust positions
```

```
Height = (base-Hrow)/scale; % calculate height in mm
Center = Hcol/scale; % calculate center in mm
row = (base-(saddle+row))/scale; % convert axial positions to mm
peakOHc(:,1) = (Lside:Rside)'/scale; % fill in radial positions in mm
peakOHc(:,2:3) = [row',intensity']; % store data

% find peak PAH intensities and positions from top to Hrow
% left side
[peakiL,IcolL] = max(ImageDATA(top+1,1:Hcol)); % find the peak PAH and column index in
first row on left side
IcolL = IcolL/scale; % convert left radial position to mm
% right side
[peakiR,IcolR] = max(ImageDATA(top+1,Hcol+1:Ncol)); % find the peak PAH and column index
in first row on right side
IcolR = (IcolR+Hcol)/scale; % convert right radial position to mm
peakPAH(1,1:2) = [IcolL,peakiL]; % store data
peakPAH(1,3) = (peakiL-background)/noise; % average and store data
peakPAH(1,4:5) = [IcolR,peakiR]; % store data
peakPAH(1,6) = (peakiR-background)/noise; % store data

peakPAH(1,10) =
2*sum(ImageDATA(top+1,1:round(Ncol/2)).*fliplr([1:round(Ncol/2)]))/round(Ncol/2)^2; %
left side radially integrated PAH LIF intensity
peakPAH(1,11) =
2*sum(ImageDATA(top+1,round(Ncol/2)+1:Ncol).*[1:round(Ncol/2)])/round(Ncol/2)^2; % right
side radially integrated PAH LIF intensity
peakPAH(1,12) = peakPAH(1,10)+peakPAH(1,11); % total radially integrated PAH LIF
intensity

i = top+1; % start from top of image
while i<Hrow-1 & peakPAH(i-top,3)>=SNR & peakPAH(i-top,6)>=SNR
    i = i+1;
    % left side
    j = scale*IcolL; % column index of previous PAH layer
    [value,saddle] = min(ImageDATA(i,j:Hcol)); % saddle in between PAH and center
    saddle = saddle-1+j;
    [peakiL,IcolL] = max(ImageDATA(i,1:saddle)); % find the peak PAH and column index on
left side
    IcolL = IcolL/scale; % convert left radial position to mm
    % right side
    j = scale*IcolR; % column index of previous PAH layer
    [value,saddle] = min(ImageDATA(i,Hcol+1:j)); % saddle in between PAH and center
    saddle = saddle+Hcol;
    [peakiR,IcolR] = max(ImageDATA(i,saddle:Ncol)); % find the peak PAH and column index
on right side
    IcolR = (IcolR-1+saddle)/scale; % convert right radial position to mm
    peakPAH(i-top,1:2) = [IcolL,peakiL]; % average and store data
    peakPAH(i-top,3) = (peakiL-background)/noise; % average and store data
    peakPAH(i-top,4:5) = [IcolR,peakiR]; % average and store data
    peakPAH(i-top,6) = (peakiR-background)/noise; % average and store data

    peakPAH(i-top,10) =
2*sum(ImageDATA(i,1:round(Ncol/2)).*fliplr([1:round(Ncol/2)]))/round(Ncol/2)^2; % left
side radially integrated PAH LIF intensity
    peakPAH(i-top,11) =
2*sum(ImageDATA(i,round(Ncol/2)+1:Ncol).*[1:round(Ncol/2)])/round(Ncol/2)^2; % right side
radially integrated PAH LIF intensity
    peakPAH(i-top,12) = peakPAH(i-top,10)+peakPAH(i-top,11); % total radially integrated
PAH LIF intensity

end

% check if PAH intensities are bigger than OH intensities at flame tip
i = Hrow;
% left side
j = scale*IcolL; % column index of previous PAH layer
[value,saddle] = min(ImageDATA(i,j:Hcol)); % saddle in between PAH and center
saddle = saddle-1+j;
[PAHlI,PAHl] = max(ImageDATA(i,1:saddle)); % find the peak PAH and column index on left
side
% right side
j = scale*IcolR; % column index of previous PAH layer
[value,saddle] = min(ImageDATA(i,Hcol+1:j)); % saddle in between PAH and center
saddle = saddle+Hcol;
[PAHrI,PAHr] = max(ImageDATA(i,saddle:Ncol)); % find the peak PAH and column index on
right side
PAHr = PAHr-1+saddle; % adjust position
[peakiL,IcolL] = max(ImageDATA(i,1:Hcol)); % find the peak on left side
[peakiR,IcolR] = max(ImageDATA(i,Hcol+1:Ncol)); % find the peak on right side
IcolR = IcolR+Hcol; % adjust position
% make a parabolic curve-fit of the OH layer if PAH intensity >= OH intensity
```

```
if PAHl==IcolL | PAHr==IcolR, OH = polyfit(peakOHc(:,1),peakOHc(:,2),2); end
while (PAHl==IcolL | PAHr==IcolR) & i<base
    axial = (base-i)/scale; % find the axial position in mm
    OHi = OH; OHi(3) = OH(3)-axial;
    radial = roots(OHi); % find the radial position of the OH layer
    if radial(1)<=radial(2)
        OHl = round(radial(1)*scale); OHr = round(radial(2)*scale);
    else
        OHl = round(radial(2)*scale); OHr = round(radial(1)*scale);
    end
    % left side
    [value,saddle] = min(ImageDATA(i,PAHl:OHl)); % find the saddle on left side
    saddle = saddle-1+PAHl; % adjust position
    [peakiL,IcolL] = max(ImageDATA(i,saddle:Hcol)); % find the peak OH and column index
on left side
    IcolL = (IcolL-1+saddle)/scale; % convert left radial position to mm
    [PAHlI,PAHl] = max(ImageDATA(i+1,1:saddle)); % find the peak PAH and column index on
left side
    % right side
    [value,saddle] = min(ImageDATA(i,OHr:PAHr)); % find the saddle on left side
    saddle = saddle-1+OHr; % adjust position
    [peakiR,IcolR] = max(ImageDATA(i,Hcol:saddle)); % find the peak OH and column index
on right side
    IcolR = (IcolR-1+Hcol)/scale; % convert right radial position to mm
    [PAHrI,PAHr] = max(ImageDATA(i+1,saddle:Ncol)); % find the peak PAH and column index
on right side
    PAHr = PAHr-1+saddle; % adjust position
    peakOHr(i-Hrow+1,1:2) = [IcolL,peakiL]; % store data
    peakOHr(i-Hrow+1,3:4) = [IcolR,peakiR];
    i = i+1;
    [peakiL,IcolL] = max(ImageDATA(i,1:Hcol)); % find the peak on left side
    [peakiR,IcolR] = max(ImageDATA(i,Hcol+1:Ncol)); % find the peak on right side
    IcolR = IcolR+Hcol; % adjust position
end

% find peak OH intensity in each row
[peakiL,IcolL] = max(ImageDATA(i:base,1:Hcol),[],2); % find the peak OH and column index
on left side
[peakiR,IcolR] = max(ImageDATA(i:base,Hcol+1:Ncol),[],2); % find the peak OH and column
index on right side
IcolL = IcolL/scale; % convert left radial position to mm
IcolR = (IcolR+Hcol)/scale; % convert right radial position to mm
peakOHr(i-Hrow+1:base-Hrow+1,1:2) = [IcolL,peakiL]; % store data
peakOHr(i-Hrow+1:base-Hrow+1,3:4) = [IcolR,peakiR];

% find peak PAH intensities and positions
i = Hrow-1;
IcolL = peakPAH(i-top,1); % radial position of previous PAH layer
IcolR = peakPAH(i-top,4); % radial position of previous PAH layer
while i<base & peakPAH(i-top,3)>=SNR & peakPAH(i-top,6)>=SNR
    i = i+1;
    % left side
    j = scale*IcolL; % column index of previous PAH layer
    k = scale*peakOHr(i-Hrow+1,1); % column index of OH layer
    if j>=k, j=k; end;
    [value,saddle] = min(ImageDATA(i,j:k)); % saddle in between PAH and OH
    saddle = saddle-1+j;
    [peakiL,IcolL] = max(ImageDATA(i,1:saddle)); % find the peak PAH and column index on
left side
    IcolL = IcolL/scale; % convert left radial position to mm
    % right side
    j = scale*peakOHr(i-Hrow+1,3); % column index of OH layer
    k = scale*IcolR; % column index of previous PAH layer
    if j>=k, j=k; end;
    [value,saddle] = min(ImageDATA(i,j:k)); % saddle in between PAH and OH
    saddle = saddle-1+j;
    [peakiR,IcolR] = max(ImageDATA(i,saddle:Ncol)); % find the peak PAH and column index
on right side
    IcolR = (IcolR-1+saddle)/scale; % convert right radial position to mm
    peakPAH(i-top,1:2) = [IcolL,peakiL]; % average and store data
    peakPAH(i-top,3) = (peakiL-background)/noise; % average and store data
    peakPAH(i-top,4:5) = [IcolR,peakiR]; % average and store data
    peakPAH(i-top,6) = (peakiR-background)/noise; % average and store data

    peakPAH(i-top,10) =
2*sum(ImageDATA(i,1:round(Ncol/2)).*fliplr([1:round(Ncol/2)]))/round(Ncol/2)^2; % left
side radially integrated PAH LIF intensity
    peakPAH(i-top,11) =
2*sum(ImageDATA(i,round(Ncol/2)+1:Ncol).*[1:round(Ncol/2)])/round(Ncol/2)^2; % right side
radially integrated PAH LIF intensity
```

```
    peakPAH(i-top,12) = peakPAH(i-top,10)+peakPAH(i-top,11); % total radially integrated
PAH LIF intensity


end
peakOHc(:,1) = peakOHc(:,1)-round(Ncol/2)/scale; % shift radial axis so center is zero
peakOHr(:,1) = peakOHr(:,1)-round(Ncol/2)/scale; % shift radial axis so center is zero
peakOHr(:,3) = peakOHr(:,3)-round(Ncol/2)/scale; % shift radial axis so center is zero
peakOHr(:,5) = (base-(Hrow:base)')/scale; % fill in axial positions in mm
peakOHr(:,6) = (peakOHr(:,2) + peakOHr(:,4))/2; % average left and right intensities
peakPAH(:,1) = peakPAH(:,1)-round(Ncol/2)/scale; % shift radial axis so center is zero
peakPAH(:,4) = peakPAH(:,4)-round(Ncol/2)/scale; % shift radial axis so center is zero
peakPAH(:,7) = (peakPAH(:,2) + peakPAH(:,5))/2; % average left and right intensities
peakPAH(:,8) = (base-(top+1:i)')/scale;  % fill in axial positions in mm
peakPAH(:,9) = ImageDATA(top+1:i,round(Ncol/2));

% save data
disp('storing data')
Nletters = length(SPE_file);
OHc_out = [SPE_file(7:Nletters-4),'PeakOHc.txt'];
OHr_out = [SPE_file(7:Nletters-4),'PeakOHr.txt'];
PAH_out = [SPE_file(7:Nletters-4),'PeakPAH.txt'];
fig_out = [SPE_file(7:Nletters-4),'PeakFIG'];
save(OHc_out, 'peakOHc', '-ascii', '-tabs');
save(OHr_out, 'peakOHr', '-ascii', '-tabs');
save(PAH_out, 'peakPAH', '-ascii', '-tabs');
plot(peakOHc(:,1),peakOHc(:,2),peakOHr(:,1),peakOHr(:,5),peakOHr(:,3),peakOHr(:,5),peakPA
H(:,1),peakPAH(:,8),peakPAH(:,4),peakPAH(:,8));
daspect([1 1 1]);
axis([-25.6 25.6 -3  48.2]);
xlabel('Radial Position (mm)');
ylabel('Axial Position (mm)');
fig_title = '40-s time averaged peak OH and PAH';
title(fig_title);
hgsave(fig_out);
```

#### 7.1.4.1.2 Ethylene IDFs from 22.7 to 73.9 mm above Burner

```
function [noise, background, center] = peakLIF_C2H4_75all(SPE_file, SNR)

% 3/17/05 - University of California Berkeley - Mark Mikofski
% peakLIF_C2H4_75all loads a 16-bit SPE image sequence of a C2H4 flame,
% corrects the data for beamprofile and stores the position and
% intensity of the pixels that represent the peak PAH and OH LIF.
% It also outputs the centerline and radially integrated intensities at
% each axial position.

if nargin<2, SNR = 3; end % set default SNR if none entered
load('Beamprofile_GOLAY.mat'); % load beamprofile correction file
beam = Beamprofile' * ones(1,512); % create matrix with the beamprofile correction as
columns
scale = 10; % scale is the number of pixels per millimeter
base = 739; % base is the number of pixels from the top of the image to the burner exit
top = 30; % top is the number of pixels from the top and bottom of the image where the
laser was clipped
noiseP = 70; % number of pixels to use for noise
Nframes = 100; % Nframes is the number of frames in the files
Ncol = 512; % number of columns (width) in SPE image
Nrow = 512; % number of rows (height) in SPE image
Nheader = 4100; % number of BYTES in Header
FrameNumberStart = 1; % first frame to read in

% matrix to contain the image data from the SPE sequence
ImageDATA = zeros(Ncol,Nrow);
IMAGE_ARRAY = zeros(Ncol,Nrow,Nframes);

% open SPE_file for reading, IEEE floating point with little-endian byte ordering
fid = fopen(SPE_file,'r','ieee-le');
origin = 'bof'; % origin = begining of file
for i = 1:Nframes
    position = Nheader+Ncol*Nrow*2*(FrameNumberStart-1)+Ncol*Nrow*2*(i-1);
    fseek(fid,position,origin); % set file position indicator
    [ImageDATA,count] = fread(fid,[Ncol,Nrow],'uint16'); % copy data to ImageDATA in 16
bit integer format
    ImageDATA = fliplr(rot90(ImageDATA,3)); % transpose imageDATA
    ImageDATA = ImageDATA./beam; % correct imageDATA for beamprofile
    IMAGE_ARRAY(:,:,i) = ImageDATA; % copy ImageDATA to IMAGE_ARRAY
```

```
    if mod(i,10) == 0, disp(i); end % show progress
end
fclose(fid); % close SPE_file
ImageDATA = mean(IMAGE_ARRAY,3); % average all frames

% noise
background = ImageDATA(top+1:top+noiseP,1:noiseP); % upper left corner
background = [background,ImageDATA(top+1:top+noiseP,Ncol-noiseP+1:Ncol)]; % upper right
corner
background = [background,ImageDATA(Nrow-top-noiseP+1:Nrow-top,1:noiseP)]; % lower left
corner
background = [background,ImageDATA(Nrow-top-noiseP+1:Nrow-top,Ncol-noiseP+1:Ncol)]; %
lower right corner
background = reshape(background,4*noiseP^2,1);
noise = std(background); % calculate standard deviation of background noise
background = mean(background); % calculate average of background noise

% find peak PAH intensities and positions
% left side
[peakiL,IcolL] = max(ImageDATA(top+1,1:round(Ncol/2))); % find the peak PAH and column
index in first row on left side
IcolL = IcolL/scale; % convert left radial position to mm
% right side
[peakiR,IcolR] = max(ImageDATA(top+1,round(Ncol/2)+1:Ncol)); % find the peak PAH and
column index in first row on right side
IcolR = (IcolR+round(Ncol/2))/scale; % convert right radial position to mm
peakPAH(1,1:2) = [IcolL,peakiL]; % store data
peakPAH(1,3) = (peakiL-background)/noise; % store data
peakPAH(1,4:5) = [IcolR,peakiR]; % store data
peakPAH(1,6) = (peakiR-background)/noise; % store data

%radial integration
peakPAH(1,10) =
2*sum(ImageDATA(top+1,1:round(Ncol/2)).*fliplr([1:round(Ncol/2)]))/round(Ncol/2)^2; %
left side radially integrated PAH LIF intensity
peakPAH(1,11) =
2*sum(ImageDATA(top+1,round(Ncol/2)+1:Ncol).*[1:round(Ncol/2)])/round(Ncol/2)^2; % right
side radially integrated PAH LIF intensity
peakPAH(1,12) = peakPAH(1,10)+peakPAH(1,11); % total radially integrated PAH LIF
intensity

i = top+1; % start from top of image
while i<Nrow-top & peakPAH(i-top,3)>=SNR & peakPAH(i-top,6)>=SNR
    i = i+1;
    % left side
    j = scale*IcolL; % column index of previous PAH layer
    if j>round(Ncol/2), j = round(Ncol/2); end % check if previous PAH was in center
    [value,saddle] = min(ImageDATA(i,j:round(Ncol/2))); % saddle in between PAH and
center
    saddle = saddle-1+j;
    [peakiL,IcolL] = max(ImageDATA(i,1:saddle)); % find the peak PAH and column index on
left side
    IcolL = IcolL/scale; % convert left radial position to mm
    % right side
    j = scale*IcolR; % column index of previous PAH layer
    if j<round(Ncol/2)+1, j = round(Ncol/2)+1; end % check if previous PAH was in center
    [value,saddle] = min(ImageDATA(i,round(Ncol/2)+1:j)); % saddle in between PAH and
center
    saddle = saddle+round(Ncol/2);
    [peakiR,IcolR] = max(ImageDATA(i,saddle:Ncol)); % find the peak PAH and column index
on right side
    IcolR = (IcolR-1+saddle)/scale; % convert right radial position to mm
    peakPAH(i-top,1:2) = [IcolL,peakiL]; % store data
    peakPAH(i-top,3) = (peakiL-background)/noise; % store data
    peakPAH(i-top,4:5) = [IcolR,peakiR]; % store data
    peakPAH(i-top,6) = (peakiR-background)/noise; % store data

    % radial integration
    peakPAH(i-top,10) =
2*sum(ImageDATA(i,1:round(Ncol/2)).*fliplr([1:round(Ncol/2)]))/round(Ncol/2)^2; % left
side radially integrated PAH LIF intensity
    peakPAH(i-top,11) =
2*sum(ImageDATA(i,round(Ncol/2)+1:Ncol).*[1:round(Ncol/2)])/round(Ncol/2)^2; % right side
radially integrated PAH LIF intensity
    peakPAH(i-top,12) = peakPAH(i-top,10)+peakPAH(i-top,11); % total radially integrated
PAH LIF intensity

end

peakPAH(:,1) = peakPAH(:,1)-round(Ncol/2)/scale; % shift radial axis so center is zero
peakPAH(:,4) = peakPAH(:,4)-round(Ncol/2)/scale; % shift radial axis so center is zero
```

```
peakPAH(:,7) = (peakPAH(:,2) + peakPAH(:,5))/2; % average left and right intensities
peakPAH(:,8) = (base-(top+1:i)')/scale;  % fill in axial positions in mm
peakPAH(:,9) = ImageDATA(top+1:i,round(Ncol/2));
center = mean((peakPAH(:,4)-peakPAH(:,1))/2);

% save data
disp('storing data')
Nletters = length(SPE_file);
PAH_out = [SPE_file(7:Nletters-4),'PeakPAH.txt'];
fig_out = [SPE_file(7:Nletters-4),'PeakFIG'];
save(PAH_out, 'peakPAH', '-ascii', '-tabs');
plot(peakPAH(:,1),peakPAH(:,8),'k',peakPAH(:,4),peakPAH(:,8),'k');
daspect([1 1 1]);
axis([-25.6  25.6  22.7  73.9]);
xlabel('Radial Position (mm)');
ylabel('Axial Position (mm)');
fig_title = '40-s time averaged peak PAH';
title(fig_title);
hgsave(fig_out);
```

### 7.1.4.2 Analysis of OH PLIF and PAH PLIF in Methane IDFs

```
function [noise, background, Height, Center, base] = peakLIF_CH4all(SPE_file, SNR)

% 9/10/2004 Mark Mikofski, U.C. Berkeley
% peakLIF_CH4all loads a 16-bit SPE image sequence of a CH4 flame,
% corrects the data for beamprofile and stores the position and
% intensity of the pixels that represent the peak PAH and OH LIF.

if nargin<2, SNR = 3; end % set default SNR if none entered
load('Beamprofile_GOLAY.mat'); % load beamprofile correction file
beam = Beamprofile' * ones(1,512); % create matrix with the beamprofile correction as
columns
scale = 10; % scale is the number of pixels per millimeter
burner = 482; % base is the number of pixels from the top of the image to the burner exit
top = 30; % top is the number of pixels from the top of the image where the laser was
clipped
noiseP = 70; % number of pixels to use for noise
Nframes = 100; % Nframes is the number of frames in the files
Ncol = 512; % number of columns (width) in SPE image
Nrow = 512; % number of rows (height) in SPE image
Nheader = 4100; % number of BYTES in Header
FrameNumberStart = 1; % first frame to read in

% matrix to contain the image data from the SPE sequence
ImageDATA = zeros(Ncol,Nrow);
IMAGE_ARRAY = zeros(Ncol,Nrow,Nframes);

% open SPE_file for reading, IEEE floating point with little-endian byte ordering
fid = fopen(SPE_file,'r','ieee-le');
origin = 'bof'; % origin = begining of file
for i = 1:Nframes
    position = Nheader+Ncol*Nrow*2*(FrameNumberStart-1)+Ncol*Nrow*2*(i-1);
    fseek(fid,position,origin); % set file position indicator
    [ImageDATA,count] = fread(fid,[Ncol,Nrow],'uint16'); % copy data to ImageDATA in 16
bit integer format
    ImageDATA = fliplr(rot90(ImageDATA,3)); % transpose imageDATA
    ImageDATA = ImageDATA./beam; % correct imageDATA for beamprofile
    IMAGE_ARRAY(:,:,i) = ImageDATA; % copy ImageDATA to IMAGE_ARRAY
    if mod(i,10) == 0, disp(i); end % show progress
end
fclose(fid); % close SPE_file
ImageDATA = mean(IMAGE_ARRAY,3); % average all frames

% noise
background = ImageDATA(top+1:top+noiseP,1:noiseP); % upper left corner
background = [background,ImageDATA(top+1:top+noiseP,Ncol-noiseP+1:Ncol)]; % upper right
corner
background = [background,ImageDATA(Nrow-top-noiseP+1:Nrow-top,1:noiseP)]; % bottom left
corner
background = [background,ImageDATA(Nrow-top-noiseP+1:Nrow-top,Ncol-noiseP+1:Ncol)]; %
bottom right corner
background = reshape(background,4*noiseP^2,1);
noise = std(background); % calculate standard deviation of background noise
background = mean(background); % calculate average of background noise

% find base of flame
```

```
[peakiL,IcolL] = max(ImageDATA(burner,1:round(Ncol/2))); % find the peak OH and column
index at the base on left side
[peakiR,IcolR] = max(ImageDATA(burner,round(Ncol/2)+1:Ncol)); % find the peak OH and
column index at the base on right side
IcolR = round(Ncol/2)+IcolR;
[peakiL,IrowL] = max(ImageDATA(1:Nrow,IcolL)); % find the peak OH and row index at the
base on left side
[peakiR,IrowR] = max(ImageDATA(1:Nrow,IcolR)); % find the peak OH and row index at the
base on right side
i = 1;
[peakiL,IrowLi] = max(ImageDATA(1:Nrow,IcolL-i)); % find the peak OH and row index at the
base on left side
[peakiR,IrowRi] = max(ImageDATA(1:Nrow,IcolR+i)); % find the peak OH and row index at the
base on right side
while IrowLi>IrowL & IrowRi>IrowR & (peakiL-background)/noise>=SNR & (peakiR-
background)/noise>=SNR
    i = i+1;
    IrowL = IrowLi; IrowR = IrowRi;
    [peakiL,IrowLi] = max(ImageDATA(1:Nrow,IcolL-i)); % find the peak OH and row index at
the base on left side
    [peakiR,IrowRi] = max(ImageDATA(1:Nrow,IcolR+i)); % find the peak OH and row index at
the base on right side
end
base = min([IrowL,IrowR]);
base = max([base,burner]);

% find peak OH intensity in each column above burner
[peakiL,IcolL] = max(ImageDATA(base,1:round(Ncol/2))); % find the peak OH and column
index at the base on left side
[peakiR,IcolR] = max(ImageDATA(base,round(Ncol/2)+1:Ncol)); % find the peak OH and column
index at the base on right side
IcolR = round(Ncol/2)+IcolR;
Lside = IcolL; Rside = IcolR; % left and right boundaries of search
peakOHc(:,1) = (Lside:Rside)'/scale; % fill in radial positions in mm
[intensity,row] = max(ImageDATA(top+1:base,Lside:Rside)); % find the index of the max
intensity above the burner
[Hrow,Hcol] = min(row); % find height and center of OH layer
Hrow = Hrow+top; Hcol = Lside-1+Hcol; % adjust positions
Height = (burner-Hrow)/scale; % calculate height in mm
Center = Hcol/scale; % calculate center in mm
row = (burner-(top+row))/scale; % convert axial positions to mm
peakOHc(:,2:3) = [row',intensity']; % store data

% find peak OH intensity in each row
[peakiL,IcolL] = max(ImageDATA(Hrow:base,1:Hcol),[],2); % find the peak OH and column
index on left side
[peakiR,IcolR] = max(ImageDATA(Hrow:base,Hcol+1:Ncol),[],2); % find the peak OH and
column index on right side
IcolL = IcolL/scale; % convert left radial position to mm
IcolR = (IcolR+Hcol)/scale; % convert right radial position to mm
peakOHr(:,1:2) = [IcolL,peakiL]; % store data
peakOHr(:,3:4) = [IcolR,peakiR];

% find peak PAH intensities and positions
% left side
[peakiL,IcolL] = max(ImageDATA(top+1,1:Hcol)); % find the peak PAH and column index in
first row on left side
IcolL = IcolL/scale; % convert left radial position to mm
% right side
[peakiR,IcolR] = max(ImageDATA(top+1,Hcol+1:Ncol)); % find the peak PAH and column index
in first row on right side
IcolR = (IcolR+Hcol)/scale; % convert right radial position to mm
peakPAH(1,1:2) = [IcolL,peakiL]; % average and store data
peakPAH(1,3) = (peakiL-background)/noise; % average and store data
peakPAH(1,4:5) = [IcolR,peakiR]; % average and store data
peakPAH(1,6) = (peakiR-background)/noise; % average and store data

peakPAH(1,10) =
2*sum(ImageDATA(top+1,1:round(Ncol/2)).*fliplr([1:round(Ncol/2)]))/round(Ncol/2)^2; %
left side radially integrated PAH LIF intensity
peakPAH(1,11) =
2*sum(ImageDATA(top+1,round(Ncol/2)+1:Ncol).*[1:round(Ncol/2)])/round(Ncol/2)^2; % right
side radially integrated PAH LIF intensity
peakPAH(1,12) = peakPAH(1,10)+peakPAH(1,11); % total radially integrated PAH LIF
intensity

i = top+1; % start from top of image
while i<Hrow-1 & peakPAH(i-top,3)>=SNR & peakPAH(i-top,6)>=SNR
    i = i+1;
    % left side
    j = scale*IcolL; % column index of previous PAH layer
```

```
    [value,saddle] = min(ImageDATA(i,j:Hcol)); % saddle in between PAH and center
    saddle = saddle-1+j;
    [peakiL,IcolL] = max(ImageDATA(i,1:saddle)); % find the peak PAH and column index on
left side
    IcolL = IcolL/scale; % convert left radial position to mm
    % right side
    j = scale*IcolR; % column index of previous PAH layer
    [value,saddle] = min(ImageDATA(i,Hcol+1:j)); % saddle in between PAH and center
    saddle = saddle+Hcol;
    [peakiR,IcolR] = max(ImageDATA(i,saddle:Ncol)); % find the peak PAH and column index
on right side
    IcolR = (IcolR-1+saddle)/scale; % convert right radial position to mm
    peakPAH(i-top,1:2) = [IcolL,peakiL]; % average and store data
    peakPAH(i-top,3) = (peakiL-background)/noise; % average and store data
    peakPAH(i-top,4:5) = [IcolR,peakiR]; % average and store data
    peakPAH(i-top,6) = (peakiR-background)/noise; % average and store data

    peakPAH(i-top,10) =
2*sum(ImageDATA(i,1:round(Ncol/2)).*fliplr([1:round(Ncol/2)]))/round(Ncol/2)^2; % left
side radially integrated PAH LIF intensity
    peakPAH(i-top,11) =
2*sum(ImageDATA(i,round(Ncol/2)+1:Ncol).*[1:round(Ncol/2)])/round(Ncol/2)^2; % right side
radially integrated PAH LIF intensity
    peakPAH(i-top,12) = peakPAH(i-top,10)+peakPAH(i-top,11); % total radially integrated
PAH LIF intensity

end
while i<base & peakPAH(i-top,3)>=SNR & peakPAH(i-top,6)>=SNR
    i = i+1;
    % left side
    j = scale*IcolL; % column index of previous PAH layer
    k = scale*peakOHr(i-Hrow+1,1); % column index of OH layer
    if j>=k, j=k; end;
    [value,saddle] = min(ImageDATA(i,j:k)); % saddle in between PAH and OH
    saddle = saddle-1+j;
    [peakiL,IcolL] = max(ImageDATA(i,1:saddle)); % find the peak PAH and column index on
left side
    IcolL = IcolL/scale; % convert left radial position to mm
    % right side
    j = scale*peakOHr(i-Hrow+1,3); % column index of OH layer
    k = scale*IcolR; % column index of previous PAH layer
    if j>=k, j=k; end;
    [value,saddle] = min(ImageDATA(i,j:k)); % saddle in between PAH and OH
    saddle = saddle-1+j;
    [peakiR,IcolR] = max(ImageDATA(i,saddle:Ncol)); % find the peak PAH and column index
on right side
    IcolR = (IcolR-1+saddle)/scale; % convert right radial position to mm
    peakPAH(i-top,1:2) = [IcolL,peakiL]; % average and store data
    peakPAH(i-top,3) = (peakiL-background)/noise; % average and store data
    peakPAH(i-top,4:5) = [IcolR,peakiR]; % average and store data
    peakPAH(i-top,6) = (peakiR-background)/noise; % average and store data

    peakPAH(i-top,10) =
2*sum(ImageDATA(i,1:round(Ncol/2)).*fliplr([1:round(Ncol/2)]))/round(Ncol/2)^2; % left
side radially integrated PAH LIF intensity
    peakPAH(i-top,11) =
2*sum(ImageDATA(i,round(Ncol/2)+1:Ncol).*[1:round(Ncol/2)])/round(Ncol/2)^2; % right side
radially integrated PAH LIF intensity
    peakPAH(i-top,12) = peakPAH(i-top,10)+peakPAH(i-top,11); % total radially integrated
PAH LIF intensity

end
peakOHc(:,1) = peakOHc(:,1)-round(Ncol/2)/scale; % shift radial axis so center is zero
peakOHr(:,1) = peakOHr(:,1)-round(Ncol/2)/scale; % shift radial axis so center is zero
peakOHr(:,3) = peakOHr(:,3)-round(Ncol/2)/scale; % shift radial axis so center is zero
peakOHr(:,5) = (burner-(Hrow:base)')/scale; % fill in axial positions in mm
peakOHr(:,6) = (peakOHr(:,2) + peakOHr(:,4))/2; % average left and right intensities
peakPAH(:,1) = peakPAH(:,1)-round(Ncol/2)/scale; % shift radial axis so center is zero
peakPAH(:,4) = peakPAH(:,4)-round(Ncol/2)/scale; % shift radial axis so center is zero
peakPAH(:,7) = (peakPAH(:,2) + peakPAH(:,5))/2; % average left and right intensities
peakPAH(:,8) = (burner-(top+1:i)')/scale;  % fill in axial positions in mm
peakPAH(:,9) = ImageDATA(top+1:i,round(Ncol/2));

% save data
disp('storing data')
Nletters = length(SPE_file);
OHc_out = [SPE_file(7:Nletters-4),'PeakOHc.txt'];
OHr_out = [SPE_file(7:Nletters-4),'PeakOHr.txt'];
PAH_out = [SPE_file(7:Nletters-4),'PeakPAH.txt'];
fig_out = [SPE_file(7:Nletters-4),'PeakFIG'];
save(OHc_out, 'peakOHc', '-ascii', '-tabs');
```

```
save(OHr_out, 'peakOHr', '-ascii', '-tabs');
save(PAH_out, 'peakPAH', '-ascii', '-tabs');
plot(peakOHc(:,1),peakOHc(:,2),peakOHr(:,1),peakOHr(:,5),peakOHr(:,3),peakOHr(:,5),peakPA
H(:,1),peakPAH(:,8),peakPAH(:,4),peakPAH(:,8));
daspect([1 1 1]);
axis([-25.6 25.6  -3  48.2]);
xlabel('Radial Position (mm)');
ylabel('Axial Position (mm)');
fig_title = '40-s time averaged peak OH and PAH';
title(fig_title);
hgsave(fig_out);
```

### 7.1.4.3 Analysis of Soot PLII from Ethylene IDFs

#### 7.1.4.3.1 Ethylene IDFs from 0 to 48.2 mm above Burner

```
function [center] = peakLII_C2H4all(SPE_file, SPE_fileNL, delta)

% 9/10/2004 Mark Mikofski, U.C. Berkeley
% peakLII_C2H4all loads a 16-bit SPE image sequence of a CH4 flame,
% subtracts an image with no laser and stores the position and
% intensity of the pixels that represent the peak soot LII.

if nargin<3, delta = 1; end % set tolerance between rows in mm
load('soot_correction.mat'); % load beamprofile correction file
beam = polyval(soot_correction,(1:512)/512)'* ones(1, 512); % create matrix with the soot
correction as a column
scale = 10; % scale is the number of pixels per millimeter
base = 482; % base is the number of pixels from the top of the image to the burner exit
top = 30; % top is the number of pixels from the top of the image where the laser was
clipped
Nframes = 100; % Nframes is the number of frames in the files
Ncol = 512; % number of columns (width) in SPE image
Nrow = 512; % number of rows (height) in SPE image
Nheader = 4100; % number of BYTES in Header
FrameNumberStart = 1; % first frame to read in

% matrix to contain the image data from the SPE sequence
ImageDATA = zeros(Ncol,Nrow);
IMAGE_ARRAY = zeros(Ncol,Nrow,Nframes);

% open SPE_file for reading, IEEE floating point with little-endian byte ordering
fid = fopen(SPE_file,'r','ieee-le');
origin = 'bof'; % origin = begining of file
for i = 1:Nframes
    position = Nheader+Ncol*Nrow*2*(FrameNumberStart-1)+Ncol*Nrow*2*(i-1);
    fseek(fid,position,origin); % set file position indicator
    [ImageDATA,count] = fread(fid,[Ncol,Nrow],'uint16'); % copy data to ImageDATA in 16
bit integer format
    ImageDATA = fliplr(rot90(ImageDATA,3)); % transpose imageDATA
    IMAGE_ARRAY(:,:,i) = ImageDATA; % copy ImageDATA to IMAGE_ARRAY
    if mod(i,10) == 0, disp(i); end % show progress
end
fclose(fid); % close SPE_file
ImageDATA = mean(IMAGE_ARRAY,3); % average all frames

% matrix to contain the image data from the SPE sequence
ImageDATANL = zeros(Ncol, Nrow);
IMAGE_ARRAYNL = zeros(Ncol, Nrow, Nframes);

% open SPE_file for reading, IEEE floating point with little-endian byte ordering
fid = fopen(SPE_fileNL, 'r', 'ieee-le');
origin = 'bof'; % origin = begining of file
for i = 1:Nframes
    position = Nheader+Ncol*Nrow*2*(FrameNumberStart-1)+Ncol*Nrow*2*(i-1);
    fseek(fid,position,origin); % set file position indicator
    [ImageDATANL,count] = fread(fid,[Ncol,Nrow],'uint16'); % copy data to ImageDATANL in
16 bit integer format
    ImageDATANL = fliplr(rot90(ImageDATANL,3)); % transpose ImageDATANL
    IMAGE_ARRAYNL(:,:,i) = ImageDATANL; % copy ImageDATANL to IMAGE_ARRAYNL
    if mod(i,10) == 0, disp(i); end % show progress
end
fclose(fid); % close SPE_file
ImageDATANL = mean(IMAGE_ARRAYNL,3); % average all frames
ImageDATA = ImageDATA - ImageDATANL;
```

```
ImageDATA = ImageDATA./beam; % correct imageDATA for beamprofile

% find peak soot intensity in each row
% left side
[peakiL,IcolL] = max(ImageDATA(top+1,1:round(Ncol/2))); % find the peak soot and column
index in first row on left side
IcolL = IcolL/scale; % convert left radial position to mm
% right side
[peakiR,IcolR] = max(ImageDATA(top+1,round(Ncol/2)+1:Ncol)); % find the peak soot and
column index in first row on right side
IcolR = (IcolR+round(Ncol/2))/scale; % convert right radial position to mm
peaksoot(1,1:2) = [IcolL,peakiL]; % store data
peaksoot(1,3) = peakiL/ImageDATA(top+1,round(Ncol/2)); % store data
peaksoot(1,4:5) = [IcolR,peakiR]; % store data
peaksoot(1,6) = peakiR/ImageDATA(top+1,round(Ncol/2)); % store data

peaksoot(1,10) =
2*sum(ImageDATA(top+1,1:round(Ncol/2)).*fliplr([1:round(Ncol/2)]))/round(Ncol/2)^2; %
left side radially integrated soot LII intensity
peaksoot(1,11) =
2*sum(ImageDATA(top+1,round(Ncol/2)+1:Ncol).*[1:round(Ncol/2)])/round(Ncol/2)^2; % right
side radially integrated soot LII intensity
peaksoot(1,12) = peaksoot(1,10)+peaksoot(1,11); % total radially integrated soot LII
intensity

i = top+1; % start from top of image
thresh = 0;
while i<Nrow & thresh~=3
    i = i+1;
    % left side
    [peakiL,IcolL] = max(ImageDATA(i,1:round(Ncol/2))); % find the peak soot and column
index on left side
    IcolL = IcolL/scale; % convert left radial position to mm
    % right side
    [peakiR,IcolR] = max(ImageDATA(i,round(Ncol/2)+1:Ncol)); % find the peak soot and
column index on right side
    IcolR = (IcolR+round(Ncol/2))/scale; % convert right radial position to mm
    % check left side
    if IcolL<peaksoot(i-top-1,1)-delta
        row1 = IcolL*10; row2 = peaksoot(i-top-1,1)*10; % covert to pixels
        [intensity,saddle] = min(ImageDATA(i,row1+1:row2)); % find the saddle
        saddle = saddle+row1; % adjust position
        [peakiL,IcolL] = max(ImageDATA(i,saddle+1:round(Ncol/2))); % find the peak soot
and column index on left side
        if (saddle+1)==IcolL+saddle, thresh = 3; end % stop search if there is no saddle
between soot and pah
        IcolL = (IcolL+saddle)/scale; % convert left radial position to mm
        if IcolL>peaksoot(i-top-1,1)+delta, thresh = 3; end % stop search
    end
    % check right side
    if IcolR>peaksoot(i-top-1,4)+delta
        row1 = peaksoot(i-top-1,4)*10; row2 = IcolR*10; % covert to pixels
        [intensity,saddle] = min(ImageDATA(i,row1:row2)); % find the saddle
        saddle = saddle-1+row1; % adjust position
        [peakiR,IcolR] = max(ImageDATA(i,round(Ncol/2)+1:saddle)); % find the peak soot
and column index on right side
        if saddle<(IcolR+round(Ncol/2)), thresh = 3; end % stop search if there is no
saddle between soot and pah
        IcolR = (IcolR+round(Ncol/2))/scale; % convert right radial position to mm
        if IcolR<peaksoot(i-top-1,4)-delta, thresh = 3; end % stop search
    end
    peaksoot(i-top,1:2) = [IcolL,peakiL]; % store data
    peaksoot(i-top,3) = peakiL/ImageDATA(i,round(Ncol/2)); % store data
    peaksoot(i-top,4:5) = [IcolR,peakiR]; % store data
    peaksoot(i-top,6) = peakiR/ImageDATA(i,round(Ncol/2)); % store data

    peaksoot(i-top,10) =
2*sum(ImageDATA(i,1:round(Ncol/2)).*fliplr([1:round(Ncol/2)]))/round(Ncol/2)^2; % left
side radially integrated soot LII intensity
    peaksoot(i-top,11) =
2*sum(ImageDATA(i,round(Ncol/2)+1:Ncol).*[1:round(Ncol/2)])/round(Ncol/2)^2; % right side
radially integrated soot LII intensity
    peaksoot(i-top,12) = peaksoot(i-top,10)+peaksoot(i-top,11); % total radially
integrated soot LII intensity

end

peaksoot(:,1) = peaksoot(:,1)-round(Ncol/2)/scale; % shift radial axis so center is zero
peaksoot(:,4) = peaksoot(:,4)-round(Ncol/2)/scale; % shift radial axis so center is zero
peaksoot(:,7) = (peaksoot(:,2) + peaksoot(:,5))/2; % average left and right intensities
peaksoot(:,8) = (base-(top+1:i)')/scale;  % fill in axial positions in mm
```

```
peaksoot(:,9) = ImageDATA(top+1:i,round(Ncol/2));
center = mean((peaksoot(:,4)-peaksoot(:,1))/2);

% save data
disp('storing data')
Nletters = length(SPE_file);
soot_out = [SPE_file(7:Nletters-4),'Peaksoot.txt'];
fig_out = [SPE_file(7:Nletters-4),'PeakFIG'];
save(soot_out, 'peaksoot', '-ascii', '-tabs');
plot(peaksoot(:,1),peaksoot(:,8),'k',peaksoot(:,4),peaksoot(:,8),'k');
daspect([1 1 1]);
axis([-25.6 25.6  -3  48.2]);
xlabel('Radial Position (mm)');
ylabel('Axial Position (mm)');
fig_title = '40-s time averaged peak soot';
title(fig_title);
hgsave(fig_out);
```

#### 7.1.4.3.2 Ethylene IDFs from 22.7 to 73.9 mm above Burner

```
function [noise,background,center] = peakLII_C2H4_75all(SPE_file, SPE_fileNL, SNR)

% 9/10/2004 Mark Mikofski, U.C. Berkeley
% peakLII_C2H4_75all loads a 16-bit SPE image sequence of a CH4 flame,
% subtracts an image with no laser and stores the position and
% intensity of the pixels that represent the peak soot LII.

if nargin<3, SNR = 3; end % set default SNR if none entered
load('soot_correction.mat'); % load beamprofile correction file
beam = polyval(soot_correction,(1:512)/512)'* ones(1, 512); % create matrix with the soot
correction as a column
scale = 10; % scale is the number of pixels per millimeter
base = 739; % base is the number of pixels from the top of the image to the burner exit
top = 30; % top is the number of pixels from the top and bottom of the image where the
laser was clipped
noiseP = 70; % number of pixels to use for noise
Nframes = 100; % Nframes is the number of frames in the files
Ncol = 512; % number of columns (width) in SPE image
Nrow = 512; % number of rows (height) in SPE image
Nheader = 4100; % number of BYTES in Header
FrameNumberStart = 1; % first frame to read in

% matrix to contain the image data from the SPE sequence
ImageDATA = zeros(Ncol,Nrow);
IMAGE_ARRAY = zeros(Ncol,Nrow,Nframes);

% open SPE_file for reading, IEEE floating point with little-endian byte ordering
fid = fopen(SPE_file,'r','ieee-le');
origin = 'bof'; % origin = begining of file
for i = 1:Nframes
    position = Nheader+Ncol*Nrow*2*(FrameNumberStart-1)+Ncol*Nrow*2*(i-1);
    fseek(fid,position,origin); % set file position indicator
    [ImageDATA,count] = fread(fid,[Ncol,Nrow],'uint16'); % copy data to ImageDATA in 16
bit integer format
    ImageDATA = fliplr(rot90(ImageDATA,3)); % transpose imageDATA
    IMAGE_ARRAY(:,:,i) = ImageDATA; % copy ImageDATA to IMAGE_ARRAY
    if mod(i,10) == 0, disp(i); end % show progress
end
fclose(fid); % close SPE_file
ImageDATA = mean(IMAGE_ARRAY,3); % average all frames

% matrix to contain the image data from the SPE sequence
ImageDATANL = zeros(Ncol, Nrow);
IMAGE_ARRAYNL = zeros(Ncol, Nrow, Nframes);

% open SPE_file for reading, IEEE floating point with little-endian byte ordering
fid = fopen(SPE_fileNL, 'r', 'ieee-le');
origin = 'bof'; % origin = begining of file
for i = 1:Nframes
    position = Nheader+Ncol*Nrow*2*(FrameNumberStart-1)+Ncol*Nrow*2*(i-1);
    fseek(fid,position,origin); % set file position indicator
    [ImageDATANL,count] = fread(fid,[Ncol,Nrow],'uint16'); % copy data to ImageDATANL in
16 bit integer format
    ImageDATANL = fliplr(rot90(ImageDATANL,3)); % transpose ImageDATANL
    IMAGE_ARRAYNL(:,:,i) = ImageDATANL; % copy ImageDATANL to IMAGE_ARRAYNL
    if mod(i,10) == 0, disp(i); end % show progress
end
```

```
fclose(fid); % close SPE_file
ImageDATANL = mean(IMAGE_ARRAYNL,3); % average all frames
ImageDATA = ImageDATA - ImageDATANL;
ImageDATA = ImageDATA./beam; % correct imageDATA for beamprofile

% noise
background = ImageDATA(top+1:top+noiseP,1:noiseP); % upper left corner
background = [background,ImageDATA(top+1:top+noiseP,Ncol-noiseP+1:Ncol)]; % upper right
corner
background = [background,ImageDATA(Nrow-top-noiseP+1:Nrow-top,1:noiseP)]; % bottom left
corner
background = [background,ImageDATA(Nrow-top-noiseP+1:Nrow-top,Ncol-noiseP+1:Ncol)]; %
bottom right corner
background = reshape(background,4*noiseP^2,1);
noise = std(background); % calculate standard deviation of background noise
background = mean(background); % calculate average of background noise

% find peak soot intensity in each row
% left side
[peakiL,IcolL] = max(ImageDATA(top+1,1:round(Ncol/2))); % find the peak soot and column
index in first row on left side
IcolL = IcolL/scale; % convert left radial position to mm
% right side
[peakiR,IcolR] = max(ImageDATA(top+1,round(Ncol/2)+1:Ncol)); % find the peak soot and
column index in first row on right side
IcolR = (IcolR+round(Ncol/2))/scale; % convert right radial position to mm
peaksoot(1,1:2) = [IcolL,peakiL]; % average and store data
peaksoot(1,3) = (peakiL-background)/noise; % average and store data
peaksoot(1,4:5) = [IcolR,peakiR]; % average and store data
peaksoot(1,6) = (peakiR-background)/noise; % average and store data

peaksoot(1,10) =
2*sum(ImageDATA(top+1,1:round(Ncol/2)).*fliplr([1:round(Ncol/2)]))/round(Ncol/2)^2; %
left side radially integrated soot LII intensity
peaksoot(1,11) =
2*sum(ImageDATA(top+1,round(Ncol/2)+1:Ncol).*[1:round(Ncol/2)])/round(Ncol/2)^2; % right
side radially integrated soot LII intensity
peaksoot(1,12) = peaksoot(1,10)+peaksoot(1,11); % total radially integrated soot LII
intensity

i = top+1; % start from top of image
while i<Nrow-top & peaksoot(i-top,3)>=SNR & peaksoot(i-top,6)>=SNR
    i = i+1;
    % left side
    [peakiL,IcolL] = max(ImageDATA(i,1:round(Ncol/2))); % find the peak soot and column
index on left side
    IcolL = IcolL/scale; % convert left radial position to mm
    % right side
    [peakiR,IcolR] = max(ImageDATA(i,round(Ncol/2)+1:Ncol)); % find the peak soot and
column index on right side
    IcolR = (IcolR+round(Ncol/2))/scale; % convert right radial position to mm
    peaksoot(i-top,1:2) = [IcolL,peakiL]; % average and store data
    peaksoot(i-top,3) = (peakiL-background)/noise; % average and store data
    peaksoot(i-top,4:5) = [IcolR,peakiR]; % average and store data
    peaksoot(i-top,6) = (peakiR-background)/noise; % average and store data

    peaksoot(i-top,10) =
2*sum(ImageDATA(i,1:round(Ncol/2)).*fliplr([1:round(Ncol/2)]))/round(Ncol/2)^2; % left
side radially integrated soot LII intensity
    peaksoot(i-top,11) =
2*sum(ImageDATA(i,round(Ncol/2)+1:Ncol).*[1:round(Ncol/2)])/round(Ncol/2)^2; % right side
radially integrated soot LII intensity
    peaksoot(i-top,12) = peaksoot(i-top,10)+peaksoot(i-top,11); % total radially
integrated soot LII intensity

end

peaksoot(:,1) = peaksoot(:,1)-round(Ncol/2)/scale; % shift radial axis so center is zero
peaksoot(:,4) = peaksoot(:,4)-round(Ncol/2)/scale; % shift radial axis so center is zero
peaksoot(:,7) = (peaksoot(:,2) + peaksoot(:,5))/2; % average left and right intensities
peaksoot(:,8) = (base-(top+1:i)')/scale;  % fill in axial positions in mm
peaksoot(:,9) = ImageDATA(top+1:i,round(Ncol/2));
center = mean((peaksoot(:,4)-peaksoot(:,1))/2);

% save data
disp('storing data')
Nletters = length(SPE_file);
soot_out = [SPE_file(7:Nletters-4),'Peaksoot.txt'];
fig_out = [SPE_file(7:Nletters-4),'PeakFIG'];
save(soot_out, 'peaksoot', '-ascii', '-tabs');
plot(peaksoot(:,1),peaksoot(:,8),'k',peaksoot(:,4),peaksoot(:,8),'k');
```

```
daspect([1 1 1]);
axis([-25.6 25.6  22.7  73.9]);
xlabel('Radial Position (mm)');
ylabel('Axial Position (mm)');
fig_title = '40-s time averaged peak soot';
title(fig_title);
hgsave(fig_out);
```

## 7.2 DDACS Programs

As described in Chapter 5, a droppable data acquisition and control system (DDACS) was employed during drop tower tests. The following is the program that was used with the DDACS.

```
model 800

// 12-9-02 what's different?
// (1) camera and video transmitter are moved from bank 2 to bank 1,
// in order to allow manual switching
// (2) signal lights moved from bank 1 to bank2
// (3) collect data on first 4 analog channels only
// do NOT collect data on analog channels 4, 5, & 6
// (4) collect 140 drop data @ 15ms/pt for 2.1s
// (5) close solenoids and turn off ignitor after 2.1s
// (6) collect 200 post drop data @ 15ms/pt for 3s
// (7) radiometer gain changed from 206.76 to 98.85
// (8) camera and pressure transducer operated manually

// 10-31-03 what's different?
// (9) rapid insertion TEM probe added to program

// 8-6-02, Mark Mikofski, UCB

// this program is used to control the rig and collect data during a 2.2s drop

// digital outputs/inputs
// pin  relay          device
// 3    1              fuel solenoid
// 5    2              air solenoid
// 6    3              fuel solenoid
// 8    4              air solenoid
// 9    5              TEM probe solenoid
// 10   6              p-transducer
// 11   7              ignitor
// 12   8              n/c
// 15   12v b1         camera
// 16   12v b2         light
// 7    input          left side input
// 13   input          right side input

// analog channels
// channel     device                  amplification
// 0           n/c, onboard temp       n/a
// 1           TC1                     ~206.76
// 2           TC2                     ~206.76
// 3           radiometer              ~98.85
// 4    not    pressure transducer     1
// 5    not    fuel flow rate          1
// 6    not    air flow rate           1

pclr 0,3,5,6,8,9,10,11,12,15,16       // initialize
rate 1: sleep 0                       // reset rate (10ms), counter
pset 0                        // turn on temp sensor
pointer = 0                   // zero pointer
print ""

print "cosmic.drop.v4 running"
```

```
print "toggle input switch ON to begin program"
print " "

loop1:

if pin(13) = 0 goto loop1     // wait for input switch to close
sleep 0: sleep 100            // check for short, ie: wait 1 sec
if pin(13) = 0 goto loop1     // check input switch again
pset 16                       // turn on light
print "light on"
print "toggle input switch OFF to take baseline data"
print " "

loop2:

if pin(13) <> 0 goto loop2    // wait for input switch to open
pclr 16                       // light off

print "light off"
print

sleep 0:sleep 100             // wait 1 second

print "collecting 100 baseline data for 5 seconds"
print " "

rate 1: sleep 0                       // set rate to 10ms; reset sleep counter

for datapoint = 1 to 100      // take 100 datapoints (5 sec)
       burst pointer,4,2      // store first 4 channels, 2 bytes
       sleep 5                // wait 50ms/pt
next datapoint

pset 16                       // turn on light

print "baseline data complete, light on"
print "toggle input switch ON to begin preflow"
print " "

loop3:

if pin(13) = 0 goto loop3     // wait for input switch to close
pset 3,5,6,8                  // preflow
pclr 16                       // light off

print "solenoids open, light off"
print " "

loop4:

if pin(13) <> 0 | pin (7) <> 0 goto loop4    // wait for release
pset 11                                      // ignite

rate 2: sleep 0                       // set rate to 5ms; reset counter

for datapoint = 1 to 140      // take 140 datapoints (2.1 sec)
       burst pointer,4,2      // store first 4 channels, 2 bytes
       sleep 3                // wait 15ms/pt
       if datapoint = 120 pset 9     // insert probe at 1.8 sec
       if datapoint = 130 pclr 9     // retract probe at 1.95 sec
next datapoint

pclr 3,5,6,8,11                       // close solenoids; ignitor off

print "solenoids closed, ignitor off"
print "collecting 200 post-drop data for 3 seconds"
print " "

rate 2: sleep 0                       // set rate to 5ms; reset sleep counter

for datapoint = 1 to 200      // take 200 datapoints (3 sec)
       burst pointer,4,2      // store first 4 channels, 2 bytes
       sleep 3                // wait 15ms/pt
next datapoint

pset 16                       // light on

print "post-drop data complete, light on"
print

print "toggle input switch ON to display data"
```

```
rate 1: sleep 0                         // reset rate, sleep counter
wait:
sleep 100                       // conserve power
if pin(13) = 0 goto wait        // wait for input switch to close
pclr 16                         // light off
pointer = 0                     // zero pointer

print
print "HIT ALT-Z TO TURN CAPTURE ON!!!!!"
print

input "hit 'Enter' to display data" whatever
print

print "baseline data, 100 pt @ 50 ms/pt = 5 s"
print "CJ      TC1     TC2     rad     pointer"
// use spaces NOT tabs, so that excel will separate columns

for datapoint = 1 to 100
        for datachan = 1 to 4
                let dataval = get(pointer,#2)
                print #8.4f, (dataval/13107.20);
        next datachan
        print #8, (pointer/8)
next datapoint
print

print "drop data, 140 pt @ 15 ms/pt = 2.1 s"
print "CJ      TC1     TC2     rad     pointer"
// use spaces NOT tabs, so that excel will separate columns

for datapoint = 1 to 140
        for datachan = 1 to 4
                let dataval = get(pointer,#2)
                print #8.4f, (dataval/13107.20);
        next datachan
        print #8, ((pointer - 800)/8)
next datapoint
print

print "post-drop data, 200 pt @ 15 ms/pt = 3 s"
print "CJ      TC1     TC2     rad     pointer"
// use spaces NOT tabs, so that excel will separate columns

for datapoint = 1 to 200
        for datachan = 1 to 4
                let dataval = get(pointer,#2)
                print #8.4f, (dataval/13107.20);
        next datachan
        print #8, ((pointer - 1920)/8)
next datapoint
print

pset 16                         // light on

print "RESET TOGGLE SWITCH TO OFF!!!!!"

rate 1: sleep 0                         // reset rate, sleep counter
wait2:
sleep 100                       // conserve power
if pin(13) <> 0 goto wait2      // wait for input switch to close
pclr 16                         // light off

print
print "HIT ALT-Z TO TURN CAPTURE OFF!!!!!"
print
print "data complete"
print "cosmic.drop.v4 finished"

stop
```

### 7.3 PAH PLIF and Soot PLII Versus Non-Dimensional Height

PAH PLIF and soot PLII intensity were graphed versus non-dimensional height, defined as the axial position divided by the flame height determined by OH PLIF. This has the advantage of highlighting the high temperature region of the flame, which occurs near the reaction zone between a non-dimensional height of zero and one. The high temperature region is where the majority of PAH and especially soot formation occur. This can be seen very clearly in Figure 7.3 (c), which depicts radially integrated soot PLII for ethylene IDFs.

However, non-dimensional height does not scale with residence time in the high temperature region, and for this reason, it was decided to present the results in Chapter 4 using axial position. In the high temperature region in buoyant flames, the initial velocity is negligible compared to the buoyant component of velocity. Therefore, the velocity field is similar in the high temperature region for flames of different air flow rate. This is useful, because it allows the axial position to be related to residence time in the high temperature region.

In contrast to the high temperature region, non-dimensional height does scale with residence time on the centerline. This is because temperatures are low on the centerline, and therefore the initial velocity of the air flow dominates over buoyant component of velocity. Graphs of centerline intensity versus non-dimensional height may provide insight into the transport and fate of PAH and soot. For example, in Figure 7.1 (f) it appears that instability is enhancing the transport of PAH to the centerline for the 1.4 slpm air flow rate ethylene IDF.

### 7.3.1 Ethylene IDFs

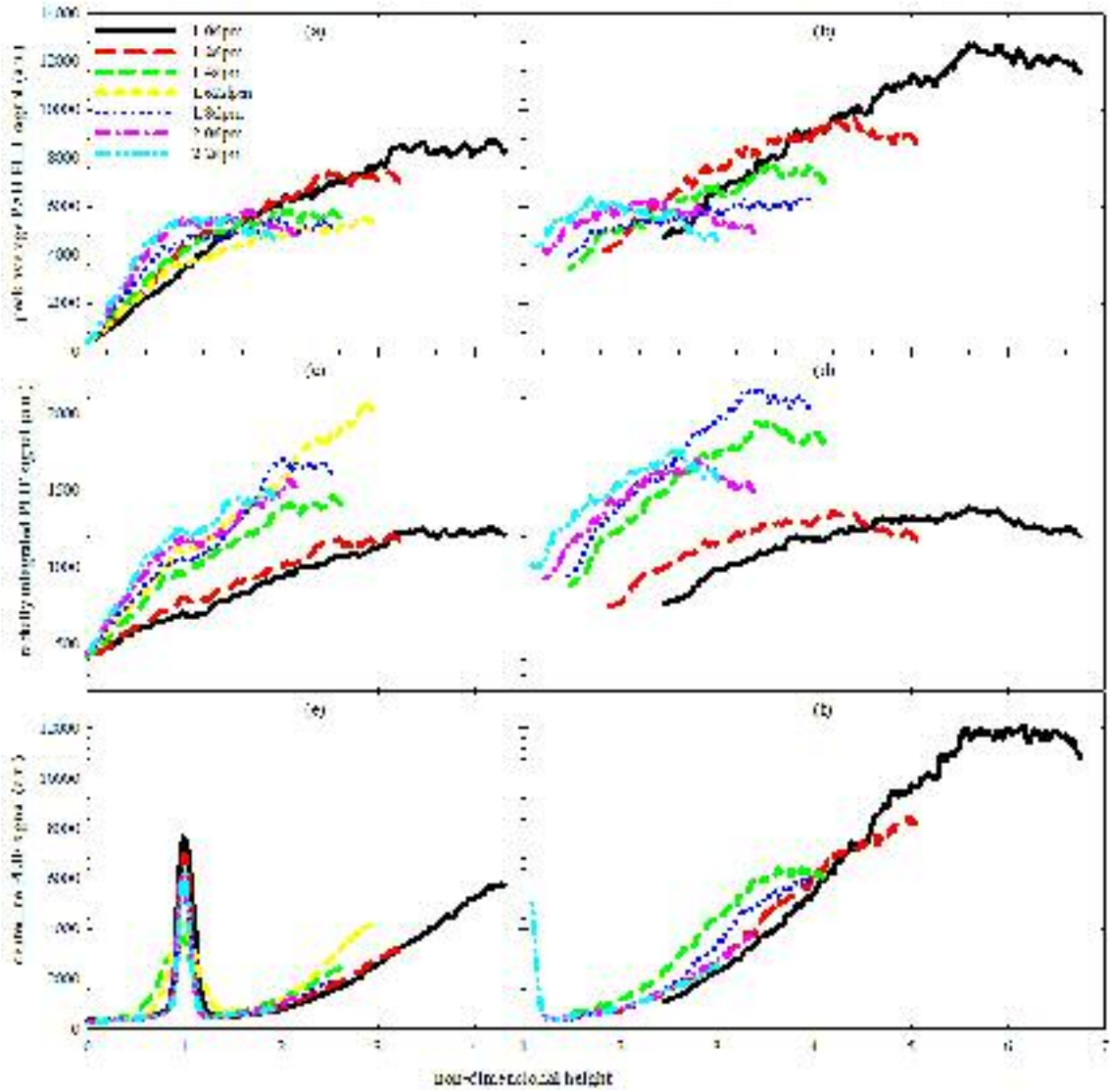

**Figure 7.1: PLIF detected with 340 nm band-pass filter in ethylene IDFs versus non-dimensional height, defined as axial position divided by flame height determined by OH PLIF. (a) Peak PAH PLIF, (b) radially integrated PLIF and (c) centerline PLIF from 0 mm to 45.1 mm, (a), (c) and (e), and 25.7 mm to 70.8 mm, (b), (d) and (f), above the burner.**

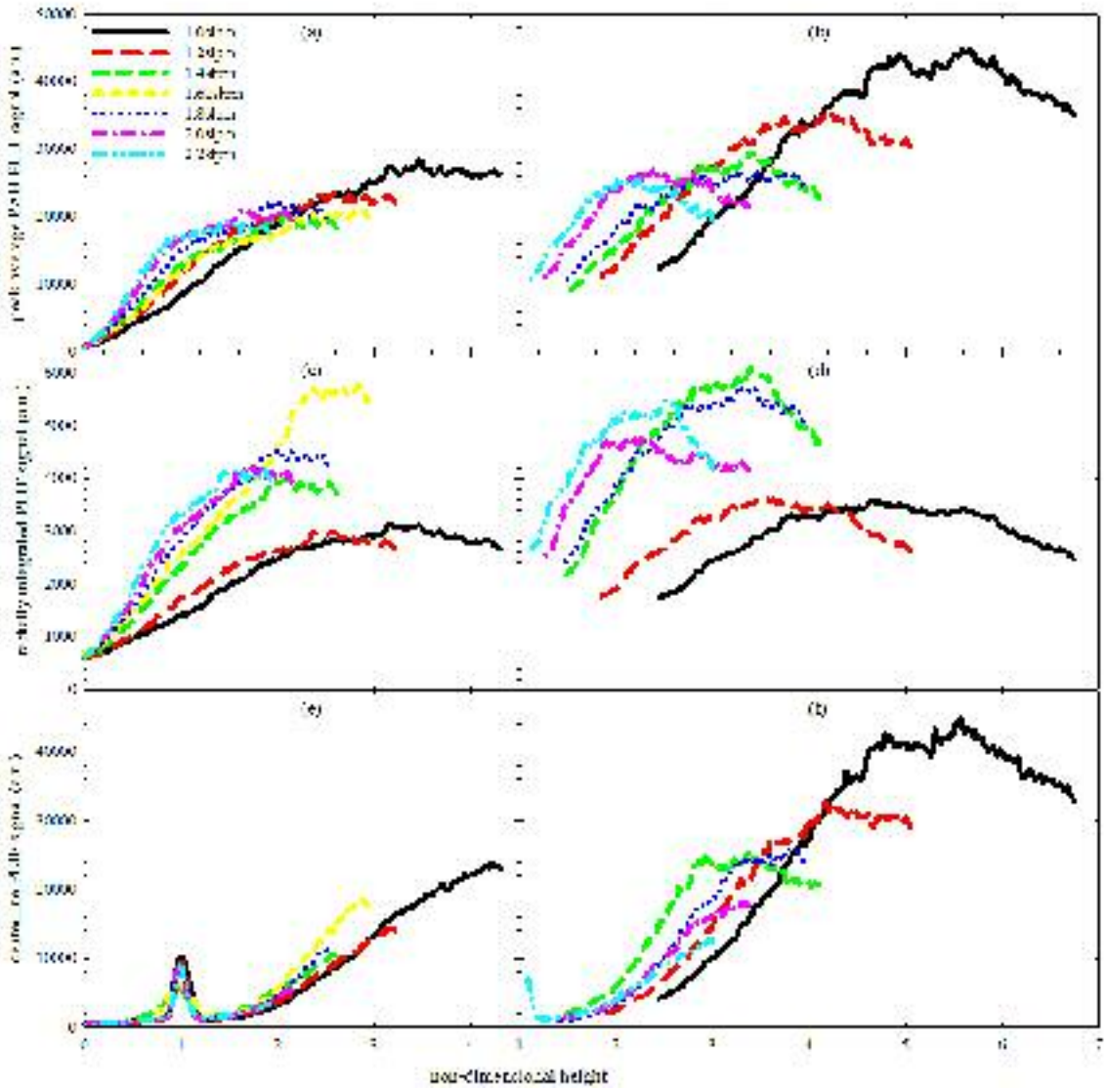

**Figure 7.2: PLIF detected with 295 nm long-pass and 450 nm short-pass filters in ethylene IDFs versus non-dimensional height, defined as axial position divided by flame height determined by OH PLIF. (a) Peak PAH PLIF, (b) radially integrated PLIF and (c) centerline PLIF from 0 mm to 45.1 mm, (a), (c) and (e), and 25.7 mm to 70.8 mm, (b), (d) and (f), above the burner.**

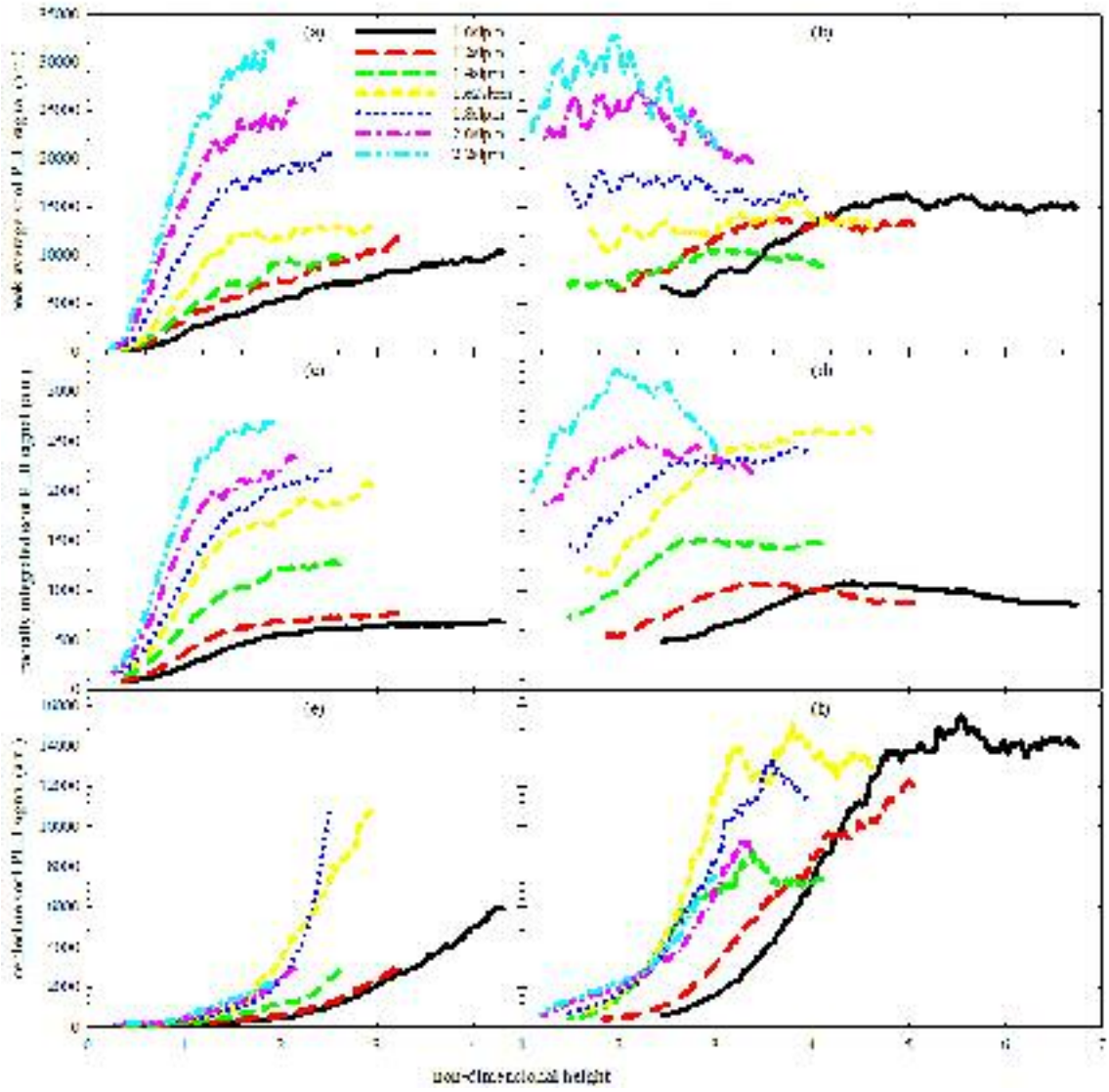

**Figure 7.3: Soot PLII detected with 570 nm long-pass filter in ethylene IDFs versus non-dimensional height, defined as axial position divided by flame height determined by OH PLIF. (a) Peak PAH PLIF, (b) radially integrated PLIF and (c) centerline PLIF from 0 mm to 45.1 mm, (a), (c) and (e), and 25.7 mm to 70.8 mm, (b), (d) and (f), above the burner.**

### 7.3.2 Methane IDFs

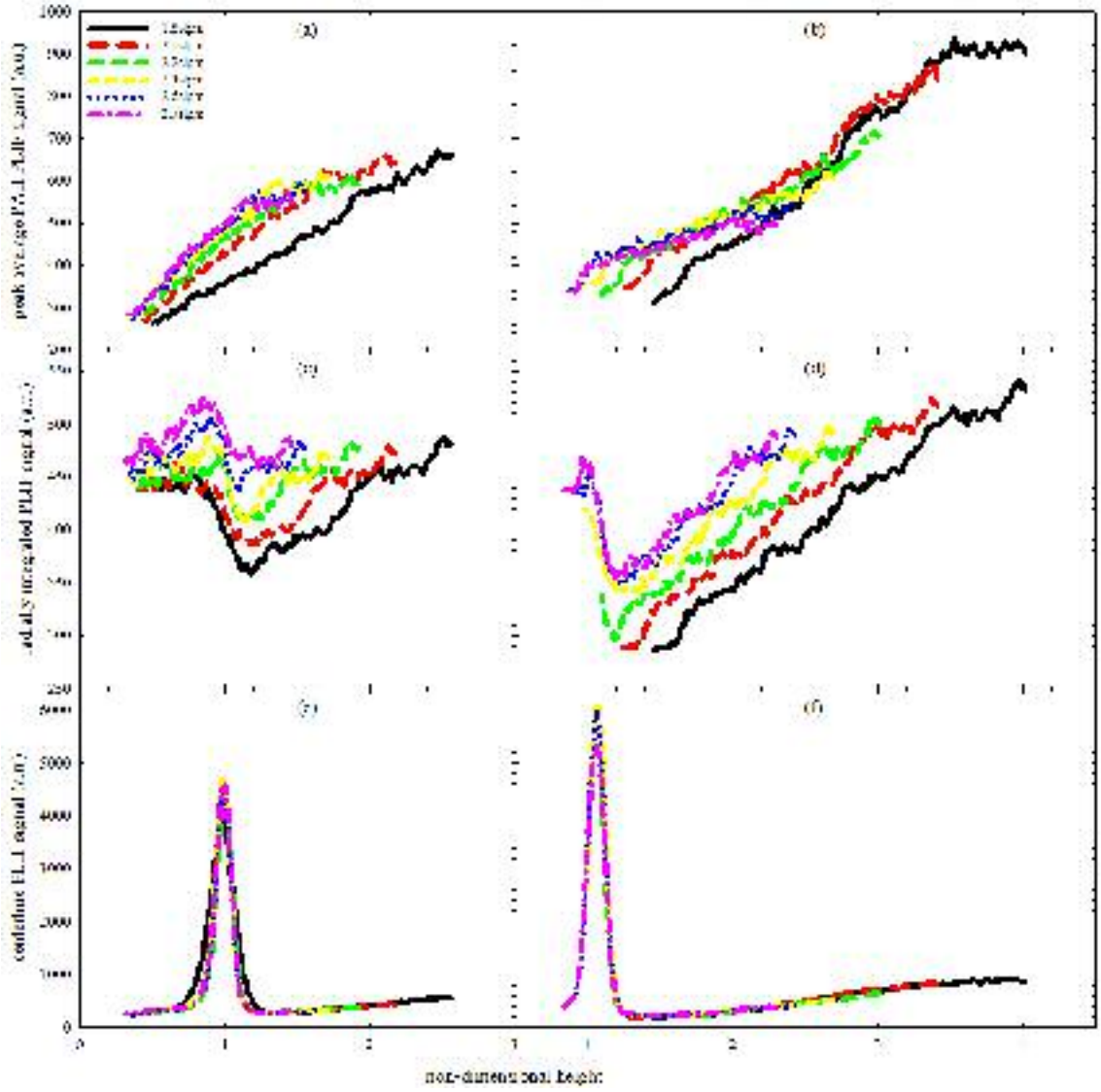

**Figure 7.4: PLIF detected with a 340 nm band-pass filter in methane IDFs versus non-dimensional height, defined as axial position divided by flame height determined by OH PLIF. (a) Peak PAH PLIF, (b) radially integrated PLIF and (c) centerline PLIF from 0 mm to 45.1 mm, (a), (c) and (e), and 25.7 mm to 70.8 mm, (b), (d) and (f), above the burner.**

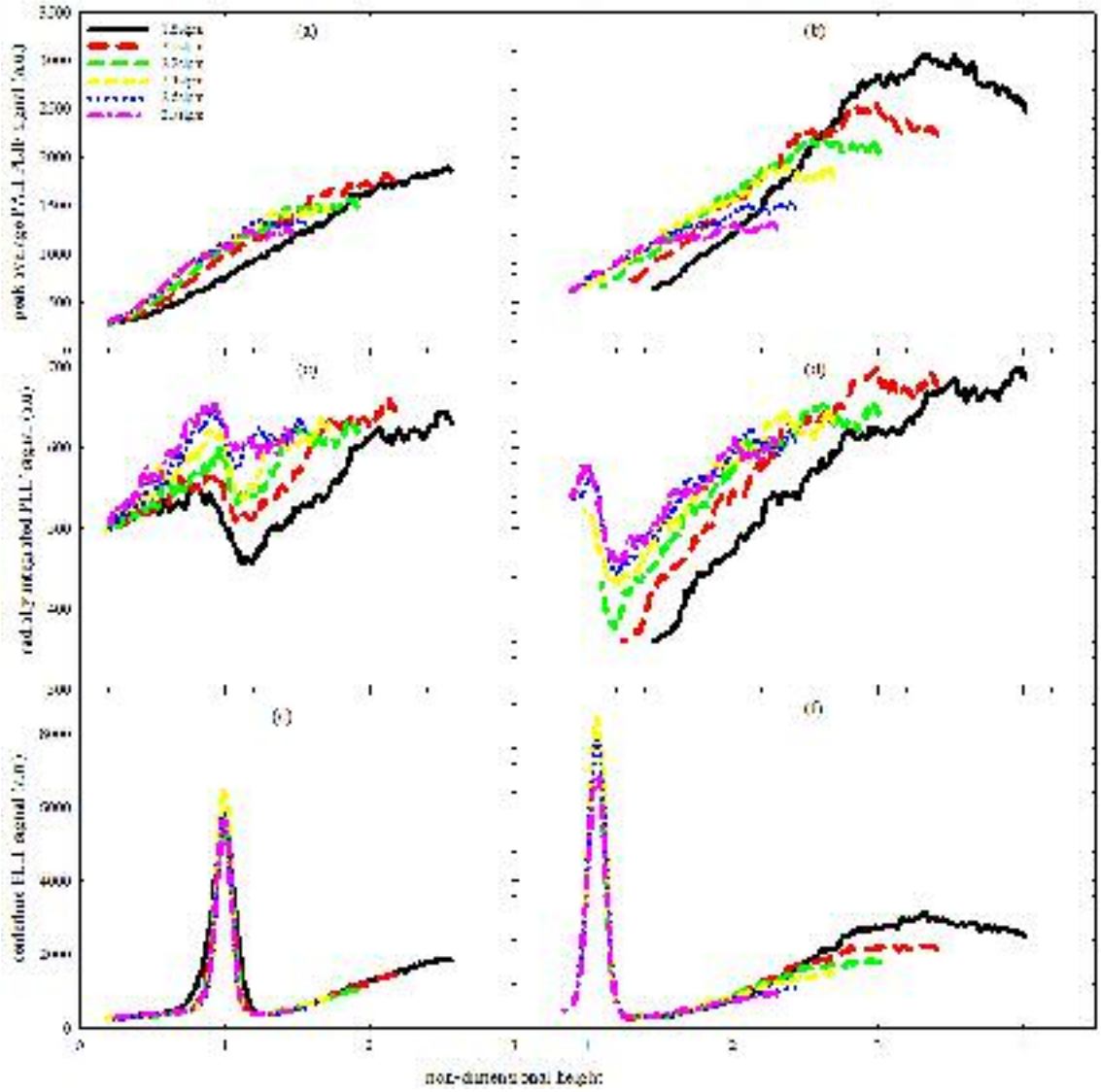

**Figure 7.5: PLIF detected with 295 nm long-pass and 450 nm short-pass fiters in methane IDFs versus non-dimensional height, defined as axial position divided by flame height determined by OH PLIF. (a) Peak PAH PLIF, (b) radially integrated PLIF and (c) centerline PLIF from 0 mm to 45.1 mm, (a), (c) and (e), and 25.7 mm to 70.8 mm, (b), (d) and (f), above the burner.**